Final Scientific / Technical Report

Reporting Period: December 2015 – September 2018

Date: September 29th, 2018

Prepared for:

U. S. Department of Energy

Submitted by:

Cummins Inc.

Columbus, IN

DUNS Number: 133262261

Prime Recipient Type: Private Company

DE-FOA-0001201: FY2015 Vehicle Technologies Program Wide Funding Opportunity Announcement

Enabling Technologies for Heavy-Duty Vehicles – Cummins 55BTE

DoE Program Award Number: DE-EE0007281

Award Type: Cooperative Research and Development Agreement

Prepared by:

Lyle E. Kocher, Ph.D.

Principal Investigator

Technical Project Leader – Advanced Engine Development

lyle.e.kocher@cummins.com / 812-377-2507

Table of Contents

Executive Summary

The Cummins 55% BTE (55BTE) program has completed the planned technical work on the project. This work includes the planned engine system demonstration in pursuit of the goal of demonstrating a peak system brake thermal efficiency (BTE) of 55%. The engine system included a high efficiency diesel engine integrated with a state-of-the-art waste heat recovery (WHR) system and an advanced aftertreatment system capable of meeting the current emissions standards. While the ultimate program goal of 55% BTE was not fully achieved due to hardware issues during the final testing phase, the program demonstrated a significant increase in reported engine system BTE for a heavy duty sized engine. The previous demonstrations in the Department of Energy funded SuperTruck 1 programs ranged between 50% - 51% BTE. The Cummins 55% BTE program demonstrated 54% BTE. Additionally, the program established a revised path-to-target showing how the system could be improved to reach the ultimate program goal of 55% BTE with some minor modification to the engine system. The changes in the revised path-to-target were unable to be completed during the course of this program due to time and money constraints placed on the program.

The program's goals were challenging in both scope and timing. Although the program's goal can be simply stated in terms of demonstrating a system efficiency of 55%, the achievement of a heavy-duty diesel engine capable of full torque curve operation, adequate transient performance, low emissions and high brake thermal efficiency (>51% BTE) had not been previously demonstrated in a heavy-duty engine. The Department of Energy funded SuperTruck 1 program only demonstrated efficiencies of 50%-51% BTE. During these efforts, much of the more-easily implementable changes had been investigated and included. This makes follow on work aiming to further increase efficiency more difficult as the bigger improvements had already been incorporated. Additionally, there were virtually no subsystems that were not improved during the SuperTruck 1 programs. This meant that the team would need to go back and try to further improve virtually all subsystems again in this effort to achieve the stated program goals.

The program made several advancements in all system areas. The combustion system was re-designed for a shorter combustion duration and lower in-cylinder heat loss. This was achieved through optimization of the fuel injection rate shape, number of spray holes, piston bowl shape, compression ratio, piston oil cooling, heat flow through the piston and in-cylinder charge motion. The air handling system was re-designed to provide cooled EGR at virtually no pumping penalty. This was achieved through implementation of a dual loop EGR system, reduction of EGR system pressure drop, and implementation of advanced turbocharger efficiency technologies. The engine friction and parasitic signature was dramatically reduced by the program through adoption of variable flow pumps, advanced rings and coatings, rollerized valvetrain, adoption of low viscosity lubricants and reduction in cylinder line bore distortion. The aftertreatment system was optimized through use of low dP substrates and an ammonia gas injection system. The WHR system development included the use of a dual-entry turbine and a mixed charger cooler. Finding and implementing these solutions in a short two-year program at the budgeted funding provided the greatest challenge for the program.

The details of these advances are covered in Section III of the report.

Section I - Accomplishments and Milestone Update

1. Introduction

The objective of the *Enabling Technologies for Heavy-Duty Vehicles: Cummins 55% BTE* (55BTE) program is to design, develop, and demonstrate a state-of-the-art diesel engine system that meets US EPA 2010 Heavy-Duty Emission Standards and achieves a peak brake thermal efficiency (BTE) of 55%.

The program objectives are:

Objective 1: Use a diesel engine system to demonstrate in a test cell peak engine system efficiency of 55% BTE.

Objective 2: Develop and demonstrate an advanced, highly integrated combustion/aftertreatment system to achieve 2010 emissions compliance.

The program will deliver 55% BTE by leveraging Cummins expertise in combustion, engine design and waste heat recovery (Cummins Engines), fuel injection (Cummins Fuel Systems), turbocharging (Cummins Turbo Technologies), and aftertreatment (Cummins Emission Solutions) to provide an integrated total system solution.

2. Schedule and Milestone Status

The Cummins 55% BTE program consists of four phases carried out over a two-year period. An overview of the work contained within each phase is detailed below.

- **Phase 1, System Design & Analysis** to develop detailed component and system designs prior to the time and cost-intensive prototyping phase.
- **Phase 2, Design Procurement & Rig Validation** to refine component and system designs prior to the time and cost-intensive prototyping phase.
- **Phase 3, Multi-Cylinder Engine Development Testing** to validate the combined system level effects of proposed system architectures and components.
- **Phase 4, Final Multi-Cylinder Engine Demonstration** in a test cell of a diesel engine system with a peak efficiency of 55% BTE that meets 2010 emissions standards to address the ultimate technical objectives of the RFP.

The major program milestones contained in the Cummins – DoE contract are listed in Table 1. The program milestones are used to track the health of the program.

Table 1: 55BTE Program Milestones

Budget Period	Milestone	Description	Delivery Date
1	M1	Lube Pump Design Complete and Procured	3/31/2016 **Complete**
1	M2	Air Handling Controls System Design Selection Complete	6/30/2016 **Complete**
1	M3	Lube Pump Design Integration Complete	09/30/2016 **Complete**
1	M4	WHR Turbine Expander Design Complete	12/31/2016 **Complete**
1	GNG1	50% BTE (Engine Only) Demonstration Complete	12/31/2016 **Complete**
2	M5	Aftertreatment System Design Complete	3/31/2017 **Complete**
2	M6	SET Emissions Demonstration Complete	6/30/2017 **Complete**
2	M7	Hot FTP Emissions Demonstration Complete	9/30/2017 **Complete**
2	M8	55% BTE Final Demonstration Complete	01/31/2018 **Complete**

3. Technical Discussion and Project Reporting

3.1 Advanced System Design

Valvetrain Design

The valve train on the diesel engine is a sub-system affecting both the open cycle and mechanical efficiency of the engine. The design work was conducted to explore analytically ISX15 valve train re-design options for increasing overall brake thermal efficiency by valve train component improvements. Figure 1 shows the typical components of the engine valve train system. Also indicated are the boundary conditions assumed for the analytical valve train parasitic loss study for a typical ISX15 engine configuration.

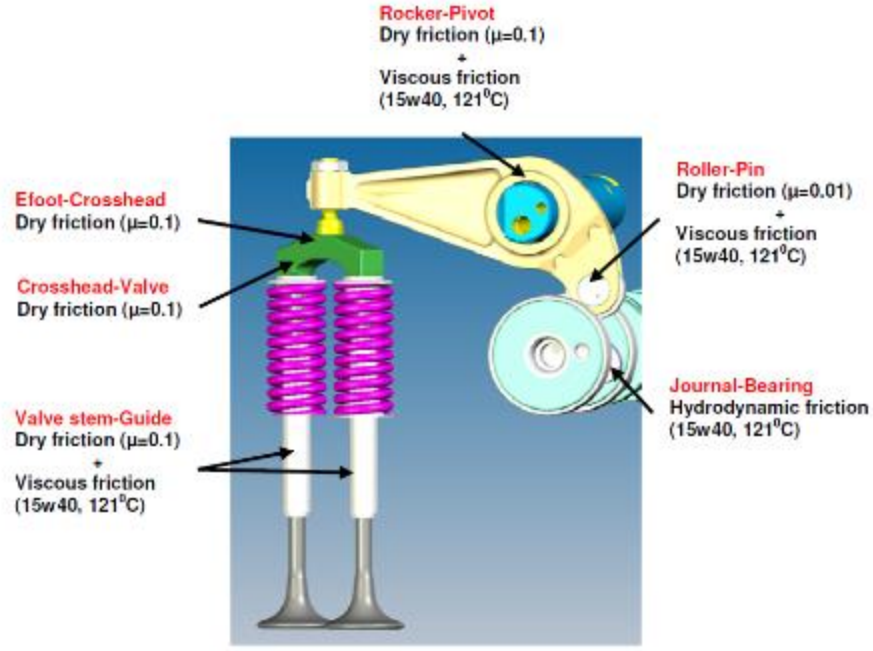

Figure 1: Various friction models used in overall estimation of valve train friction.

The results of the analytical study show the valve train parasitic losses and their proportional contributions from various valve train components at various engine operating points. It is observed that the work against gas forces and rocker pivot friction are significant contributors to the overall valve train parasitic

loss. The analytical study further predicts a ~10% reduction in overall valve train power loss if spring rate is reduced by 80%. Furthermore, reducing cam journal diameters showed only minor benefits using bushings.

Further study of the work against gas pressures has led to the finding that the spring preload is a significant contributor to the valve train loading. The spring preload is a function of the maximum pressure differential across the valve against which the valve should remain closed during engine operation.

Figure 2 shows the spring load versus valve lift for various spring rate and preload combinations. Figure 3 shows the spring load comparison across various options.

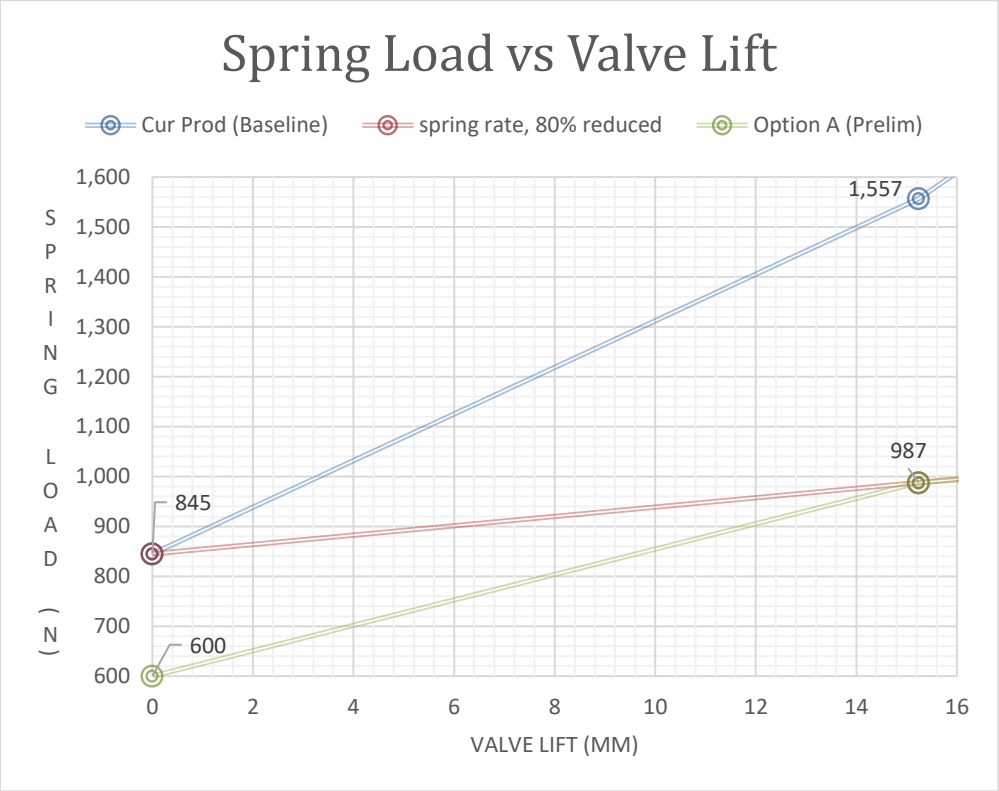

Figure 2: Spring load versus Valve Lift comparison

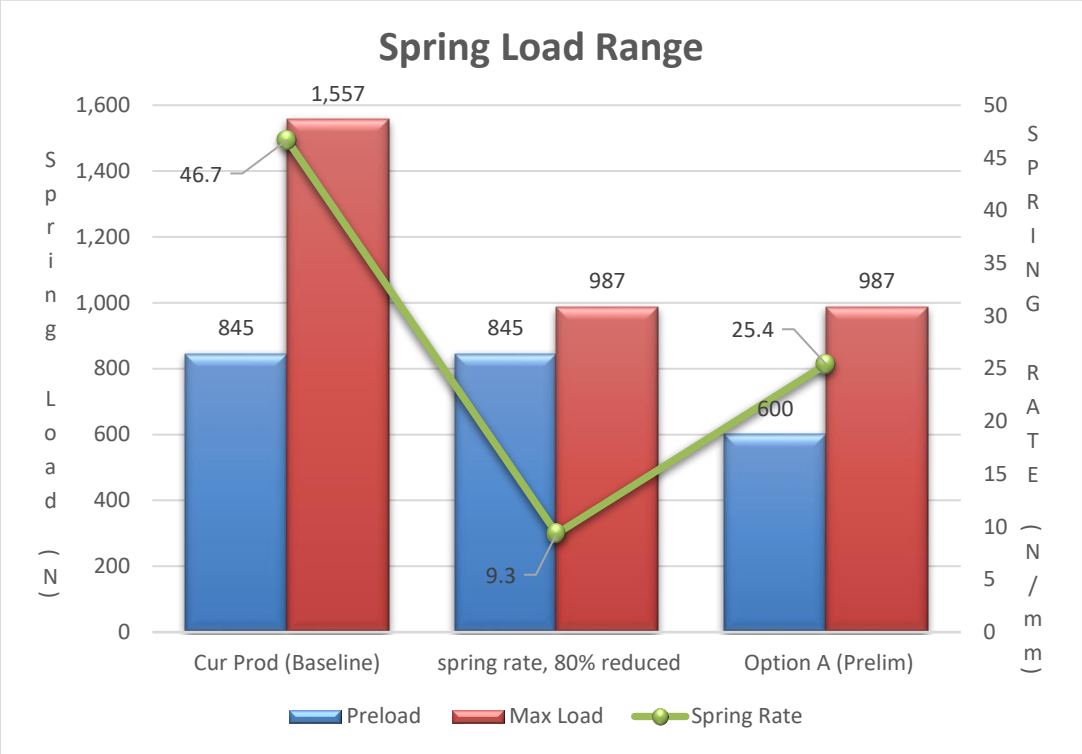

Figure 3: Spring Load Range Comparison

Another approach pursued, is incorporating rolling element bearings into the valve train at the moving contacts. Designing of roller bearing rocker pivots is intended to reduce the rocker pivot friction. Additionally, rolling contact bearings tend to have a lower oil flow requirement than their journal bearing counterparts which would enable oil pump downsizing, thus increasing BTE. It also simplifies oiling strategy to overhead by eliminating numerous oil cross-drillings found throughout rocker arm / rocker shaft assemblies. A design concept to incorporate ball bearings on the existing ISX15 camshaft is shown in Figure 5.

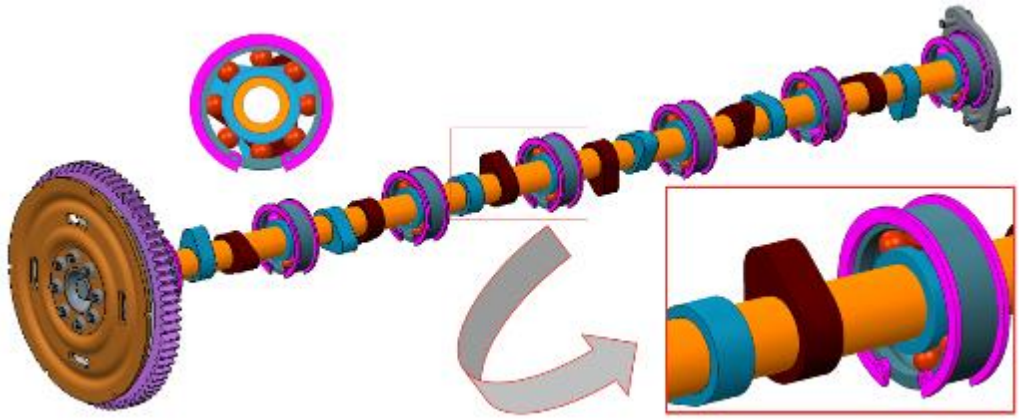

Figure 4: ISX15 ball bearing camshaft concept

A third approach is also adopted to reduce the overall weight and inertia of the valve train components. This includes 1) lighter materials and weight reduction for the rocker arm, 2) reducing the valve effective mass (valves, crossheads, spring retainers, and lash adjusters), 3) use of hollow valves and 4) reduction in

roller follower mass and polar moment of inertia about roller pin. Figure 6 shows a valve train system concept incorporating all the above design changes in comparison to the original ISX15 valve train shown in Figure 5.

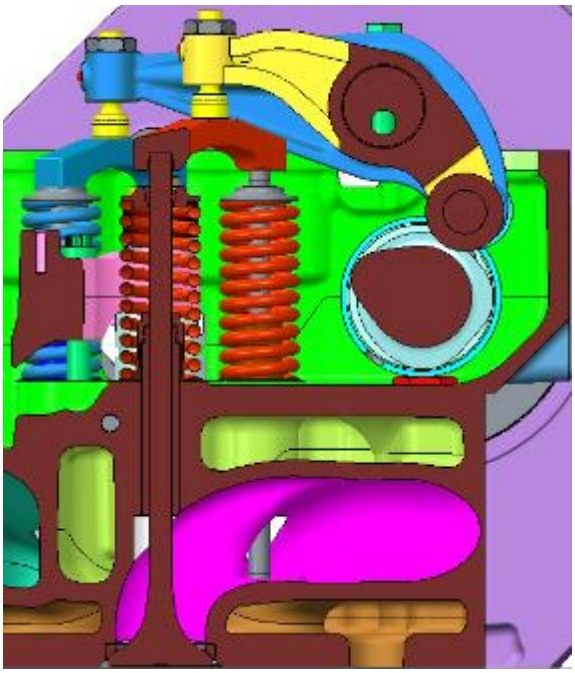

Figure 5: Existing ISX 15 Valve train layout

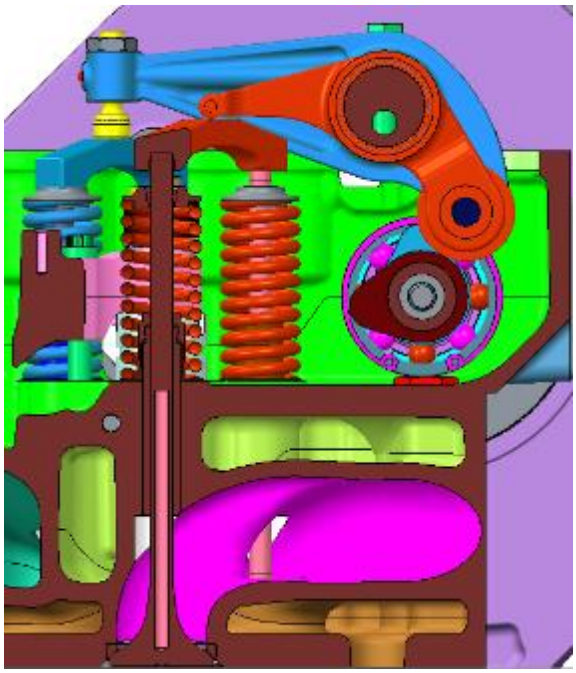

Figure 6: Optimized OPTION A valve train concept layout

The preload requirement for valves was determined by performing force balance on the valves (see Figure 7). The gas forces on the intake valves (see Figure 8) and exhaust valves (see Figure 9) were determined across the cycle using a calibrated GT model.

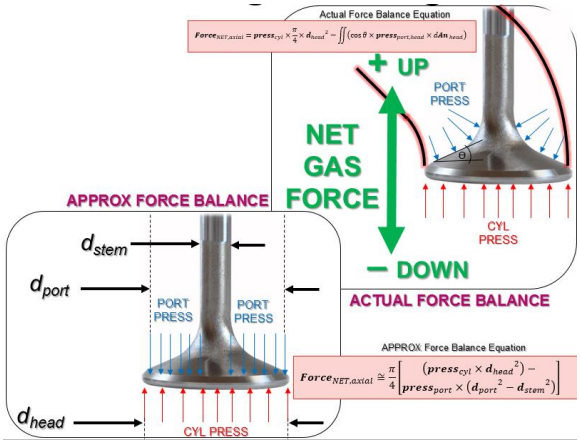

Figure 7: Gas force calculation for spring preload determination

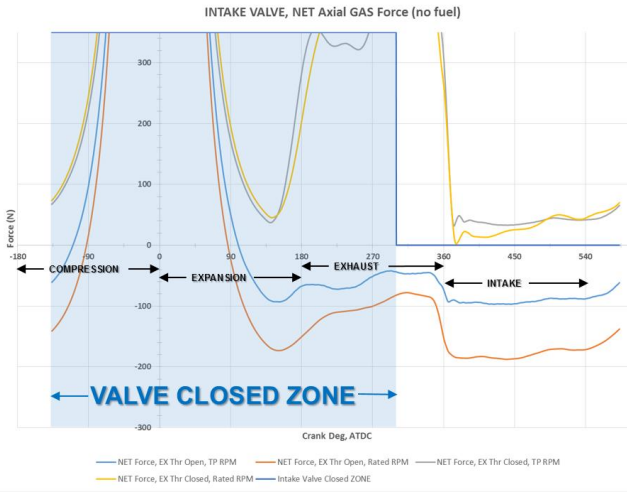

Figure 8: Intake valve gas forces v/s crank angle

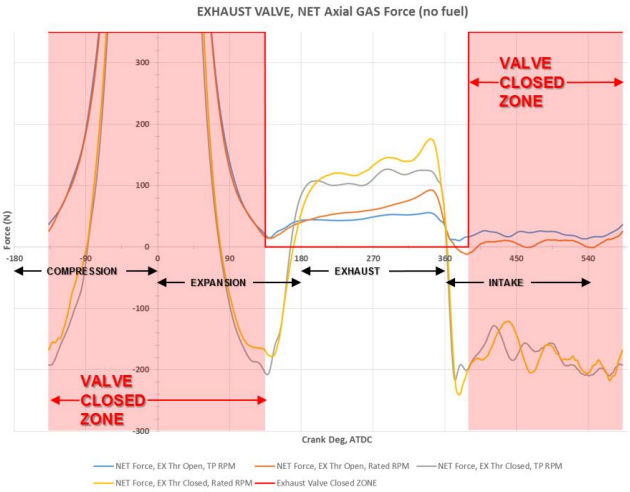

Figure 9: Exhaust valve gas forces v/s crank angle

GT valve train cam contact force design of experiments (DOE) study was conducted to assess the occurrence of no follow conditions at different speeds and spring loads. The results indicate speeds at which the cam contact force will be zero for various cases. Based on this information, two sets of springs were procured – a) Aggressive design spring set b) Conservative design spring set. The aggressive design spring is 65% reduction in spring loads from current product. The conservative design spring is around 35% reduction in spring loads from current product. The spring preload is critical in keeping the valve closed against gas pressure and responsible for the operating loads on the valve train.

Based on the GT valve train analysis, the polar moment of inertia needs to be reduced by 36% from the existing current product design. Considering this, the rocker arms were re-designed for reduced inertia while maintaining the same the stiffness. To match the stiffness with the current product valve train, comparative ALD iteration were conducted to match the valve side tip displacement of the new design with the current product. Furthermore, fatigue calculations were performed to ensure the new lightweight rocker arm design does fail during operation.

In addition to the cam shaft, other bearing interfaces within the valve train were also optimized to replace journals with roller bearings. Detailed analysis and design work was conducted in collaboration with the bearing supplier to replace the cam follower, rocket pivot and tip roller bearings. Of all the bearing joints in the system, the replacement of the tip ball joint to the tip roller bearings is a new, unique and difficult piece of the design. This joint was critically analyzed with regards to possible misalignment in the system and design to accommodate it during operation.

The replacement of all journals in the valve train system with roller bearings leads to a considerable reduction in the oil flow requirements. GT analysis study of the base engine lube system showed that 25-30% of the oil flow was required for the overhead on the base engine. The bearing supplier's rig testing results predict a cam roller follower requires between 0.25 and 20 cc/min for adequate cooling. Based on this information, an estimated flow requirement for the new system design came out to ~0.01 to ~0.86 LPM for entire valve train. This is the flow required by the roller bearing overhead valve train against ~26 LPM for the existing journal bearings based production valve train achieving a substantial oil flow reduction and thereby reducing lube system parasitic. All the major components related to this low parasitic valve train have been kicked off with suppliers for procurement.

With oil flow being so low, it was recommended by the supplier to drip individually at the bearing locations to get the maximum bearing life. To enable this and provide sight access to the valve train during

operation, a new valve cover was designed as shown in Figure 10. The lube is fed to the valve cover through a single external feed as shown and then distributed through the integrated oil circuit under the valve cover. The sealed sight windows clearly show the valve train during operation and lube dripping on the bearings as evident during the rig testing. The overhead lube circuit was designed to meet the supplier drip requirements and achieve an even flow distribution as seen in Figure 11.

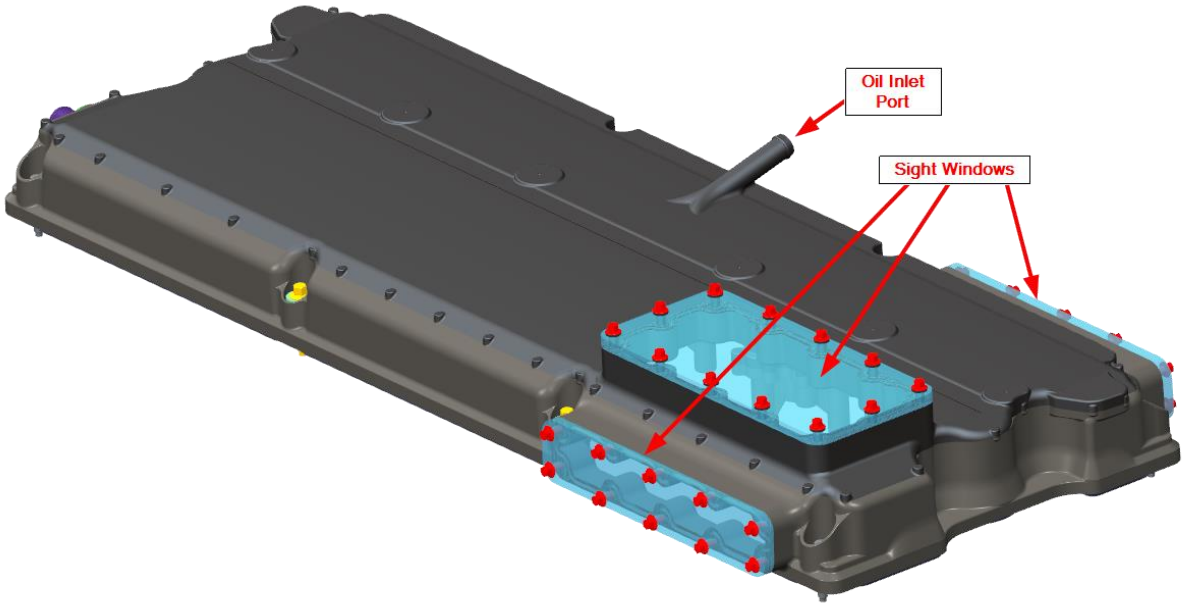

Figure 10: Valve cover design for roller bearing valve train

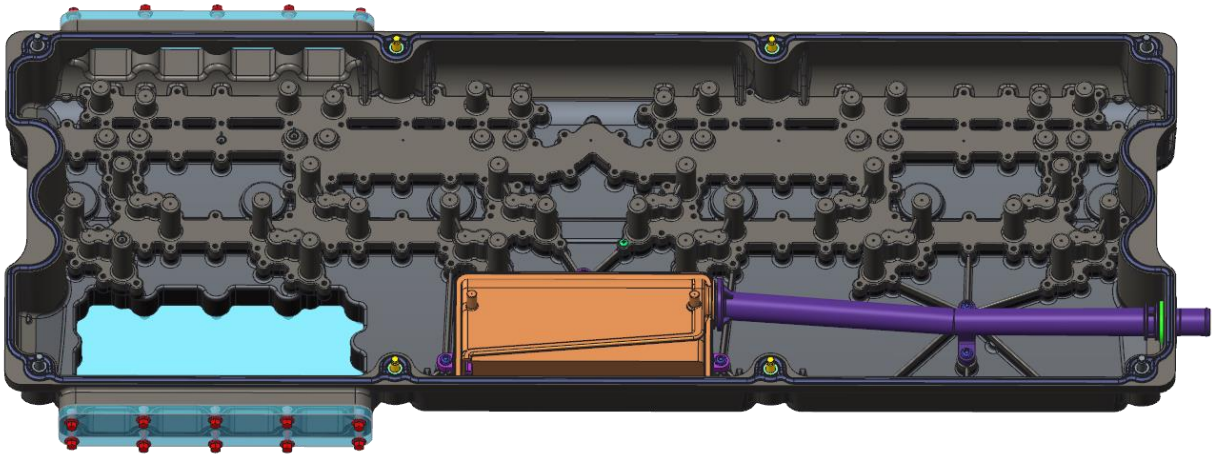

Figure 11: Oil feed passages integrated into the valve cover

The challenge with making this valve cover was its large expanse across the length of the engine. It was difficult to find suppliers that had the tooling to make this in one piece within the lead times for the program. Considering this and the procurement lead time, the new valve cover was 3D printed in glass filled nylon which has been tested previously to work in an engine environment. Due to its sheer size, it was printed in six pieces and then bonded together to form the final part as shown in Figure 12. The tongue and groove was designed around the lube passages to enable effective sealing and assembly. To achieve a “drips per second”

flow rate needed by the roller bearings, the feed pressure needed to be throttled down to less than 1 psia using an external valve.

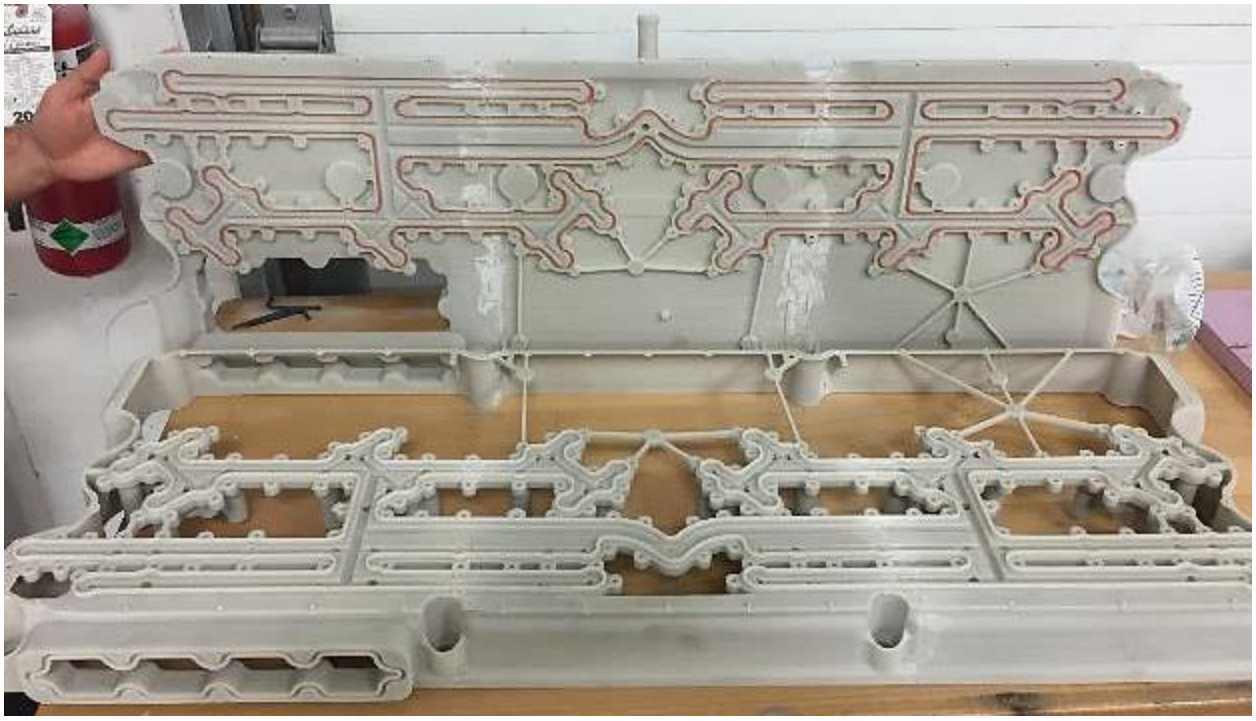

Figure 12: 3D printed valve cover with sections showing the internal oil feed circuit

One novel feature of our valve train design is the replacement of the spherical joint to roller on crossheads which actuate the valves in pairs. This requires an effective lash setting method to prevent substantial misalignment that can drive stresses in the roller pin joint. To achieve this, accurate shims were used set valve lash and stress analysis was conducted as shown in Figure 13. The deflection analysis is shown

in Figure 14 which shows the deflection is held within 4 microns. Figure 15 shows the procured crosshead part.

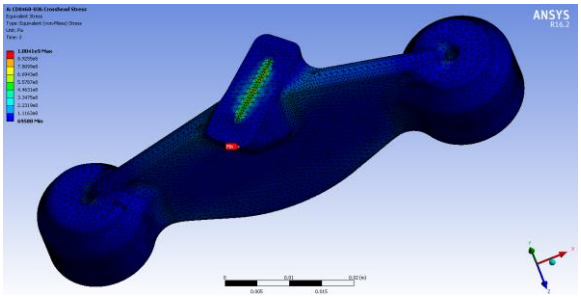

Figure 13: Stress analysis for crosshead

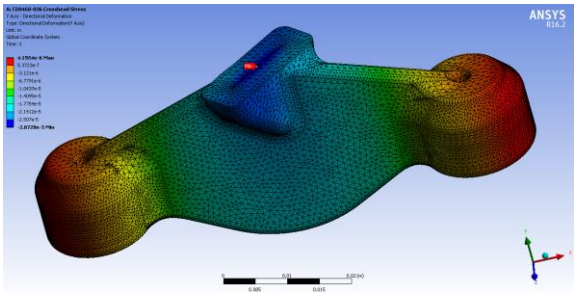

Figure 14: Deflection analysis for crosshead

Figure 15: Crosshead design procured

Since all journal bearings in the overhead are replaced with cylindrical roller joints, another challenge was encountered in the assembly of these components. The supply chain being geared towards simple journal shaft assemblies, it was hard to find suppliers with expertise in making roller rocker assemblies. Because of this, an assembly process and fixture had to be designed to slip and retain the rollers in the rockers while installing the pins. Figure 16 shows the rocker assembly fixture with spring loaded push rods to hold the rollers in place while the pins are assembled. Figure 17 shows the actual rocker assembly with the pins in place.

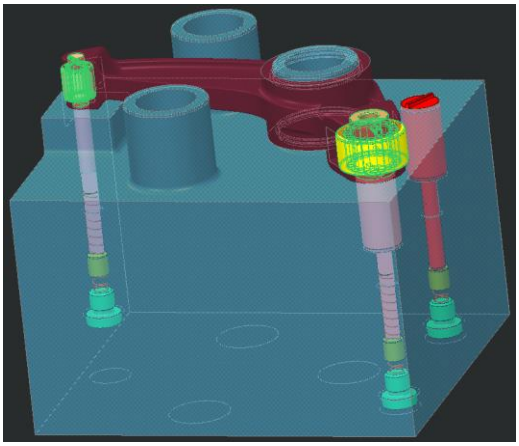

Figure 16: Rocker bearing assembly fixture design

Figure 17: Rocker bearing assembly fixture

Figure 18 shows the completed rocker assembly with roller bearings and pins pressed in place. The center bearing roller is held in place by a temporary sleeve until the rocker are assemble on the rocker shaft. Figure 19 shows the final assembled rocker shaft. The complete overhead assembly on the production head is shown

in Figure 20. Figure 21 shows a still image of the oil dripping at precise locations at 1400 engine rpm. The lube flow to the overhead was substantially reduced as evident from the testing results.

Figure 18: Roller bearing rocker assembly

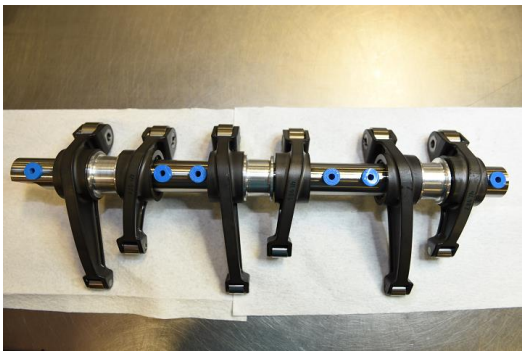

Figure 19: Assembled rocker shaft

Figure 20: Fully assembled overhead roller bearing valve train

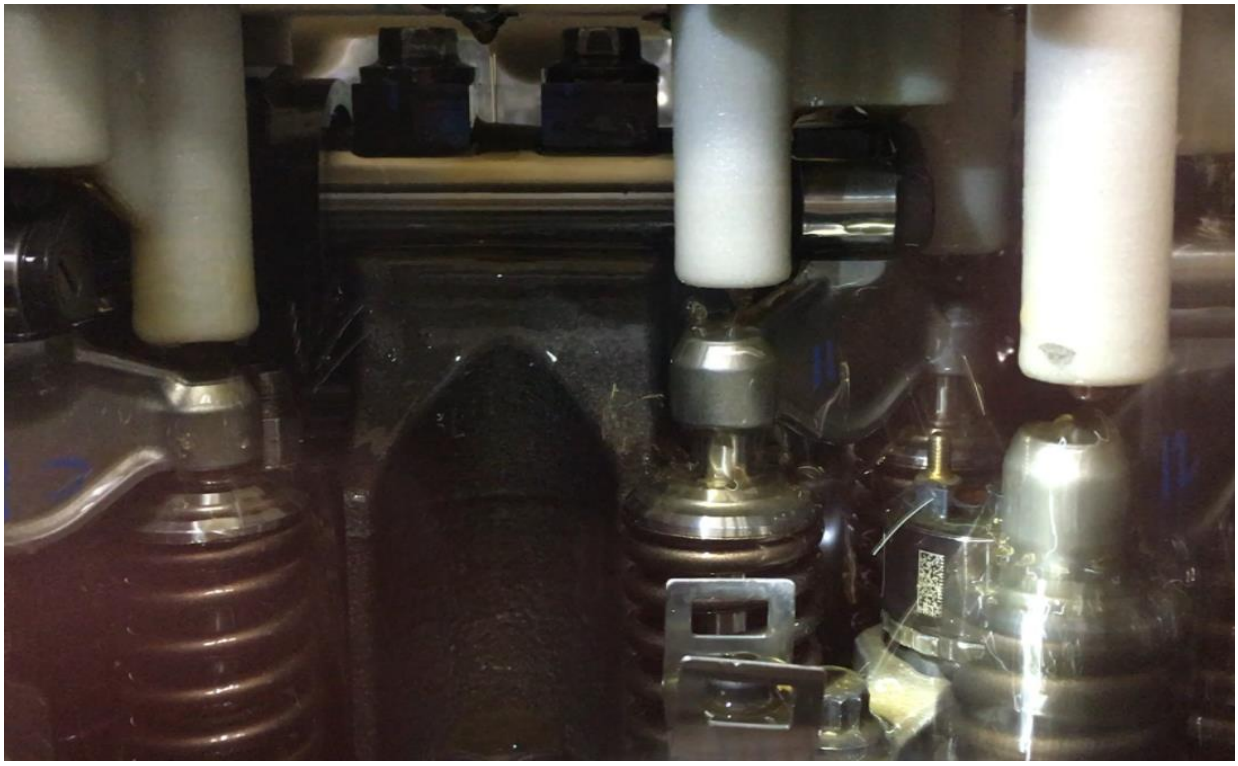

Figure 21: Oil dripping at various moving joints at 1400 engine RPM

To enable the reduced flow to the overhead and reduce parasitic power loss for the lube pump, an external oil routing setup was devised. Figure 22 shows the components of this and a schematic flow layout. The pressurized lube from the lube pump is channeled out from the block and fed to a low delta P filter arrangement. This flow is then directed through a low delta P oil cooler. From the oil cooler it is branched

into 3 circuits – 1) the valve cover and overhead lube circuit; 2) the turbocharger bearings and 3) to the main rifle to feed the main bearings and rod.

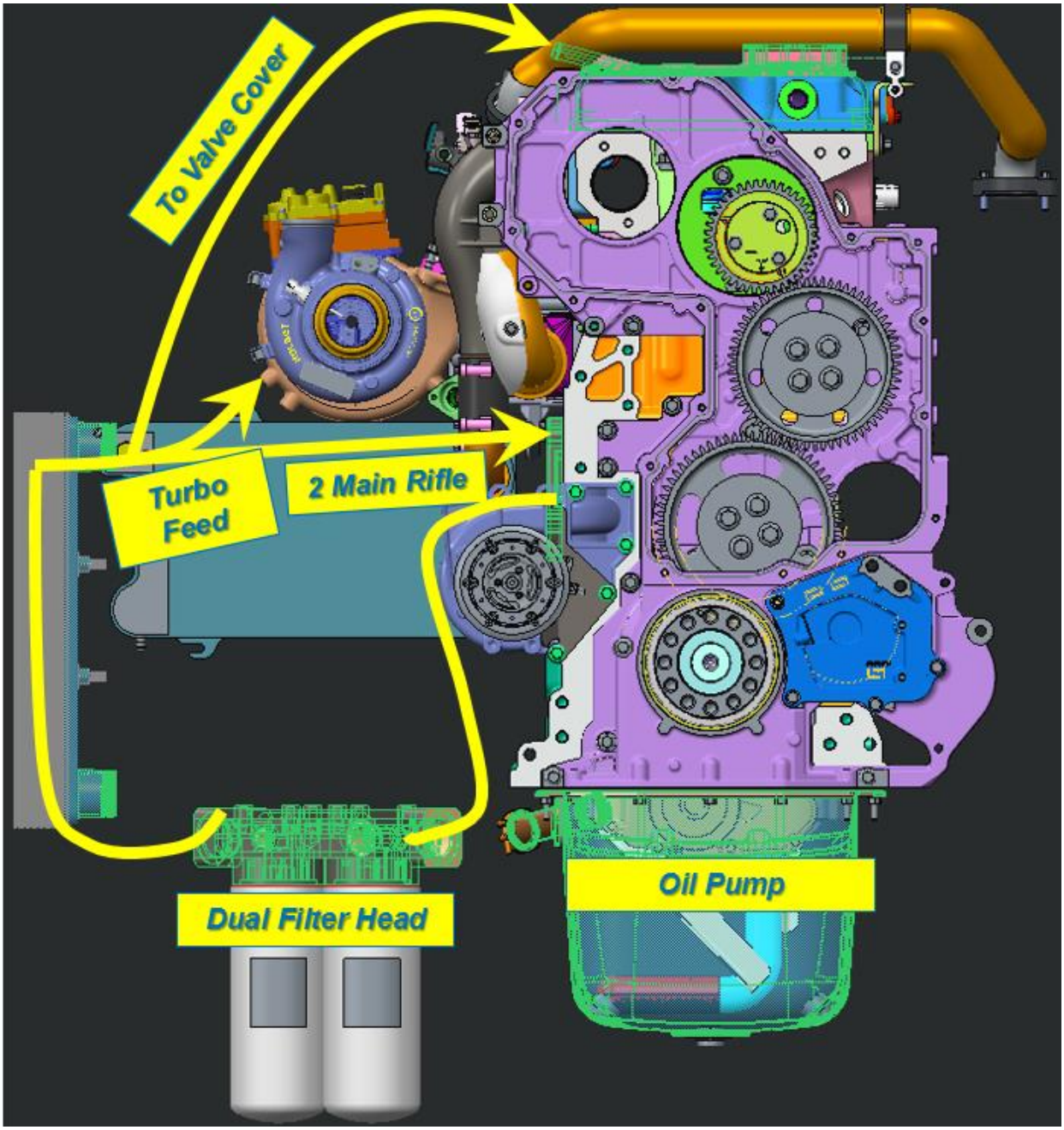

Figure 22: Schematic of external lube circuit layout for 55% BTE Testing

The roller element bearing valve train designed for the engine was successfully tested on a component test rig. To enable it to be tested on a firing engine, additional optimization was performed for the valve train lubrication system to make it robust to withstand the engine vibration while achieving even oil flow distribution.

Figure 23 shows a metallic production valve cover modified to accommodate the new low flow overhead lubrication system. This is achieved by a system of 7 rails acting as oil feed passages mounted on the valve cover as seen in Figure 24. The feed through these is regulated by a control valve mounted on the top of the

valve cover. The valve cover also accommodates sealed openings for the six cylinder pressure sensor conduits.

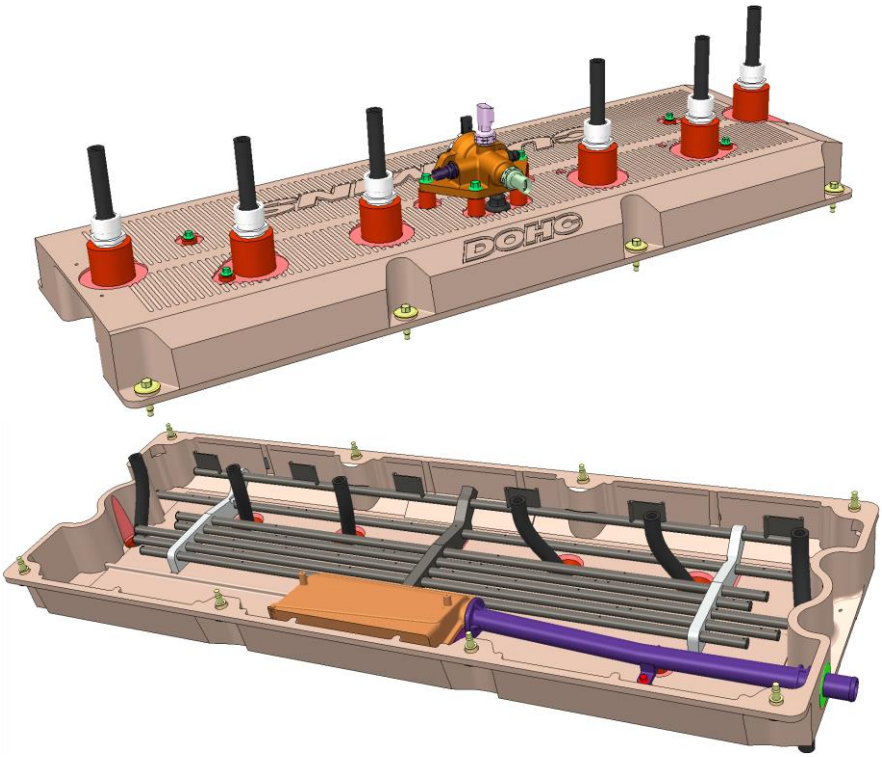

Figure 23: Valve cover design for roller bearing valve train

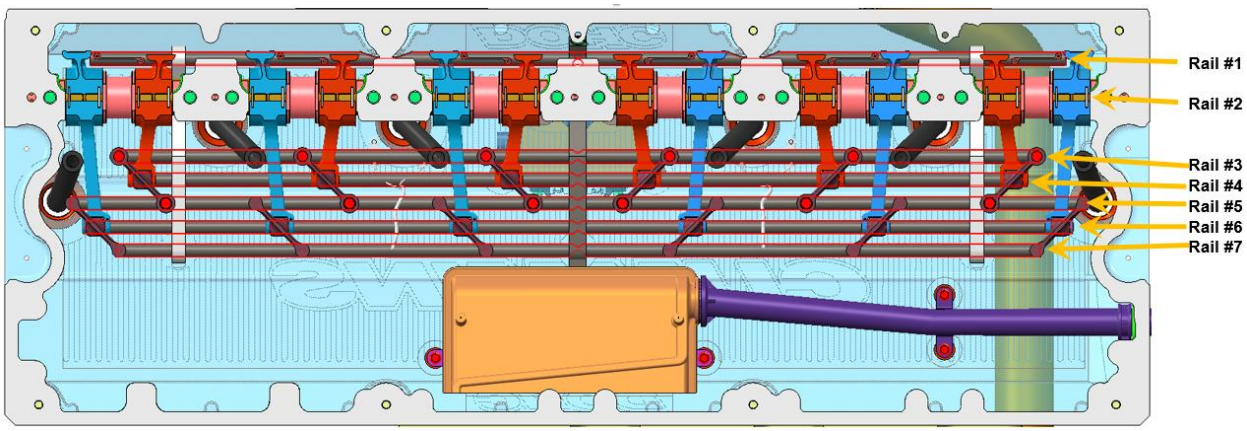

Figure 24: Overhead lubrication system rails configuration

There is a central manifold which evenly distributes the incoming flow along the 7 rails which run longitudinally along the valve cover. Figure 25 shows the construction of this manifold. It also shows the detail cross section of the control valve and sensors. The valve is an automotive solenoid valve which has a precise control on the flow rate and can regulate the pressure upstream depending on the oil viscosity. The inlet to the manifold is position as close as possible to highest point to enable even distribution of the incoming flow.

The elevation required at Rail #2 is due to clearance required with the rocker shaft mounts which run longitudinally under the valve cover.

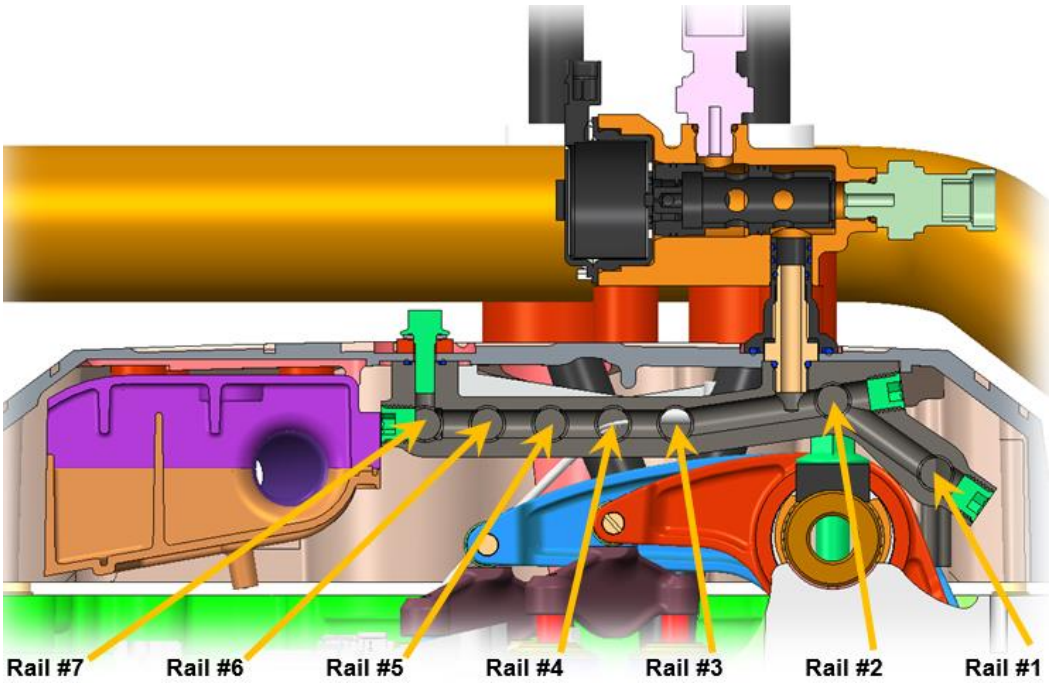

Figure 25: Central distributor manifold and control valve

Figure 26 shows the oil flow coming to the valve housing from the main engine oil supply post the filter. The oil enters the inlet of the solenoid valve. The valve opening is controlled by the actuator through controls logic, based on the pressure and flow rate characteristics of the system. The controlled stream of oil exits the valve outlet and enters the sealed connector between the solenoid valve housing and the valve cover and enters the central distributor manifold. The manifold then distributes the flow across the rails flowing through which they reach the orifices located above the required locations on the valve train components and drip down lubricating them effectively.

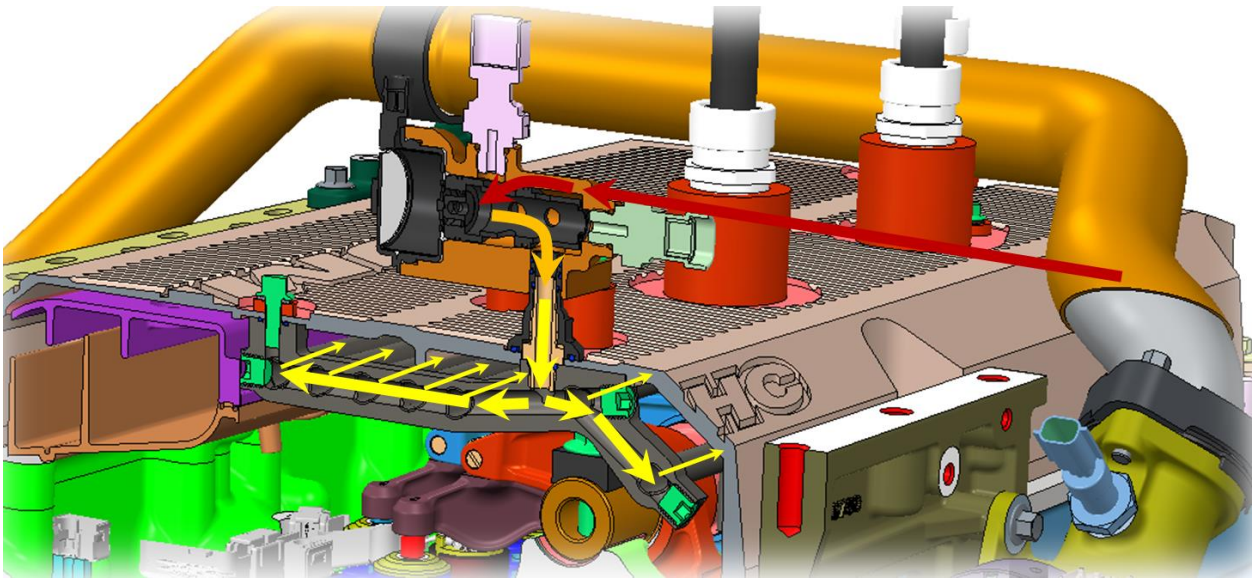

Figure 26: Oil control and flow through the distributor manifold

To optimize the distribution of this flow to ensure sufficient oil reaches all components after minimizing the total oil flow to the overhead, CFD analysis was conducted considering startup and design point operating conditions. The cold oil has higher viscosity and thus leads higher pressure even at low flow rates which has cause the valve train components to starve if the valve is regulated at a set pressure. Figure 27 shows the CFD analysis pressure distribution across all the rails at 1.98 psig inlet pressure using 5W-30 motor oil. The roller element bearing supplier recommends a maximum flow rate of 20 cc/min and minimum of 0.25 cc/min at each of the component locations. Figure 28 shows the flow distribution streamlines at the distributor manifold. Figure 28 shows the graphical flow distribution across each rail at cold start up case of 25°C where the oil is the most viscous. As seen from the curves the flow rate in all the rails at each point is optimized around the 20 cc/min mark. Figure 29 shows the graphical representation of the flow rates for the design point condition where it is again seen that flow rate is within the recommended rate at a much lower regulation pressure due to lower oil viscosity at 115° C.

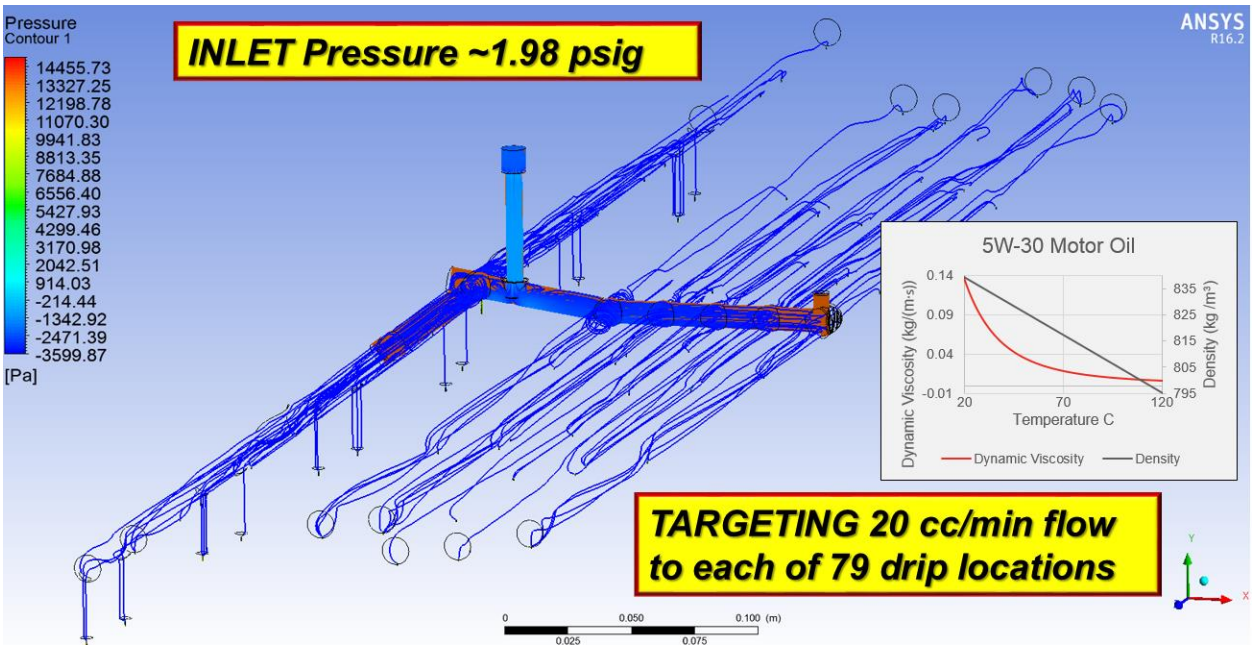

Figure 27: CFD Oil Circuit Results – Overhead lube circuit (115 C Oil, MAX flow condition)

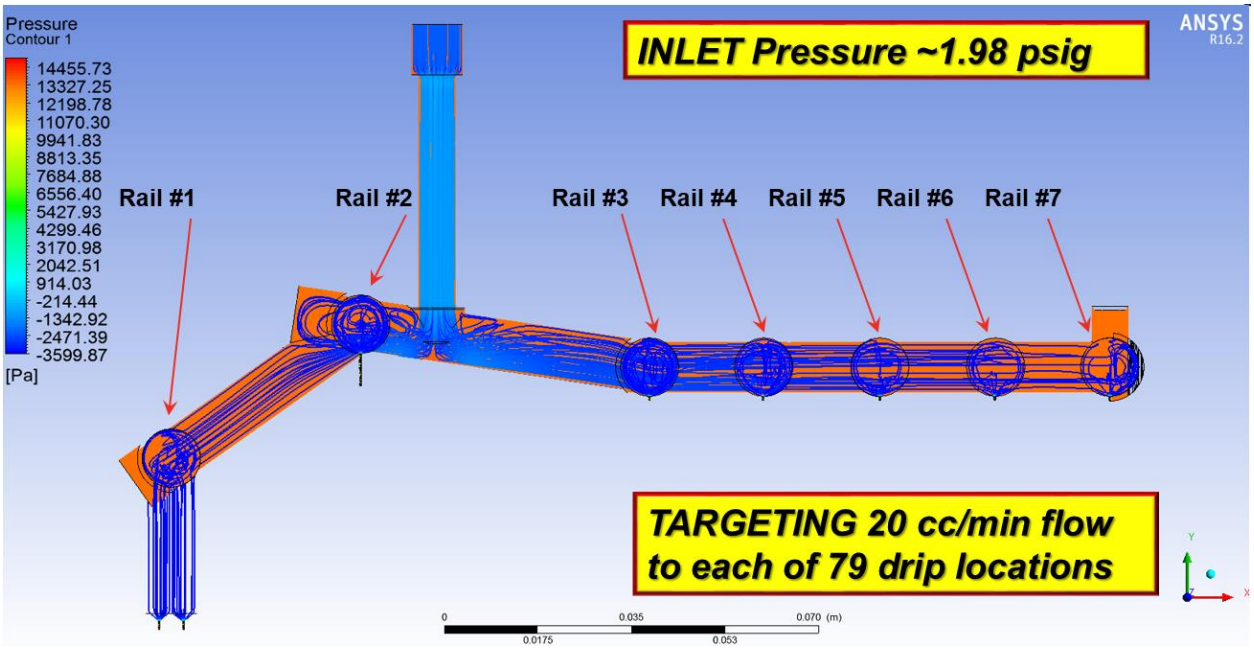

Figure 28: CFD Oil Circuit Results – Overhead distributor Manifold (115 C Oil, MAX flow condition)

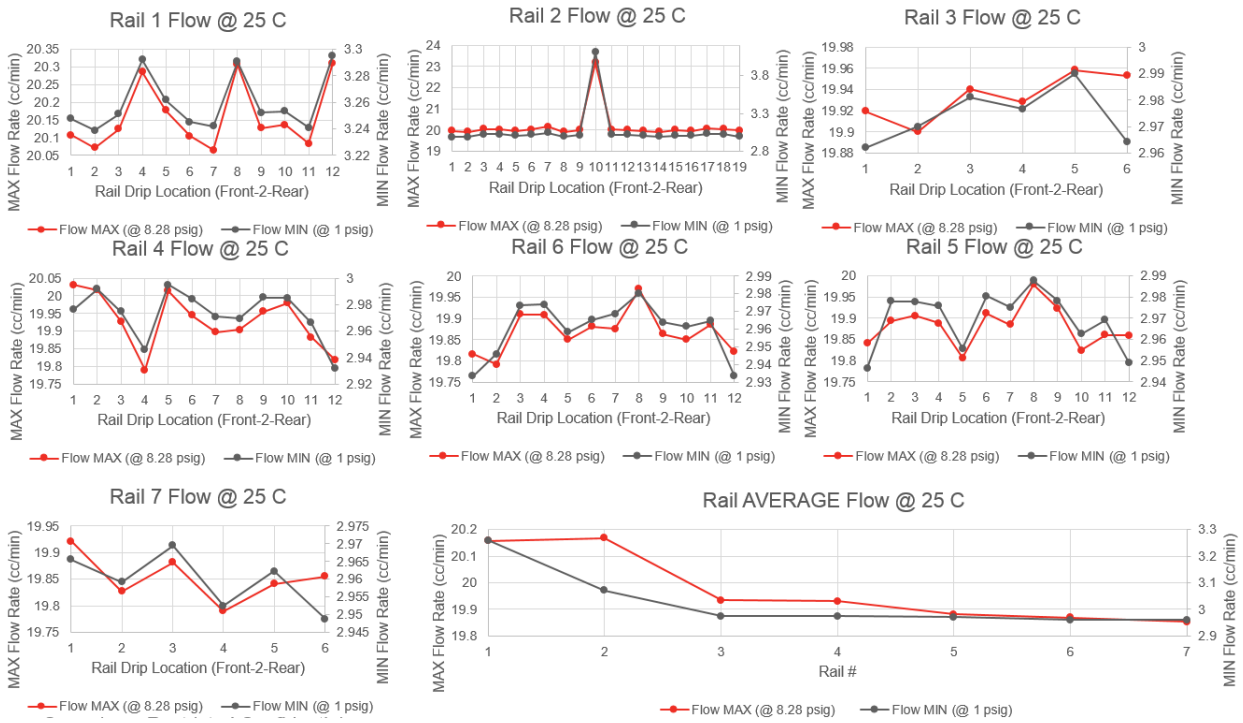

Figure 29: CFD analysis results – Oil flow distribution @ 25C (Startup case)

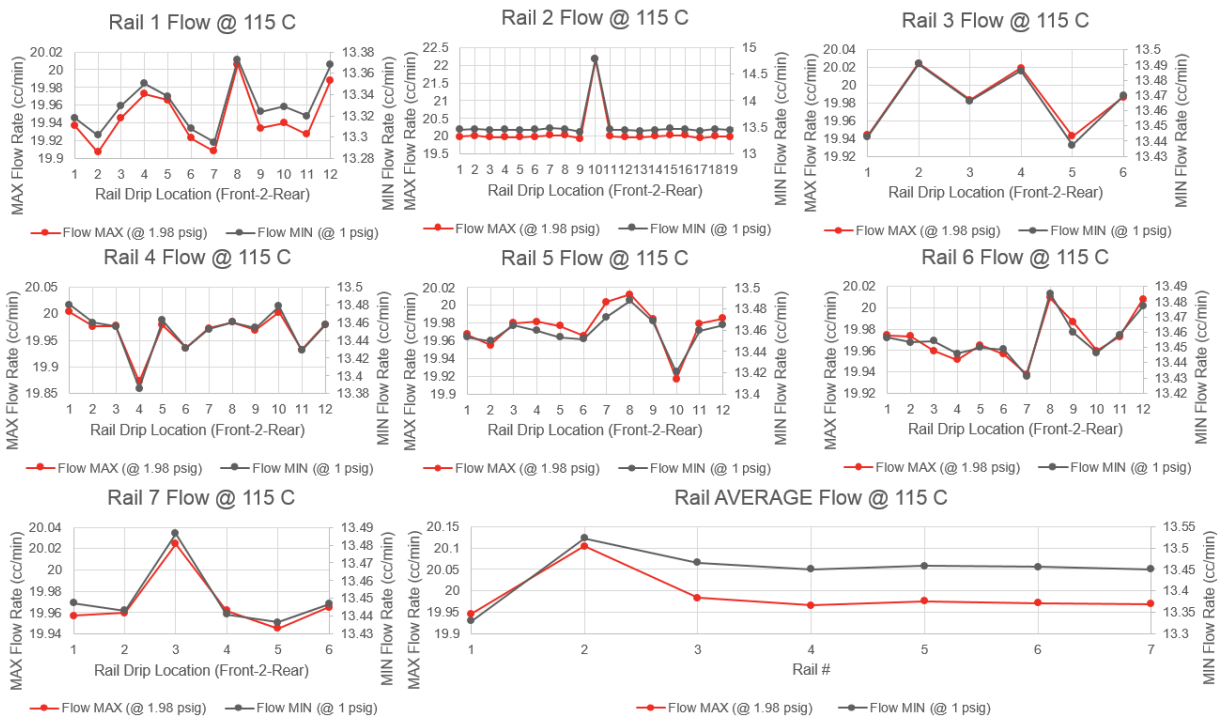

Figure 30: CFD analysis results – Oil flow distribution @ 115C

Figure 31 shows the test hardware with the external lube system which consists of the dual filter and low back pressure WHR oil cooler with larger diameter lines as opposed to the restrictive internal block passages.

Figure 32 shows the baseline current production lube system that was tested for comparison. Figure 33 shows the results of the test indicating improvement by reduction in back pressure as seen from the curves.

Figure 31: External oil system for 55% BTE engine

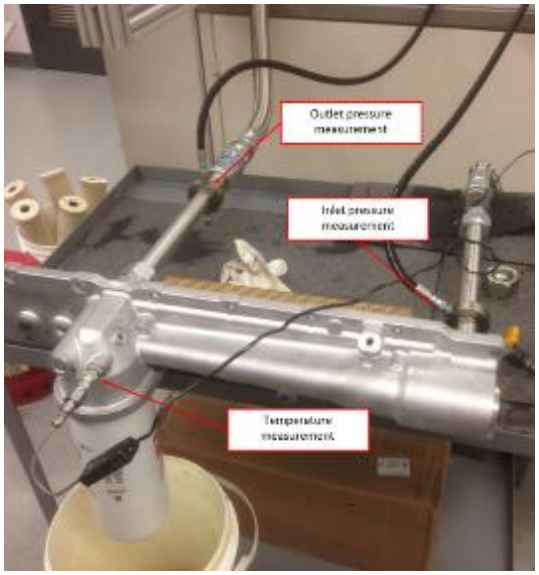

Figure 32: Baseline current production oil system

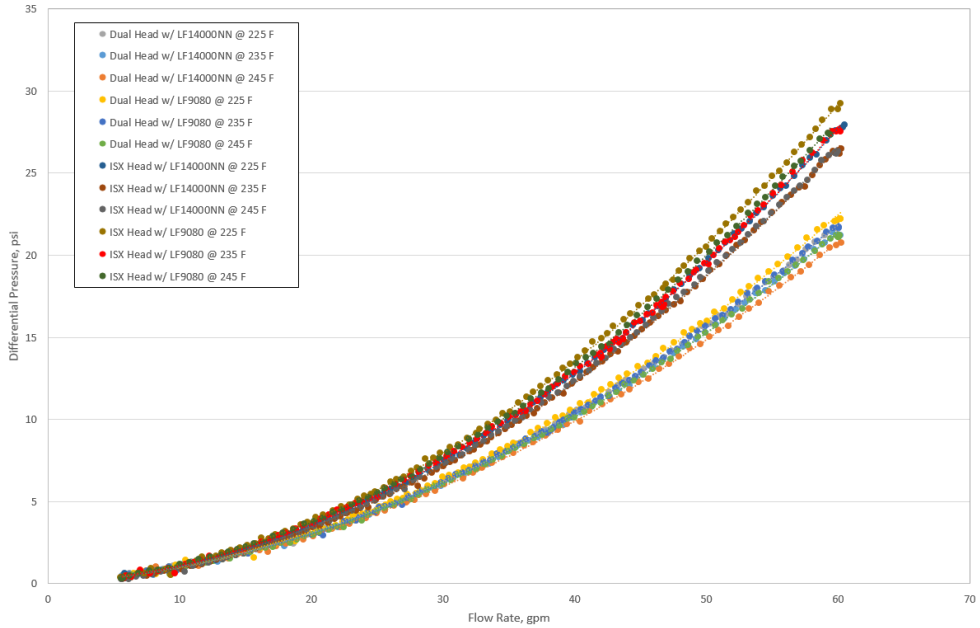

Figure 33: 55% BTE proposed oil circuit pressure drop bench testing results

Air Handling Design

The exhaust air handling system for the base engine comprises of the exhaust manifold and turbocharger designed to drive high-pressure exhaust gas recirculation (HP EGR). The program utilized a combination of low-pressure exhaust gas recirculation (LP EGR) and high pressure EGR loop to improve BTE gains from the air handling system. Figure 34 shows the flow geometry for the existing ISX 2015 manifold with VG Turbine which was used for CFD analysis to assess base engine manifold performance. This manifold is optimized for

driving EGR in the high pressure loop and has considerable flow restrictions to create positive pressure differential with the intake manifold.

Another approach for improved BTE design is using a fixed-geometry (FG) turbine with divided wall and a pulse capture exhaust manifold to drive the FG turbocharger. This option pars well with the low-pressure EGR option. Figure 35 shows an existing pre-EGR manifold with fixed geometry turbine.

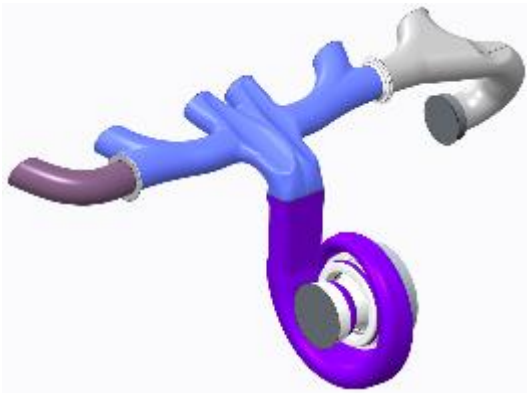

Figure 34: ISX 2015 manifold (TB1469) and A84 single inlet VG Turbo flow geometry

Figure 35: ISX 1999 Manifold (TB1436) and B84 dual inlet Turbo flow geometry

The variable geometry pulse capture exhaust manifold design started off with Concept 1 shown in Figure 36 which a flow optimized manifold with central exhaust gas recirculation (EGR) take-off. The central EGR take-off helps prevent the need for a flow combiner downstream reducing complexity and reducing flow losses. The manifold and the outer were designed and it's packaging with the VG turbo on engine was confirmed as shown in Figure 37. This served as a starting point for the flow cavity optimization to capture pulses for driving the turbo and high pressure (HP) EGR flow.

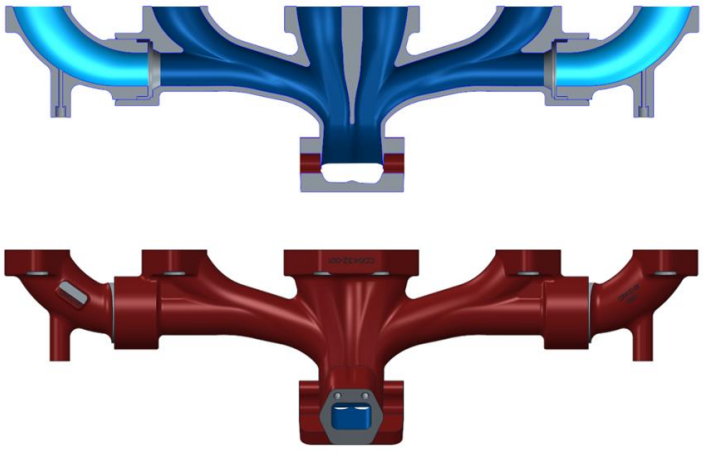

Figure 36: Central take-off VG pulse capture manifold design

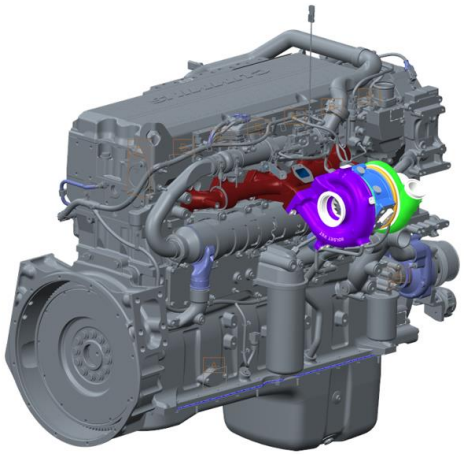

Figure 37: Exhaust manifold with VG turbo on engine

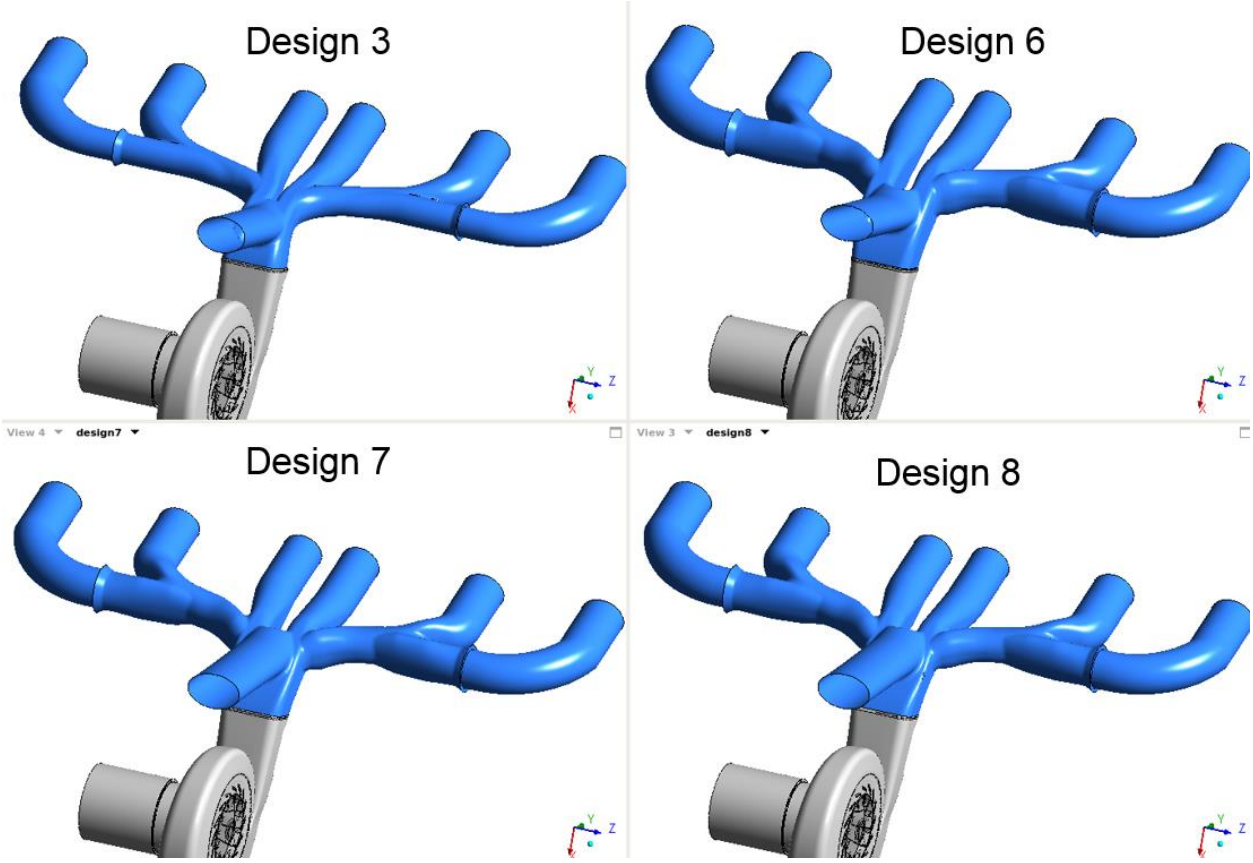

Figure 38: Concept iterations for VG flow geometry optimization

Several designs and coupled-CFD iterations were completed to optimize the flow geometry to drive EGR flow while improving turbine efficiency from the baseline SuperTruck non-pulse capture manifold. Some of the various concepts looked at can be seen in Figure 38. In the initial stage, Design 3 showed the best performance compromise between driving EGR flow comparable to the SuperTruck air handling system as can be seen in Figure 40 which shows the cycle averaged EGR mass flow rate for the various concepts. However, the Design 3 suffered from an extremely high loss coefficient which reduced and was not the most efficient design from a flow perspective. To counter this from the design iteration 5 onwards, new behavioral modeling technique was implemented to achieve a cobra-head style geometry for the flow cavity. The

comparison of these designs with Design 3 is shown in Figure 39. This design showed substantial reduction in the flow losses as shown by the reduction in PMEP and loss coefficient as compared to Design 3.

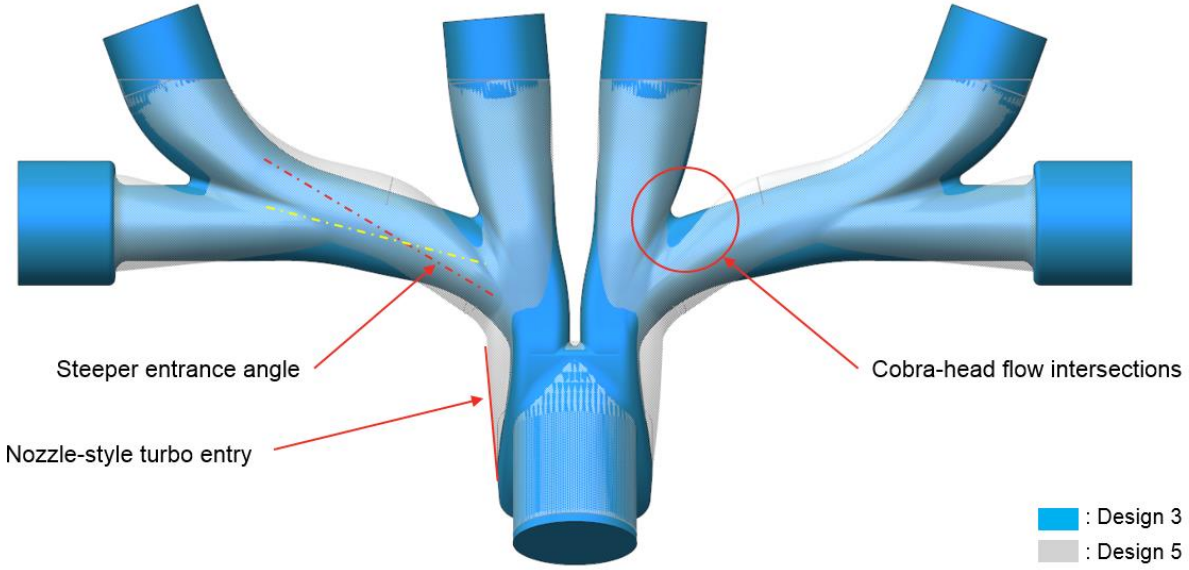

Figure 39: Comparison of Design 3 vs Design 5

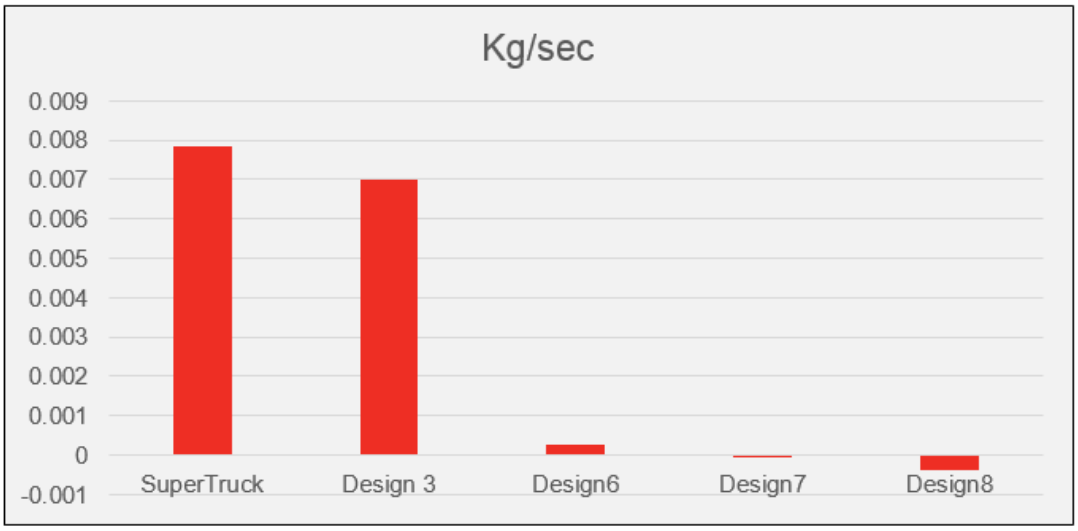

Figure 40: EGR mass flow rates from coupled CFD analysis

The cobra-head style design failed to flow exhaust gases to the exhaust gas recirculation (EGR) take-off as shown in Figure 40. Several iterations were conducted to help better drive EGR flow with the lower loss coefficient design of Concept 5. The exhaust passage was optimized in the subsequent iterations to help drive EGR flow. However, all designs seem to show almost negligible EGR flow as seen in Figure 40. Design 6 seemed to give marginally the most EGR flow out of all the iterations.

Considering this, Design 6 was considered the primary concept to proceed with and alternate ways to drive the EGR flows were considered without affecting the overall air handling system efficiency. One method was to throttle the VG turbo to create sufficient back pressure to drive the EGR. To assess this, the

performance team looked at design point operation of the 50% closed VG turbine and it still lies within the highest efficiency zone.

Given this, the efficiency tradeoff of using the VG closing to drive EGR flow was considered a reasonable compromise to achieve an overall higher system efficiency solution. The final flow design iteration taken forward for analysis was the Design 6 and the outcomes of the final couple CFD analysis are summarized in Figure 41. The Design 6 55VG has a lower loss coefficient than Design 3 and thereby lower PMEP. It however takes a slight hit on the turbine efficiency but is still higher than the Super truck air handling system which is the benchmark. Figure 42 shows the cycle averaged EGR mass flow rate comparison and the Design 6 55VG can flow higher rates for high pressure EGR. Thus, the Design 6 55VG now has best characteristics from an air handling perspective and predicted to be the highest BTE benefit solution amongst the available alternatives using VG turbocharger.

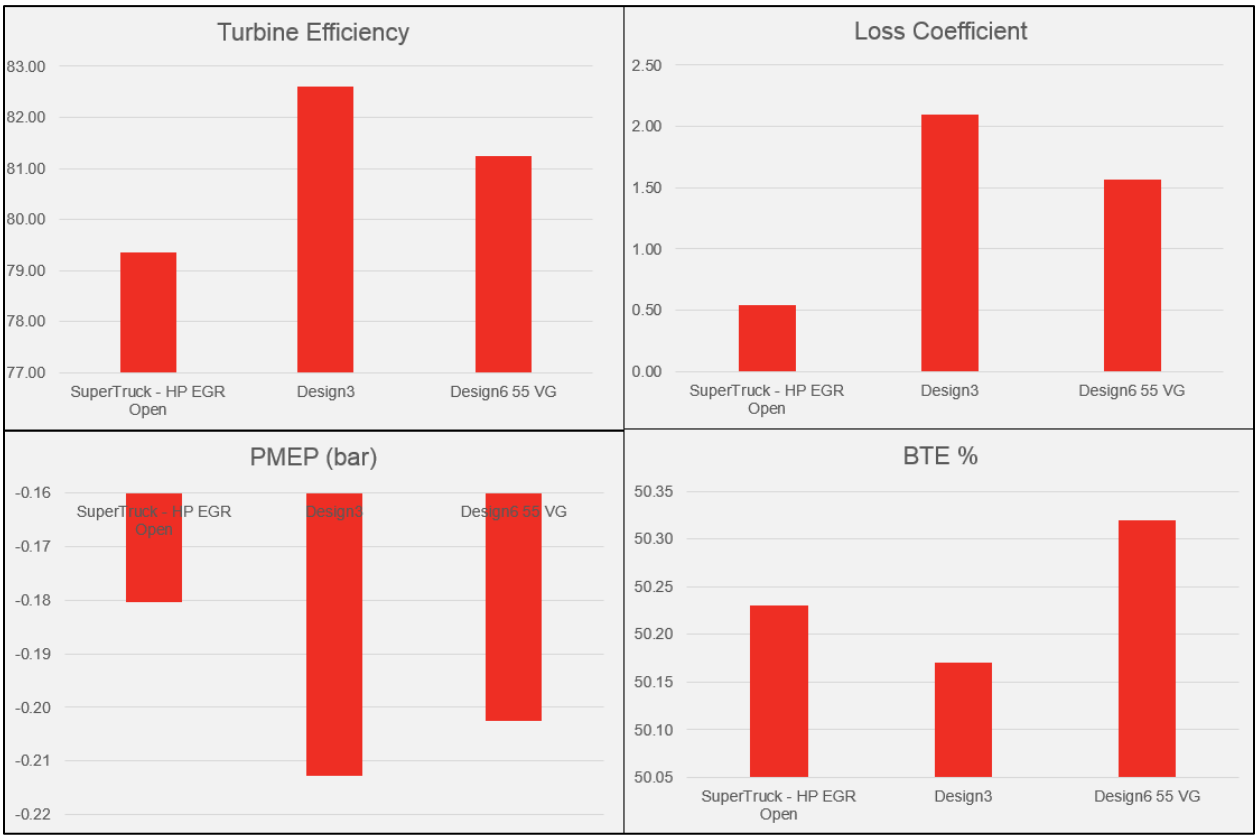

Figure 41: Final VG flow cavity coupled CFD analysis results summary comparison

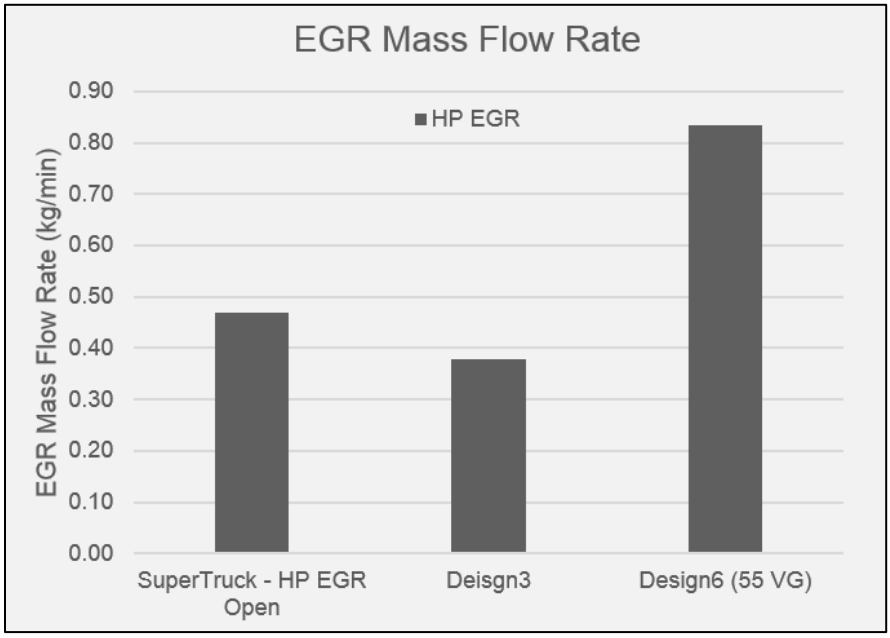

Figure 42: EGR mass flow rate comparison

Several iterations of the outer exhaust manifold casting design were explored for structural analysis, as shown in Figure 43. The key challenges on the structural side turned out to be the mass of the heavy variable geometry turbocharger reducing the structural integrity of the manifold. As can be seen, various ribbing concepts were designed and analyzed to provide sufficient structural support for the turbo.

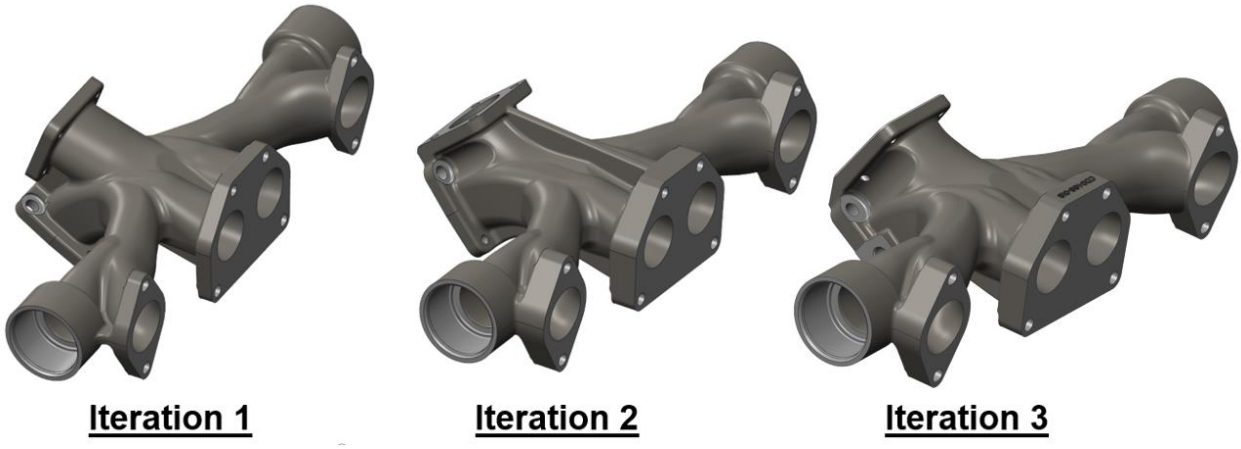

Figure 43: Various VG pulse capture manifold concept iterations explored

The iterations were analyzed structurally using thermal boundary conditions to assess the manifolds fatigue strength capabilities. The best concept was iteration 3, the detailed design of which is shown in Figure 44 and the final casting in Figure 45.

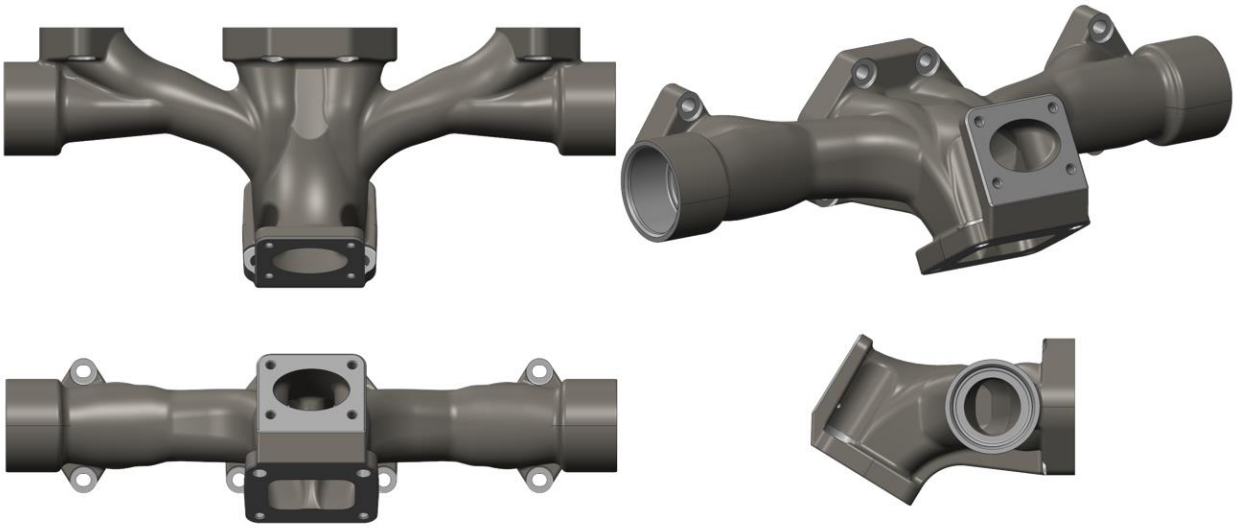

Figure 44: Final VG pulse capture manifold design (Detailed View)

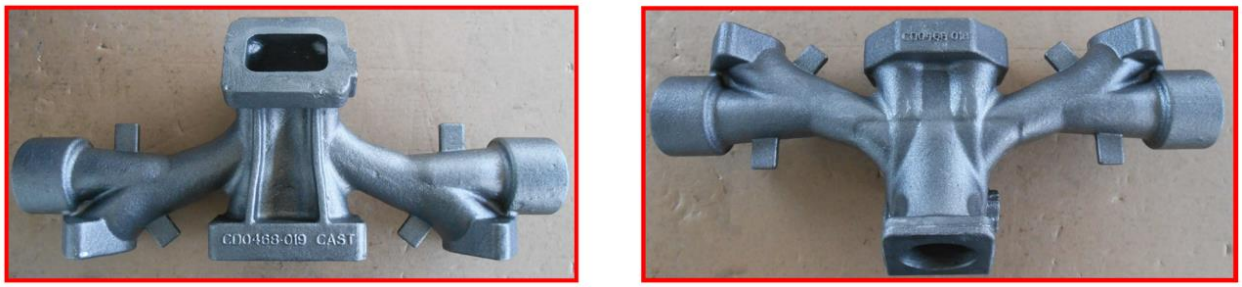

Figure 45: Final VG pulse capture manifold casting at supplier

Design work was also conducted on the fixed geometry (FG) turbo pulse capture exhaust manifold. Several iterations of the flow cavity design were completed and analyzed using CFD to obtain the best flowing manifold which retains the pulse energy of the exhaust. Figure 46 shows the baseline non-EGR FG manifold used on the previous ISX99 Heavy Duty engine. Figure 47 shows the proposed design with EGR take off for hot-side EGR valve. The dead volume created between the cold side EGR valve and the manifold was observed to affect pulse flow performance adversely. Figure 48 shows the proposed FG pulse capture manifold design on engine with the hot-side EGR valve. Figure 49 shows the CFD results summary indicating the proposed design with hot-side EGR valve performs as good as the non-EGR split manifold.

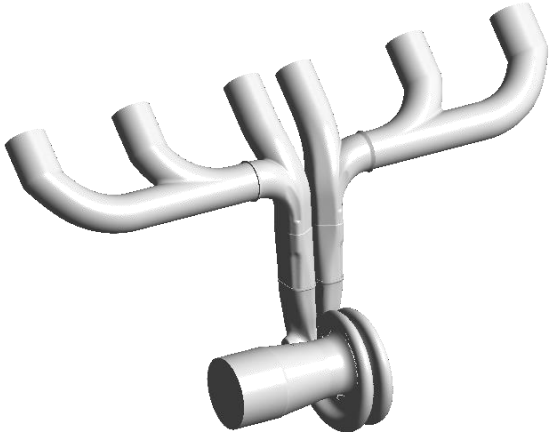

Figure 46: Baseline non-EGR manifold flow cavity

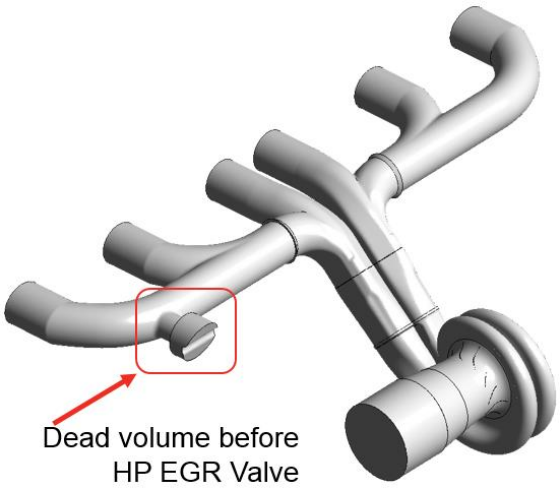

Figure 47: Proposed FG design with EGR

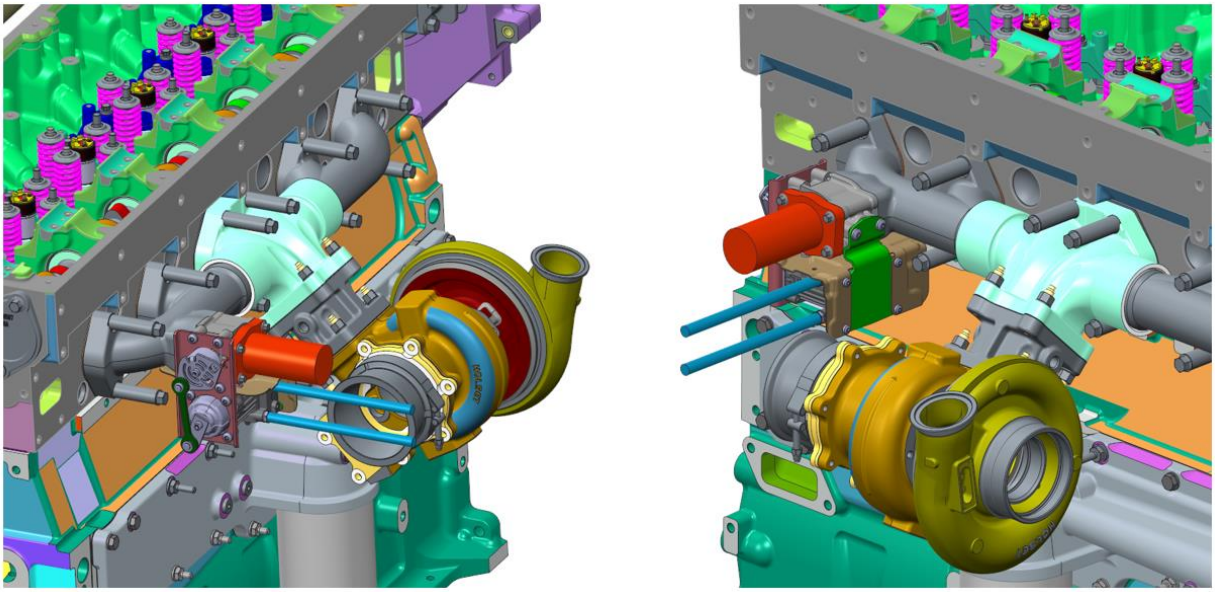

Figure 48: Proposed FG exhaust manifold design with hot-side EGR valve on engine

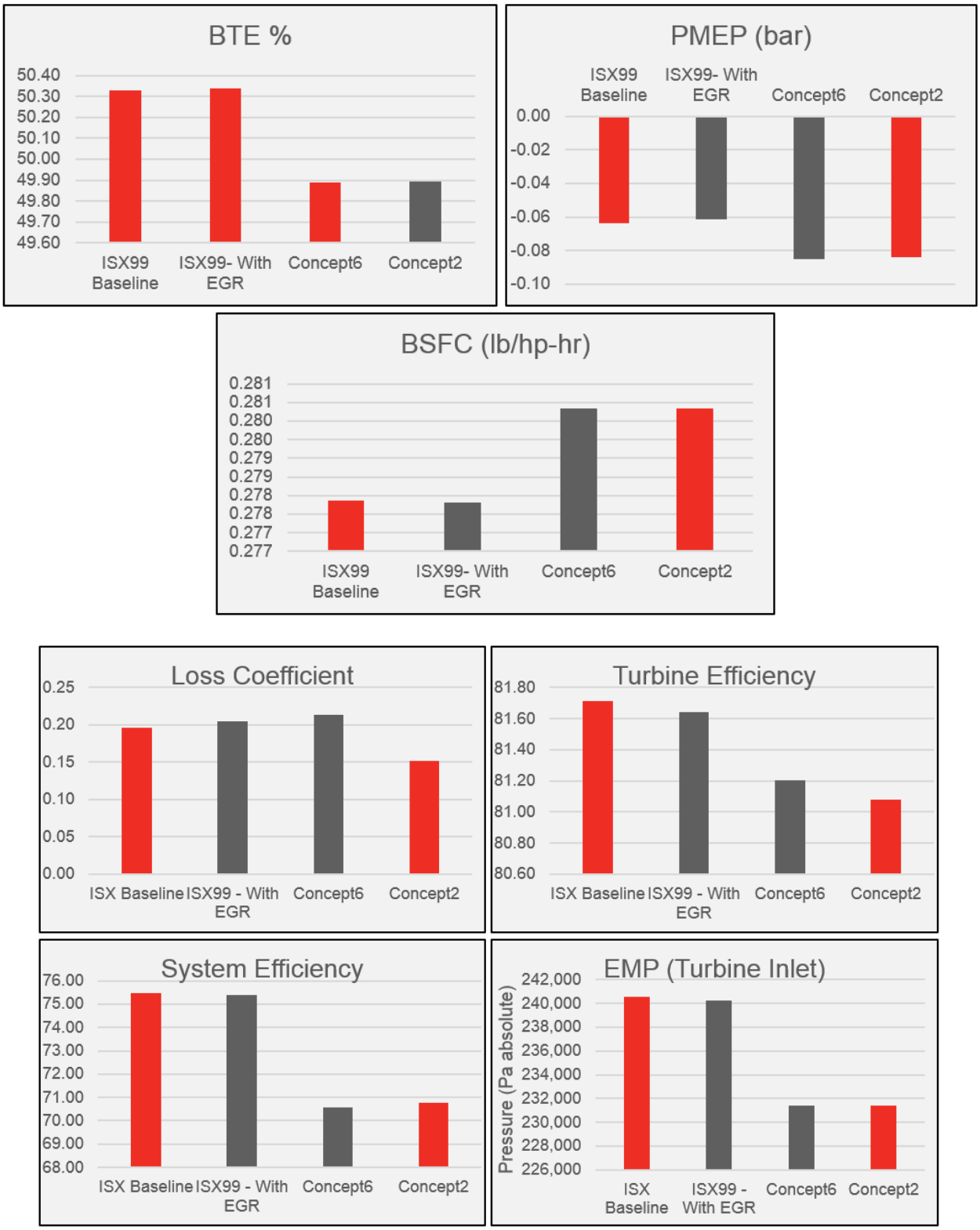

Figure 49: Comparison of flow performance between baseline and proposed FG design

Waste Heat Recovery Design

The overall envelope of the expander and the interface details were specified as also the direction of rotation for the expander as shown in Figure 50. A single stage gear reduction coupled with a belt drive matched to the design point engine speed with the highest efficiency operating speed of the expander.

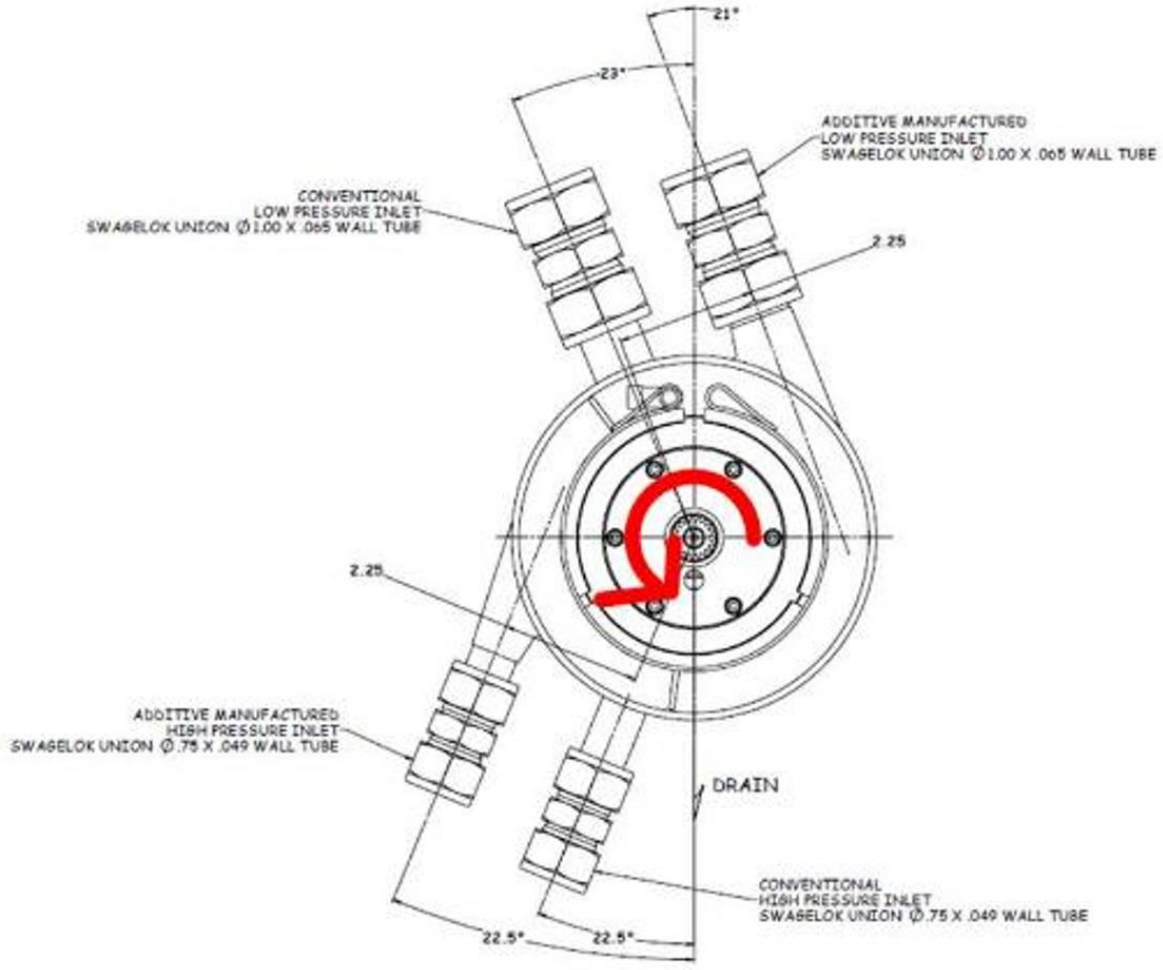

Figure 50: Expander Envelope

The recuperator design is shown in Figure 51. The recuperator flow design has significant bearing on the upstream turbine expansion ratio and efficiency. Achieving minimized flow restrictions within this component leads to better WHR performance. Considering this, the flow velocity profiles were optimized during the end casting designs to obtain a gradual flow expansion and contraction from and to the flanges

and the core as can be seen in Figure 52. This is aimed to achieve the lowest pressure drop across the recuperator.

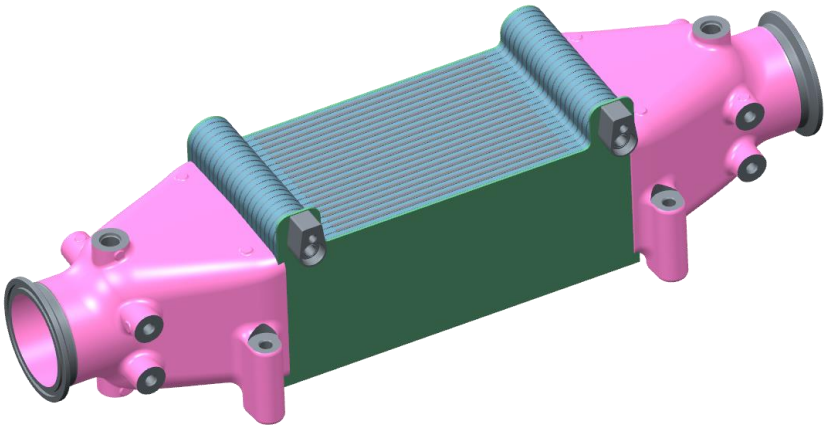

Figure 51: 55% BTE WHR Recuperator Design

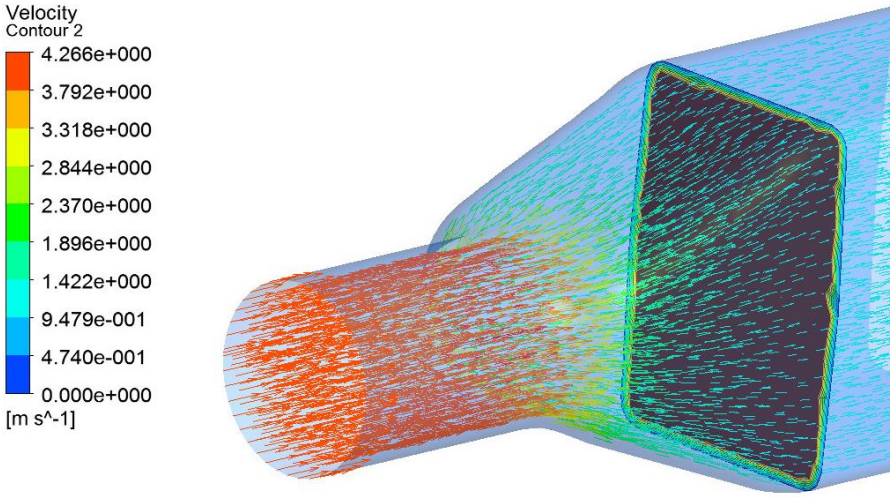

Figure 52: 55% BTE WHR Recuperator flow analysis

Figure 51 shows the WHR power drive and recuperator assembly mounted on the engine stand. The WHR power drive takes the heat energy extracted from the engine wasted energy and converted to shaft power by expanding in the turbine which rotates at 28000 rpm. The gearbox reduces this speed down with a single gear mesh which is followed by further speed reduction down to engine crank speed via a belt drive. The belt drive also acts as a damper for the torsional vibrations of the reciprocating engine. The belt ratio of 2.8:1 is achieved via different diameter of the belt pulleys. The recuperator is mounted on a separate bracket close to the expander outlet to substantially reduce the back pressure on the expander outlet. A bellows connection is used to take up the tolerance stack between the two components.

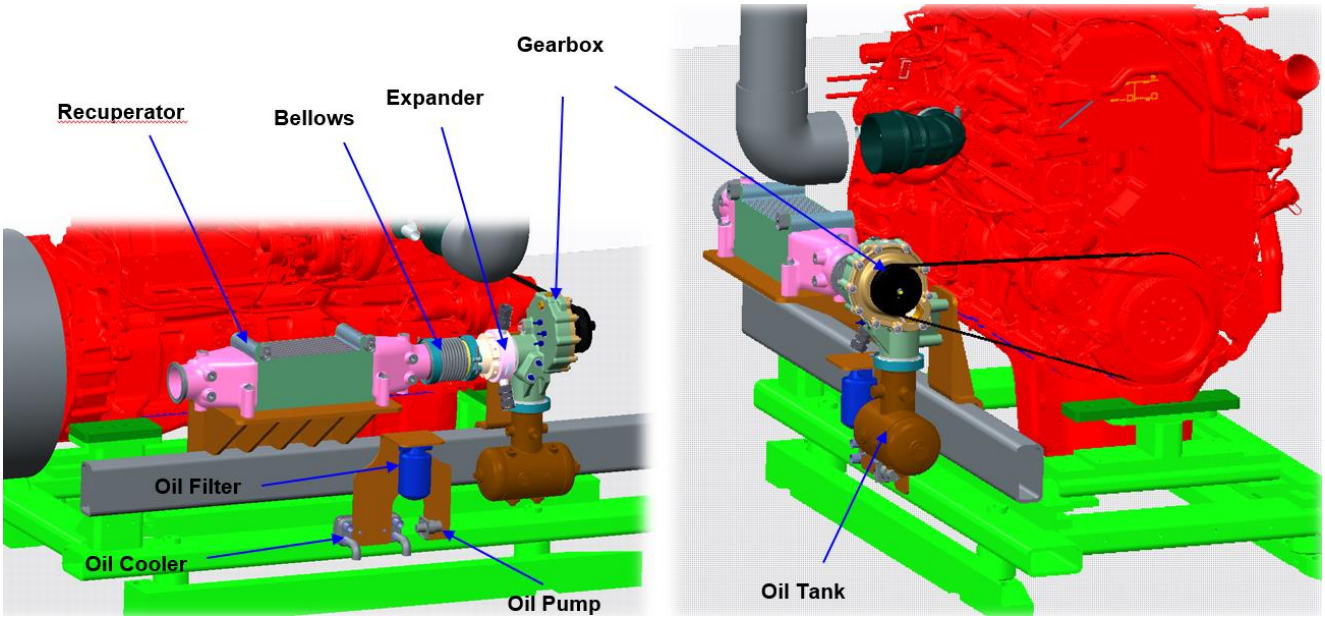

Figure 53: WHR power drive and recuperator assembly

The WHR power drive design is shown in Figure 54 which shows the gear housing with turbine expander assembled. The gearbox oil sump tank is mounted to the bottom of the gear housing by means of V-Band clamp. Ports and sight glasses are integrated into the component design to enable instrumentation and inspection. Figure 55 shows the expander and gearbox lubrication design. The oil for the bearings and gear mesh is supplied through the oil inlet port in the gear housing which feeds into a rifle that provides oil to the bearings and the gear mesh. Additional ports for feeding oil to the bull gear bearings are provided. Most of the oil flow drains from the expander and is kept away from the moving gear mesh to reduce windage losses. The portion of oil that finds its way to the gear mesh drains through the large opening into the oil sump. The oil sump is connected to an external electric oil pump which feeds it to the oil cooler and filter and then back to the oil inlet on the gear housing. The gear box is a closed system which is isolated from the atmosphere by means of a shaft seal. There is an oil scraping feature added at the outlet of the recuperator to return oil

leaked into the working fluid back to the oil sump. The lubrication system and its regulation is an important design feature in enhancing the power output of the waste heat recovery system.

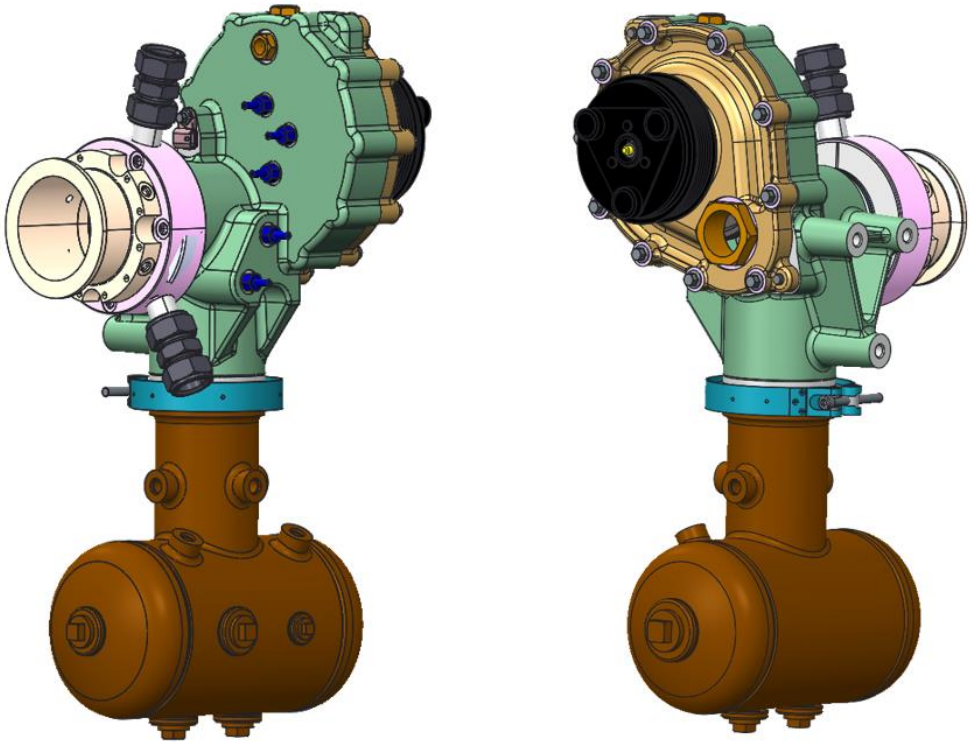

Figure 54: WHR Power Drive Design

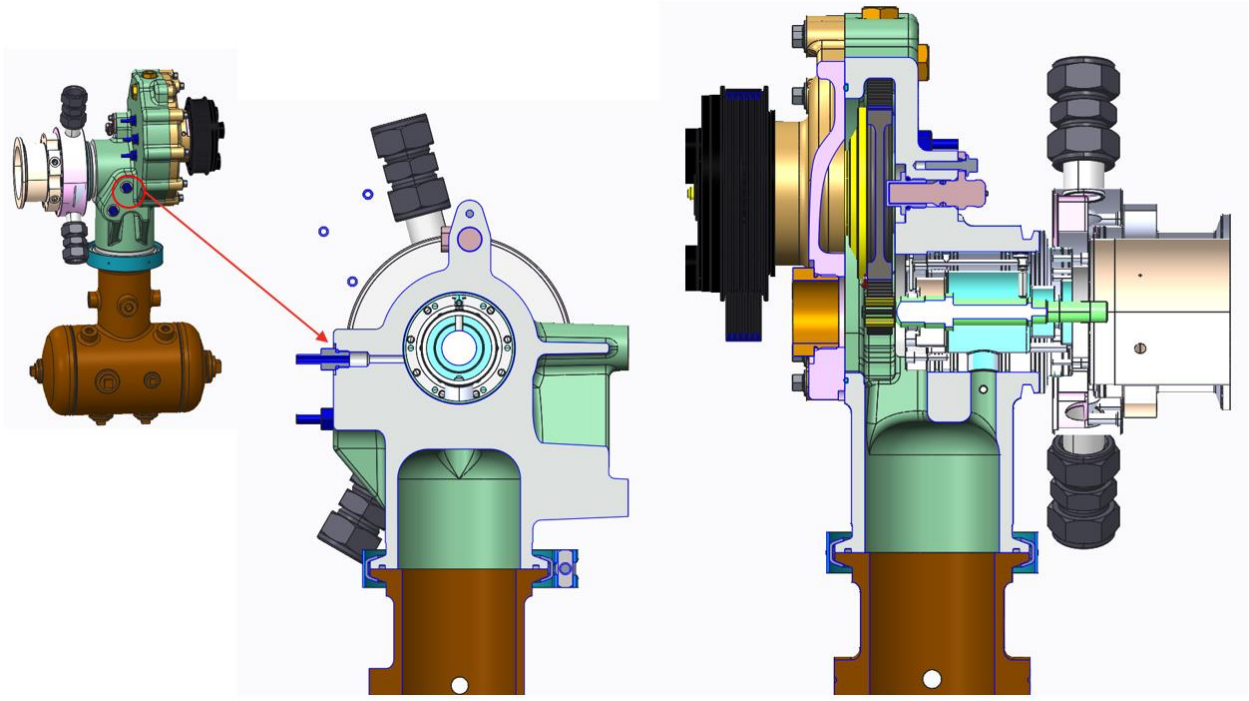

Figure 55: WHR gearbox oil lubrication and drain design

The WHR architecture selected includes extracting heat from the charge air flow and transferring it to the working fluid. To enable this the intake system of the engine is now coupled with the waste heat recovery system by the means of a mixed charge cooler. Figure 56 shows the overall layout of the intake system with

the mixed charge cooler (MCC) mounted on the top of the engine. This layout enables the most optimal flow arrangement for the intake system. The size of the MCC core is set by the WHR system and the current layout provides the entitlement that can be achieved with this system. The system is mounted off-engine to minimize the engine vibrations from being transmitted to the aluminum cooler. To enable this, the cooler core is mounted on a separate bracket and the system is isolated from the engine by means of flexible coupling. The boosted air flow from compressor outlet needs to be diffused gradually to the core and then transmitted to the intake ports on the head. This leads to a four-piece system design consisting of the MCC inlet manifold, MCC core, the MCC exit manifold and the intake manifold.

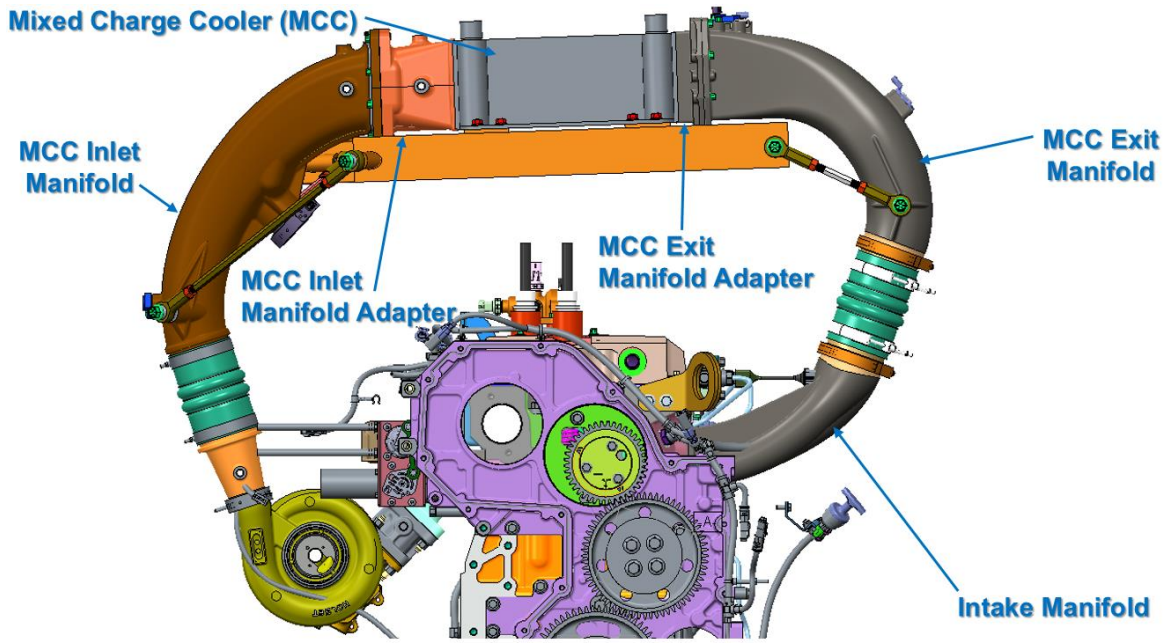

Figure 56: Valve cover design for roller bearing valve train

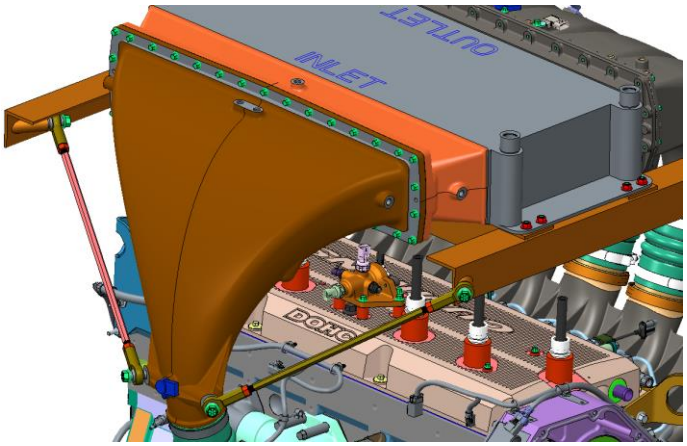

Figure 57: MCC inlet manifold and mounting

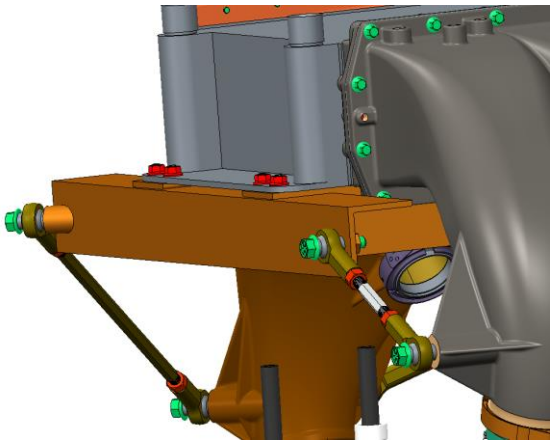

Figure 58: MCC outlet manifold and mounting

Figure 57 shows the structure of the MCC inlet manifold. It also shows the mounting struts to support the weight of the manifold. This prevents it from imparting structural loads to the sealing flange face and the core welded joint. The MCC inlet does the job of diffusing the charge from the compressor outlet to the MCC core. Figure 59 shows the plots from the CFD flow analysis for the MCC inlet. As is seen the swirling flow of the charge coming out of the compressor is effectively diffused to the MCC core cross-section. In a traditional

engine set up this diffusion occurs in a very short section on the charge air cooler. The presence of the WHR MCC enables us to achieve a lower pressure drop intake flow solution as can be seen in the table shown in Figure 60. The table shows a comparison of total and static pressure drop encountered by the charge flow in the MCC inlet which is seen to be very low compared to the traditional setup.

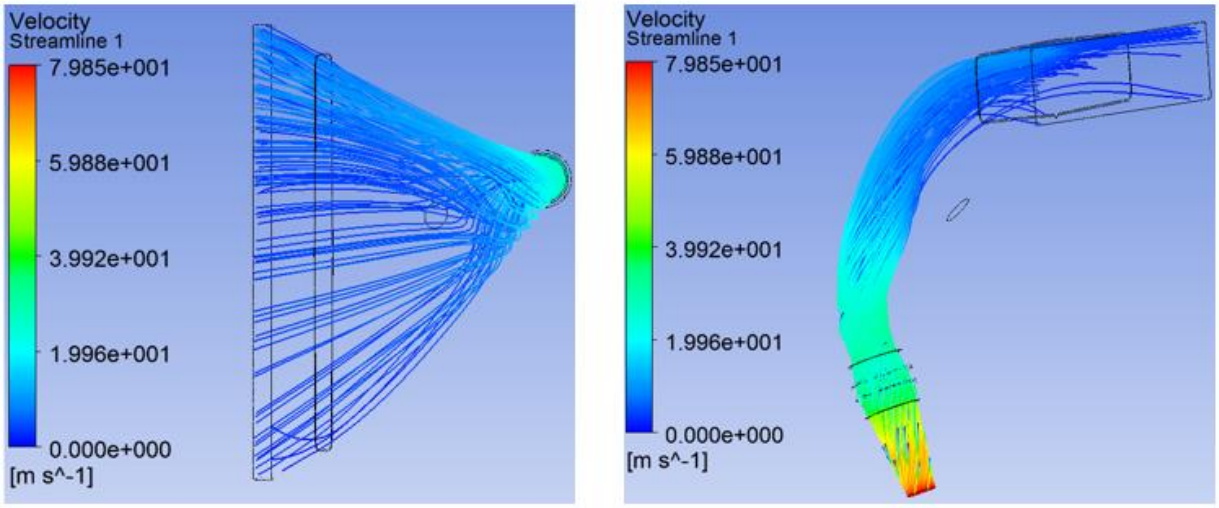

Figure 59: MCC inlet flow CFD analysis (velocity streamlines)

Pressure drop (no core)	Fluent [kPa]	CFX [kPa]	HD intake manifold [kPa] (reference)
Static-to-Static	-3.6	-4.6	-
Total-to-Total	2.3	1.3	4.8

Figure 60: CFD analysis results – Pressure drop across MCC inlet

Figure 61 shows the flow distribution analysis performed by the heat exchanger supplier showing uniform distribution across the core. This minimizes the pressure drop across the core and increases the cooling effectiveness. The fins within core also enable effective mixing of the high pressure EGR that is introduced upstream in the MCC inlet. Thus, this achieves a homogenously mixed charge flow at the outlet of the MCC.

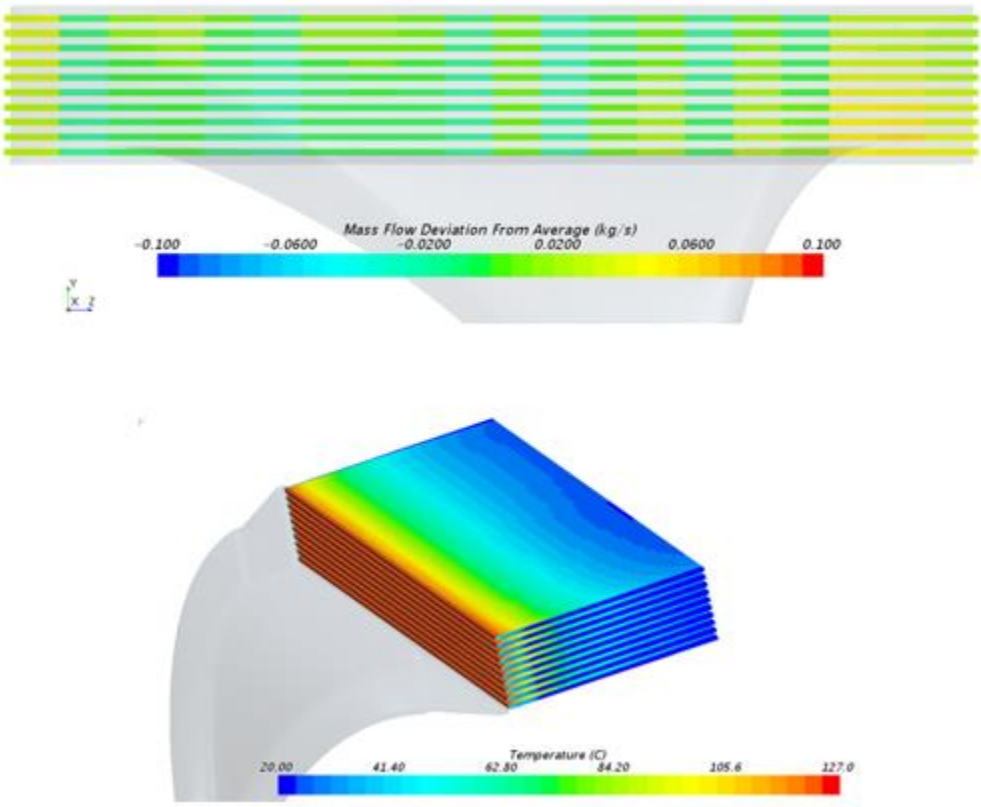

Figure 61: CFD Analysis Results – MCC core flow and temperature distribution

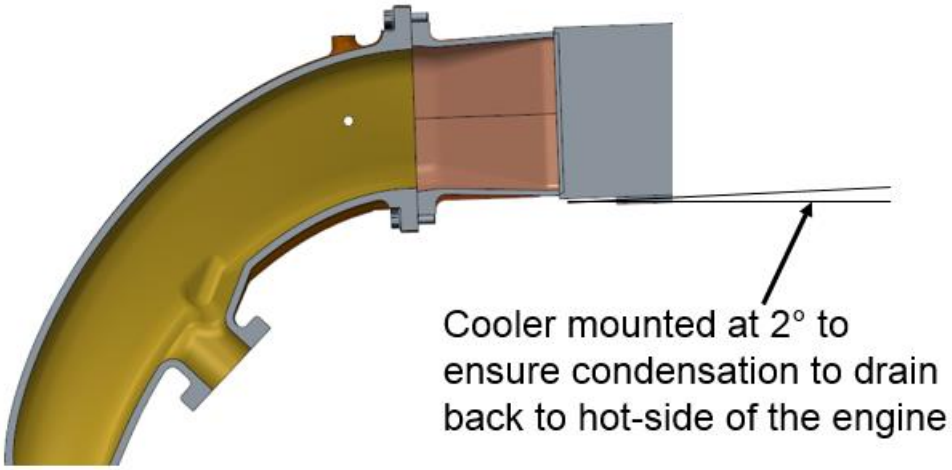

Figure 62: Tilt to provide gravity drain for condensate management

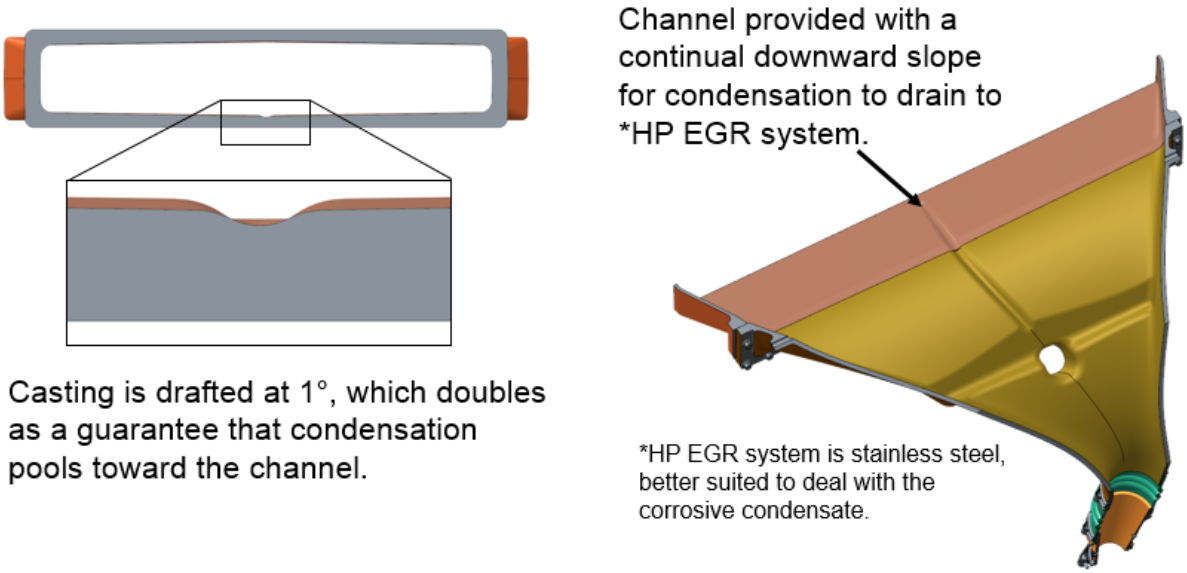

Figure 63: Drain features added to assist condensate collection

To manage condensate generated by the recirculation and cooling of the exhaust gas, the mixed charge cooler is mounted at a 2° drain angle with the horizontal as shown in Figure 62 . This enables the condensate to gravity drain to the cold side of the engine. A condensate collection trough is designed into the MCC inlet casting as shown in Figure 63. The casting draft directs the condensate flow along the center parting line and the collection trough channels it to the high pressure EGR inlet through which it drains into the stainless steel high pressure EGR cooler which can handle the condensate without corrosion.

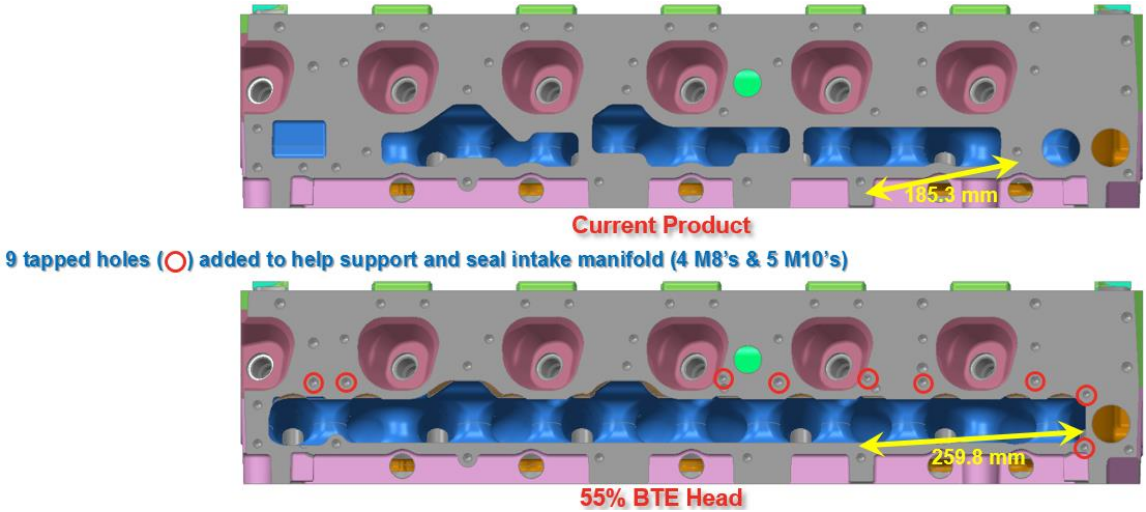

Figure 64: Intake plenum machined for improved charge induction

Figure 64 shows the modifications made to the existing production engine cylinder head to open up the flow paths to front and rear cylinders. This enables a more direct flow path to majority of the intake ports and thus helps reduce cylinder to cylinder variation of trapped charge mass as can be seen in Figure 65. The Rev1-Ext results are analysis runs considering port extensions driving flow very close to the individual ports.

As is seen, in both cases the new intake system design is substantially better at charge induction and reducing cylinder to cylinder variation as compared to the baseline production engine.

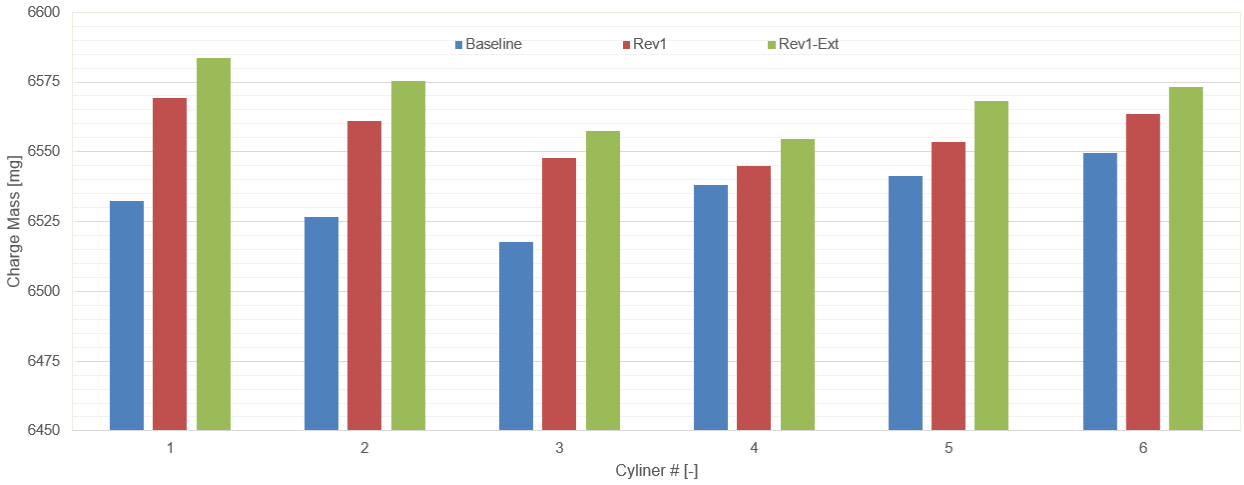

Figure 65: CFD results of Cylinder to Cylinder trapped massed compared to production engine

The above results are achieved by designing a split runner style intake manifold and charge induction system as shown in Figure 66. The MCC outlet gradually divided the homogenous charge flow coming out the MCC core into 6 individual runners. The runners are further gradually subdivided into 12 individual port runners in the intake manifold which feed the individual ports in the head. The MCC outlet and intake flow cores are designed to enable a linear area schedule from the MCC core to the intake ports. The splitting also enables circular geometry to accommodate hose couplings between the off-engine MCC and the on-engine intake manifold.

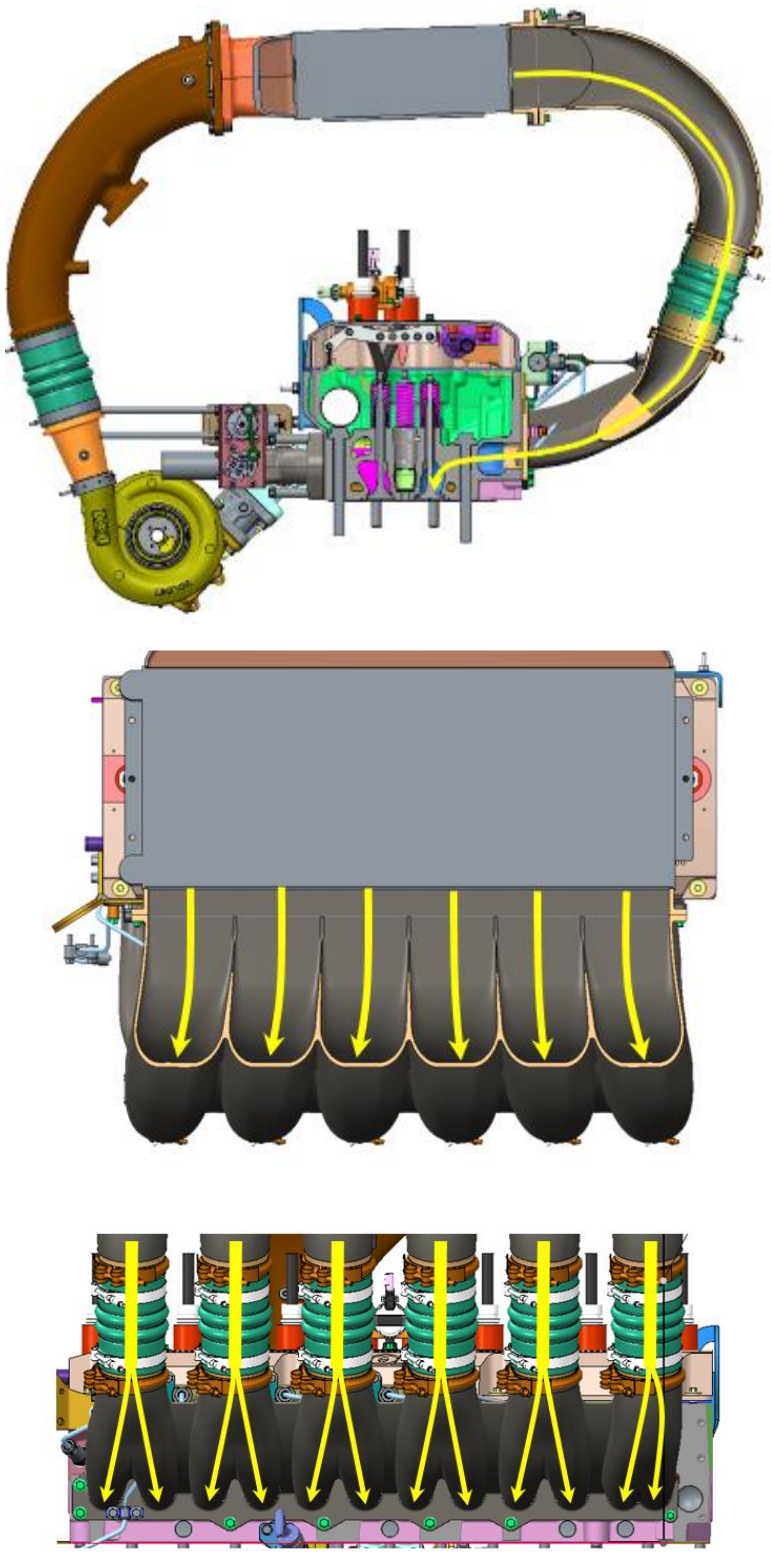

Figure 66: Split runner style intake manifold and charge induction system design

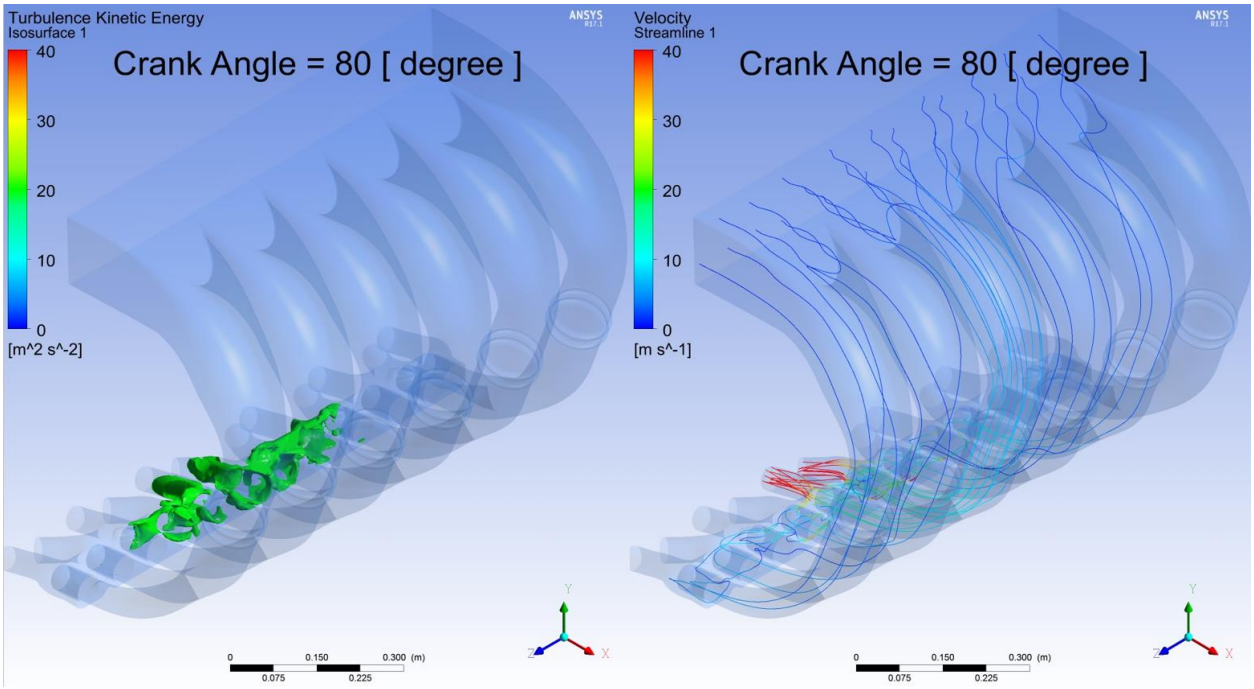

Figure 67: Charge induction system CFD analysis (Turbulence energy contours and streamlines)

Figure 67 shows the streamlines and turbulence energy contours for charge induction system designed for the 55% BTE engine. The streamlines show the flow from the core being split into the runner and channeled to the intake ports as the intake valves open. The turbulence energy plot shows substantial reduction in the losses in this design which shows up in the increased trapped mass.

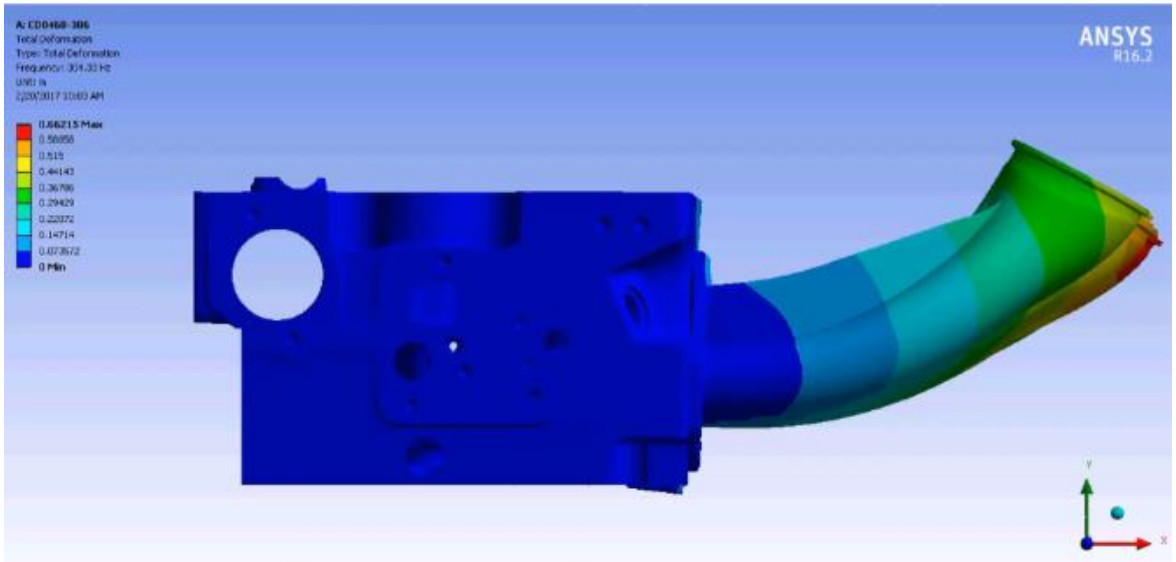

Figure 68: Modal Analysis results for the intake manifold on-engine

The intake manifold being mounted to the cylinder head will experience engine vibrations. Figure 68 shows the modal analysis results for the intake manifold indicating its first mode frequency is above 300 Hz and therefore has limited risk from engine vibration related fatigue issues.

To extract higher efficiency from the WHR Power Drive system, timing belt option was analyzed without any addition idler pulleys or swing arm tensioners to keep drive parasitic to a minimum. One of the belt suppliers

performed analysis on this concept and recommended a timing belt drive solution that would work for the given setup. The hardware recommended by the supplier was their off-the-shelf product which needed modification to fit the test setup. Figure 69 shows the modifications made to the crank pulley and

Figure 70 shows the design of the WHR output pulley with a timing belt drive.

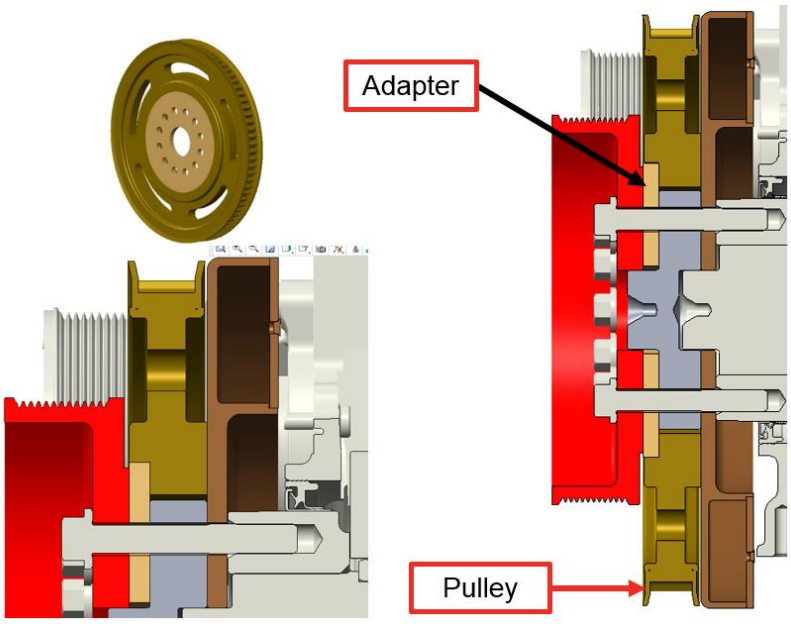

Figure 69: Crank timing belt pulley design

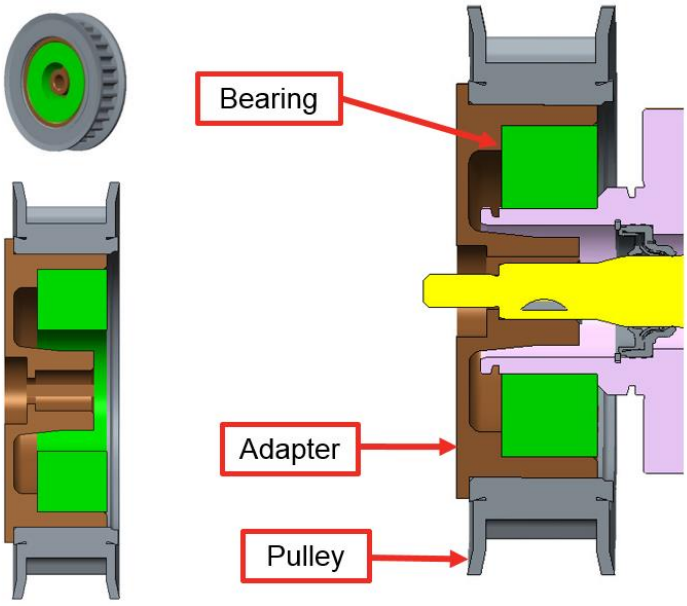

Figure 70: Waste Heat Recovery output shaft pulley design

For the WHR HP EGR loop, it was desirable to package the hardware as close to the engine as possible to better retain heat in the system (shorter loop), while also providing a means to channel EGR condensation to a convenient collection point in the system. Concerns regarding the acidity of EGR condensation (occurring during engine shut down) pooling up in either the cylinder head's intake ports or the mixed charge cooler's (MCC) core drove an MCC design layout featuring a core tilted by 2° relative to horizontal. The 2° MCC core tilt, however, was not enough to prevent the condensation from pooling down in the turbo which was to be

avoided. Thus, the HP EGR Loop was chosen as the ideal path for condensation to flow through and collect for periodic drainage. This solution was chosen due to the HP EGR loop consisting of stainless steel components better suited to combat EGR condensation corrosion. The main challenge during the HP EGR loop design effort was coming up with a layout satisfying the following constraints:

Mount on-engine with as short a loop as possible (heat retention)
Includes
Pierburg 50mm HP EGR valve
Prototype exhaust manifold component already procured
Cummins current product venturi casting (control strategy measures EGR ΔP)
Mahle WHR HP EGR HX
Off-the-shelf bellows (for assembly tolerance & thermal growth allowance)

While also orienting components and tube geometry to channel EGR condensation to a dedicated collection point. The resulting layout can be seen in Figure 71 through Figure 74 below:

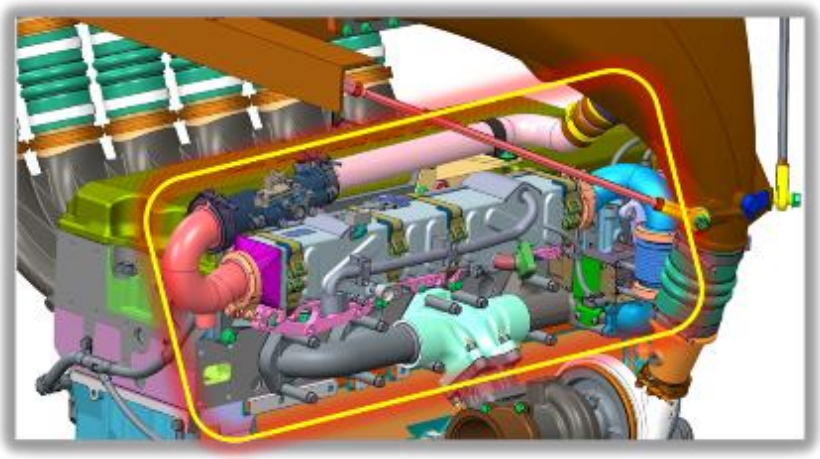

Figure 71: WHR HP EGR Loop Hardware design layout on engine

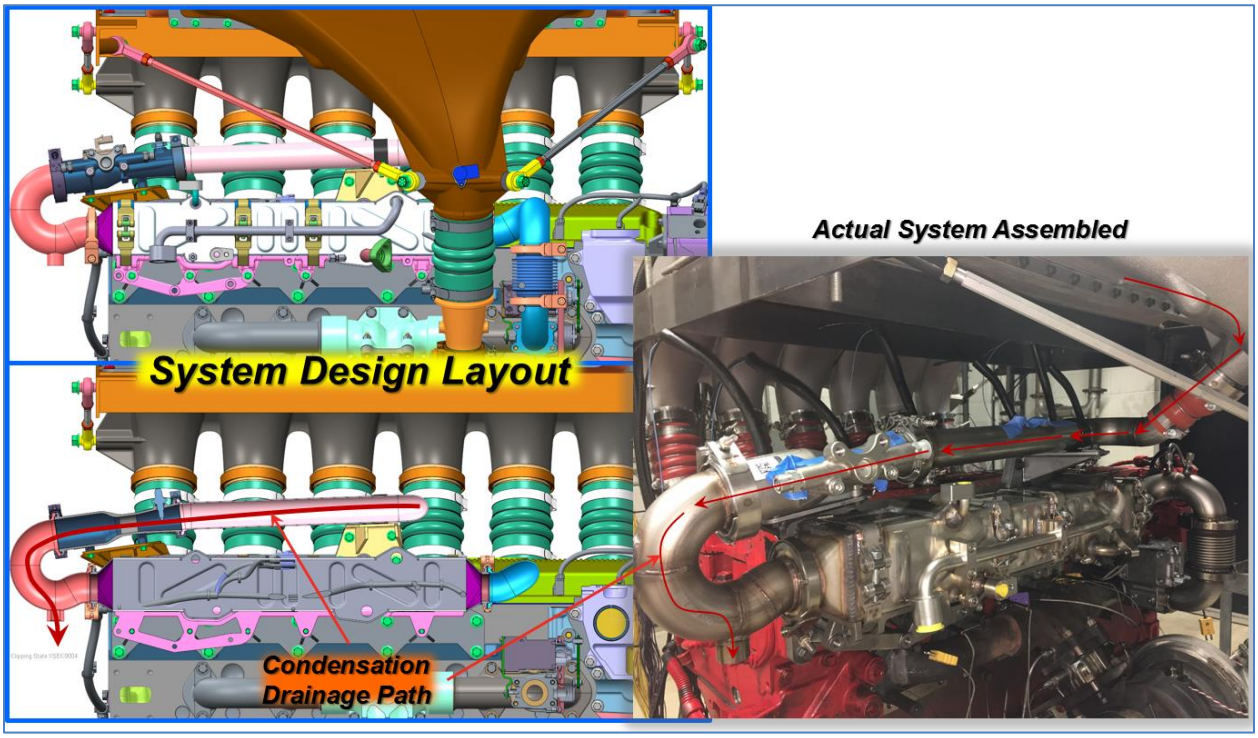

Figure 72: WHR HP EGR Loop Hardware design layout on engine

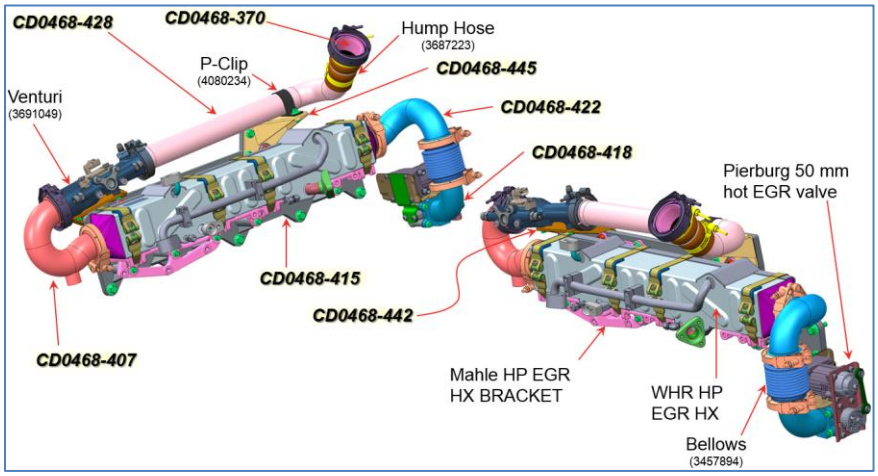

Figure 73: WHR HP EGR Loop individual components

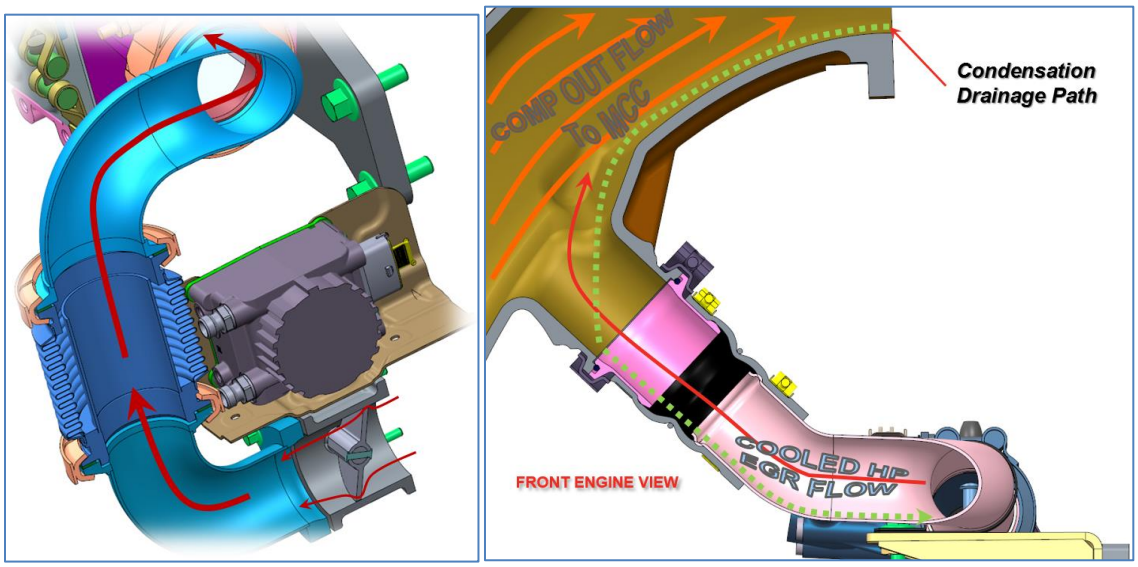

Figure 74: WHR HP EGR Loop Condensation Management Path

Aftertreatment Design

The main goal of designing the ammonia gas mixer for the aftertreatment was to achieve efficient mixing of the ammonia gas injected into the exhaust gas stream in the same space as the production DEF mixer while achieving extremely low back-pressure. Several design concepts with various mixer configurations and spray-hole sizes were explored and analyzed through CFD to target the required uniformity while keeping an extremely low back pressure. Figure 75 shows the best iteration of all the designs analyzed in this study. The concept shows a series of 5 annular rings with 102 holes sized to achieve uniform distribution of ammonia gas in the exhaust flow at various operating points. The central tube acts as feed for the ammonia gas and has 10 smaller sized holes to achieve even flow distribution across the channels. The nozzles are located

facing the exhaust such the spray ammonia gas in the opposite direction of the exhaust flow generating turbulence.

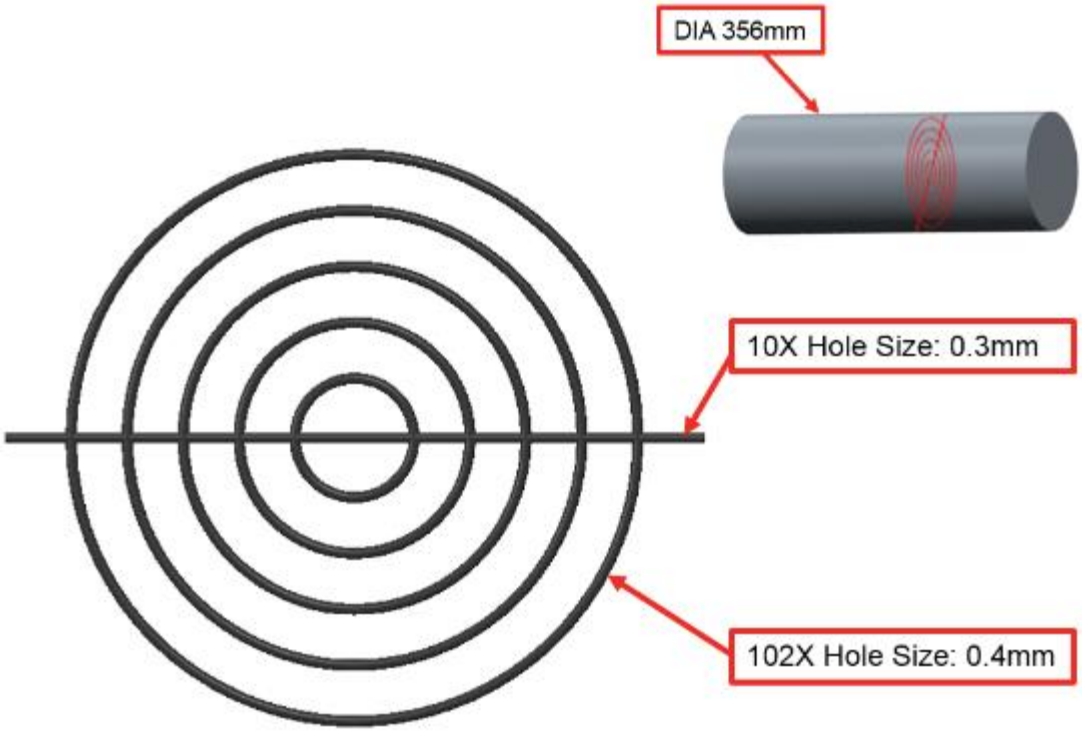

Figure 75: After treatment ammonia mixer concept design (Low delta P design)

Figure 76 shows the two species CFD analysis performed in Fluent to determine the mass fraction and uniformity at various location in the mixer at one of the modal points. As is seen the mass fraction is zero at the inlet indicating the injected ammonia gas does not reach the upstream catalyst. For this concept, a 92% area averaged uniformity is achieved the outlet of the current product space claim while additional 310 mm length increases the uniformity to 95%. Figure 77 shows the velocity vectors and streamlines for the injected ammonia gas at that same modal point. The pressure difference across this optimized mixer is 4.23 Pa based on analysis which substantially low and meets the design requirements. Further work to improve this design within the same space constraint is in progress.

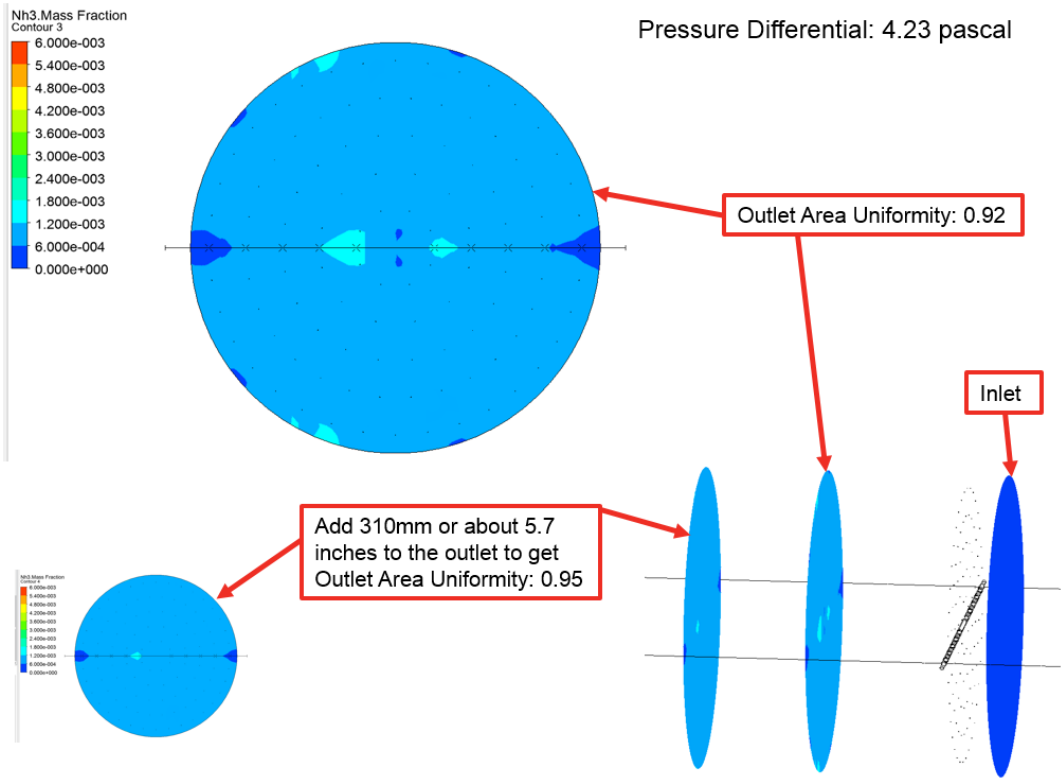

Figure 76: After treatment ammonia mixer concept CFD analysis (mass fraction and uniformity)

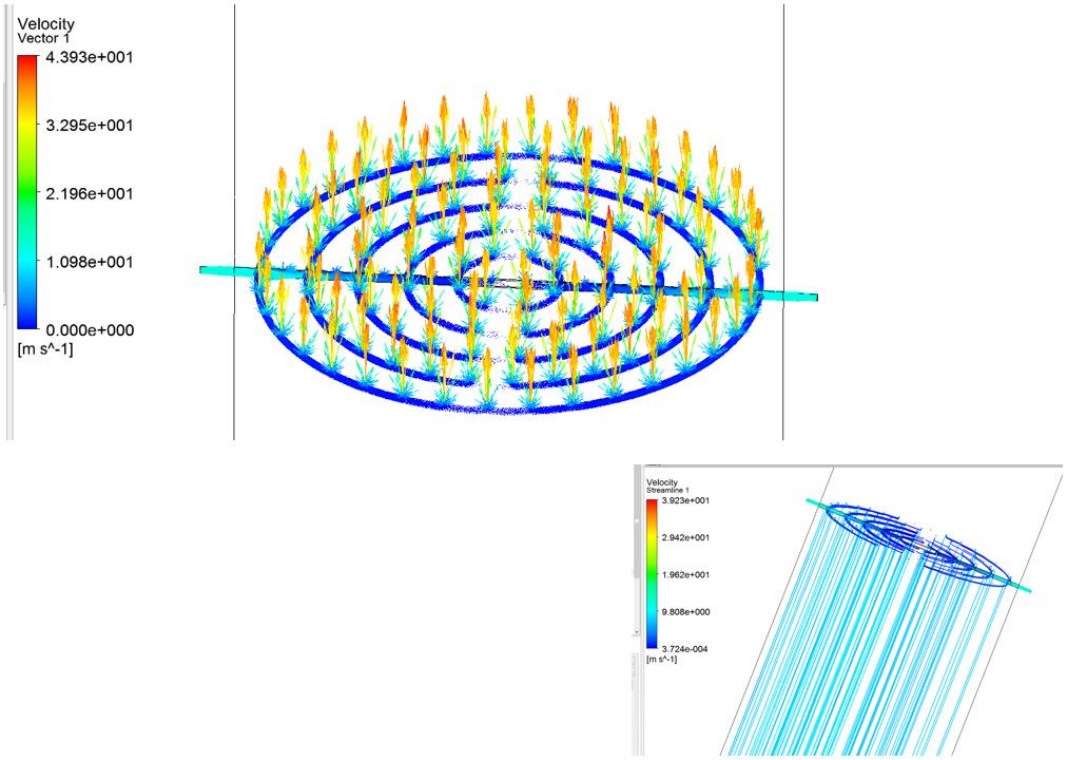

Figure 77: After treatment ammonia mixer concept CFD analysis (velocity vectors and streamlines)

3.2 Combustion CFD

There were two major aspects of 3-D combustion CFD studied in detail during the program:

- First, CHT (Conjugate Heat Transfer), for solving for fluid and solid heat transfer simultaneously in the same software applications; this was also a functional excellence task (tool development)
- Second, combustion system optimization (baseline model calibration, piston profile optimization, injector optimization)

List of Piston Designs Analyzed – Initial study

In the initial stages of the program, Low Heat Transfer Piston (LHP) designs are looked at to reduce engine heat loss and improve engine efficiency. 3D diesel combustion CFD analysis is run with LHP designs from Cummins and external piston suppliers.

Combustion analysis is run with the following piston designs.

Piston designs from CMI:

1. Baseline Steel with Oil Cooling
2. CMI-LHP1 with Oil Cooling
3. CMI-LHP1 without Oil Cooling

Piston designs from Supplier1:

4. Baseline Steel with Oil Cooling
5. SUP1-LHP1 with Oil Cooling
6. SUP1-LHP1 without Oil Cooling
7. SUP1-LPH1-1 with Oil Cooling
8. SUP1-LPH1-1 without Oil Cooling
9. SUP1-LHP1-5 with Oil Cooling
10. SUP1-LHP1-5 without Oil Cooling
11. SUP1-LHP2 with Oil Cooling
12. SUP1-LHP2 without Oil Cooling
13. SUP1-LHP2-1 with Oil Cooling
14. SUP1-LPH2-1 without Oil Cooling
15. SUP1-LHP3 without Oil Cooling
16. SUP1-LPH3-1 without Oil Cooling

Piston designs from Supplier2:

17. Baseline Steel with Oil Cooling
18. SUP2-LHP1
19. SUP2-LPH2

Thermal modeling of piston is run by Computational Experimental Fluid Dynamics group for internal piston designs and at suppliers for external piston designs.

Results from initial LHP survey

Out of the LHP designs that were analyzed and considering the proposed designs from external piston suppliers, SUP1-LPH2-1 without Oil Cooling gives highest heat loss reduction to piston bowl of 42% and improvement of 1.51 points in closed cycle efficiency compared to baseline steel piston followed by SUP2-LPH2 which gives 42% reduction in heat loss to piston bowl and 1.4 points increase in closed cycle efficiency.

The LHP designs from Cummins show lower heat loss reduction improvement in closed cycle efficiency compared to external designs due to lower heat input from combustion modeling to thermal modeling (scaling of heat flux on piston) with Cummins thermal modeling, difference in modeling of air gap (convective boundary condition in Cummins pistons modeling and no convection in air gap in external pistons modeling) and possible differences in other boundary conditions of thermal modeling between internal and external piston thermal modeling.

With hotter piston, not only there is reduction in heat loss and improvement in closed cycle efficiency but also there is increase in exhaust energy, slight increase in peak cylinder pressure and peak heat release rate, increase in NOx and reduction in PM.

CHT (Conjugate Heat Transfer) analysis – Combustion / Piston separate

During the initial analysis study, piston thermal and combustion CFD analyses of Low Heat Transfer Piston (LHP) designs from Cummins and external piston suppliers were run where combustion CFD modeling was run for closed cycle (from intake valve closing to exhaust valve opening) only. The closed cycle combustion heat flux on the piston crown was scaled down to account for open cycle heat transfer and scaled heat flux was applied as boundary condition in thermal modeling of piston. Different scaling factors were used between analyses with internal designs (0.15) and external designs (0.2). In Q2, the thermal and combustion analyses of the best internal LHP designs and baseline steel piston are run using same scaling factor of 0.2 as used in analyses of external piston designs. Thermal barrier coating (TBC) is added to the best internal piston design looked in Q1 and is analyzed as well in Q2. Also, conjugate heat transfer modeling of piston using one tool, CONVERGE has been started.

Low Heat Transfer (LHT) Piston Inferences

Closed cycle diesel combustion analysis is performed with LHP designs from three suppliers. Out of the LHP designs that are looked at and considering the proposed designs from external piston suppliers, the best design gives improvement of 1.51 points in closed cycle efficiency with 42% reduction in heat loss to piston bowl compared to baseline steel piston followed by a second and third design which give increase of 1.49 points and 1.4 points in closed cycle efficiency with 40% and 42% reduction in heat loss to piston bowl respectively.

With hotter piston, not only there is reduction in heat loss and improvement in closed cycle efficiency but also there is increase in exhaust energy, slight increase in peak cylinder pressure and peak heat release rate, increase in NOx and reduction in PM.

Assessment of radiation models in CONVERGE

Background

Thermal barrier coating (TBC) and low heat transfer piston (LHP) designs are used to improve engine thermal efficiency by reducing the engine heat loss at cylinder walls. “Lower peak, longer tail” AHRR is observed when TBC or LHP is applied.

Our current combustion CFD process with CONVERGE cannot capture this trend in AHRR. Two suspecting causes studied in this report are:

1. The lack of radiation modeling capability in current CFD tool (CONVERGE V2.2).
2. The inaccurate temperature wall models current CFD tool (CONVERGE V2.2).

In the report, both radiation models and temperature wall models are investigated.

CFD cases and studies

The calibration at rated point is used as the baseline case for this study. Two studies are conducted: the first one study the effects of available radiation models. Three different radiation model options are included:

- Radiation model off
- Radiation model on with simple soot model
- Radiation model on with detailed soot model

The second study is to exam the effects of wall temperature on radiation models. When TBC or LHP designs are applied, piston wall temperature will be higher with greater radiation.

Table 2: Two Studies for the Radiation Assessment

3 options	Study 1	Study 2
Radiation model off	Effects of radiation models on pressure & HRR for baseline settings	With higher piston T (200 K), effects of radiation models on pressure & HRR
Radiation model on w/ simple soot model		
Radiation model on w/ detail soot model		

Radiation Study Results

Figure 78 shows the comparisons between three radiation model options, it is clear that very little difference can be observed.

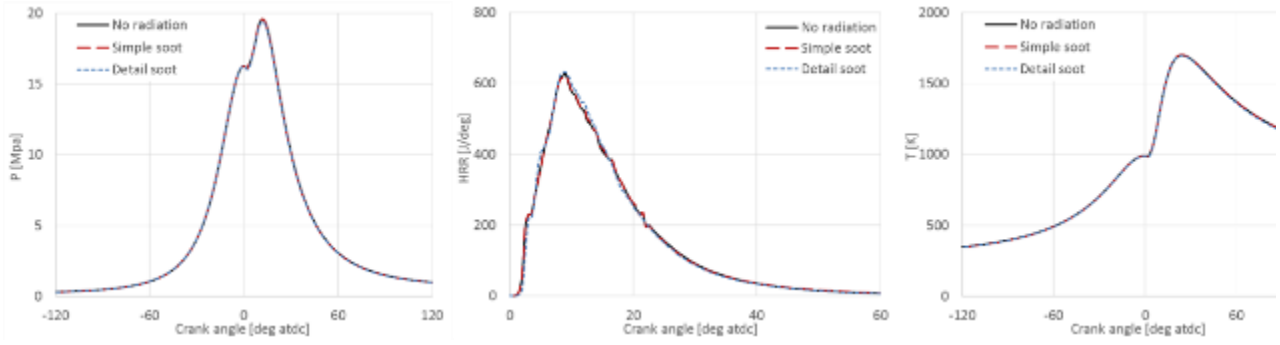

(a) (b) (c)

Figure 78: Comparison between 3 radiation model options, (a) in cylinder pressure, (b) apparent heat release rate, (c) mean temperature

Figure 79 and Figure 80 show similar comparisons between two wall temperatures and similarly, not much difference is observed. Different wall temperature gives different radiation energy transfer. The purpose for this study is to evaluate the capability of current radiation models to capture the wall temperature effects.

From Figure 78, Figure 79 and Figure 80, it can be concluded that current radiation models do not show noticeable impact on predicted results, further improvement is needed. By communicating with CONVERGE code vendor, it is confirmed that:

- Current radiation models are developed based on simple geometries (none engine cases) and they have not been validated against engine configurations.
- Current radiation models only capture the heat transfer between cylinder walls, radiation from soot is not considered yet.

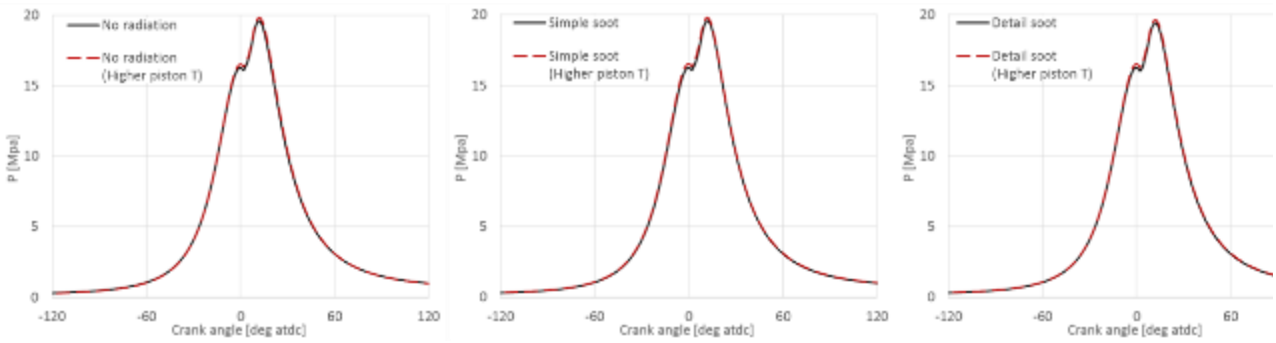

(a) (b) (c)

Figure 79: Pressure between 2 piston temperatures with three radiation model options, (a) no radiation model, (b) radiation model on with simple soot model, (c) radiation model on with detailed soot model

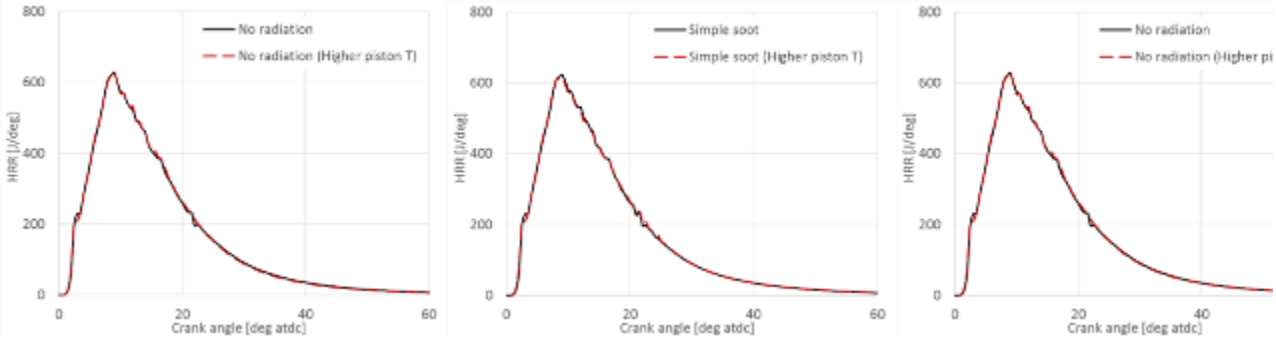

(a) (b) (c)

Figure 80: Apparent heat release rate between 2 piston temperatures with three radiation model options, (a) no radiation model, (b) radiation model on with simple soot model, (c) radiation model on with detailed soot model

Conclusions of radiation model assessment

The three radiation models in CONVERGE V2.3 are assessed in this report, two systematic studies are carried out to assess the radiation models available in CONVERGE V2.3. It can be observed that:

- The “lower peak, longer tail in AHRR” is NOT observed with 3 current radiation models.
- Very little difference is observed in the comparisons of pressure, AHRR and temperature, which shows little impact of current radiation models.
- Current radiation models have not been validated on engine configurations.
- Current radiation model only captures the radiation between walls, not including soot.

Assessment of temperature wall models in CONVERGE

The flow and temperature field in the near wall region is complex, therefore very fine mesh resolution is needed to resolve this region. To reduce the mesh resolution requirement in this region, wall models are used. A temperature wall model will provide a temperature profile in the near wall region, based on which, heat flux is calculated.

As discussed in Section 1.2.2, three wall model options are studied in this report:

- Option 1: Amsden (1997)
- Option 2: Han and Reitz (1997)
- Option 3: Angelberger et al. (1997)

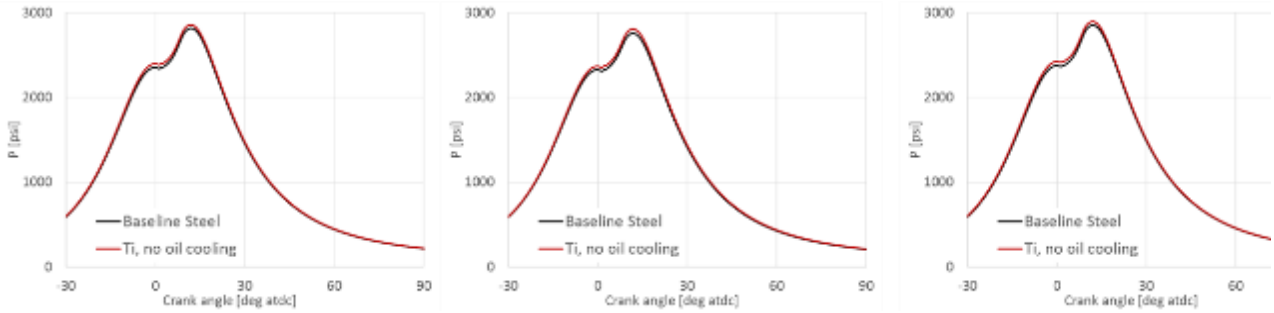

(a) (b) (c)

Figure 81: Pressure between two piston bowl designs with three temperature wall model options (a) wall model option 1, (b) wall model option 2, (c) wall model option 3

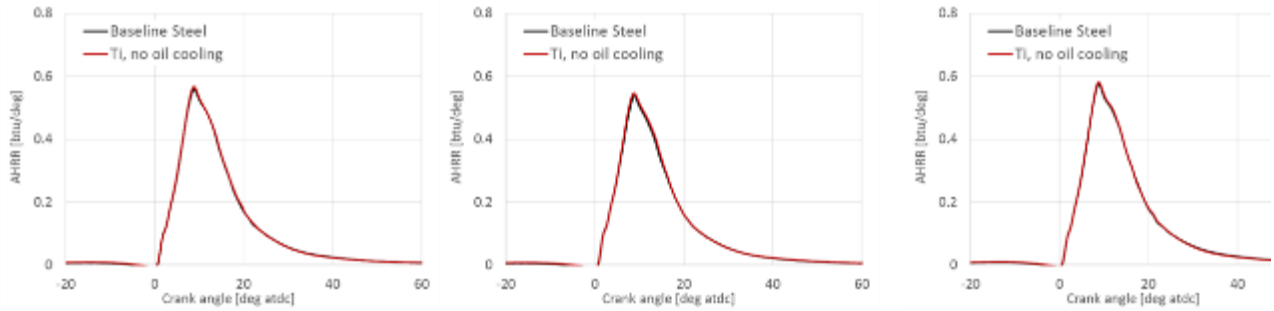

(a) (b) (c)

Figure 82: Apparent heat release rate between two piston bowl designs with three temperature wall model options (a) wall model option 1, (b) wall model option 2, (c) wall model option 3

Figure 81 and Figure 82 show the pressure and AHRR of two piston bowl designs with three different wall models. The "lower peak, longer tail in AHRR" is NOT observed; Rev3 bowl with higher wall temperature gives slightly higher pressure and AHHR than the baseline steel bowl and this trend is consistent with three wall model options. More advanced wall models can be assessed in the future work.

Conclusions of temperature wall model assessment

The temperature wall models in CONVERGE V2.2 are assessed. Systematic comparisons are made, it is observed that:

- The "lower peak, longer tail in AHRR" is NOT observed with temperature wall models available in CONVERGE V2.2
- Slightly higher P and AHRR observed for Rev3 bowl than steel bowl; this trend is consistent with three wall model options.
- More advanced temperature wall models are needed.

Conjugate heat transfer – combustion / piston simultaneous analysis

Conjugate heat transfer (CHT) analyses of low heat transfer pistons in the past were run using multiple tools, one for combustion modeling and one or two for piston thermal modeling. Closed cycle simulation of combustion modeling was followed in the approach. The closed cycle averaged heat flux on the piston crown from combustion modeling was scaled down to account for open cycle heat transfer and applied as boundary

condition in the piston thermal model. The approach required an iterative process between the combustion and piston thermal modeling to achieve converged thermal solution. There are uncertainties in thermal predictions following this approach that come from scaling of heat flux and steady state modeling approach. In Q3, CHT modeling of piston is run using CONVERGE where full cycle is modeled and thermal modeling is run as a transient problem with running multiple engine cycles to reach steady state thermal solution on the piston solid.

Methodology

There are two pieces in the CHT analysis of piston using CONVERGE – oil cooling modeling and CHT modeling of piston, both run in CONVERGE but separately. The geometry domains of these two models are shown in Figure 83.

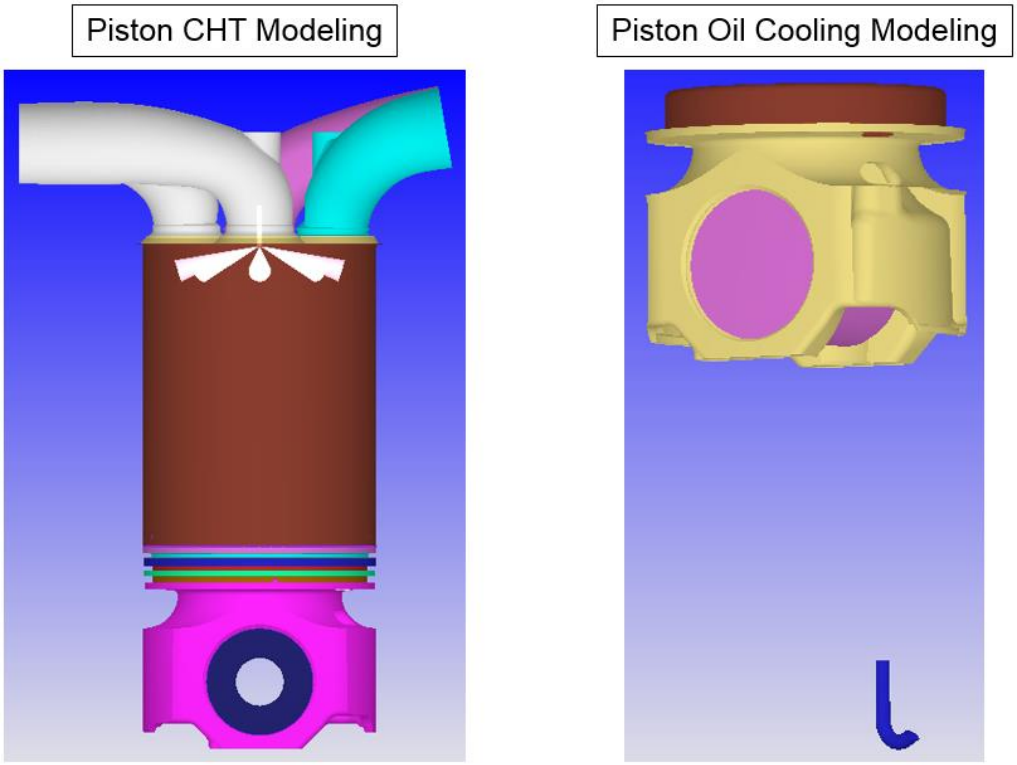

Figure 83: Geometry Domains of Conjugate Heat Transfer Modeling of Piston and Oil Cooling Modeling

Oil cooling model which consists of oil gallery, under-crown, piston pin and piston cooling nozzle is run using Volume of Fluid (VOF) approach. Multiple engine cycles are run until steady state is achieved with respect to consecutive cycle-to-cycle variation. Heat transfer coefficients and oil temperature on the oil gallery are taken from oil cooling modeling and applied as convective boundary condition on oil gallery in the CHT modeling of piston. The CHT model consists of intake and exhaust ports, valves, in-cylinder geometry and piston solid which includes lands, grooves, under-crown, skirt and pin. CHT model is run for multiple engine cycles until stead state thermal solution on piston solid is achieved.

Results of Oil Cooling Modeling of LHT Piston

The oil cooling modeling is run for 10 to 20 engine cycles to reach steady state. The heat transfer information (near wall fluid temperature and heat transfer coefficients) on the oil gallery and bottom of piston that includes undercrown, skirt and pin are time averaged for one cycle (720 deg) after reaching steady

state. Figure 84 shows temporal evolution of heat transfer coefficients (HTC) in oil gallery and bottom of piston for initializations of oil = 0%, 2% and 5%. Figure 85 and Figure 87 show cycle averaged spatial distribution of heat transfer coefficients (HTC) in oil gallery and bottom of piston respectively. Figure 86 and Figure 88 show cycle averaged spatial distribution of fluid (air/oil) temperature in oil gallery and bottom of piston respectively. Results in these figures show that HTCs in oil gallery and bottom of piston increase with initialization oil which is because of sloshing of oil during the piston motion. The temperatures of fluid inside gallery and on the bottom of piston are very similar between with and without initialization of oil because the fluid temperature is dictated by wall (gallery, piston bottom) temperature boundary conditions which are kept constant between with and without initialization of oil.

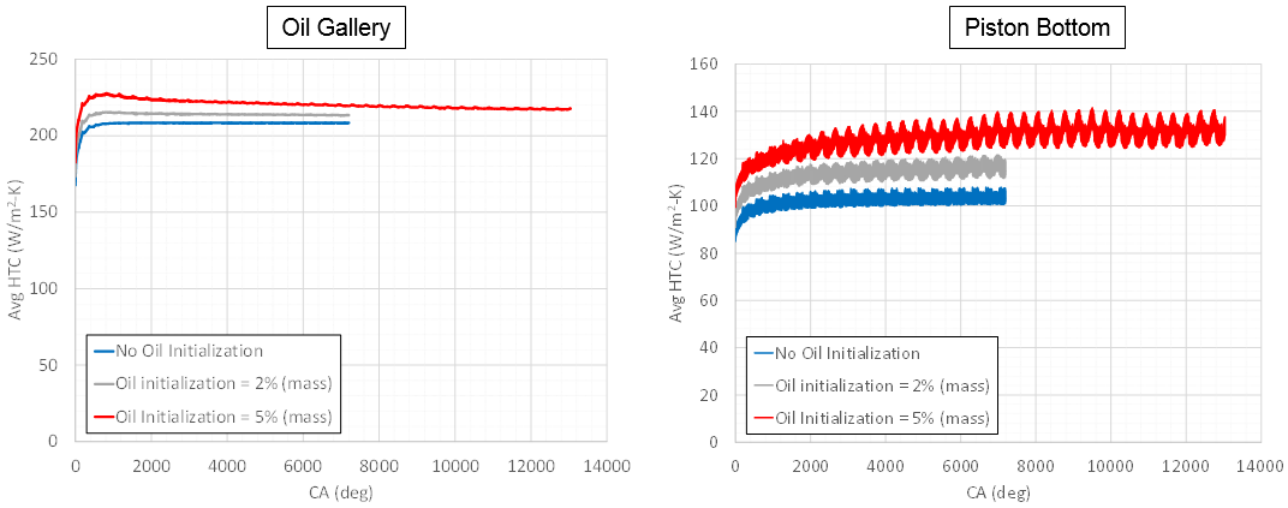

Figure 84: Spatial Averaged Heat Transfer Coefficients in Gallery and Bottom of Piston

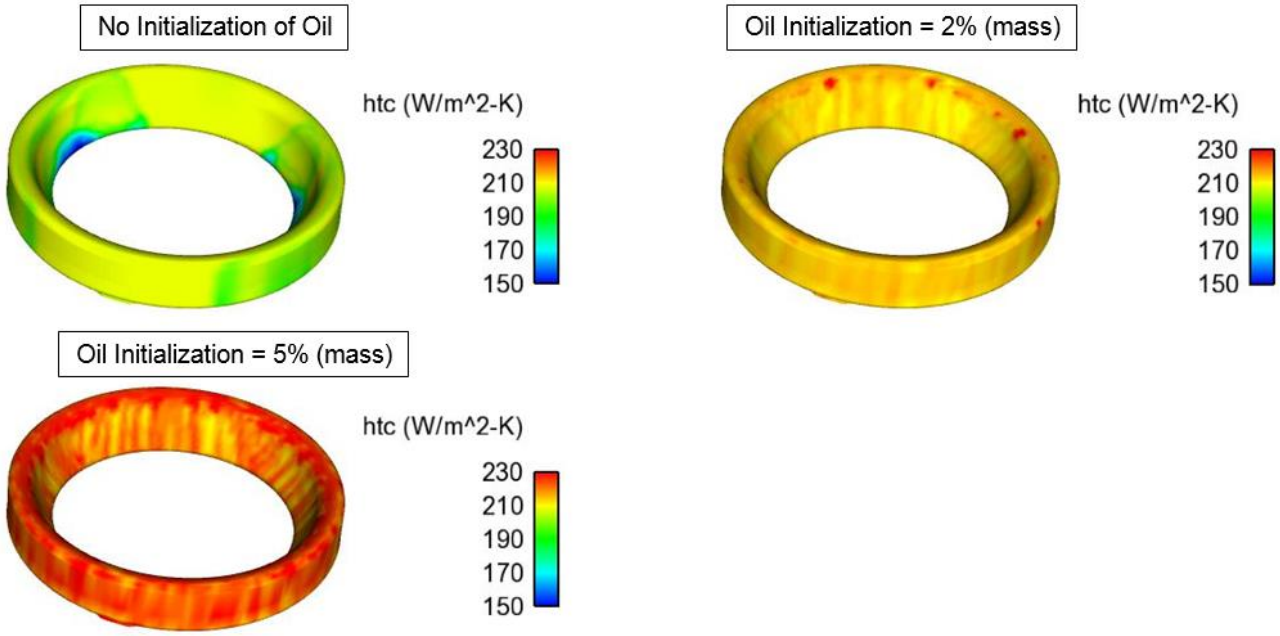

Figure 85: Cycle Averaged Heat Transfer Coefficients in Gallery

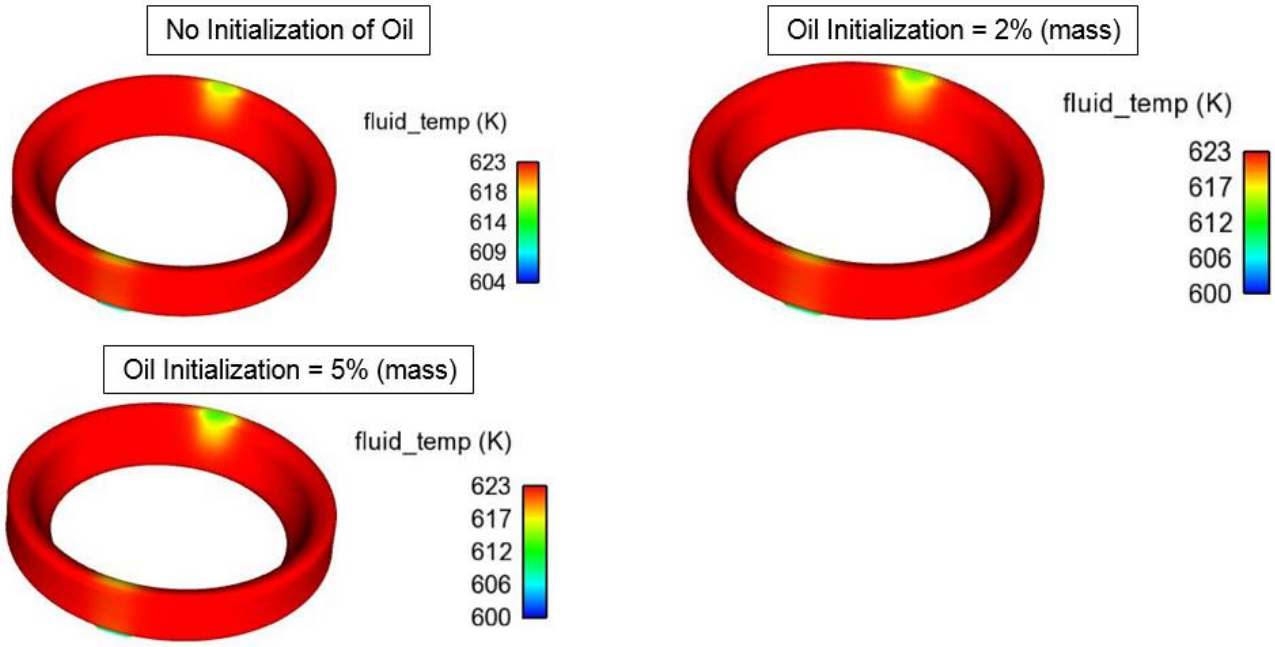

Figure 86: Cycle Averaged Fluid Temperature in Gallery

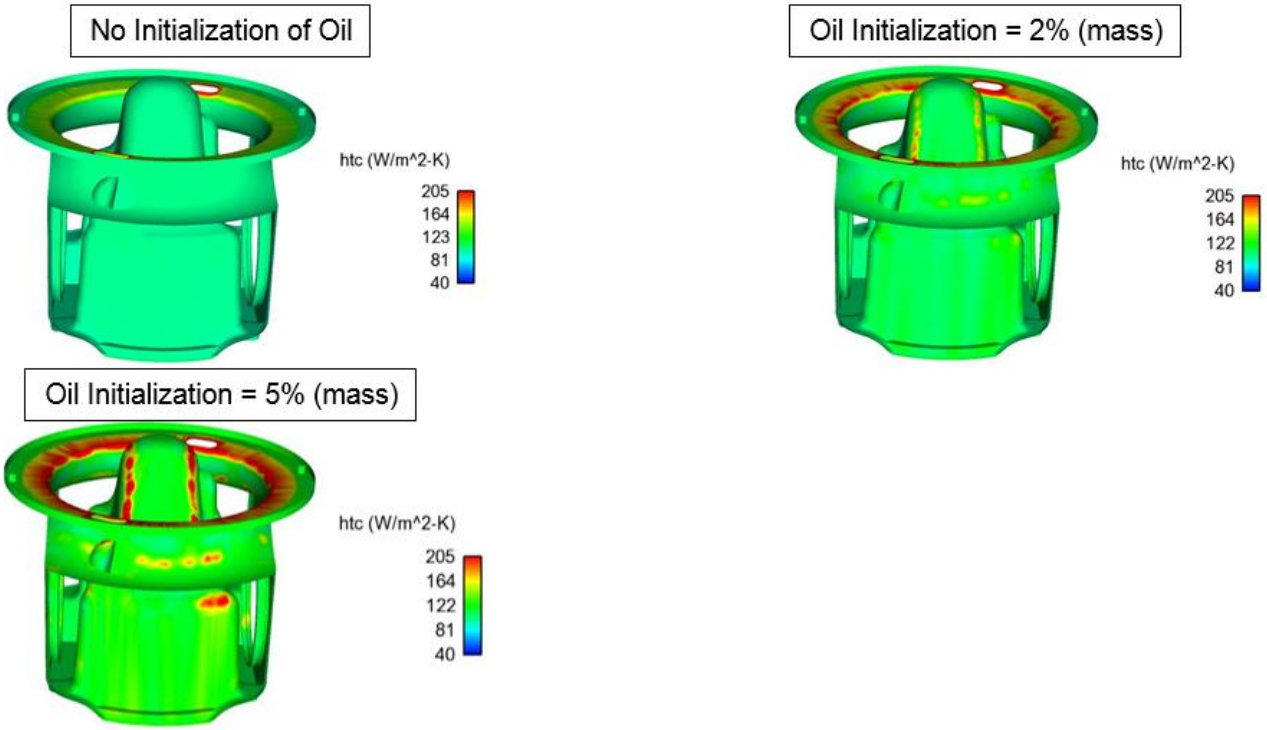

Figure 87: Cycle Averaged Heat Transfer Coefficients on Bottom of Piston

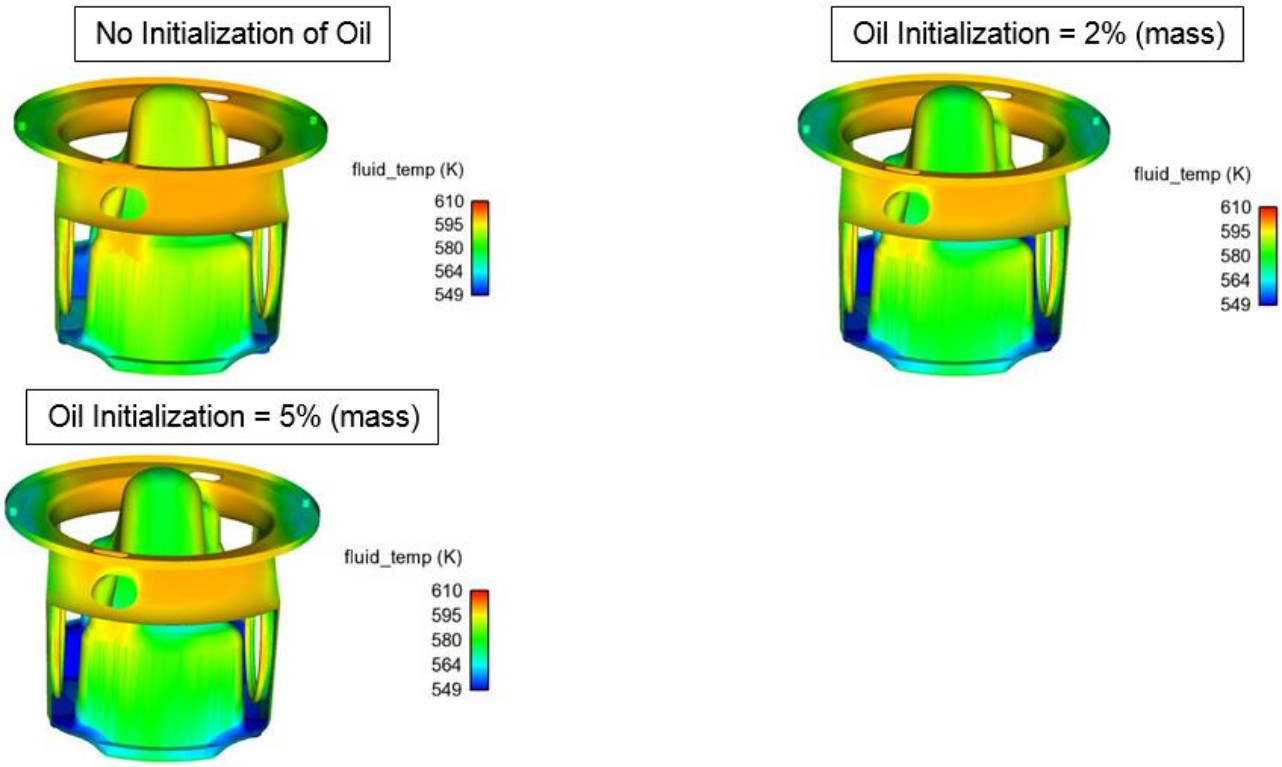

Figure 88: Cycle Averaged Fluid Temperature on Bottom of Piston

Results of Combustion and CHT Modeling of LHT Pistons

Results of combustion and CHT modeling with LHT piston were discussed in detail in Q3 report. Only results of sensitivity study of initialization of oil in gallery and piston bottom regions are shown in this report. Figure 89 shows locations of thermocouple on LHT piston which are used for comparison of temperature predictions of CHT modeling of piston with experimental measurements.

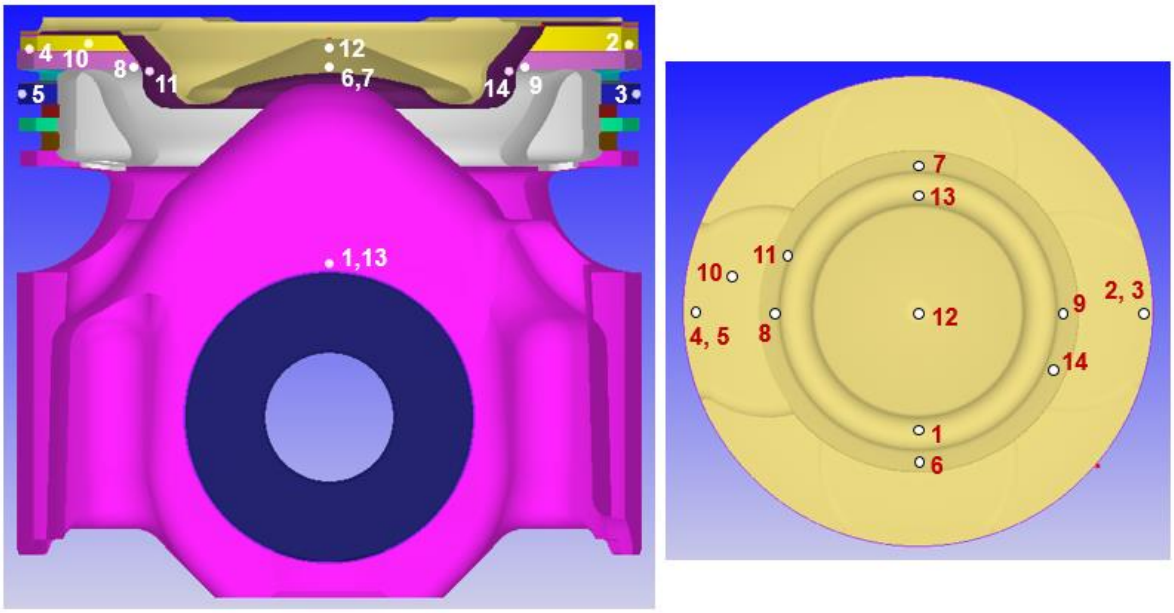

Figure 89: Thermocouple Locations on LHT Piston

Figure 90 shows temperature predictions of LHT piston for sweep of initialization of oil and thermocouple measurements. There is no significant impact on temperature predictions with 2% initialization of oil and slight reduction in temperatures at bowl rim locations with 5% initialization oil compared to temperature predictions with no initialization of oil in gallery and piston bottom regions. The reduction in temperatures at bowl rim locations come from slightly increased cooling with sloshing of oil. Temperatures at lands, grooves, pin bore and crown are not impacted with 2% and 5% initialization of oil.

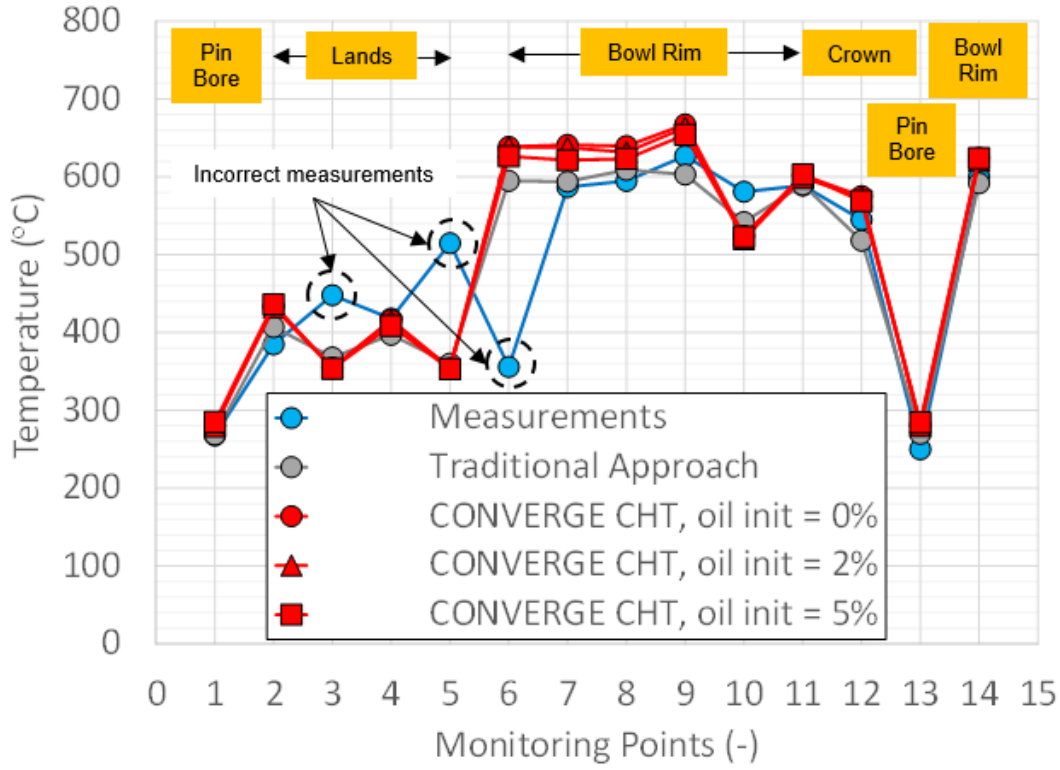

Figure 90: Comparison of Temperature Predictions and Thermocouple Measurements of LHT Piston

Piston Supplier CHT Modeling

CHT modeling of LHT piston from a piston supplier was started. The piston has 0.4 mm coating of TBC on steel piston crown, airgaps underneath the crown and on the side with no oil gallery. First step of building oil cooling model of piston is completed and VOF simulation has been run. Boundary conditions of oil cooling modeling (VOF simulation) with piston are shown in Figure 91.

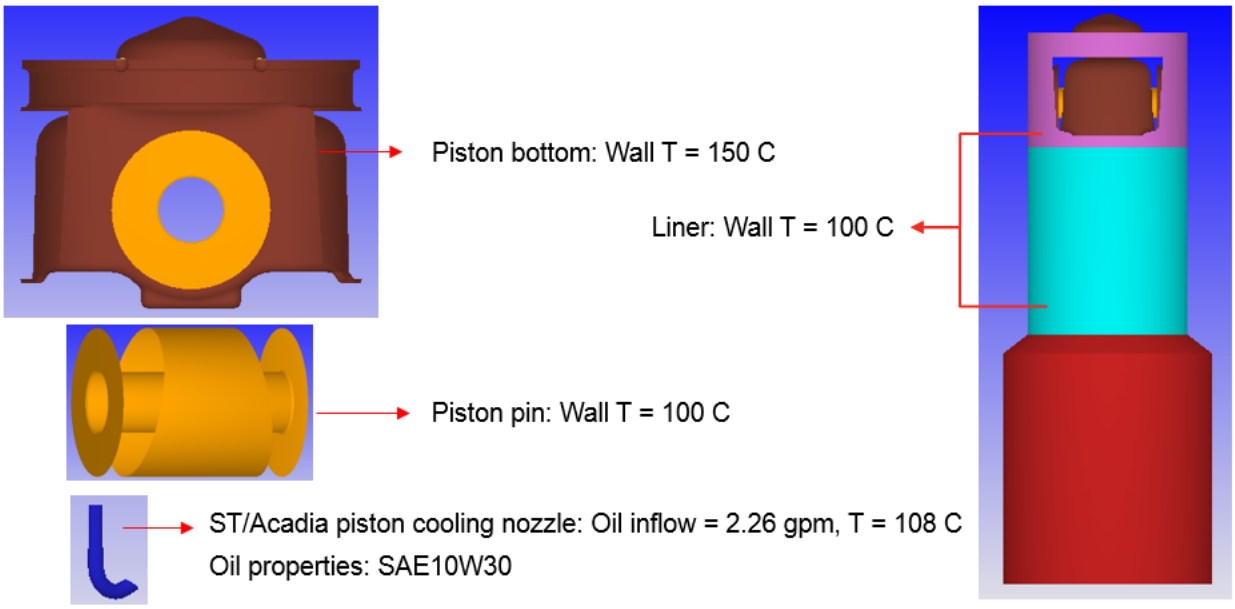

Figure 91: Boundary Conditions of Oil Cooling Modeling with LHT Piston

As there is no oil gallery, oil coming from piston cooling nozzle hits on the bottom of the piston and splashing starts. Figure 92 shows temporal evolution of heat transfer coefficients (HTC) on bottom of piston. Figure 93 shows spatial averaged HTC and oil temperature on bottom of piston. The location of peak HTC corresponds to where oil jet from piston cooling nozzle hits the piston. The undercrown temperature is relatively hotter because of boundary condition of 150 °C imposed on the piston bottom. Rest of the portions of piston bottom are cooler because of oil splash.

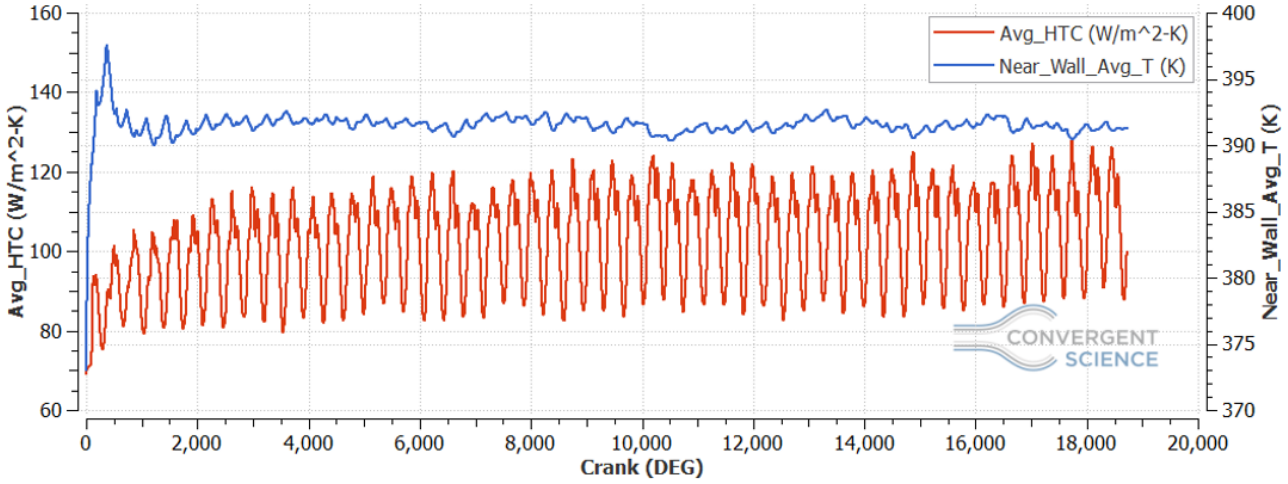

Figure 92: Spatial Averaged HTC and Oil Temperature on Bottom of Piston

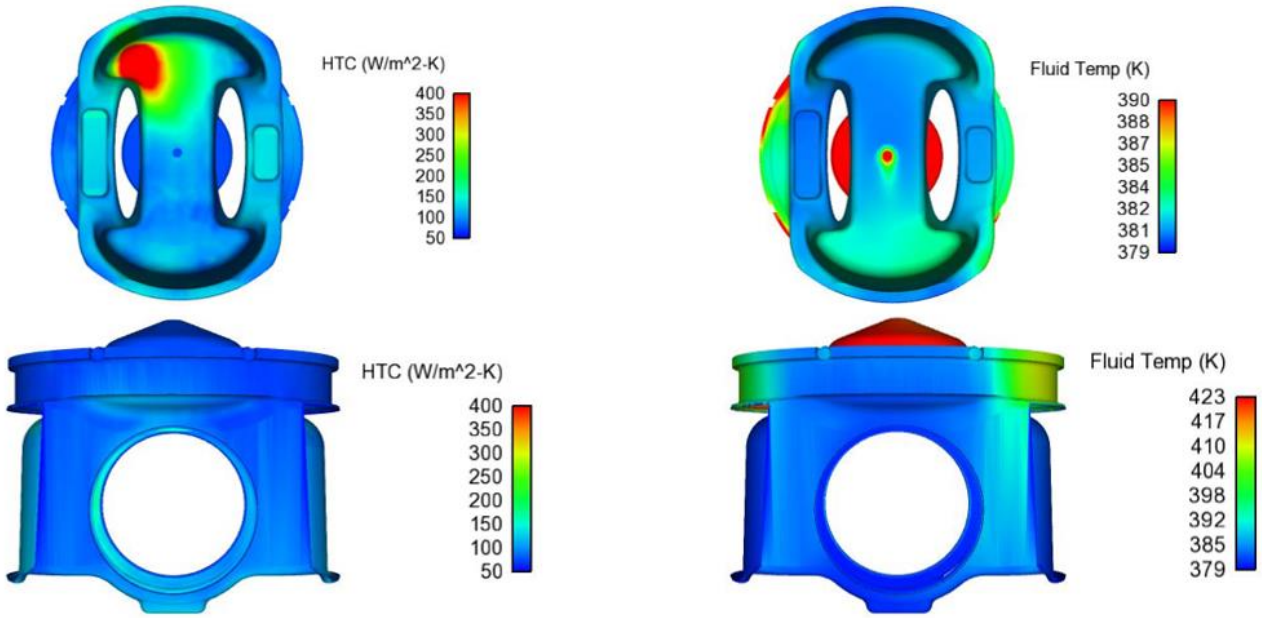

Figure 93: Cycle Averaged HTC and Oil Temperature on Bottom of Piston

CHT (new method) contd. – Oil cooling & CHT modeling in Converge contd.

About half way through the program, continuing the development of this novel tool for simultaneous fluid/solid heat transfer modeling, Conjugate Heat Transfer (CHT) modeling of a low heat transfer (LHT) piston was started with oil cooling modeling. The piston with no oil gallery was run with oil flow from piston cooling nozzle in the last quarter. In this quarter, Conjugate Heat Transfer (CHT) modeling of the piston is run to look

at piston temperature predictions and compare them with templug and thermal paint measurements of temperature. Also, sensitivity study of boundary conditions of piston solid in CHT model is run to look at the impact of boundary conditions on piston temperature.

Initial Results of CHT Modeling of LHT Piston

The CHT model is run for 3 to 5 engine cycles to get to a steady state piston temperature. After the piston reaches a steady state temperature, temperature distribution on piston bowl surface is looked and compared with thermal paint measurements of temperature on piston surface which is shown in Figure 84. Except the center of piston bowl, temperature distribution matches qualitatively well with measurements but maximum temperature is under predicted largely and average surface temperature is under predicted close to 60 °C.

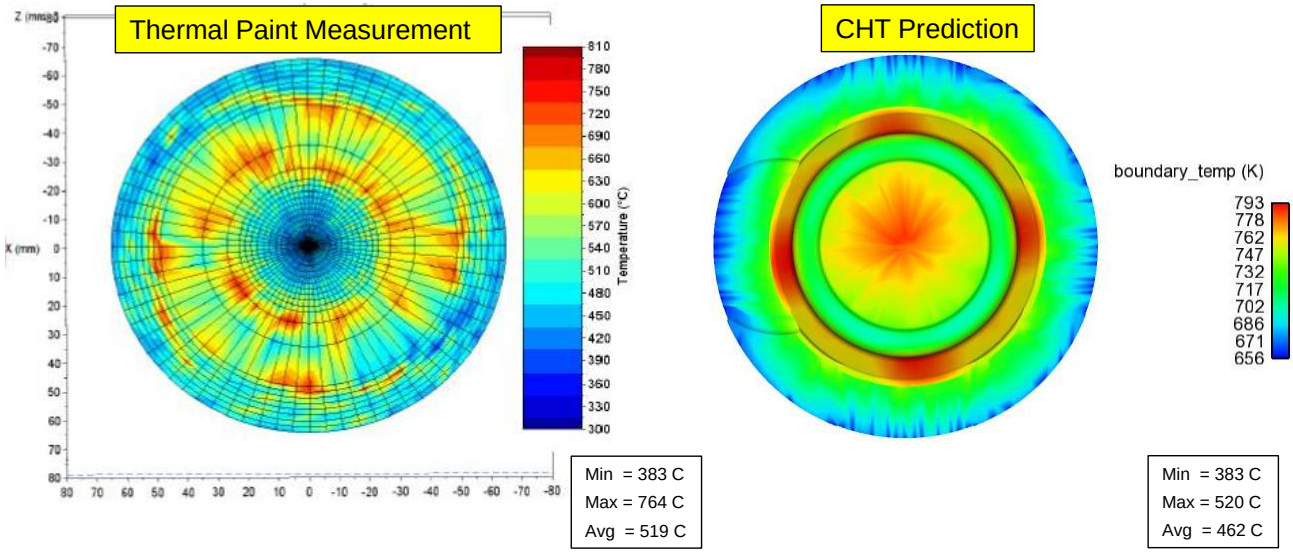

Figure 94: Comparison of Piston Bowl Surface Temperature Predictions with Measurements

There are 34 locations in the LHT piston covering bowl/crown, under-crown, lands, pin boss and skirt where temperatures are measured. Figure 87 shows the comparison of temperature predictions and templug measurements. Temperature predictions at locations of top land, bowl bottom, pin boss, under-crown and skirt match well with measurements and temperatures at bowl ramp locations are highly overpredicted and some overprediction and underprediction of temperatures at second land and bowl edges respectively. One of the locations (30) on the under-crown had bad measurement of temperature. There are uncertainties in thermal barrier coating thickness over the surface of the piston crown and modeling of airgap which could lead to differences in piston temperature predictions and measurements.

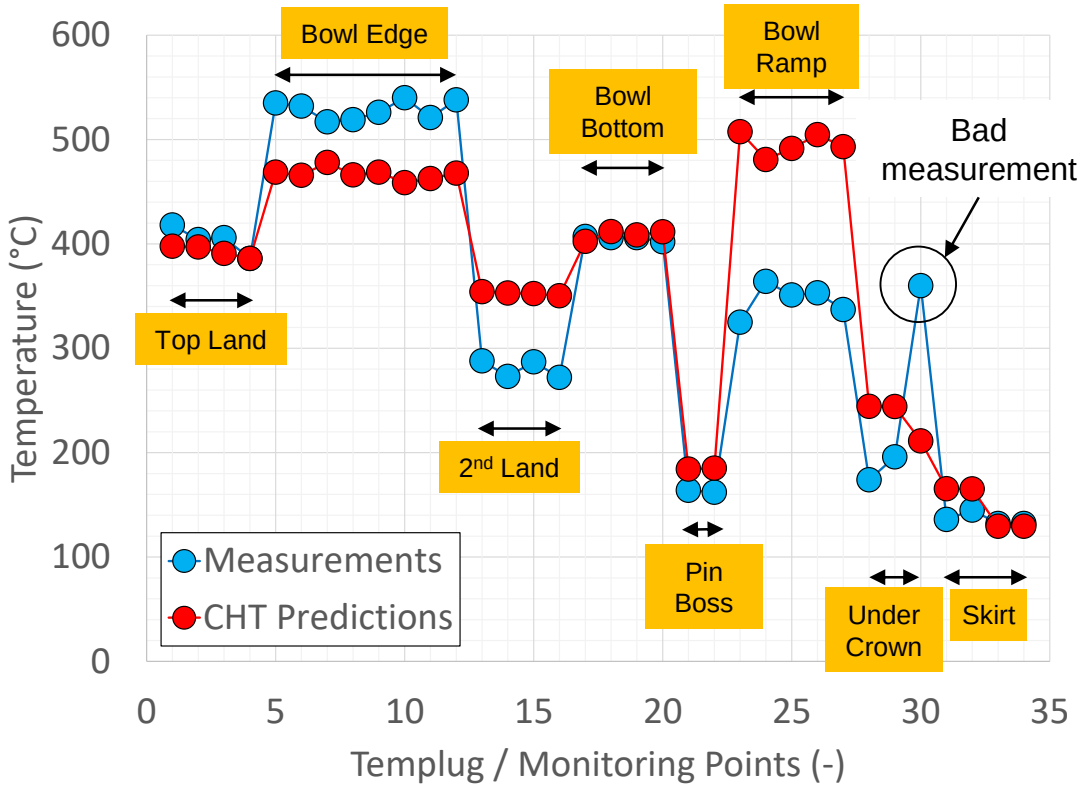

Figure 95: Comparison of Temperature Predictions and Templug Measurements of LHT Piston

Sensitivity Study of Boundary Conditions of Piston Solid

Sensitivity study of various boundary conditions of piston solid shown in **Error! Reference source not found.** is run to look at the impact of boundary conditions on piston temperature and improvement in temperature predictions with measurements. Figure 89 shows thermal resistance sensitivity study where thermal resistance was decreased from baseline value of 0.001 to 0.0005 (50% reduction) and 0.00025 (75% reduction). Measurements of coating thickness showed much lower than 0.4 mm intended thickness at most of the regions of piston surface. So, a sensitivity study is run with lower thermal resistance values from baseline. Decreasing the thermal resistance increased piston temperature as expected. Temperature predictions at bowl edge, bowl ramp and bowl bottom locations increased with lower thermal resistance and temperature at other locations (lands, pin boss, undercrown, skirt) are hardly impacted.

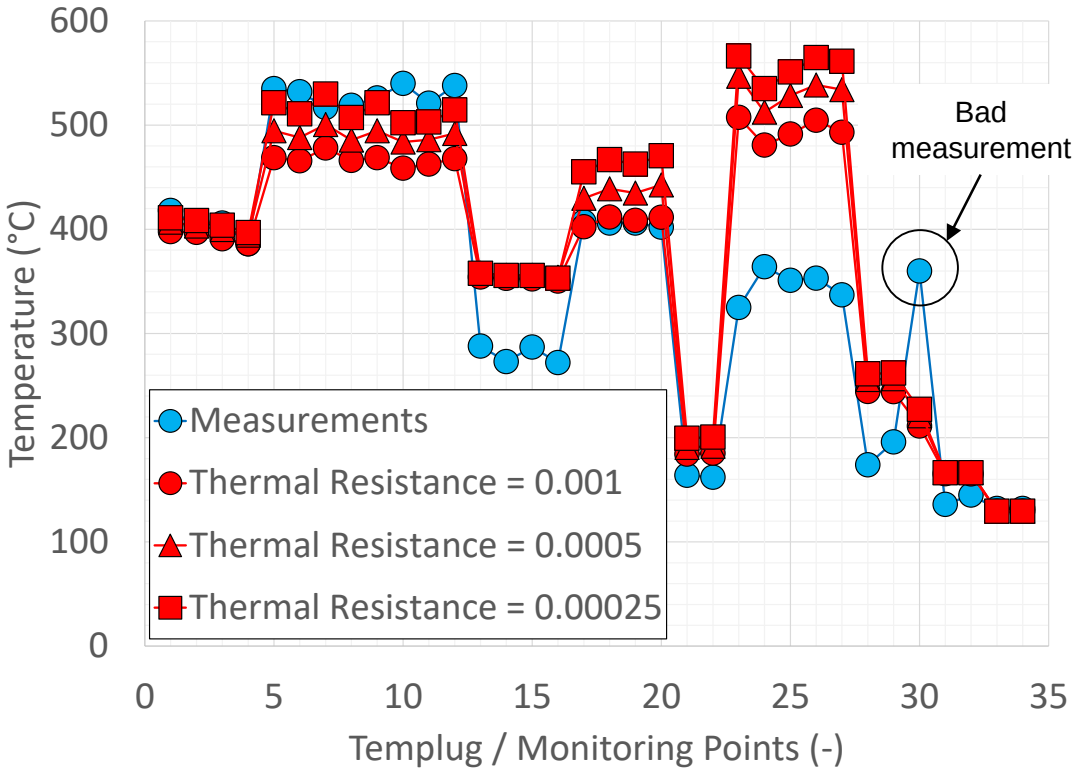

Figure 96: Thermal Resistance Sensitivity Study

Figure 90 shows comparison of temperature predictions of piston bowl surface with using lower thermal resistance and thermal paint measurements. Temperature match is improved from baseline match shown in Figure 84. There is still over prediction of piston surface temperature which is due to the difference between how thermal resistance setup in CFD modeling and how TBC in engine testing work - TBC increases surface temperature and lowers temperature underneath the coating surface while higher thermal resistance decreases surface temperature and temperature underneath the surface.

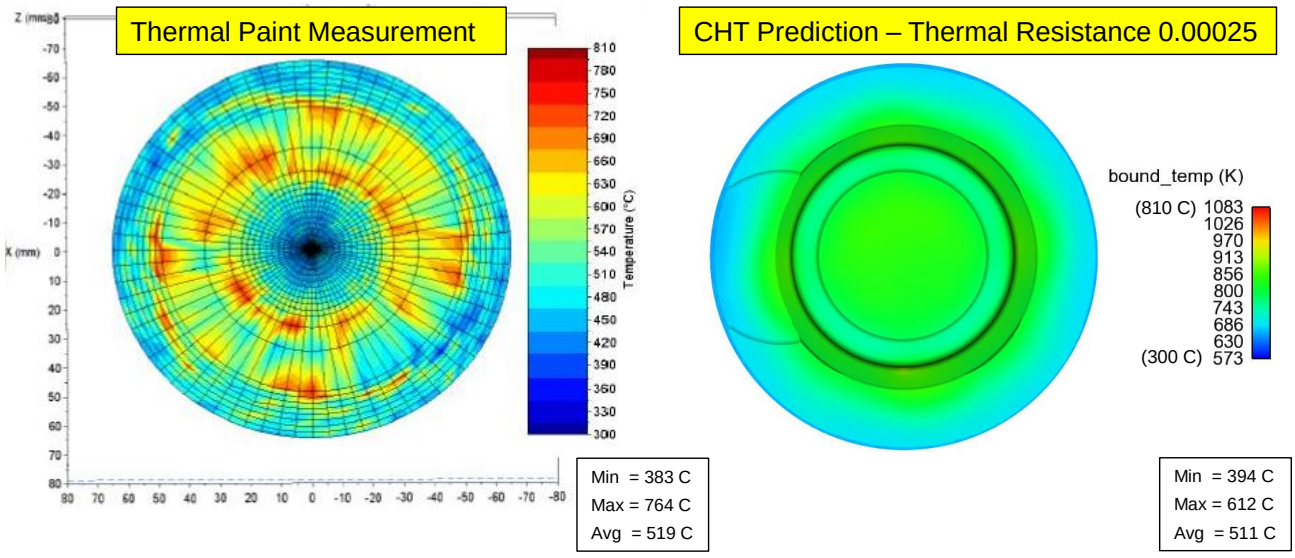

Figure 97: Comparison of Piston Bowl Surface Temperature Predictions with Measurements

Figure 98 shows sensitivity study of HTC values used in convective boundary conditions of airgaps. Increasing HTC of airgaps from 100 to 500 provides significant cooling of entire piston solid. Temperatures dropped more than 100 °C on bowl locations.

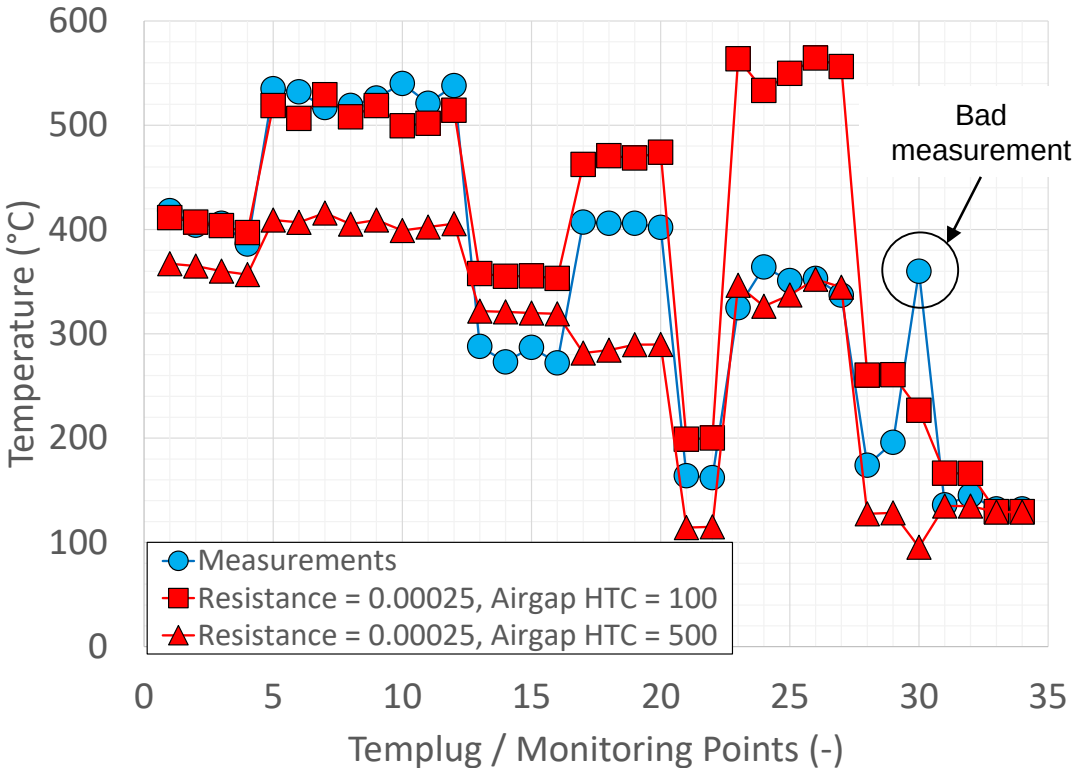

Figure 98: Sensitivity Study of Air-Gaps Boundary Conditions

The crown boundary in CHT modeling is classified into multiple boundaries and imposed appropriate thermal resistance values based on non-uniform coating thicknesses seen in measurements.

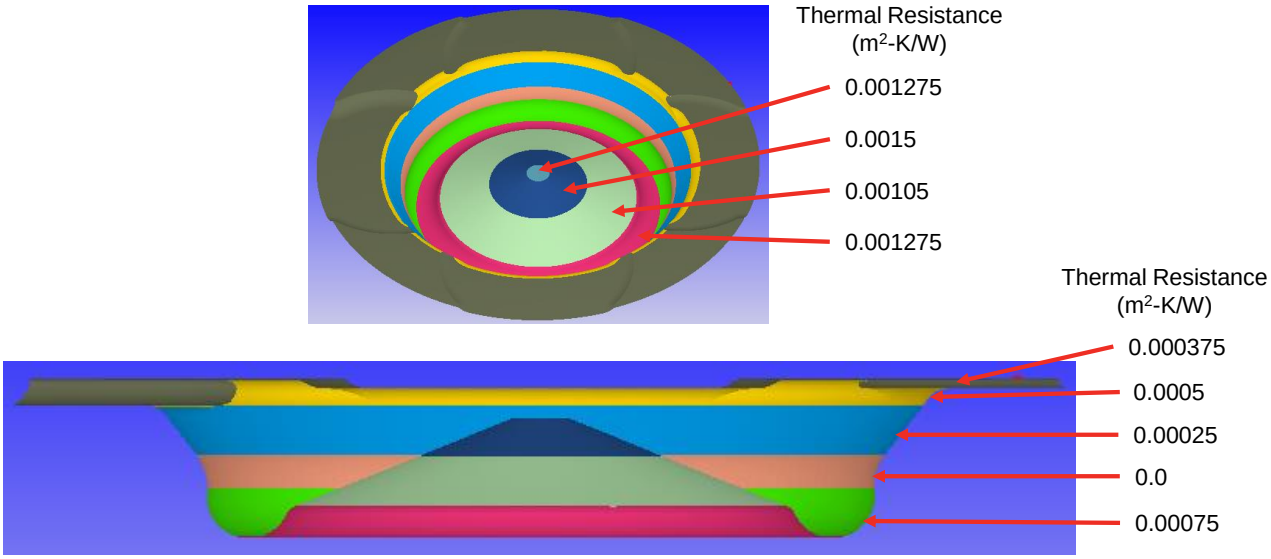

Figure 99: Classification of Crown Boundaries Based on Non-Uniform Coating Thickness

Figure 100 shows comparison of piston temperature predictions using single crown boundary and multiple crown boundaries approach with templug measurements. There is improvement in temperature predictions at bowl ramp locations with having multiple crown boundaries.

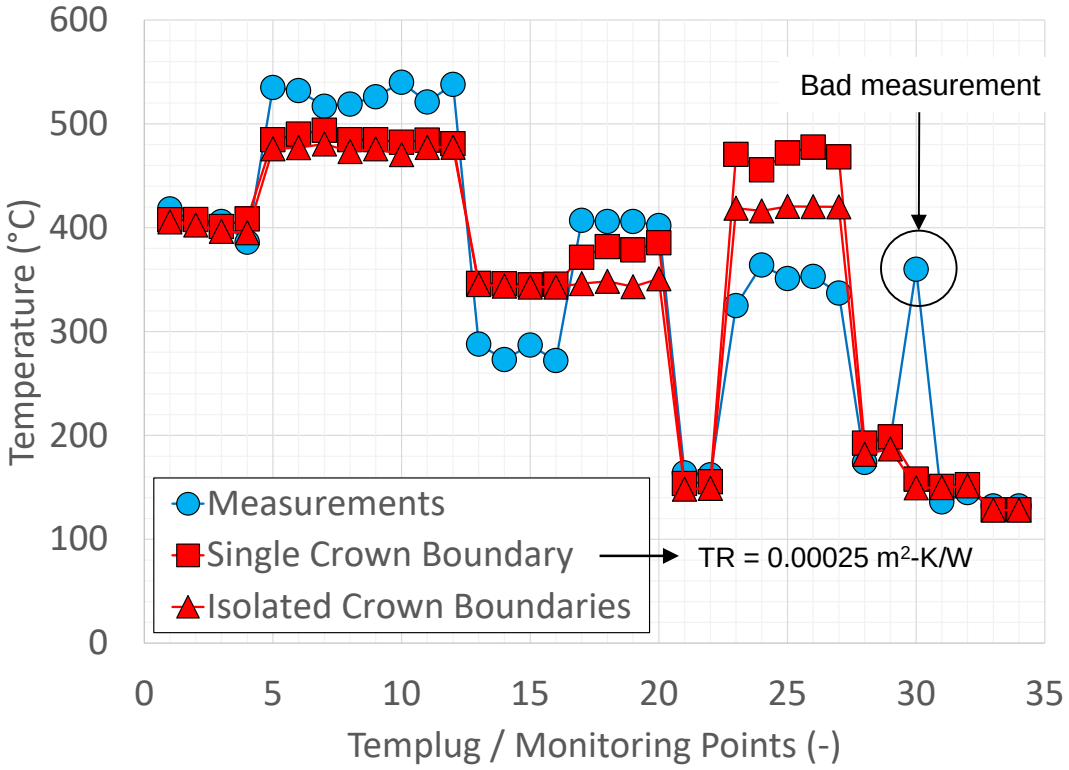

Figure 100: Comparison of Piston Temperature Predictions with Single Crown Boundary vs. Multiple Crown Boundaries

Results of CHT Modeling of LHT Piston

Sensitivity study of boundary conditions shows that thermal resistance values on piston crown and HTC values on airgaps surface have huge impact on piston temperature. Figure 91 and Figure 102 show comparison of predictions of cylinder pressure and heat release rate with engine data respectively. There is reasonably good match of cylinder pressure and heat release rate predictions with engine data. Figure 92 shows the comparison of temperature predictions using revised boundary conditions and templug measurements. Very good match of temperature predictions with measurements is achieved at top land, second land, pin boss, undercrown and skirt locations. There are some differences of temperature of 30 °C - 50 °C between predictions and measurements at locations of edge, ramp and bottom of bowl. There could be uncertainties in coating thickness of the piston with templug and trapped mass captured in cylinder at IVC in the model which would impact piston temperature. Also, there are uncertainties in the modeling of airgaps which as well impact piston temperature.

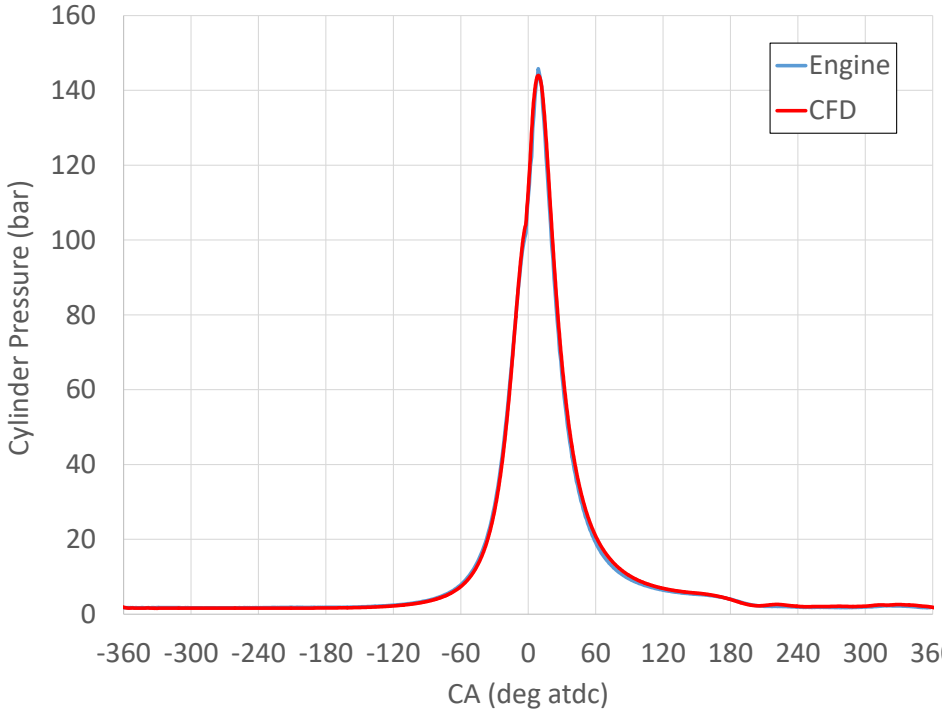

Figure 101: Cylinder Pressure

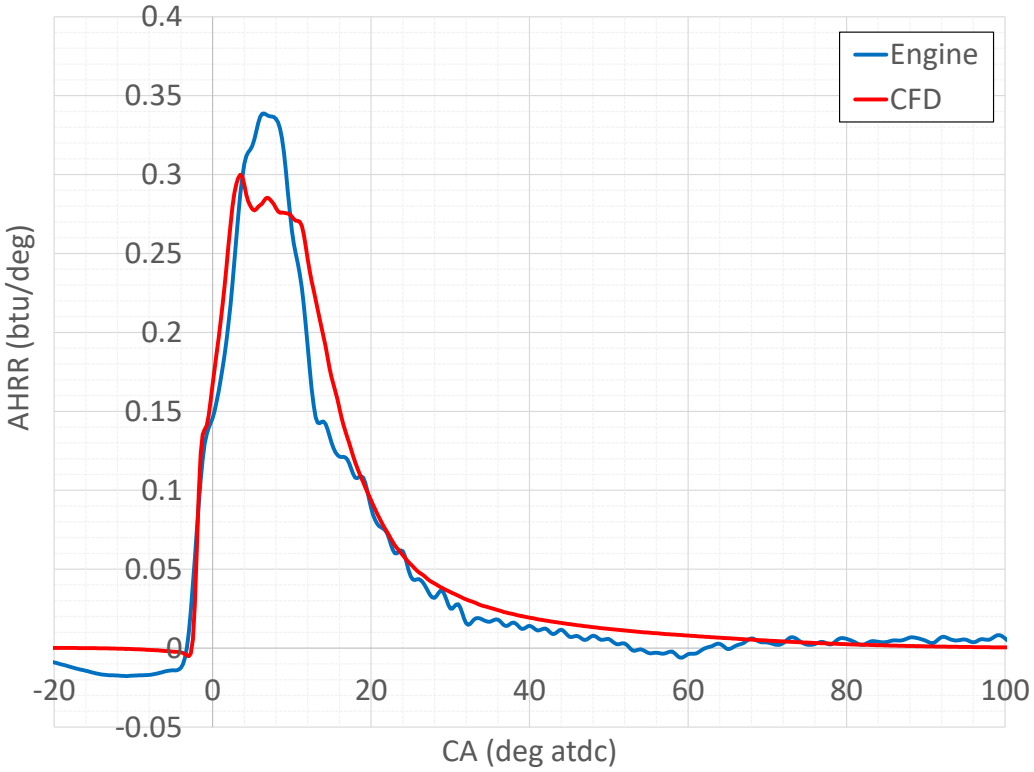

Figure 102: Apparent Heat Release Rate

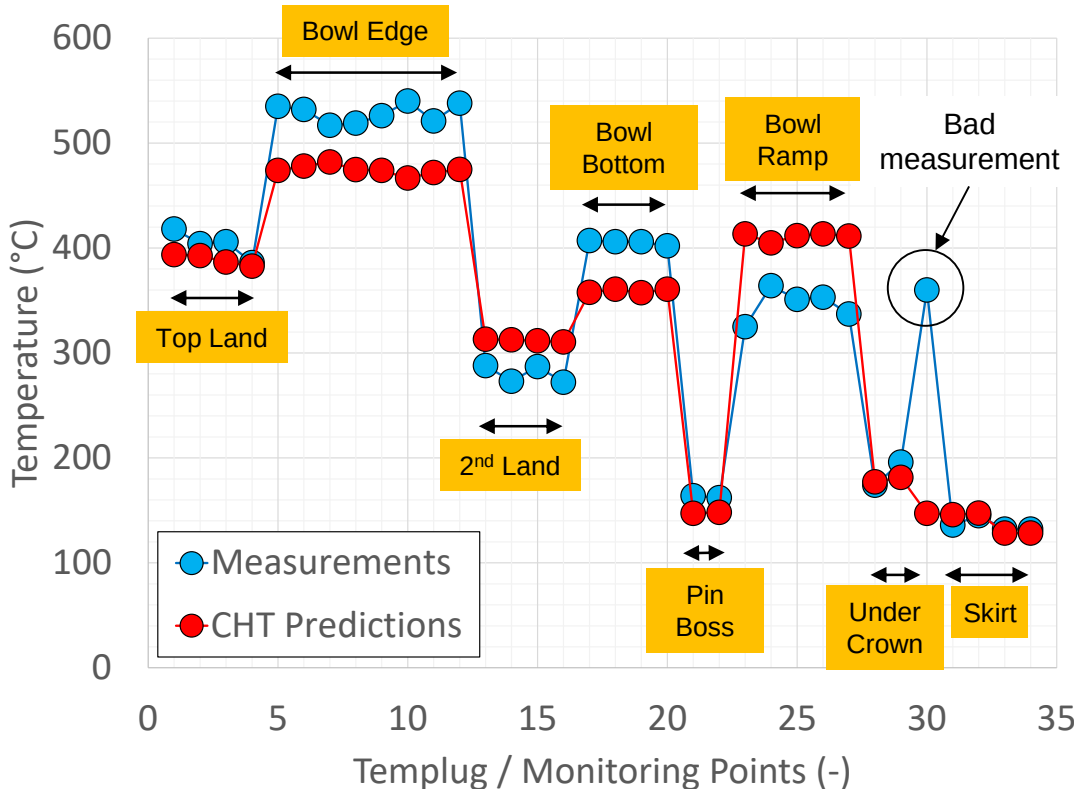

Figure 103: Comparison of Temperature Predictions and Templug Measurements of FM HiTherm Piston

Inferences (oil cooling / CHT modeling)

- Thermal resistance and air-gap HTC values are the most important boundary conditions that have huge impact on piston temperature.
- Except the center of piston bowl where there is over prediction of temperature, temperature distribution on the rest of the piston bowl surface matches qualitatively well with measurements. Maximum surface temperature is under predicted largely.
  - TBC is modeled through thermal resistance. TBC increases surface temperature and lowers temperature underneath the coating while higher thermal resistance decreases surface temperature and temperature underneath the surface. Difference between how thermal resistance setup in model and TBC in experiments work causes the differences in temperature predictions on the piston surface.
- CHT model predictions of temperature match well with templug measurements at lands, pin boss, under-crown and piston skirt.
- There are some differences between CHT model predictions of temperature and templug measurements around edges and bottom of piston bowl
  - There could be uncertainties in coating thickness of the piston with templug and trapped mass captured in cylinder at IVC in the model which impact piston temperature
  - There are uncertainties in modeling of airgaps which impact piston temperature

- Air gap modeling detailed analysis found important to predict HTC and T on airgaps as immediately following task
- Also, realized to analyze 0.4 mm TBC modeling to compare approaches of thermal resistance vs. TBC modeling as an immediately following task

Combustion CFD – Combustion System Optimization

Model Recalibration Results

Figure 104, Figure 105 and Figure 106 show the pressure traces and heat release rate curves for the 1-degree BTDC (Run Point 1824), 3 degrees BTDC (Run Point 1826) and 5 degrees BTDC (Run Point 1828) start of injection timings respectively. As the plots show, CFD can capture the in-cylinder pressure and heat release with acceptable accuracy.

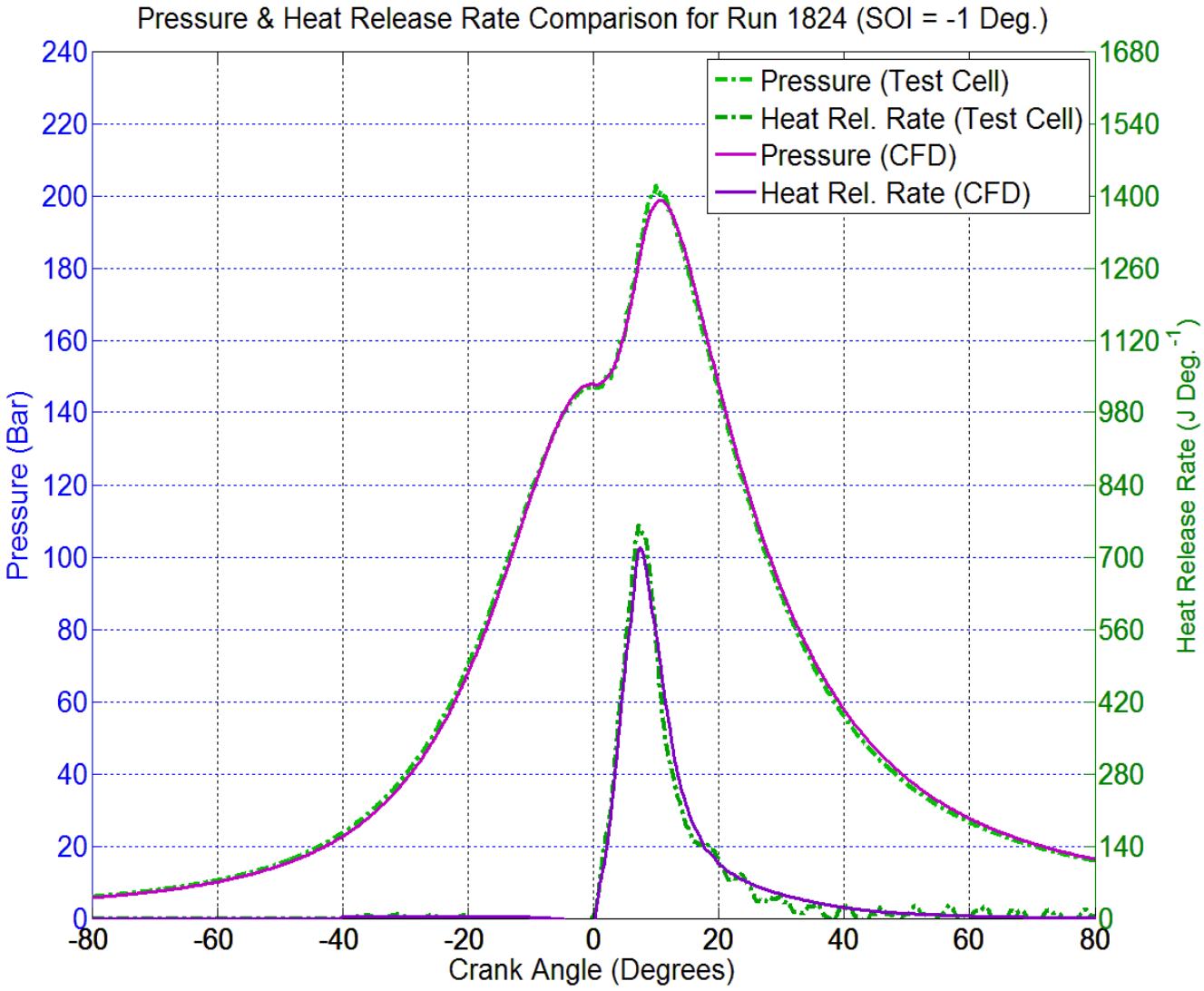

Figure 104: Pressure Trace & Heat Release Rate Curve Comparison with Experiment for Run 1824 (SOI = 1-degree BTDC)

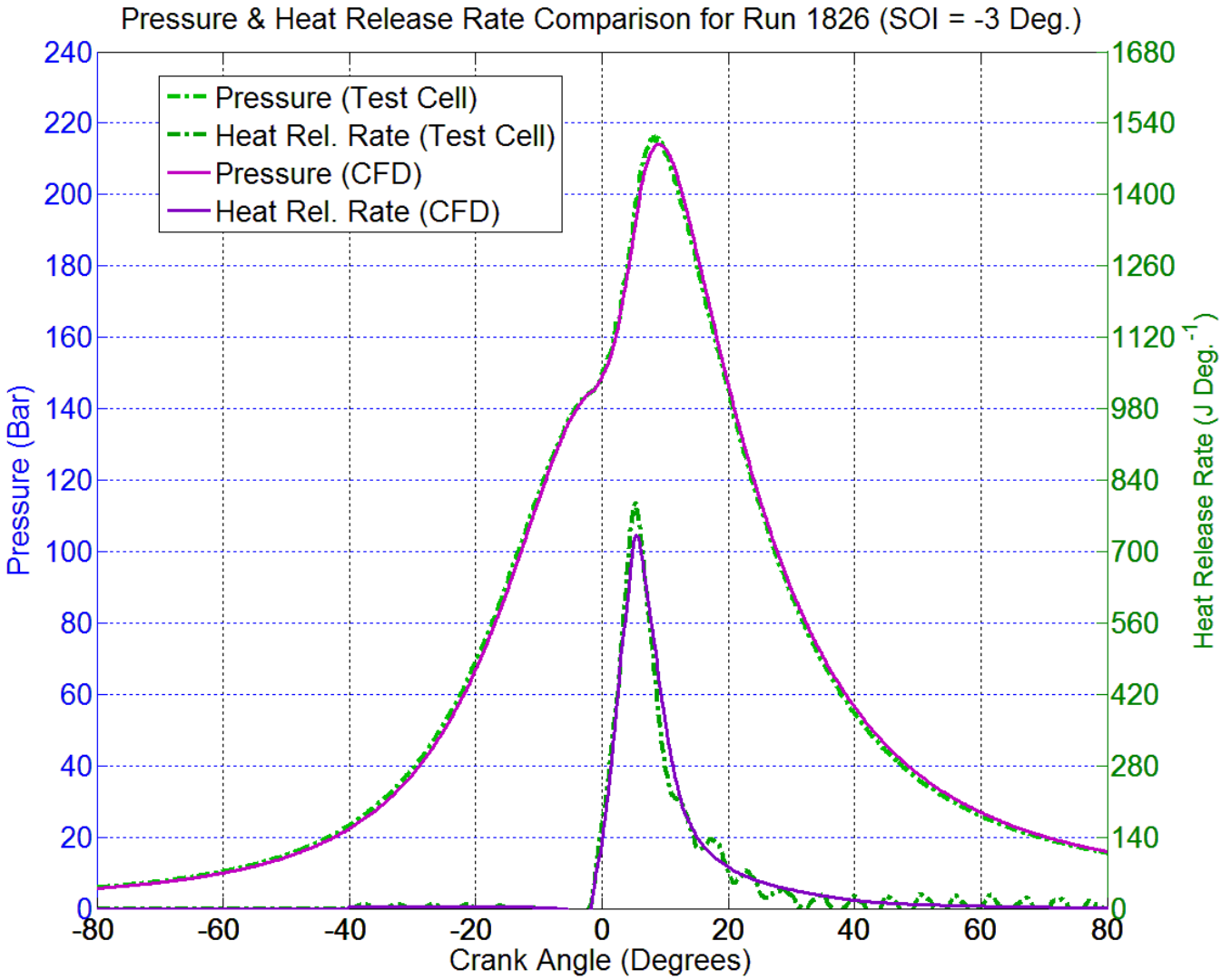

Figure 105: Pressure Trace & Heat Release Rate Curve Comparison with Experiment for Run 1826 (SOI = 3 degrees BTDC)

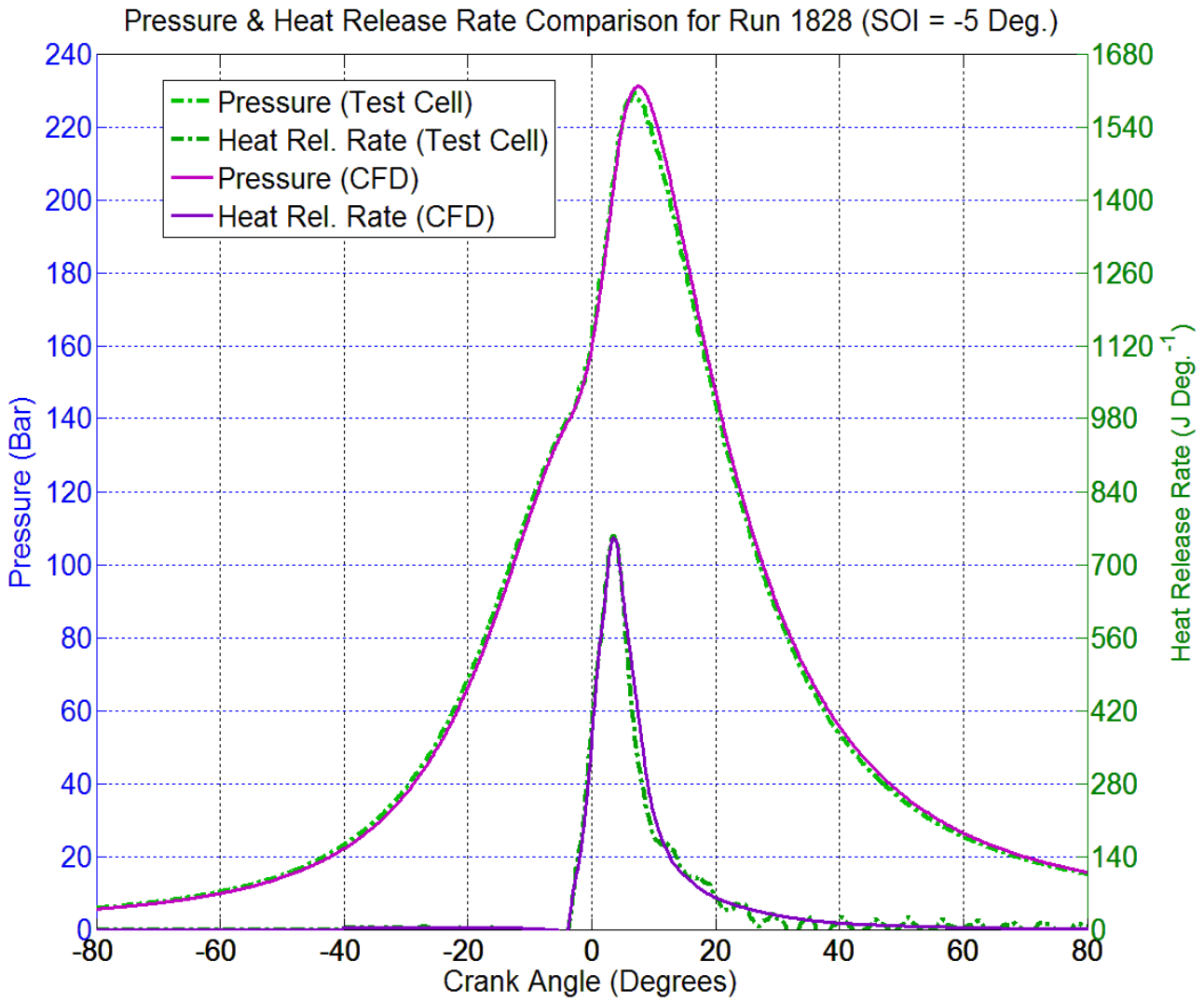

Figure 106: Pressure Trace & Heat Release Rate Curve Comparison with Experiment for Run 1828 (SOI = 5 degrees BTDC)

Figure 107: Gross Indicated Thermal Efficiency Comparison between Test Cell & CFD for the Start of Injection Timing Sweep at 1400 Bar Rail Pressure. and Figure 108 show the gross indicated thermal efficiency and emissions trends respectively for the different run points. Overall, the emissions predictions are acceptable since the trends observed in the experiments are well captured in the CFD simulations. However, the thermal efficiency appears to be consistently over-predicted by about 3%, even though the directional trend captured by the simulation matches that of the experiments. It is therefore necessary to examine the in-cylinder energy balance and identify the discrepancy between the simulation and experiments.

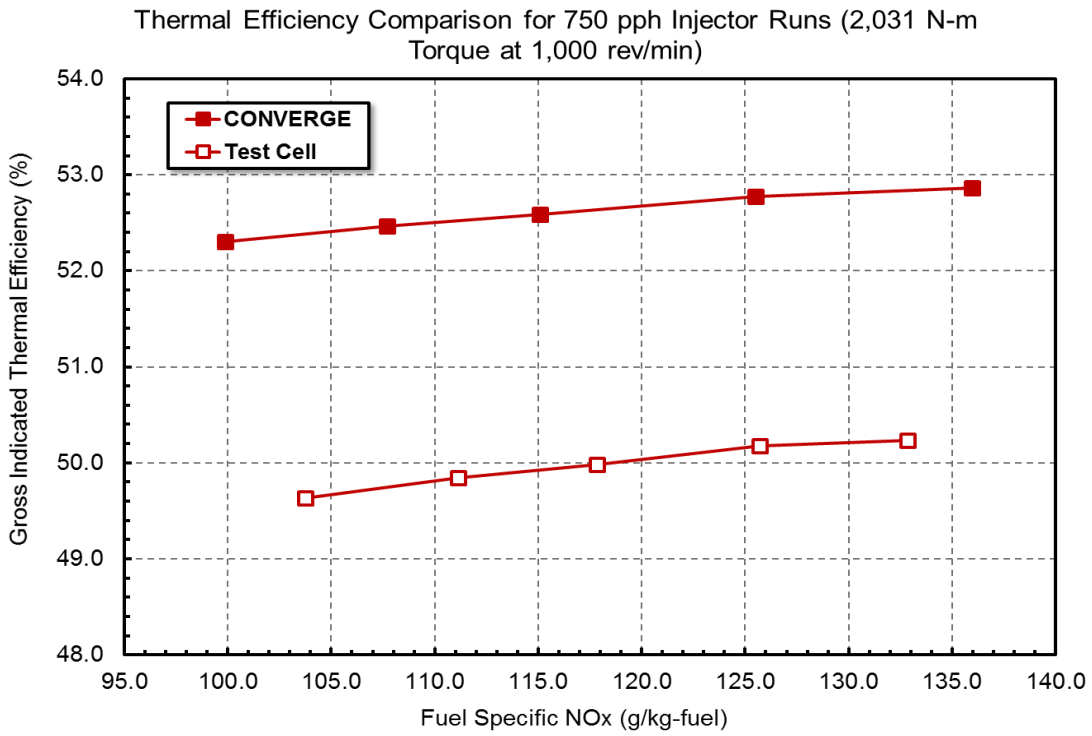

Figure 107: Gross Indicated Thermal Efficiency Comparison between Test Cell & CFD for the Start of Injection Timing Sweep at 1400 Bar Rail Pressure.

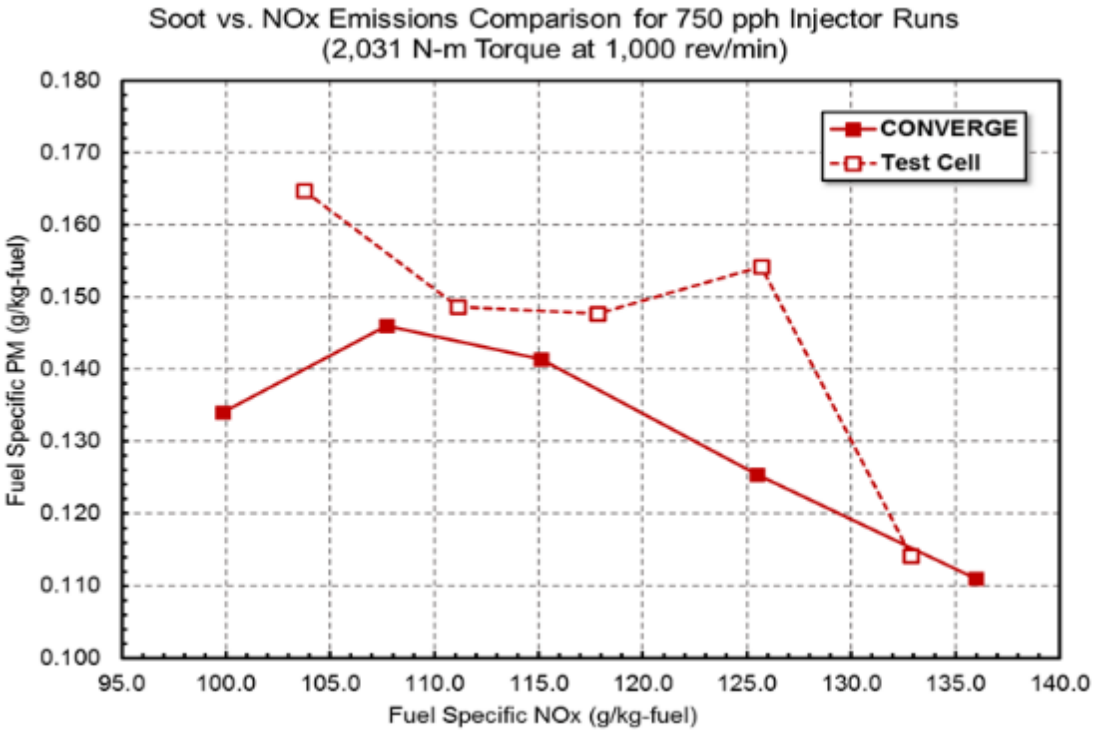

Figure 108: NO_x and PM emissions Comparison between Test Cell & CFD for the Start of Injection Timing Sweep at 1400 Bar Rail Pressure.

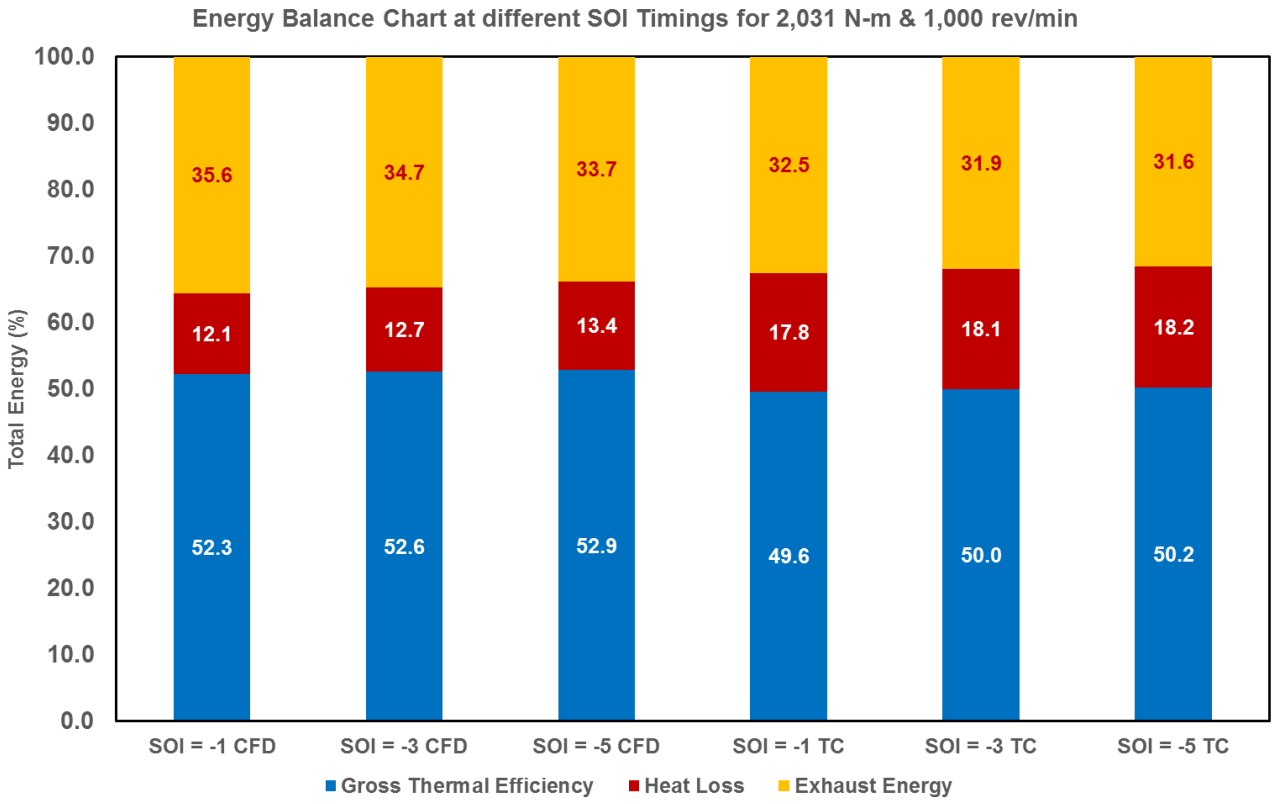

Figure 109: Energy Balance Bar Chart showing the percentage of total fuel energy distributed among useful work and the sources of energy loss. Note that TC stands for Test Cell Experimental results while CFD stands for the simulation results.

From the energy balance bar chart shown in Figure 109, the in-cylinder heat loss is lower than that observed in experiments, and that the exhaust energy is higher. This results in a higher percentage of the fuel energy converted to useful work. The discrepancy between the CFD predictions and test data is mainly due to the under prediction of heat losses which could be in turn a consequence of the uncertainties in boundary wall temperature. The modeling approach of using a fixed wall temperature may also not be appropriate as in reality there could some fluctuations in the surface temperature during an engine cycle. Another possible cause for this heat loss discrepancy may be due to uncertainty in the in-cylinder trapped mass at Intake Valve Closure (IVC).

The rail pressure sweep results at SOI timings of 2 degrees BTDC are shown in Figure 110 and Figure 111. Once again, as the plot in Figure 110 shows, there is about a 2.4% discrepancy in the thermal efficiency between the experiments and CFD simulations, although the directional trend is captured. The emissions trends are properly captured by the CFD simulations as shown in Figure 111, but the absolute values of NO_x appear to be under-predicted.

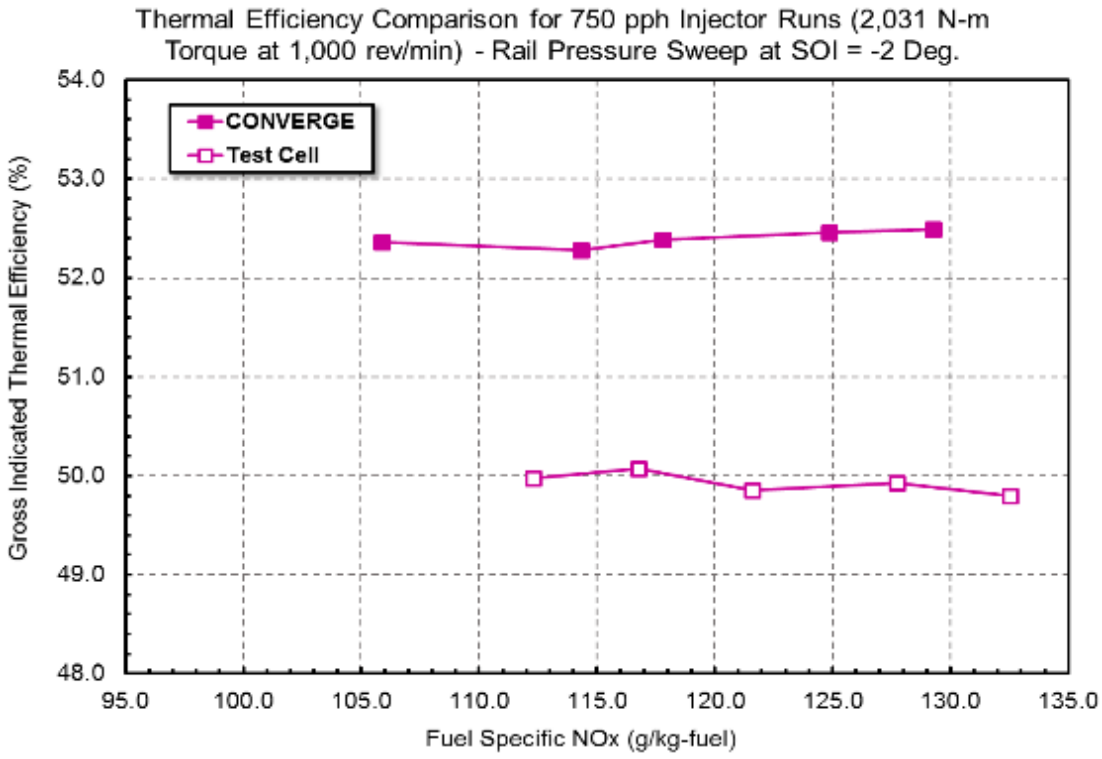

Figure 110: Gross Indicated Thermal Efficiency Comparison between Test Cell & CFD for the Rail Pressure Sweep at Start of Injection Timing of 2 degrees BTDC. (1400 Bar to 1800 Bar with 100 Bar Intervals)

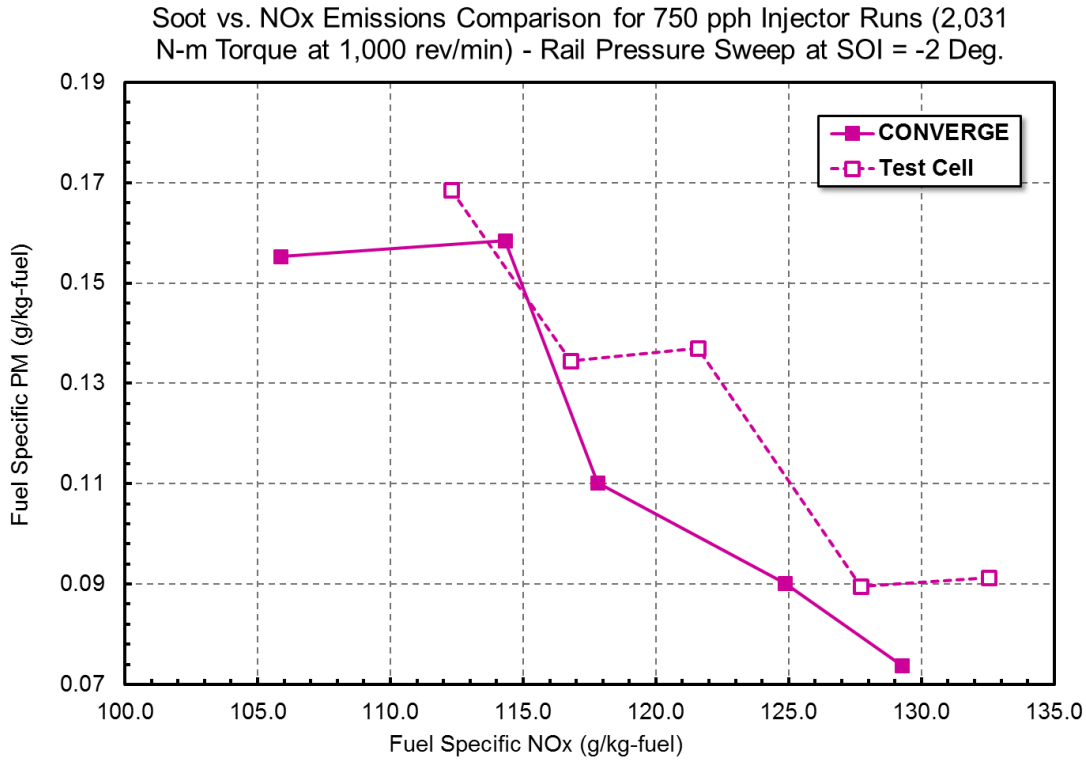

Figure 111: Emissions Comparison between Test Cell & CFD for the Rail Pressure Sweep at Start of Injection Timing of 2 degrees BTDC. (1400 Bar to 1800 Bar with 100 Bar Intervals)

Injection Rateshape Optimization

The three different rateshapes were fed into CONVERGE, and an injection timing sweep was performed for each rateshape. As the pressure and heat release rate plots (for the middle injection timing of 3 Degrees BTDC) in Figure 112 and Figure 113 show, the faster opening, and in turn the faster fuel flow rate will allow better entrainment and mixing with the in-cylinder charge, which reduces the ignition delay and therefore advances the start of combustion slightly. The peak cylinder pressure is also higher as a result.

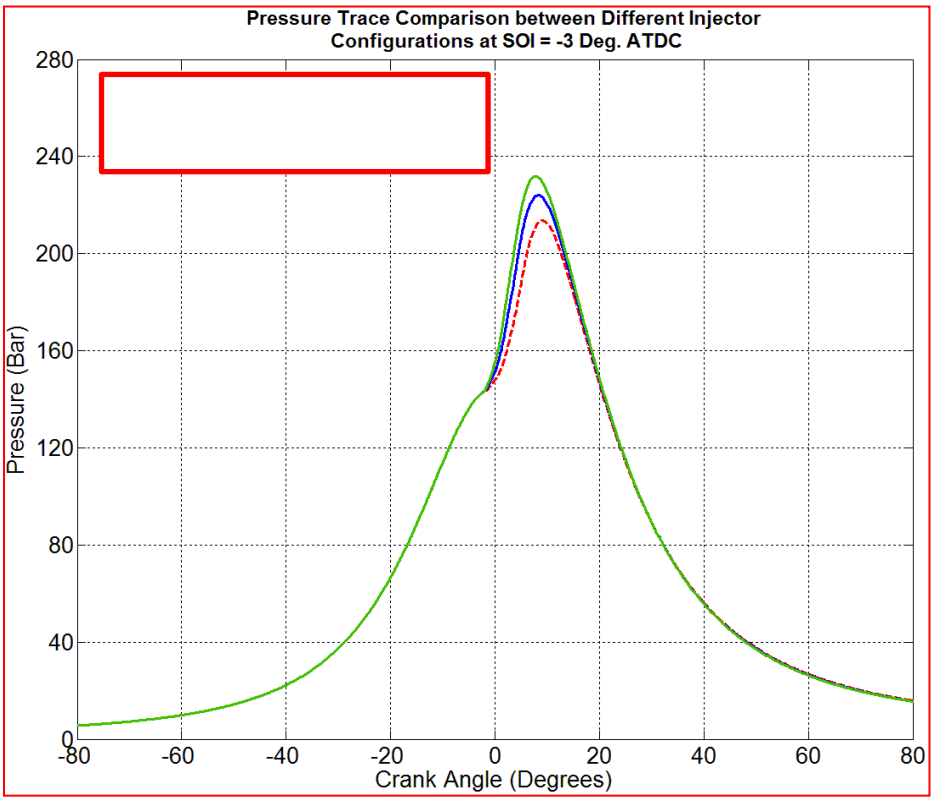

Figure 112: Pressure Trace Comparison between Different Gain Orifice/Maximum Pilot Valve Lift Combinations

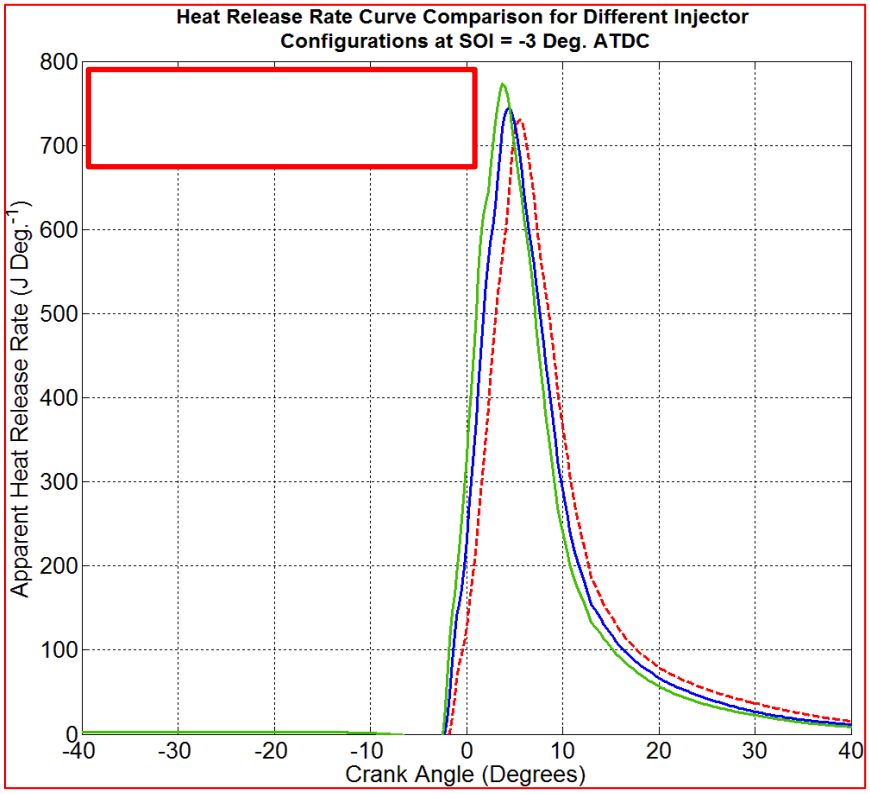

Figure 113: Heat Release Rate Curve Comparison between Different Gain Orifice/Maximum Pilot Valve Lift Combinations

From the gross indicated thermal efficiency plot shown in Figure 114, it is seen that the shorter rateshape from the higher gain orifice and the higher maximum pilot valve lift gives higher thermal efficiency values due to better mixing at all injection timings except for a start of injection timing of 5 Degrees BTDC. However, on a similar NO_x basis, the thermal efficiency values are similar.

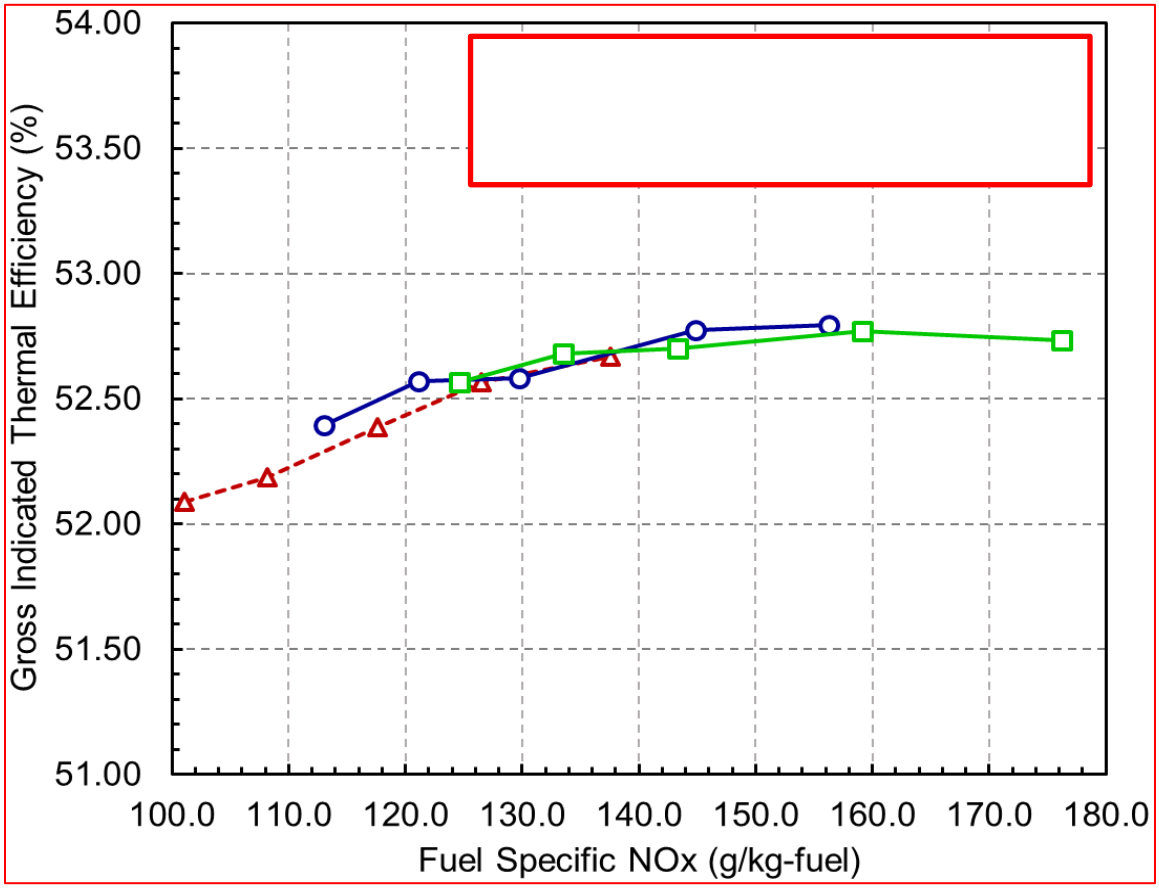

Figure 114: Gross Indicated Thermal Efficiency Trends for Different Gain Orifice/Maximum Pilot Valve Lift Combinations

Figure 115 shows the emissions trends for the three different gain orifice/pilot valve lift combinations. The faster injection leads to lower soot emissions due to the better mixing and air entrainment, but higher NO_x emissions because of the higher combustion temperatures.

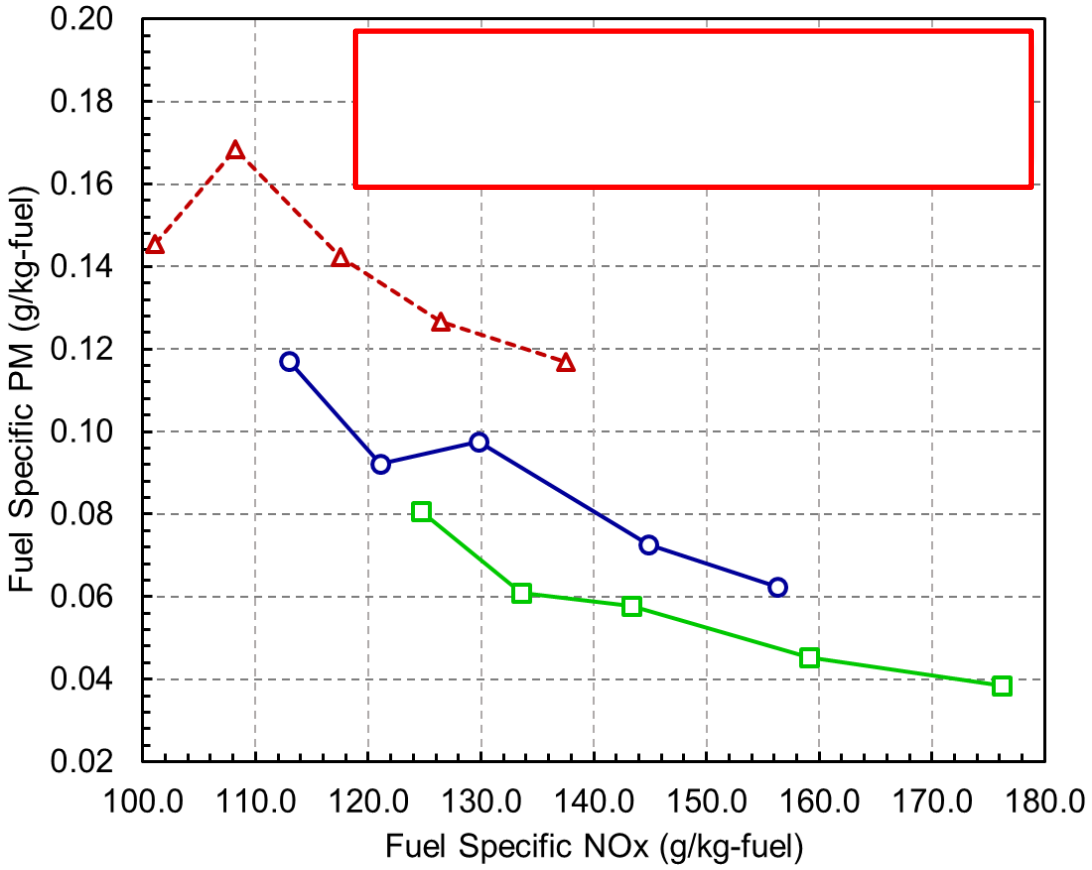

Figure 115: Emissions Trends for Different Gain Orifice/Maximum Pilot Valve Lift Combinations

High Cup Flow Injector Configuration Study: Impact of Number of Nozzle Holes on Engine Performance and Emissions

The number of nozzle holes sweep was performed for both two different injectors. For each injector, 10-hole and 12-hole configurations were investigated. To ensure the same mass flow rate across the nozzles for each injector, the nozzle hole diameter was adjusted for each configuration accordingly.

To more clearly observe the difference between the 10-hole and 12-hole configurations across injectors, the efficiency results for these configurations were re-plotted on the same axes, as shown in Figure 116.

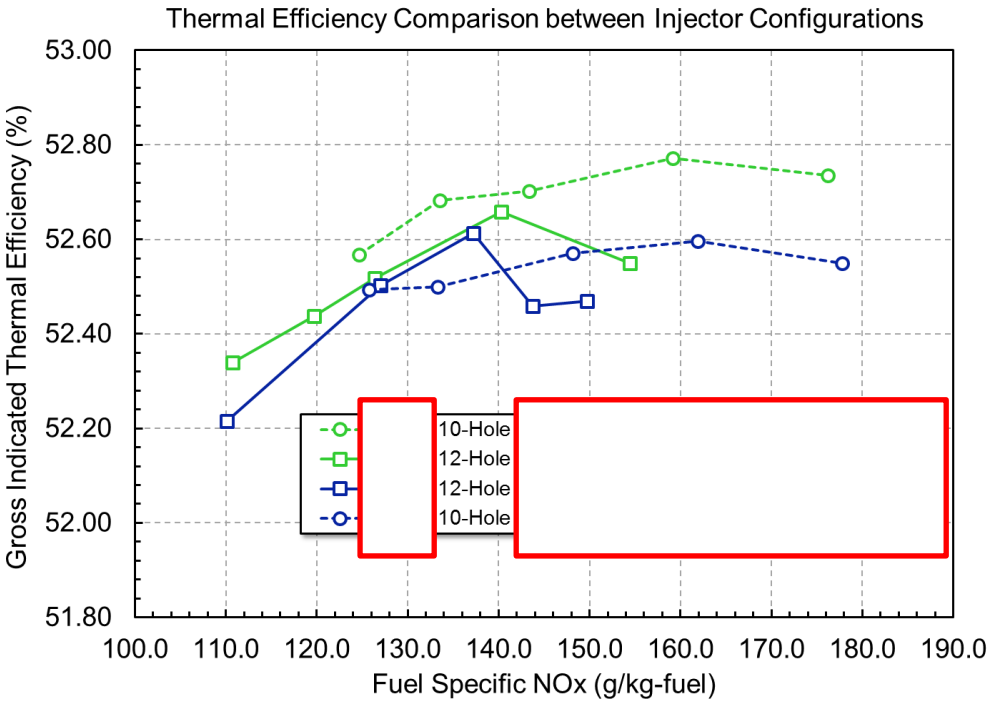

Figure 116: Gross Indicated Thermal Efficiency Comparison across Injectors for 10 & 12 Nozzle Hole Configurations

The green line injector shows a bigger improvement in efficiency over the blue line injector for the 10-hole configuration, while the difference in efficiency across injectors for the 12-hole configuration is not that significant. This probably has to do with poorer entrainment because of plume-to-plume interactions from different nozzles that are placed closer together in the 12-hole configuration.

As in the thermal efficiency analysis, the emissions for the 10 and 12-hole configurations were re-plotted on the same axes (shown in Figure 117) to more clearly observe the difference between the two different configurations across injectors. The green line injector has higher soot emissions than the blue line injector for both the 10 and 12-hole configurations.

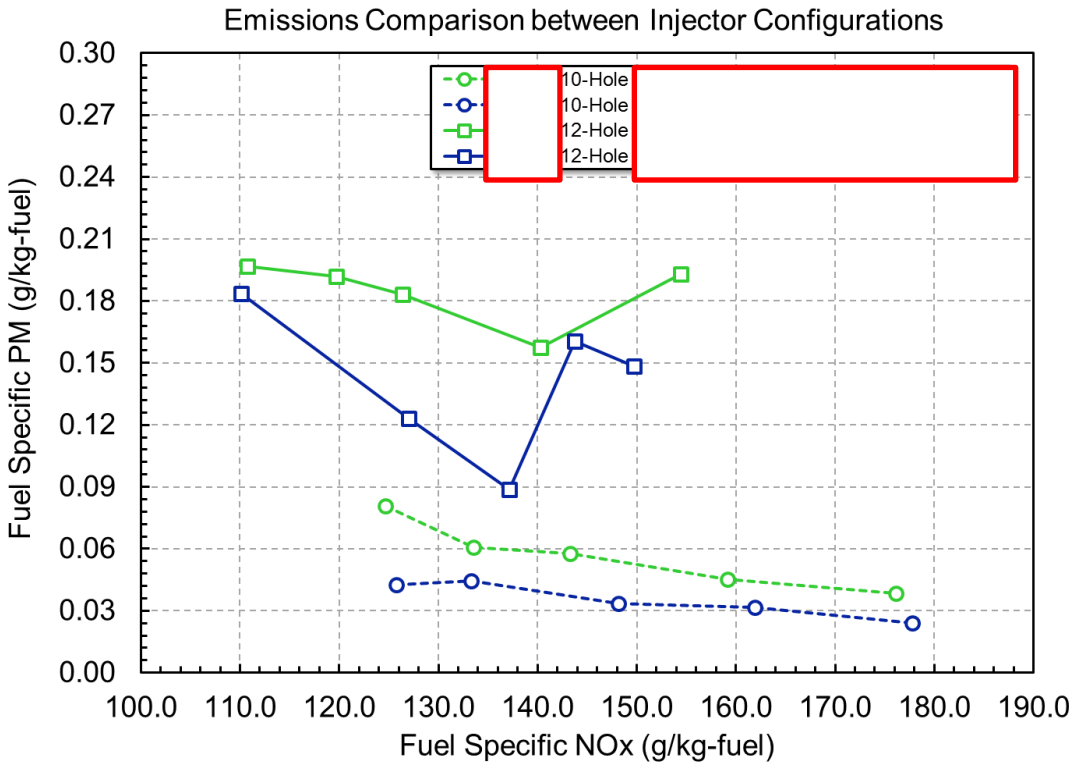

Figure 117: Emissions Trends for 10 and 12-Hole Configurations across Cup Flow

Model Calibration for 36-degree Sector Domain

Before the 36-degree sector domain could be used for the bowl optimization study, the model had to be validated to the full 360-degree geometry. CFD simulations were run using the 36-degree sector domain at the torque-speed condition of 2,031 N-m/1,000 $\mathrm{rev} \cdot \mathrm{min}^{-1}$, for SOI timings from 1-degree BTDC to 5 Degrees BTDC at 1-degree intervals. As shown by the pressure traces and heat release rate curves in Figure 112, the sector domain results and the full geometry results show an acceptable match in terms of combustion phasing and peak cylinder pressure location. The peak cylinder pressure and peak apparent heat release rate are slightly higher for the sector domain, which is due to differences in swirl arising from the use of a simplified head without valve recesses and a piston bowl without valve pockets.

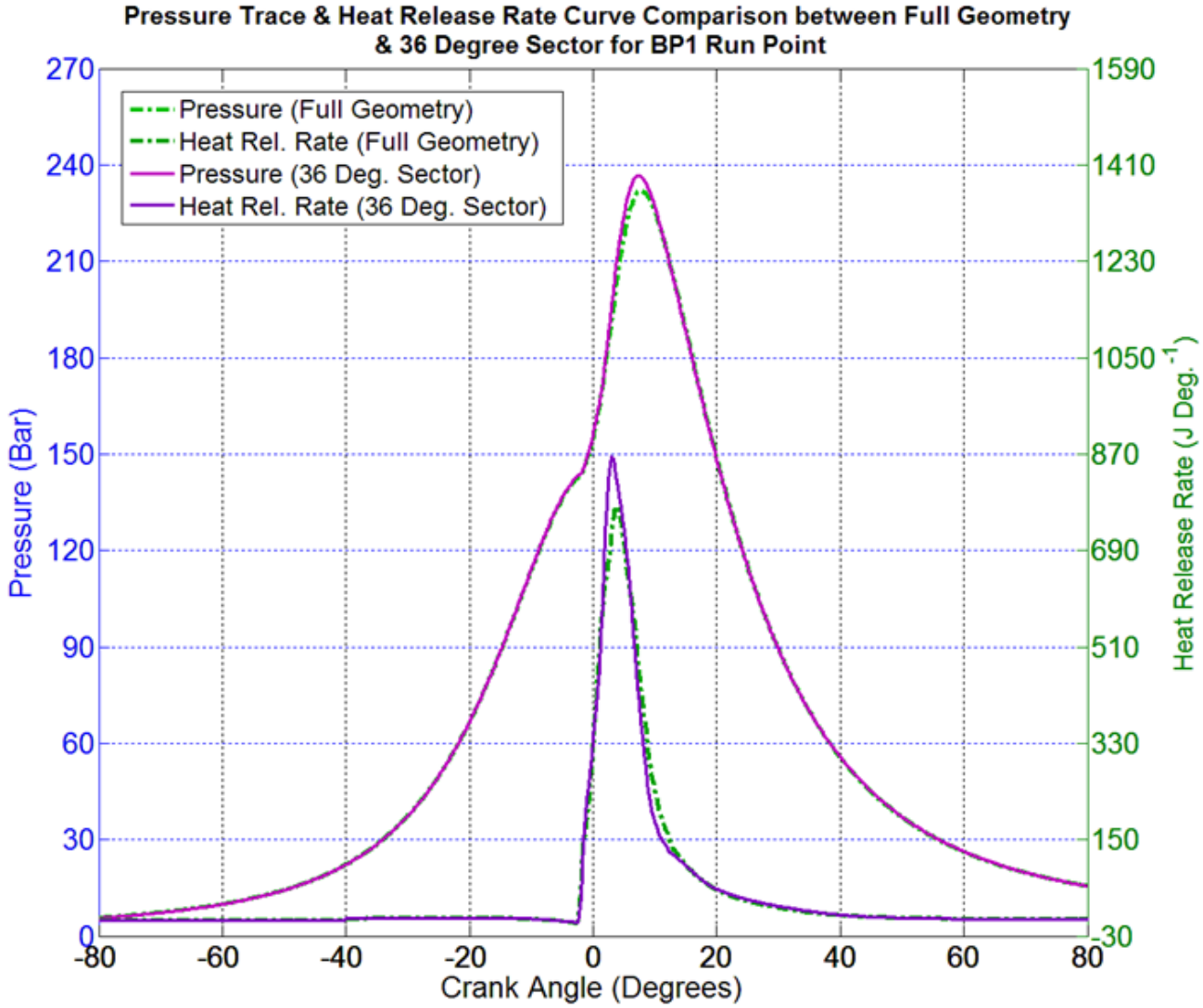

Figure 118: Pressure Trace Comparison between Different Gain Orifice/Maximum Pilot Valve Lift Combinations

The gross indicated thermal efficiency plot shown in Figure 114 and the emissions plot shown in Figure 115 show that the Figure 114 trends are properly captured by CFD for the sector domain, albeit the efficiency and emissions values are slightly higher and lower respectively than the full geometry simulations. Like the peak cylinder pressure and peak heat release rate, the reason for this slight difference is the slightly higher swirl in the sector domain arising from the simplified head and lack of valve pockets. Nevertheless, because the trends and start of combustion are properly captured, the sector domain model can be considered validated to the full geometry cases, and therefore the sector domain can be used for the bowl optimization study.

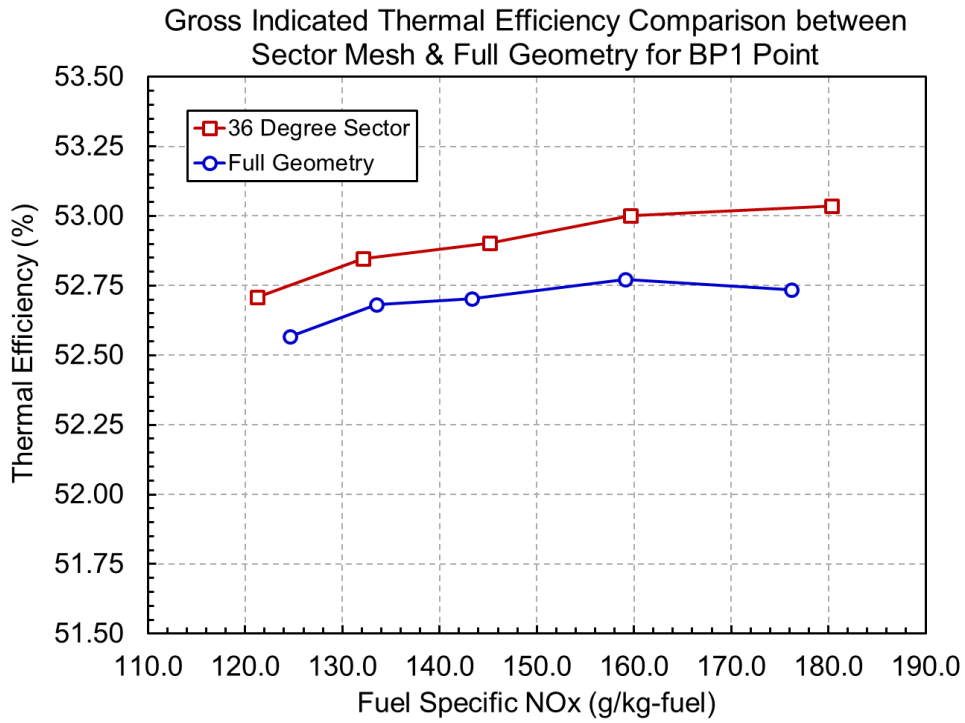

Figure 119: Gross Indicated Thermal Efficiency Trends for Different Gain Orifice/Maximum Pilot Valve Lift Combinations

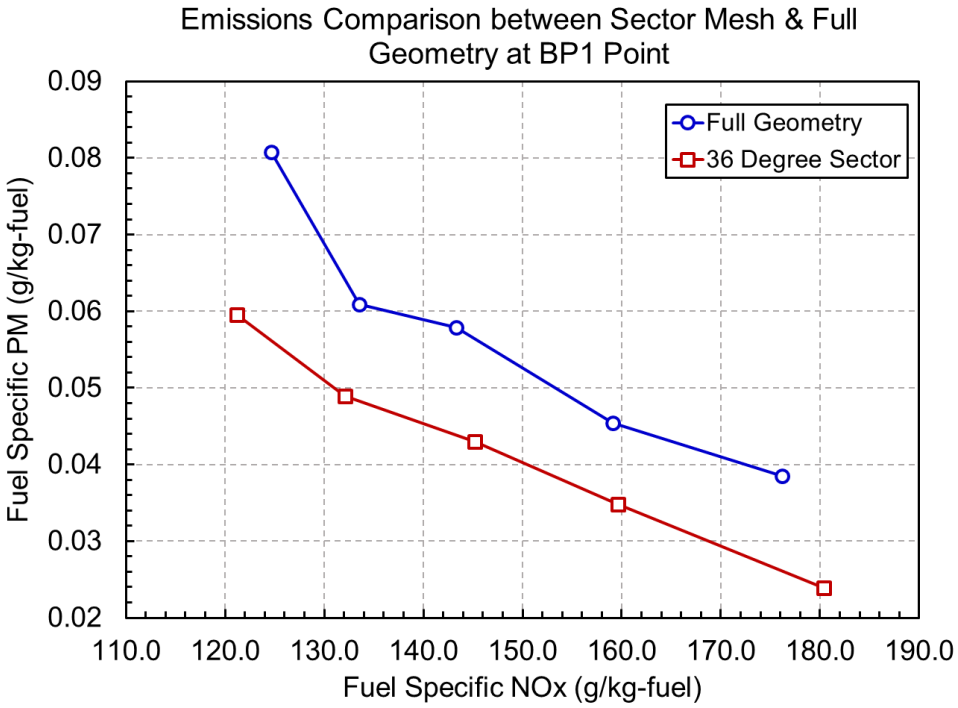

Figure 120: Emissions Trends for Different Gain Orifice/Maximum Pilot Valve Lift Combinations

Piston Bowl Optimization Template

New piston bowls were developed using an in-house piston bowl optimization template developed by the Cummins Combustion Research Team.

Bowl Optimization –Creating New Bowl Profiles

Previous studies conducted as part of the other engine programs showed that the ISG bowl profile, which has no ski jump, showed an improvement in the thermal efficiency and emissions over the current production ISX15 bowls. It was therefore decided that the ISG bowl profile be used as the template for the bowl optimization study. Because the ISG engine platform is for the 12-liter engine with a different bore and stroke, the ISG bowl had to be scaled to the ISX15 platform for the current study, and some minor modifications had to be made to the scaled bowl to get the compression ratio of the bowl profile to 21:1. The dimensions/geometric parameters for both bowls are given in Table 3.

Table 3: Geometric Parameters of New Bowl Profiles (1st Iteration)

Bowl Profile	ST21	ISG12-RS	MG211	MG212	MG213	MG214	MG215
Pip Height (mm)	4.75	4.33	4.33	4.33	4.33	4.42	4.42
Pip Radius (mm)	3.49	1.77	1.77	1.77	1.77	1.86	1.86
Floor Angle (Degrees)	21.95	31	31	34	34	31	35.5
Ski Ratio	0.345	0	0	0	0	0	0
Bowl Radius (mm)	46.5	46.8	46.8	46.5	46.5	48	49
Target Angle (Degrees)	23	20.5	8.5	13.5	32	25	24.7
Target Radius (mm)	1.64	1.67	1.70	2.31	2.14	1.54	1.54

For the ISG bowl, the target region has been moved inward towards the injector tip, and the ski jump does not exist. In addition, the floor angle is also steeper at 31 degrees instead of 21.95 degrees for the SuperTruck bowl. These three features were the most influential on the combustion performance and emissions, and so they were modified to create new bowls that were derivatives from the scaled ISG bowl. The bowls are numbered MG211 to MG215, and their geometric parameters are given in Table 3. Note that there is a no-cut zone in the piston beyond which material cannot be removed, due to the presence of the oil gallery and under-crown region. All bowl profiles were therefore created such that they avoided the no-cut zone completely.

The bowl profiles created using the in-house template were converted to the sector domain geometry using CONVERGE's Make-Surface utility, and an injection timing sweep at the best fuel economy point was performed for each bowl profile. Figure 121 and Figure 122 show the gross indicated thermal efficiency and emissions results respectively for the new bowls. It can be seen apart from MG212, which has comparable efficiency values as those of the baseline SuperTruck bowl, all other ISG bowl variants show significant improvement in thermal efficiency over the baseline ST21. Up to a 0.55-point improvement in GITE is observed with the best bowl MG213.

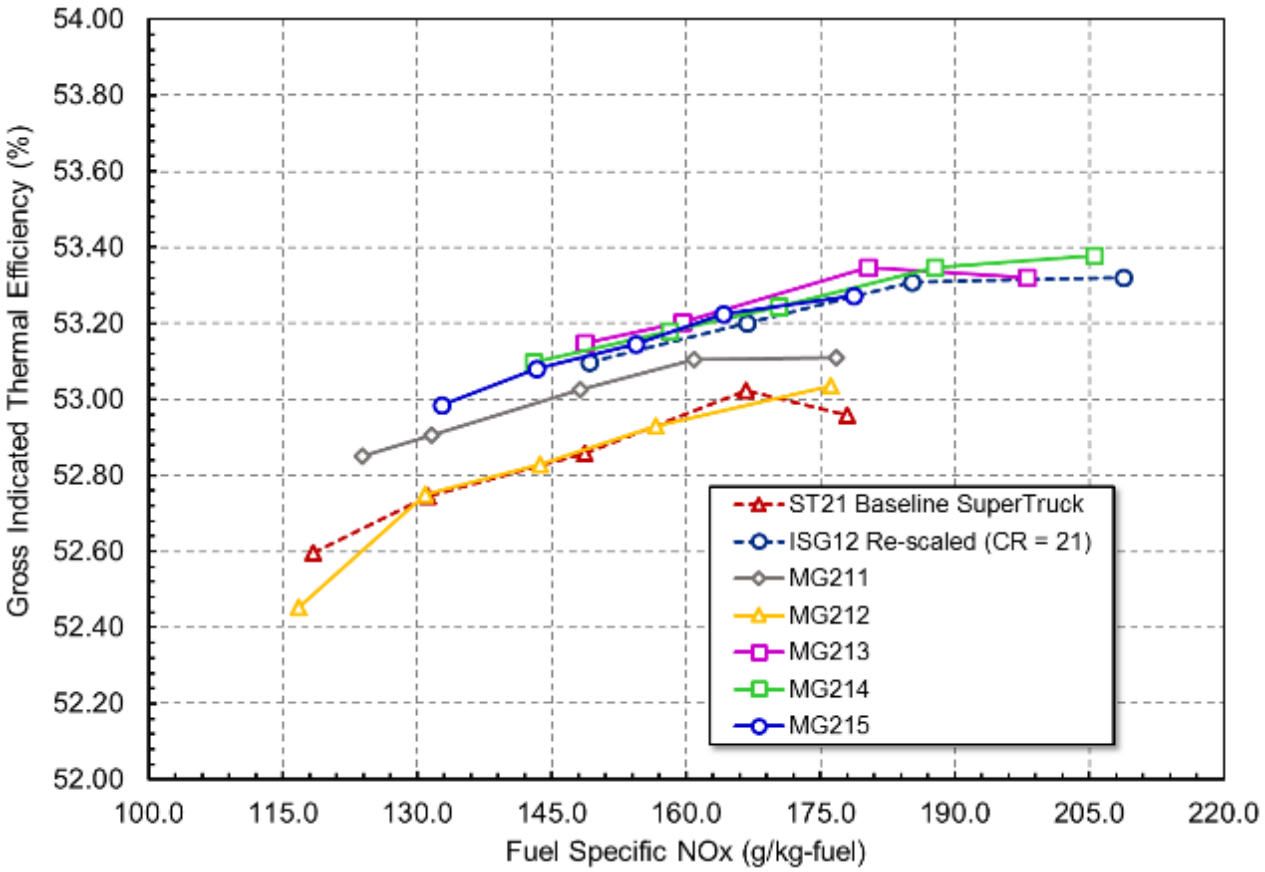

Figure 121: Gross Indicated Thermal Efficiency vs. NOx for the new bowl profiles

From the emissions trends shown in Figure 122, MG212 and MG215 show higher soot emissions than that of the baseline SuperTruck bowl, while the rescaled ISG12 bowl, MG213 and MG214 show lower soot emissions than the baseline SuperTruck bowl.

The results show that moving the target region further inward towards the injector tip, along the line of spray helps improve the efficiency and emissions. In addition, the increase in the reentrant depth also increases the circulation of the plume within the reentrant portion, and the steeper floor angle makes it more challenging for the flow to climb along the floor towards the center of the bowl. Because of these three features, the heat loss at the piston bowl decreases compared to the baseline SuperTruck bowl and thermal efficiency is thereby increased.

However, moving the target region even further inward than was done for MG213 can be detrimental; there exists a “sweet spot” beyond which the fuel economy and emissions deteriorate. In addition, the floor angle also can be too steep for the flow to climb upwards towards the center of the combustion chamber, resulting in poorer mixing along the floor and therefore a higher soot formation in that region. For these reasons, MG215 showed worse thermal efficiency and even worse emissions than MG213. It was therefore decided that MG213 now be used as the new baseline for the next iteration of bowl profiles. The next sub-section covers the 2nd iteration in the bowl optimization process.

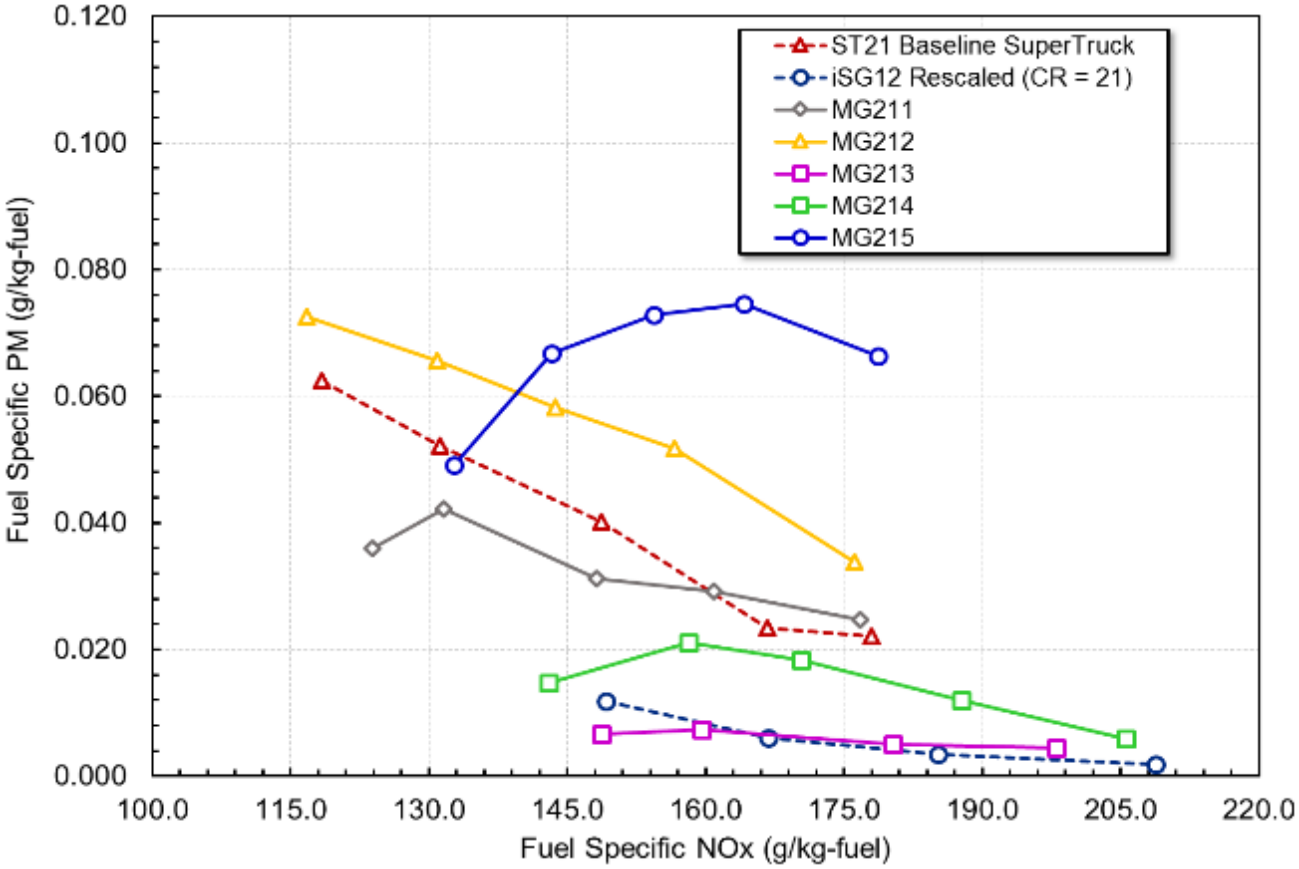

Figure 122: Soot vs. NOx emissions for the new bowl profiles

Bowl Optimization – 2nd Iteration with MG213 as New Template

As mentioned earlier, MG213 was used as the new baseline template for the creation of new bowl profiles in the 2nd iteration. Based on the results shown in the previous section, it was decided that the new bowls have their spray target regions situated between that of MG213 and the baseline SuperTruck bowl, and that their maximum floor angle limit was MG213's floor angle of 32 degrees. A total of 11 bowl profiles was created. Table 4 and Table 5 show the geometric parameters. Bowls BG210 to BG215 have the same bowl radius as that of the baseline SuperTruck bowl, while bowls BG216 to BG2111 have different bowl radii.

As in the 1st iteration of bowl optimization, an SOI sweep was performed for each of these 11 bowls at the best fuel economy point. The efficiency results are shown in Figure 123, and Figure 124 shows the emissions results. From these plots, it can be observed that BG213 and BG216 are the bowls that give the best efficiency and emissions among all the bowls, and therefore these bowls were selected for further analysis. The analysis details for BG213 and BG216 will be covered in the following sub-section.

Table 4: BG210 to BG215 Geometric Parameters

Bowl Profile	MG213	BG210	BG211	BG212	BG213	BG214	BG215
Pip Height (mm)	4.33	4.66	4.66	4.66	4.66	4.66	4.66
Pip Radius (mm)	1.77	3.49	3.49	3.49	3.49	3.49	3.49
Floor Angle (Degrees)	34	31	29	32.1	33	25	26.3
Ski Ratio	0	0	0	0	0	0	0
Bowl Radius (mm)	46.5	46.5	46.5	46.5	46.5	46.7	46.7

Target Angle (Degrees)	32	20.9	20	22.5	26	14	15
Target Radius (mm)	2.14	2.05	2.41	2.01	1.80	3.08	4.62

Table 5: BG216 to BG2111 Geometric Parameters

Bowl Profile	MG213	BG216	BG217	BG218	BG219	BG2110	BG2111
Pip Height (mm)	4.33	4.66	4.94	4.66	4.66	4.61	4.66
Pip Radius (mm)	1.77	3.49	3.54	3.49	3.49	3.72	1.89
Floor Angle (Degrees)	34	32	32.3	32	31	29.3	29.5
Ski Ratio	0	0	0	0	0	0	0
Bowl Radius (mm)	46.5	45.5	44	47	48	50.5	48.5
Target Angle (Degrees)	32	20.7	20.5	24	28	43	41
Target Radius (mm)	2.14	2.83	3.70	2.83	2.83	2.57	2.31

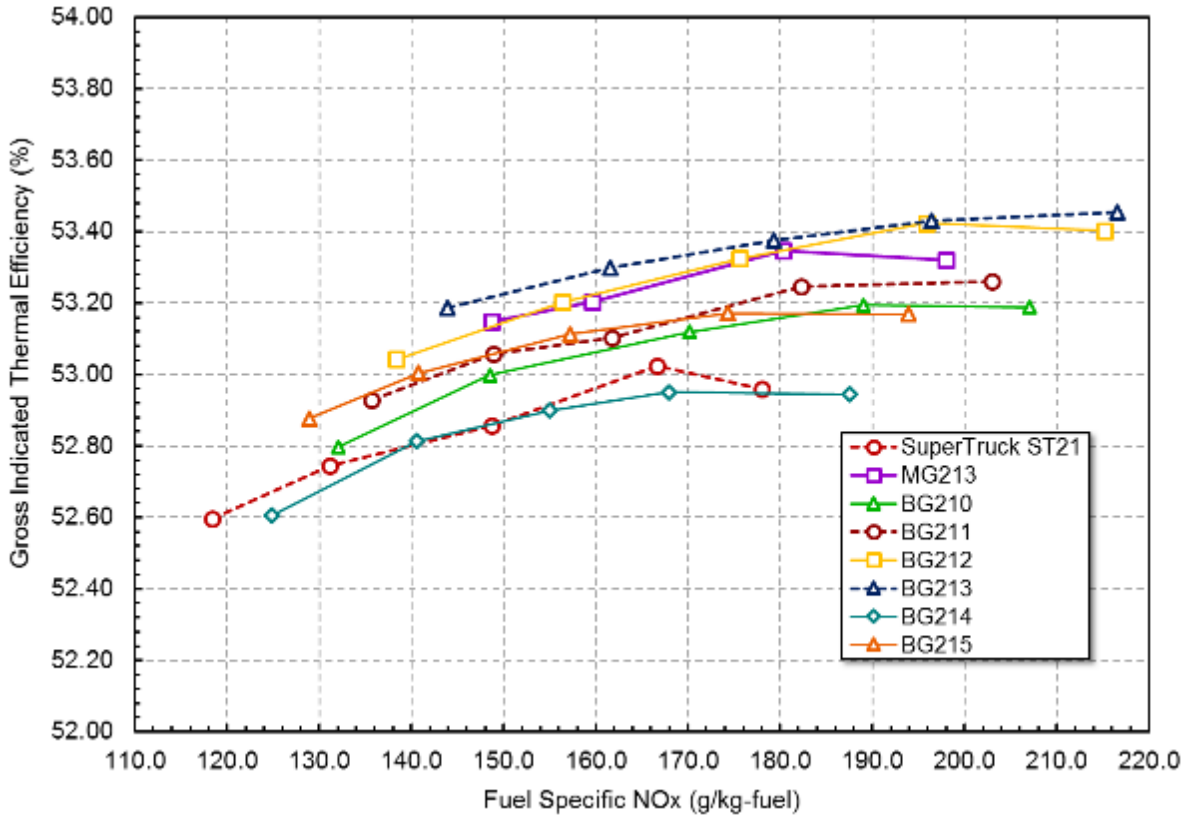

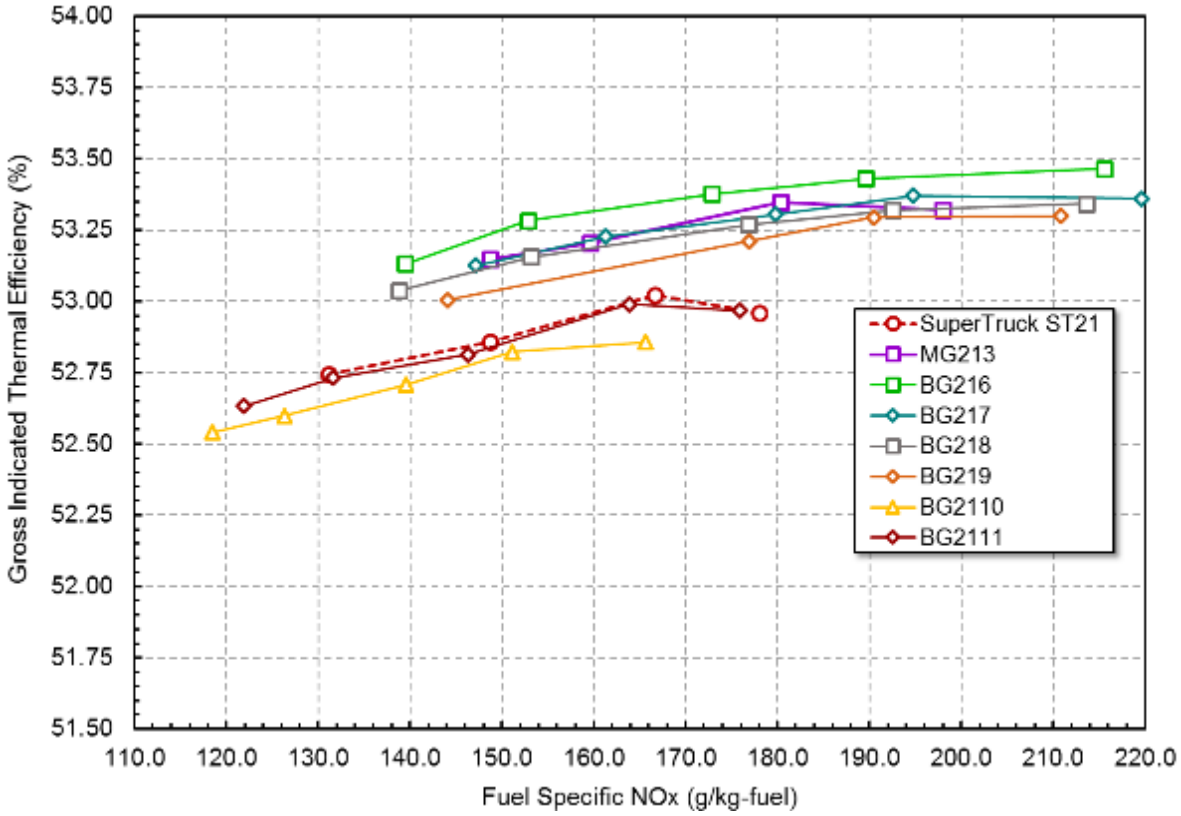

Figure 123: Gross Indicated Thermal Efficiency Trend Plots for (Top): BG210 to BG215, and (Bottom): BG216 to BG2111

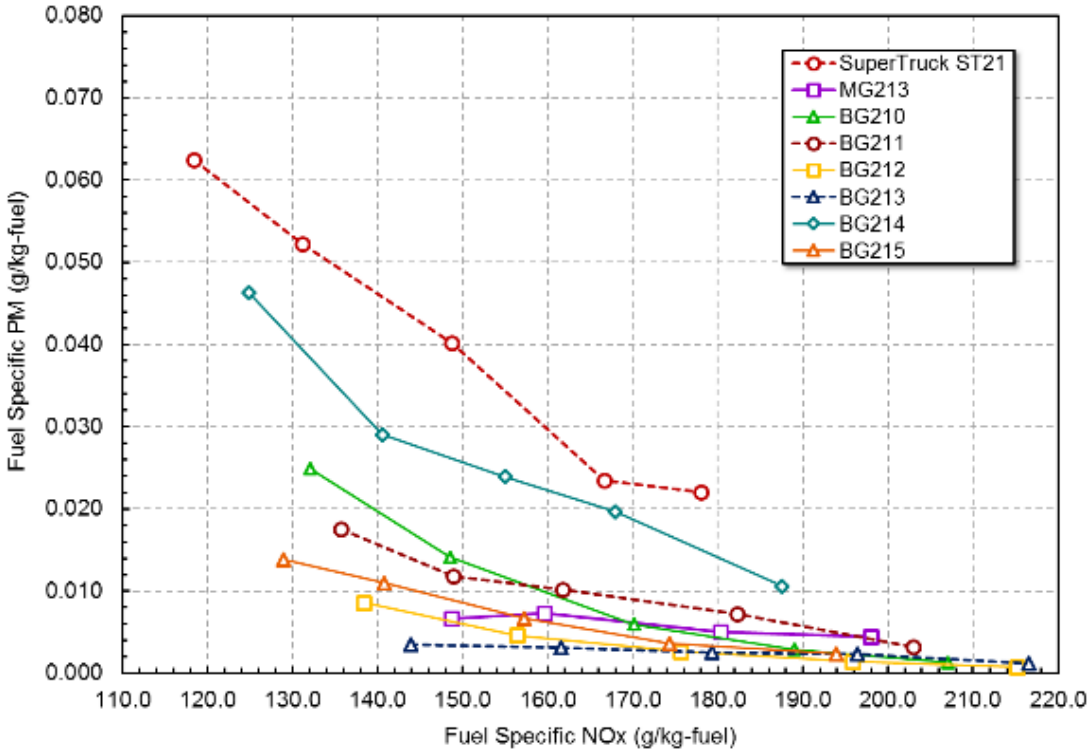

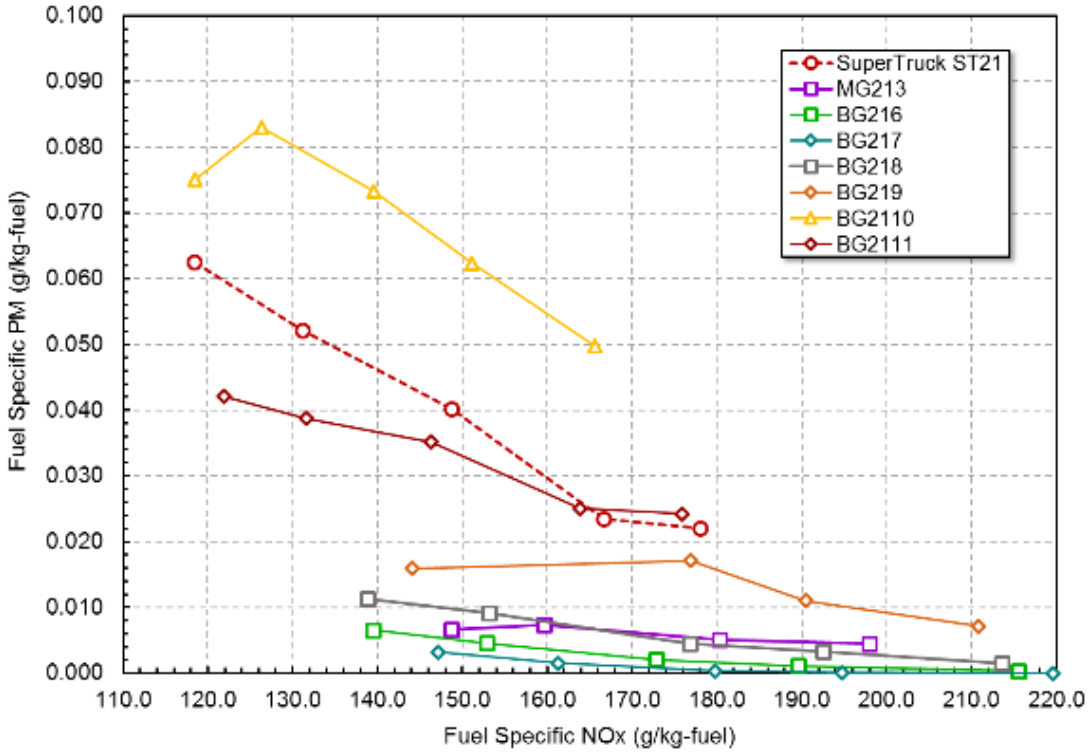

Figure 124: Soot Emissions Trends for the new bowls. (Top): BG210 to BG215 and (Bottom): BG216 to BG2111

Detailed Analysis of Successful Bowls BG213 and BG216

As mentioned in the previous sub-section, it was found that bowls BG213 and BG216 offered the highest efficiency gains over the baseline ST (Super Truck) bowl and the lowest soot emissions of the new bowls analyzed. A more detailed analysis of the successful bowls was performed so as to identify the features responsible for the improvements observed. Primarily, a more detailed pressure and heat release analysis, an in-cylinder energy balance analysis and in-cylinder visualization were performed. This sub-section describes in detail the analyses.

Figure 127 and Figure 128 show the pressure traces and heat release rate curves respectively for the baseline SuperTruck, BG213 and BG216 bowls. It can be observed that the peak cylinder pressure is higher for BG213 than for the other two bowls. In addition, for both BG213 and BG216, the expansion pressure is consistently higher than the expansion pressure for ST21 till a crank angle of 50 degrees ATDC. As a result, a greater quantity of expansion work is produced. Moreover, in the heat release rate plots shown in Figure 128 (especially in the magnified plot), it can be seen that although ST21 shows a higher peak heat release rate, the heat release rate curves for BG213 and BG216 are “stretched out” over a wider duration, indicating that a greater quantity of fuel energy is being converted to useful work.

Figure 129 and Figure 130 show the in-cylinder energy balance and the in-cylinder heat loss respectively for the three bowls. It can be seen that for both BG213 and BG216, the in-cylinder heat loss is lower than that for the baseline SuperTruck bowl, which gives rise to the thermal efficiency gains. The heat loss on the piston surface for the new bowls is lower than it is for the SuperTruck bowl, while the head heat losses and

liner heat losses are quite similar. This shows that the piston heat transfer is lowered, allowing an improvement in the thermal efficiency.

To more clearly understand the features of the new bowls causing the improvement in thermal efficiency, it is necessary to perform in-cylinder visualization of the flow field. It can be seen that while the temperature distribution looks quite similar among the bowls till a crank angle of 30 degrees ATDC, beyond this point, the differences are more clearly observed. The steeper floor angle of 32 and 33 degrees for BG213 and BG216 respectively, compared to ST21's floor angle of 21.95 degrees hinders the ascent of the high temperature plume along the floor, and this high temperature plume starts to separate from the floor and travels upwards towards the head at crank angles of 45 and 60 degrees ATDC. Moreover, the ski jump in the baseline SuperTruck bowl also influences the circulation, and it can be seen that due to this, as well as the shallower floor angle, the high temperature plume remains behind during the later portion of the expansion stroke unlike in BG213 and BG216. As a result, the temperature gradient at the piston surface for ST21 causes a higher piston heat transfer rate, compared to BG213 and BG216 where the high temperature plume is already moving towards the head. In addition, the target region being moved further inward for BG213 and BG216, as well as upward, causes the spray plume to hit the piston surface earlier and undergo more circulation, which contributes to better mixing and the slower plume climb along the floor. Also, more importantly, since the spray plume hits the target region earlier, the fluid momentum is significantly reduced and plume-to-plume interactions are minimized, contributing to the better mixing as well. All these aforementioned features cause the heat loss at the piston surface to be lower for the new bowls over the baseline SuperTruck bowl, which in turn causes the thermal efficiency to improve.

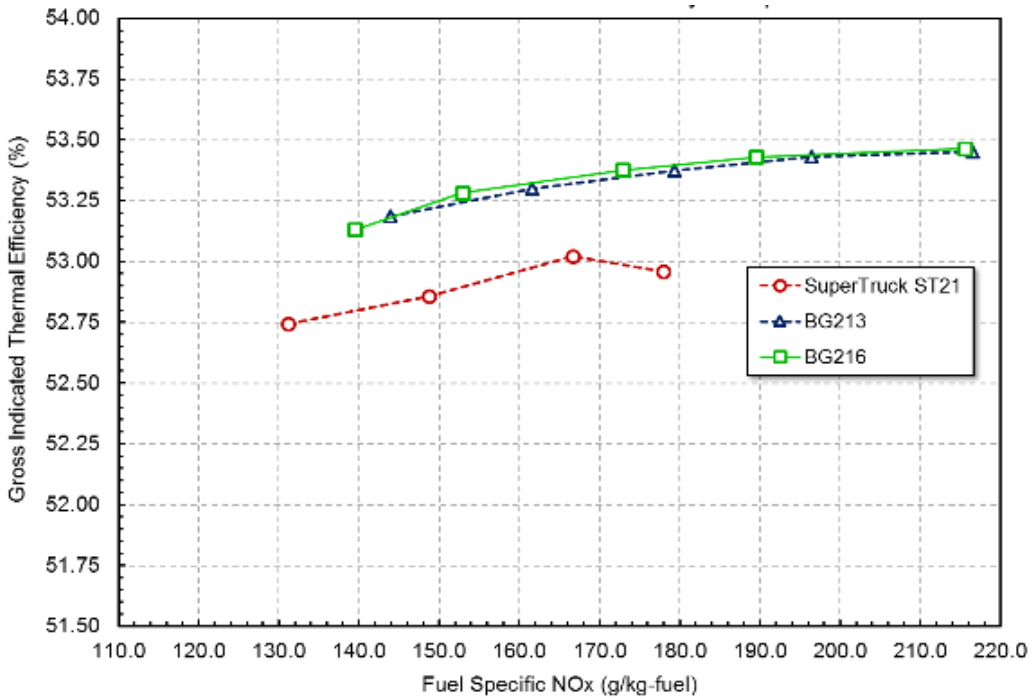

Figure 125: Thermal Efficiency Comparison between Best Bowls BG213 and BG216 & Baseline SuperTruck Bowl

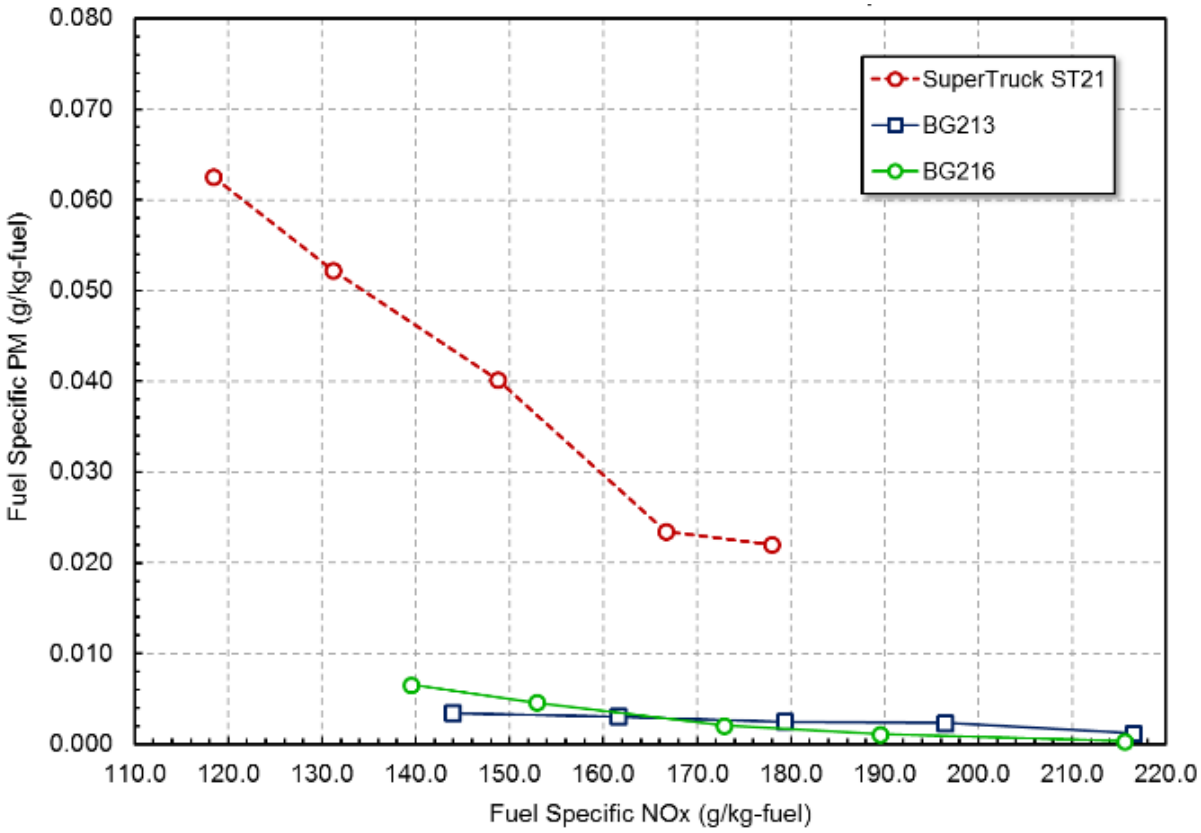

Figure 126: Emissions Comparison between Baseline SuperTruck Bowl and Successful Bowls BG213 and BG216

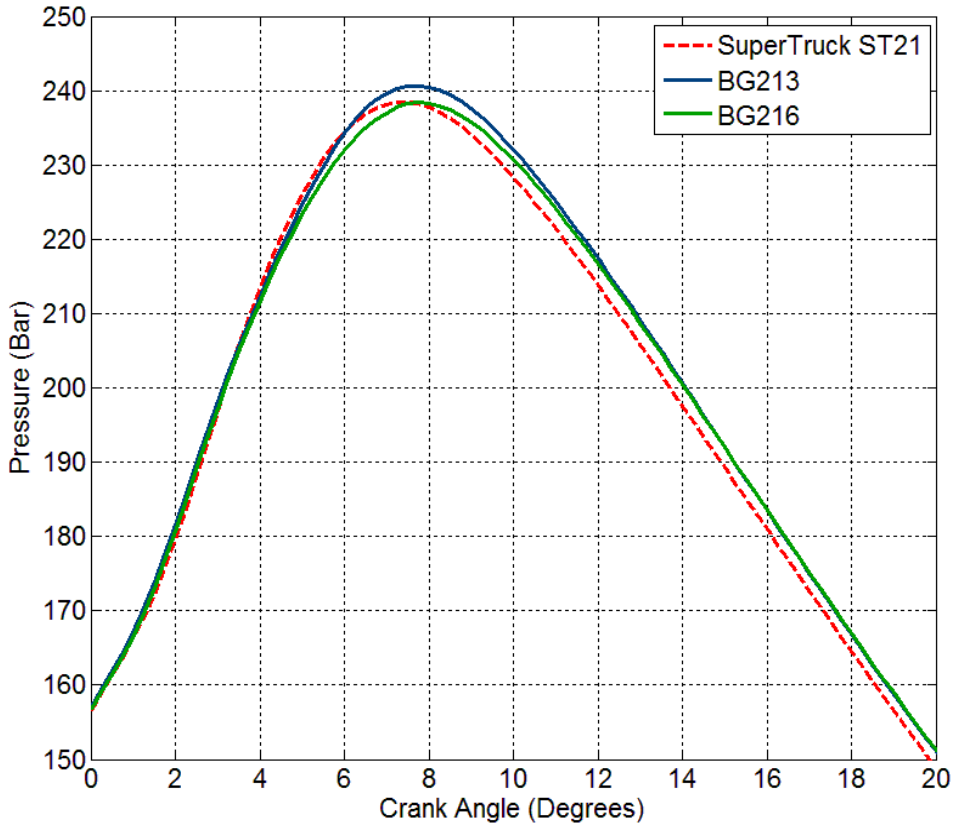

Figure 127: Pressure Traces for Best Bowls BG213 and BG216. (Top): From Crank Angle 50 Degrees BTDC to 50 Degrees ATDC. (Bottom): Magnified View from TDC to 20 Degrees ATDC

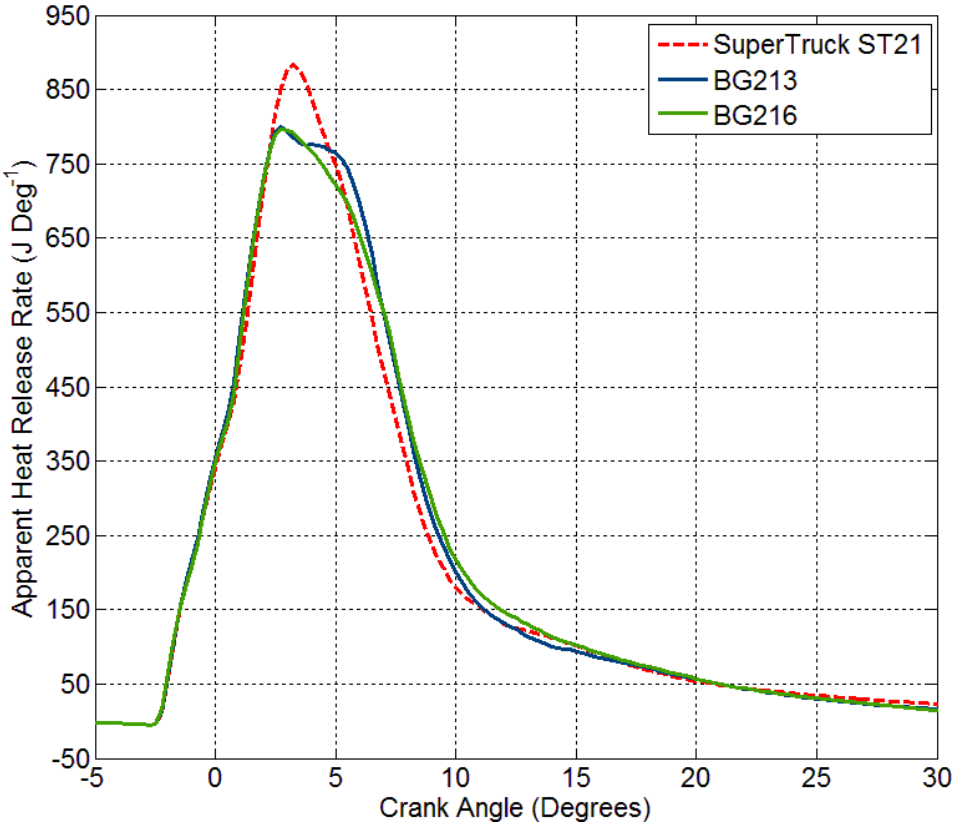

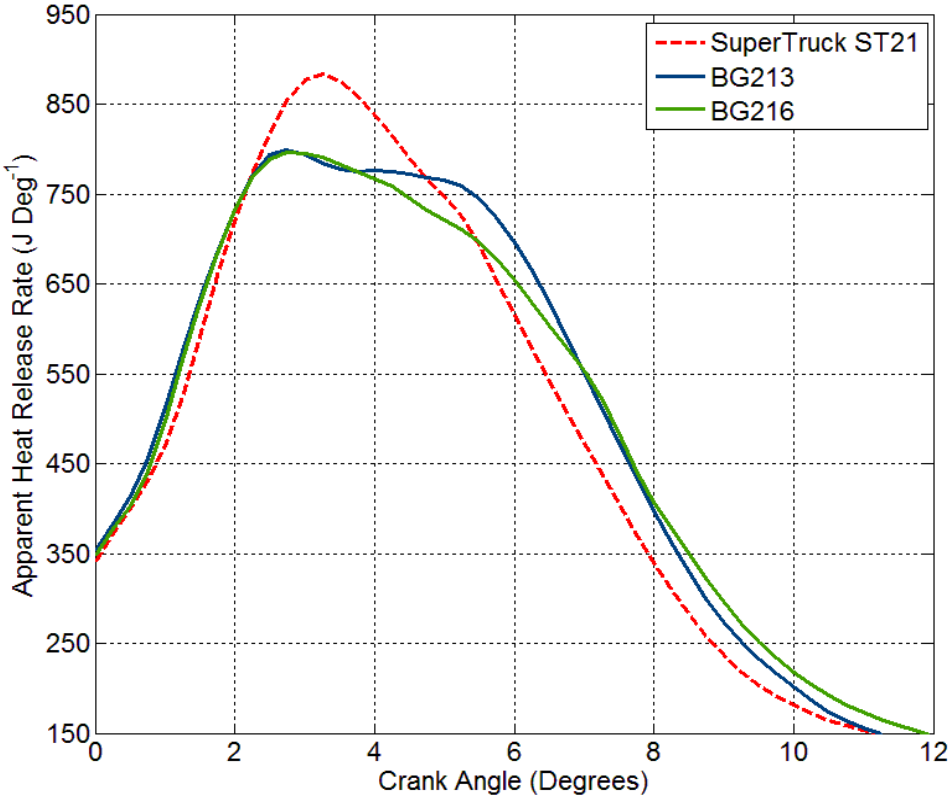

Figure 128: Apparent Heat Release Rate Curves for Best Bowls BG213 and BG216. (Top): From Crank Angle 5 Degrees BTDC to 30 Degrees ATDC. (Bottom): Magnified View from TDC to 12 Degrees ATDC.

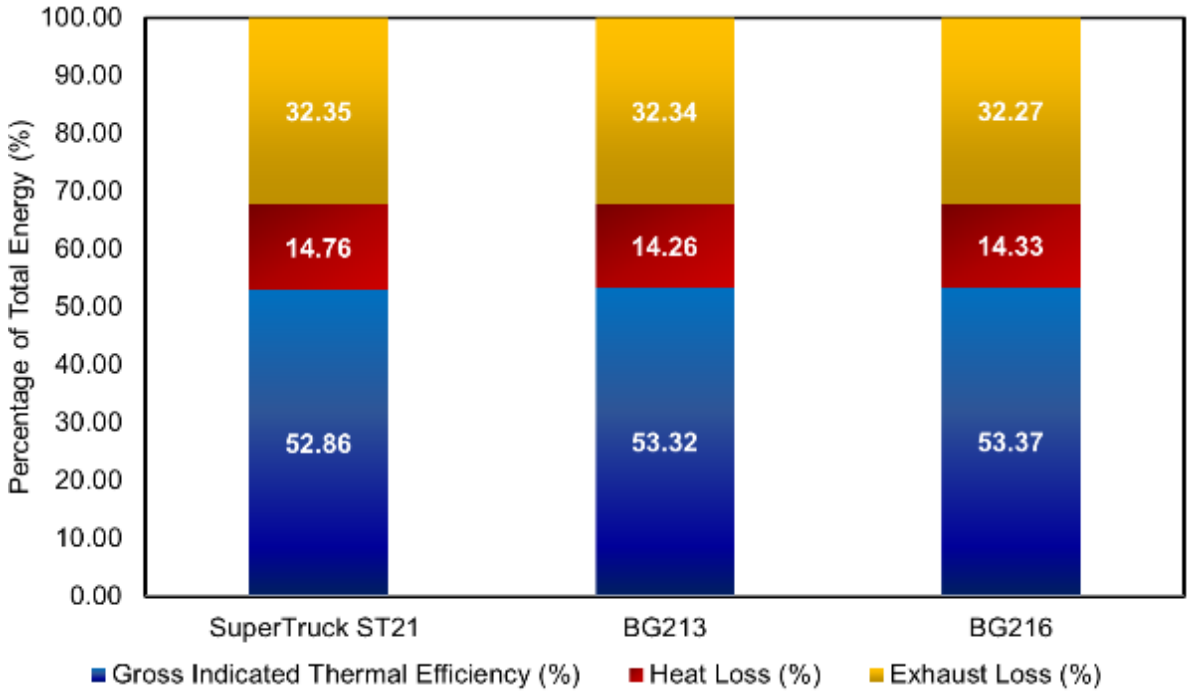

Figure 129: In-cylinder Energy Balance Comparison between ST21 and Best Bowls

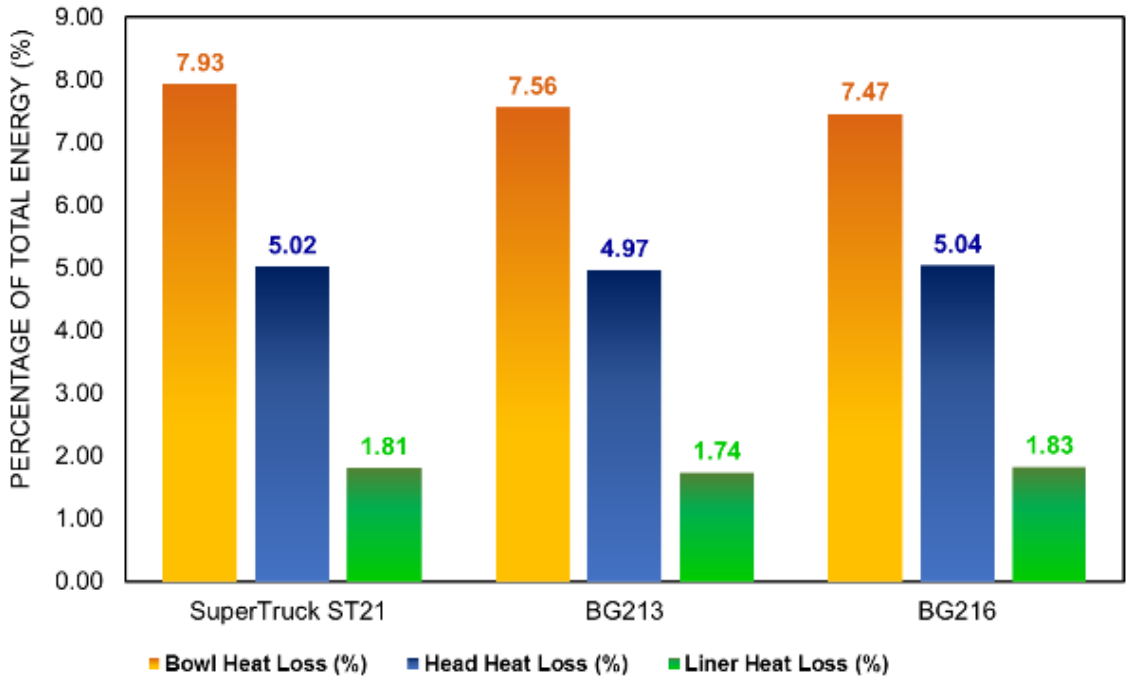

Figure 130: In-cylinder Heat Loss Distribution Comparison between ST21 and Best Bowls

Conclusions

In the final part of this optimization study, a piston bowl optimization study was executed to develop piston bowl designs that were optimally matched to the selected injector configuration. It was determined that moving the spray target region inward and upward, and removing the ski jump allowed better circulation and entrainment in the reentrant region. In addition, a steeper floor angle also caused the high temperature plume to ascend more slowly along the floor, and thereby separate from the piston surface. The more inward target region along the line of spray also helped reduce spray momentum and decreased the probability of plume-to-plume interactions, facilitating better air entrainment and therefore contributing to better mixing. These aforementioned features allowed lower heat losses from the piston surface and a more efficient combustion process, thereby improving the thermal efficiency and lowering soot emissions. Two such bowls, BG213 and BG216 were created.

3.3 Engine Cycle Simulation

1-D simulation efforts focused mostly on the Air Handling aspects of the system. It was realized that the A/H (turbo, exhaust manifold, and the valve optimization; mainly focusing on the turbo matching) sub-system performance was going to be a critical part of the path to target efficiency. The analysis results were also quite helpful in communicating with the turbo supplier on a constant basis in sharing technical information in a 2-way manner. 1-D analysis also helped in finalizing the path to target initially, refining along the way, and even finalizing the path to target (eventually identifying the gap between the actual efficiency achieved vs. efficiency goal and also verify whether the final technology palette of choice on the whole system itself could be sufficient to bridge that gap). Much of the report here, however, focused on air-handling aspects of the performance.

Early in the program, the system integration efforts were focused around investigating the benefits of improved air-handling architecture using GT-Power cycle simulation tool. The GT-Power model was

calibrated to SuperTruck engine data and served as a baseline to explore and compare different air-handling architectures. Some of the highlights of these efforts were

- Identifying improved turbocharger hardware for engine testing
- Understand the benefits of HP, LP & DL EGR architectures on improving engine only BTE.
- Cycle simulation studies to identify further improvements in increasing OCE.
- Cycle simulation studies involving design of experiments to arrive at optimal air-handling system architecture as a function of engine only BTE and engine out BSNOx within the thermal and mechanical design constraints.
- Identify the exhaust throttle for engine testing based on sizing work study in GT-Power.

Air Handling System

Figure 131 shows the schematic diagram of air-handling system. The baseline GT-Power model was modified to capture both the HP cooled EGR loop as well as the LP cooled EGR loop for the analysis work.

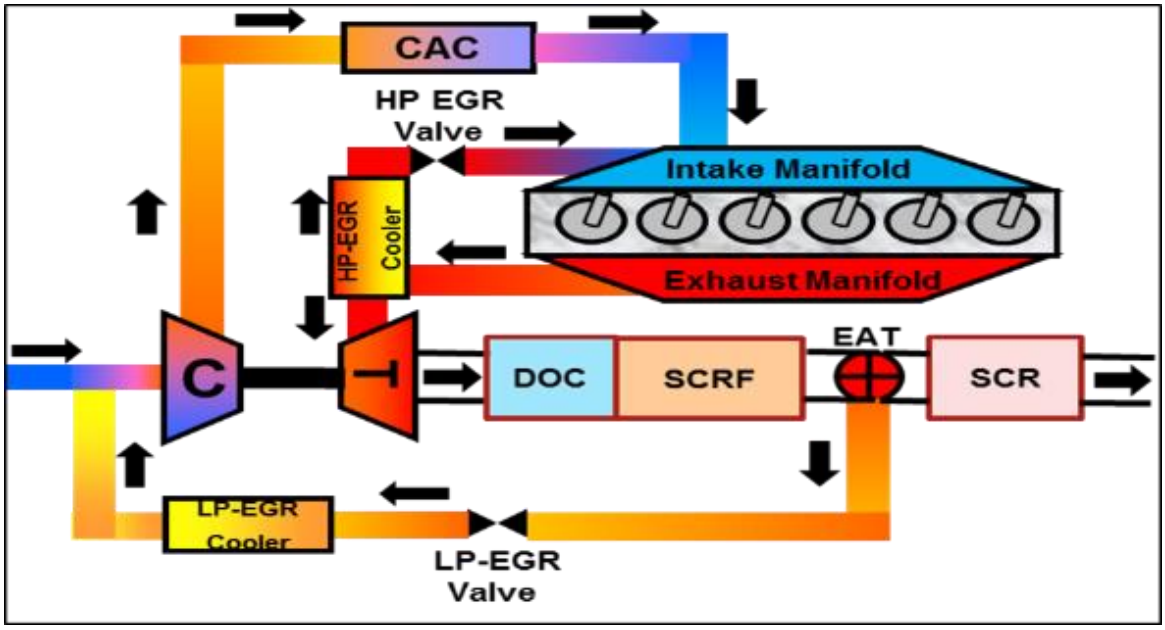

Figure 131: 55BTE Air Handling Architecture Schematic

The baseline model was configured for a HE400 VG turbocharger with the L85J73- F72E83MS compressor-turbine aero specification. The predictive combustion model [Di-pulse] version was calibrated to 4140 steel pistons, 21.4 CR with a 7 hole - high cup flow injectors. Several turbocharger maps were initially evaluated to understand the rematch process due to the addition of LP EGR loop in the architecture. Preliminary analysis led to identifying the following turbocharger hardware for detailed investigation before the hardware selection and procurement.

- HE500 VGT – K98K68RBT Compressor & A84M81SM31SX single entry Turbine
- HE500 WGT– K98K68RBT Compressor & B84G87-16sq.cm mixed flow divided entry wastegated turbine
- HE500 WGT – K98K68RBT Compressor & B84G87-22sq.cm mixed flow divided entry wastegated turbine

HE-500 VGT Analysis

The analysis was done with the supplier provided maps for the VGT hardware. Although a previously calibrated GT model was used, potential changes to the air handling hardware resulted in a larger compressor and turbine hardware to facilitate the operation of LP EGR loop. Figure 132 shows the compressor map comparison between the L85J73 and K98K68 hardware.

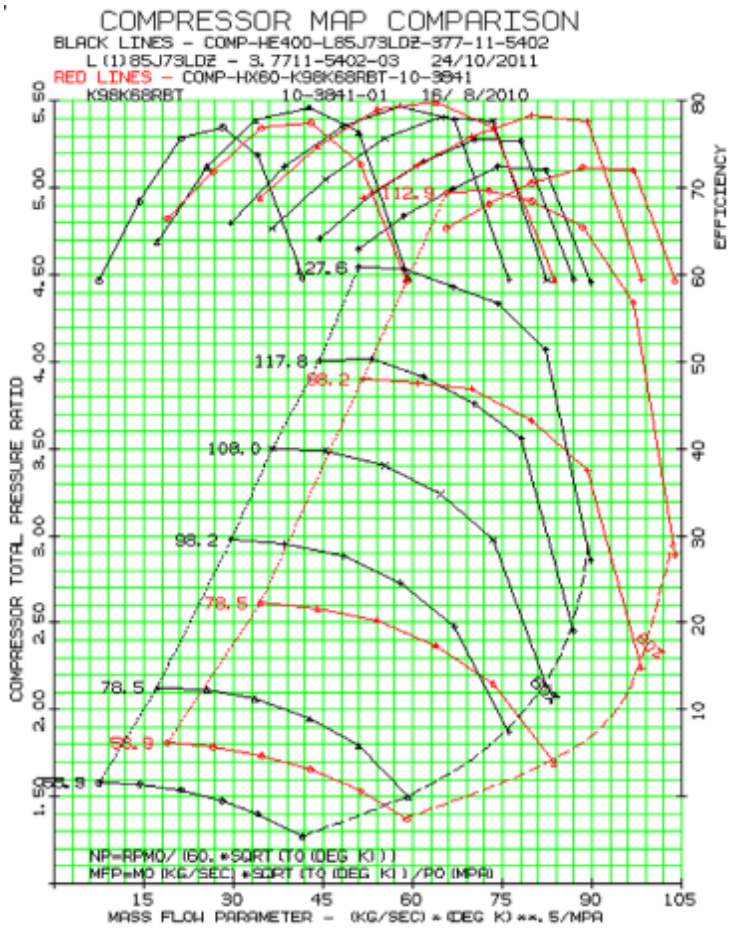

Figure 132: Compressor Map Comparison

Figure 133 below shows the cylinder pressure comparison between CFD prediction and the calibrated GT-Power predicted combustion model for CP2 engine condition with LP EGR. In future, further calibration work will need to be performed after acquiring engine data with the representative hardware.

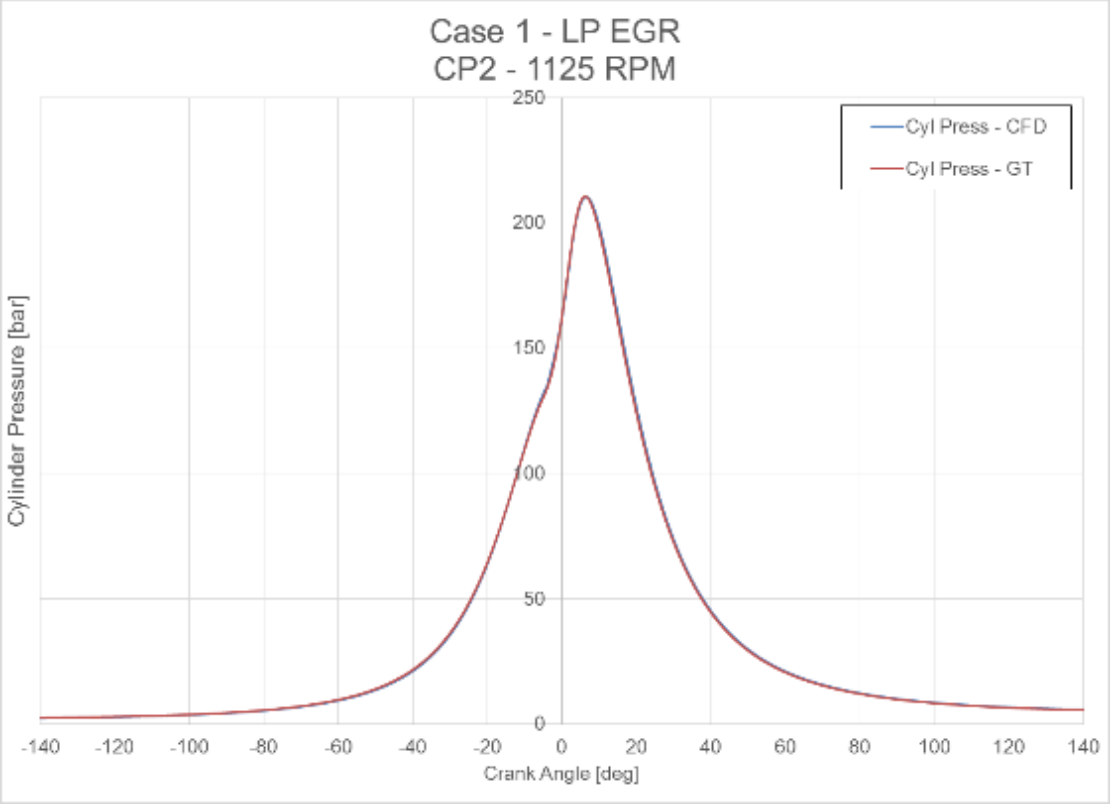

Figure 133: Cylinder Pressure [#1] Comparison - CFD vs. GT-Power

Exhaust Manifold Design & Optimization

The SuperTruck manifold is a single-entry design and is designed for HP EGR loop. Further opportunities exist to improve this exhaust manifold design for a DL EGR architecture when used in conjunction with the VGT. Future work will investigate opportunities to improve this design through transient decoupled CFD with a combined exhaust manifold and turbine approach.

With the motivation towards using LP EGR, divided entry turbine housing in combination with a divided entry exhaust manifold provides some opportunities to improve OCE which could potentially result in BTE improvement. As a preliminary approach, divided entry manifold that was designed for NO EGR application from the ISX-99 product was used in GT-Power to analyze the benefits with LP EGR.

Future work will address optimizing the divided entry manifold design to appropriately match the turbo hardware utilizing CFD techniques. The air handling analysis was performed at 1000 RPM engine speed and 2034 Nm brake torque [75% of maximum torque] by initially evaluating different manifold options coupled to a simple turbine and K98 compressor map. The fuel system reference inputs were selected for the model based on SuperTruck program's best BTE point. The objective of this analysis was to understand turbine sizing and efficiency requirements and arrive at the needed flow and pressure ratio range values to specify the hardware. For both the manifolds DOEs were run in the model to simulate the effects of different turbine sizes and turbine efficiencies on BTE, PMEP, NOx and AFRs. Initial analysis was performed without flowing any EGR to understand the BTE, PMEP, AFR and the NOx capability for different turbine sizes and turbine efficiencies. Later, similar sweeps were then performed on the turbine sizes and efficiencies by opening the EGR valve completely to assess AFR, EGR levels and the NOx capability without the aid of exhaust throttle.

Similar DOE simulations were also performed by opening the EGR valve completely and also closing the exhaust throttle by 25% to assess emissions and performance tradeoffs.

The turbine orifice diameter was varied to simulate different turbine housing critical areas and the turbine efficiency was varied. Figure 134 shows the turbine corporate flow parameter and turbine expansion ratio contours as a function of the independent variables when flowing no EGR with the divided manifold.

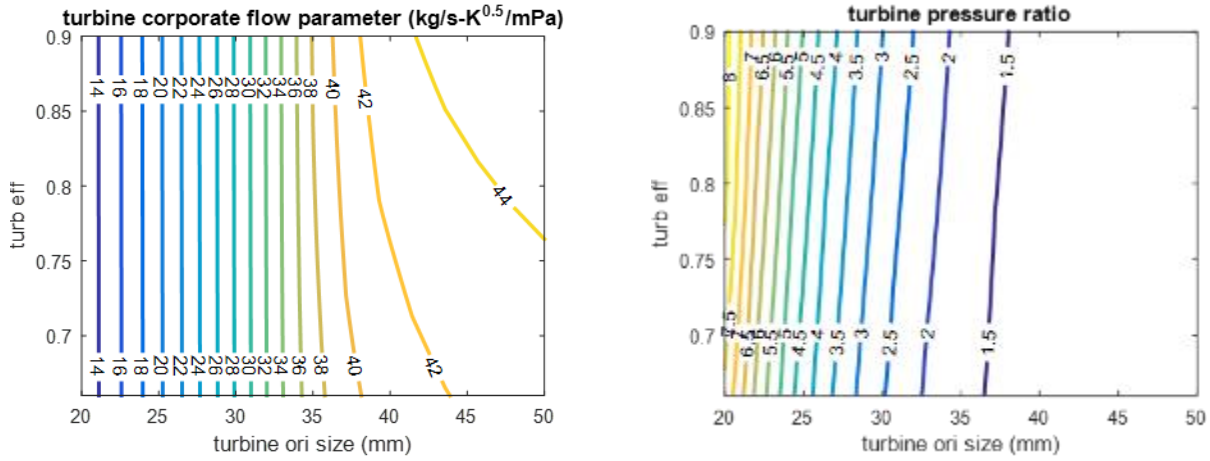

Figure 134: Effect of Turbine Orifice Size & Efficiency on Turbine Flow & Expansion Ratio

With respect to improving OCE using a divided entry exhaust manifold and a divided entry turbine housing, the valve events also play an important role towards improving engine breathing by reducing pumping work. The valve lift events used for analyzing the two manifolds are different. The exhaust lift used for the ISX99 manifold is higher and opens earlier than the lifts used in SuperTruck manifold. The intake lifts on used for both the manifolds are fairly similar. Figure 135 shows the comparison of intake and exhaust valve lifts used on ISX99 and the SuperTruck manifold.

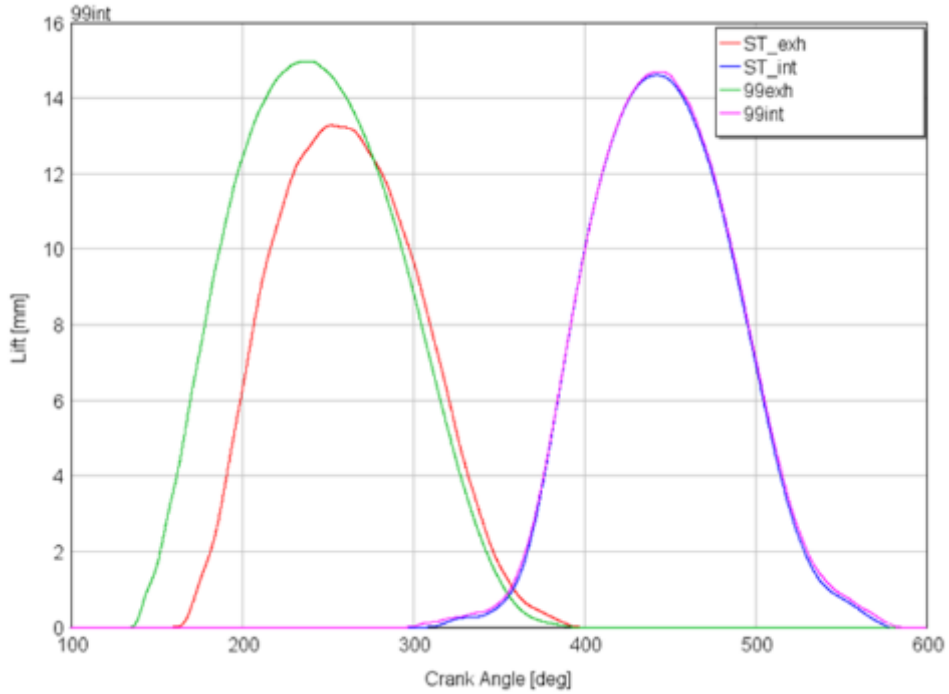

Figure 135: Comparison of Valve Lift Events

Figure 136 summarizes the results of BTE, BSNOx, A:F Ratio, % EGR and PMEP from simulation outputs for the single-entry manifold running LP EGR with wide open EGR valve and exhaust throttle set at 100mm effective flow diameter.

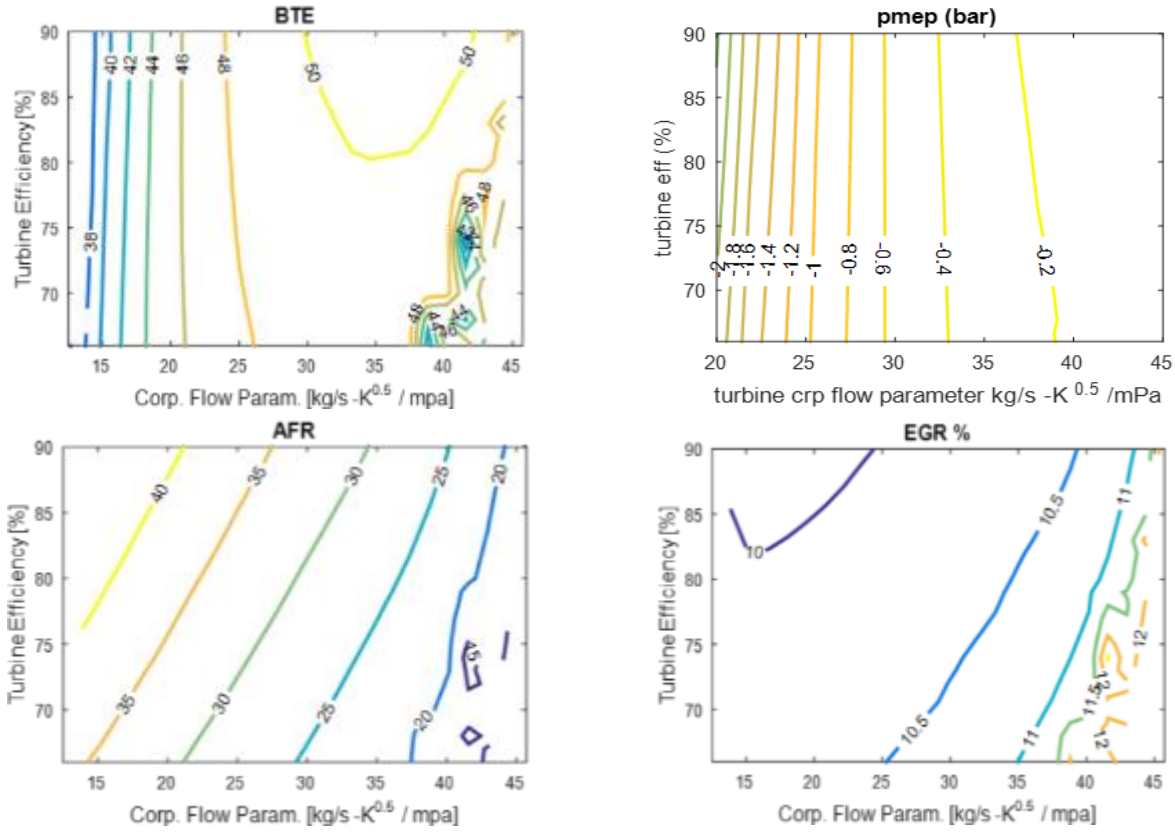

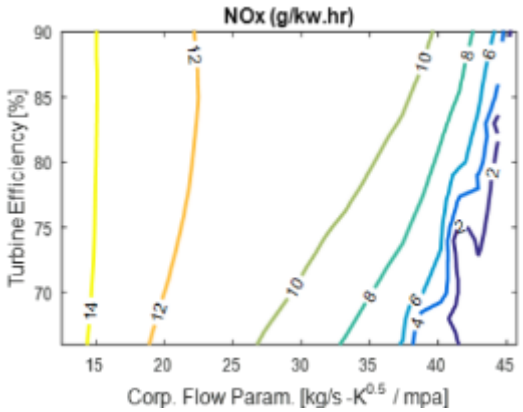

Figure 136: Single Entry Manifold Results with Simple Turbine Analysis

The maximum BTE region can be achieved with > 80% turbine efficiency in LP EGR loop when optimized at EO BSNOx between 8 – 10 g/kW-hr. However, it is important to note that PMEP values are still negative in the regions of interest where we want to maximize BTE. Hence the motivation to investigate the divided entry manifold with larger exhaust valve lift and duration in combination with the divided simple turbine approach. Figure 137 shows the simulation results for a divided entry manifold concept.

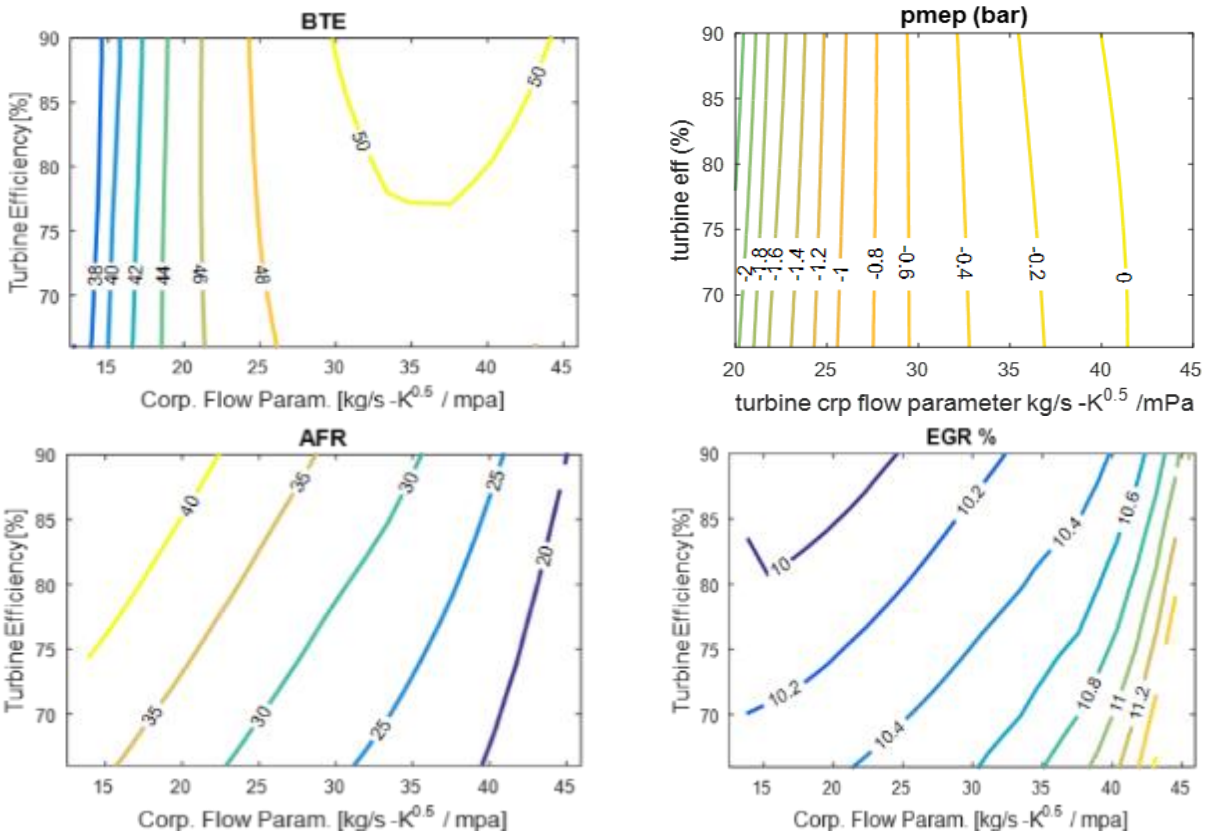

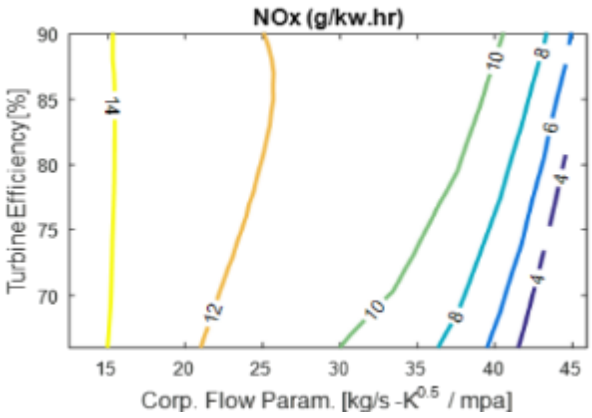

Figure 137: Divided Entry Manifold with Simple Turbine Analysis

By comparing results between Figure 136 and Figure 137, it can be concluded that for both divided and single-entry manifolds, a turbine flowing around 35 kg/s-K^0.5/mPa corrected turbine mass flow with > 80% turbine efficiency coupled to a K98K68 compressor would be a reasonable target to achieve maximum BTE at 1000 RPM. The divided entry manifold does offer the benefit of achieving positive PMEP with increasing turbine flow through larger critical housing areas. However, the increase in OCE is offset by the decrease in closed cycle efficiency due to lower charge-fuel ratios. Further increasing turbine efficiency and optimizing the manifold design for positive pumping would provide possible opportunities to increase BTE values close to the program target. The results from simple turbine analysis drove some of the hardware selection for both VGT and divided entry fixed geometry wastegate turbine hardware as mentioned previously.

System Optimization (early efforts)

A Latin hypercube design of experiments was setup with calibrated GT-Power model to investigate LP EGR loop, HP EGR loop & DL EGR loop architectures as a function of air-handling actuator positions, combustion and fuel system references. Figure 138 shows the output response of BTE vs Engine out BSNOx emissions for the VGT hardware at 1000 RPM engine speed using the DOE approach. A maximum BTE of 50.2% can be achieved at 15 g/kw.hr EO BSNOx. However, given the aftertreatment system's capability to achieve high NOx conversion efficiency under both steady state and transient drive cycles, our conservative target for EO NOx is between 8 – 10 g/kW-hr which yields a BTE of 49.9 – 50.0%.

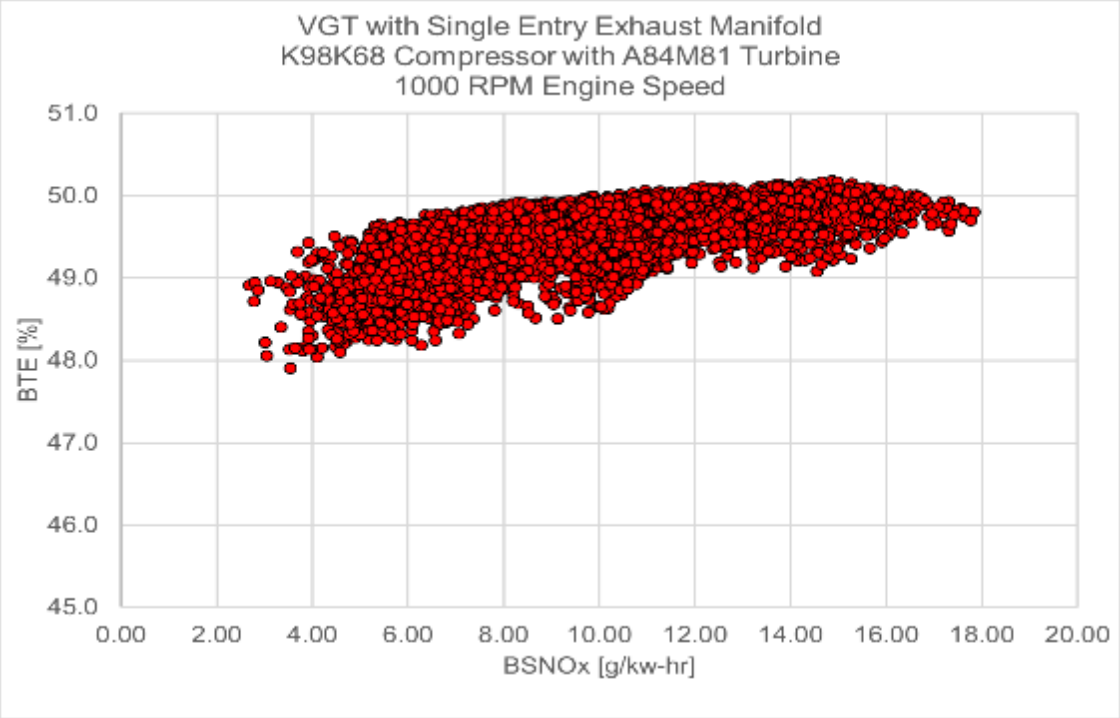

Figure 138: BSNOx vs BTE for a VGT with Single Entry Exhaust Manifold

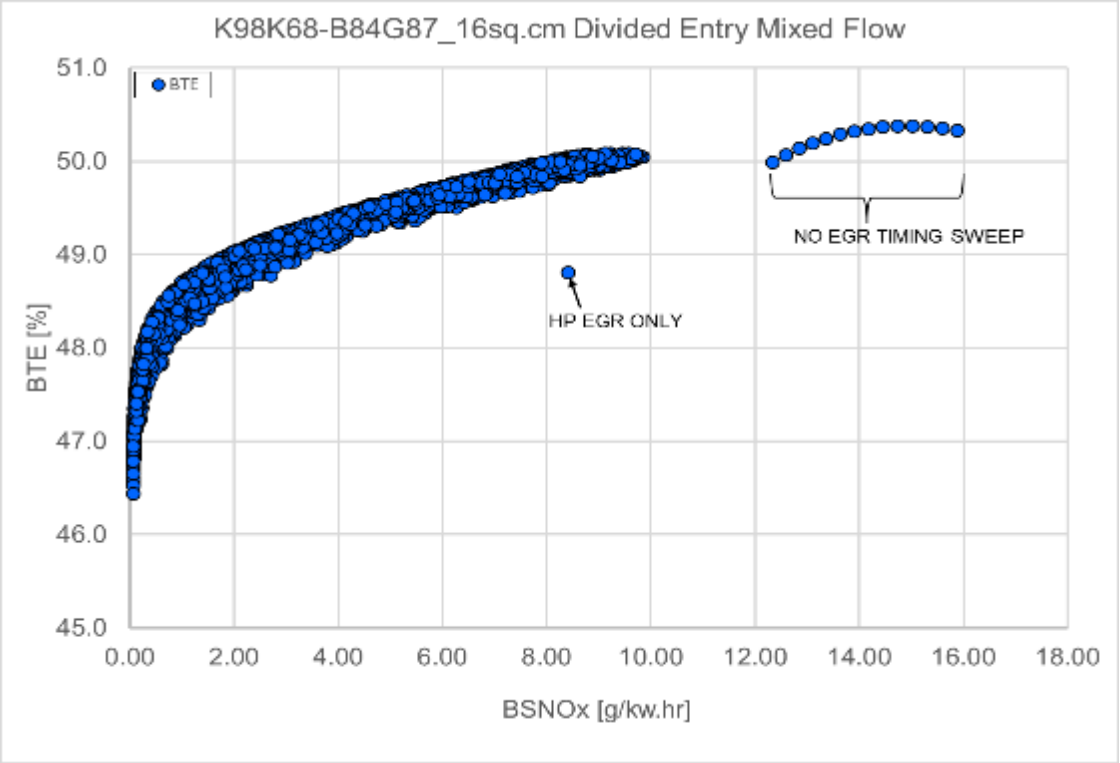

Figure 139: BSNOx vs BTE for a Divided Entry Turbine & Exhaust Manifold

A similar analysis approach was followed for the divided entry turbine in combination with a divided entry exhaust manifold and a longer duration exhaust valve event with higher valve lift profile. Figure 139 summarizes the bubble plot of BTE vs BSNOx for the fixed geometry divided entry hardware. Both the VGT and FGT divided entry hardware seem to exhibit similar peak BTE efficiency numbers of 50.4% at 15 g/kw.hr EO BSNOx. However, the VGT tends to provide better robustness at < 6 g/kw.hr BSNOx with more solution

space when compared against the fixed geometry divided entry hardware. The divided entry hardware does perform well in LP EGR only mode, however suffers a significant BTE penalty under HP EGR only mode due to additional throttling losses.

Further optimization runs were performed to maximize the BTE as a function of EO NOx within the mechanical and thermal design constraints. The resulting DOE data was then utilized to build a Multiple-Linear Regression (MLR) model. This MLR model was then utilized to optimize the system under the constraints of maximized brake efficiency at a target BSNOx level while keeping cylinder pressure less than 238 bar.

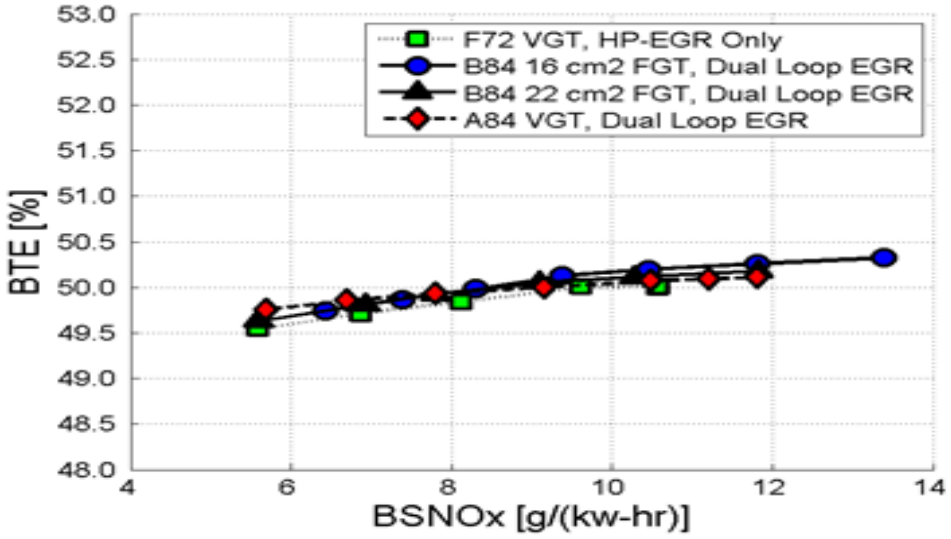

Figure 140: Optimized BTE vs BSNOx for Various Turbomachinery Options

Figure 140 demonstrates that despite the turbomachinery selected, the resulting system efficiency is very similar to only marginal improvements as a function of different BSNOx levels. However, the system efficiency achieved does differ as illustrated in Figure 141.

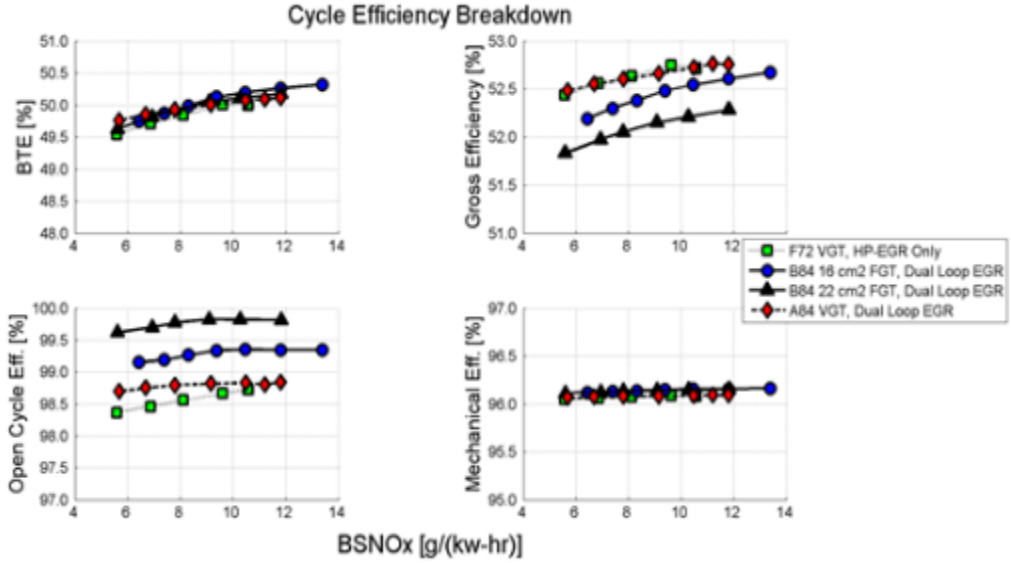

Figure 141: Cycle Efficiency Breakdown for Optimized BTE Conditions for Various Turbomachinery Options

Figure 141 demonstrates that the fixed-geometry, B84 turbine options tend to result in higher open cycle efficiency; however, they pay a penalty in gross efficiency relative to the VGT options. The current assumption is that aftertreatment system would be capable of meeting 0.27 g/kw.hr tailpipe emissions on a HD

certification cycle with 8 g/kw.hr EO NOx emissions. With this assumption, Figure 142 illustrates the maximum BTE that could be achieved based on analysis across different turbo, exhaust manifold and EGR architectures.

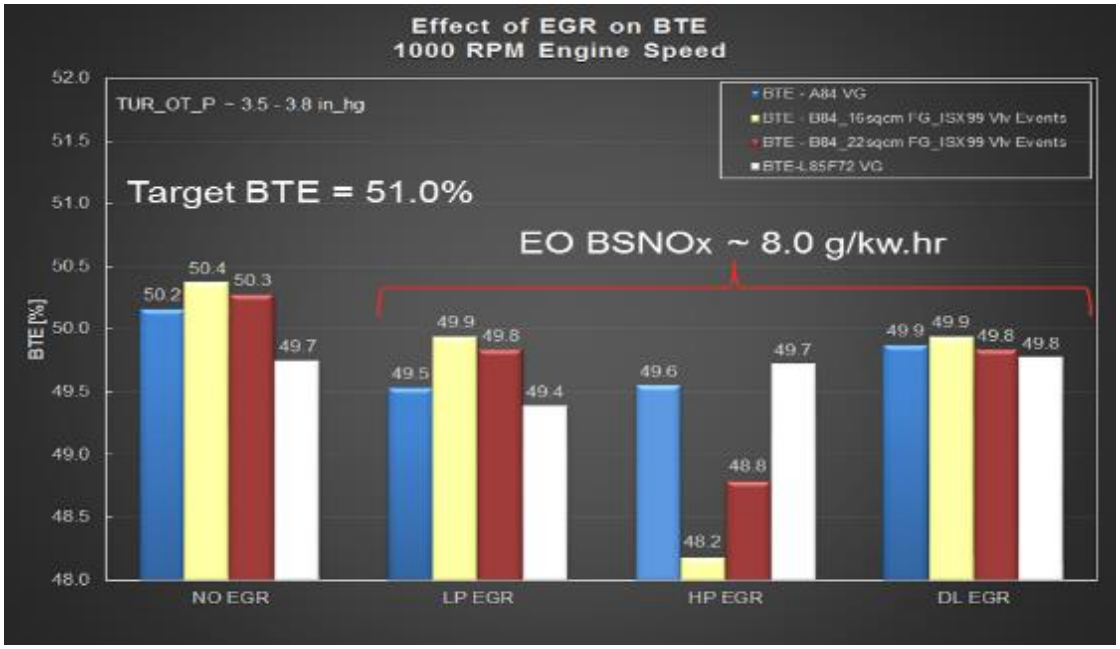

Figure 142: Air Handling Analysis Summary

The VGT architecture performs the best in DL EGR mode and offers a 0.2% ΔBTE improvement when compared to the HP cooled EGR system. The divided entry turbine and exhaust manifold performs the best in LP EGR mode and can match the performance of VGT with less complicated architecture, controls and lower cost possibly.

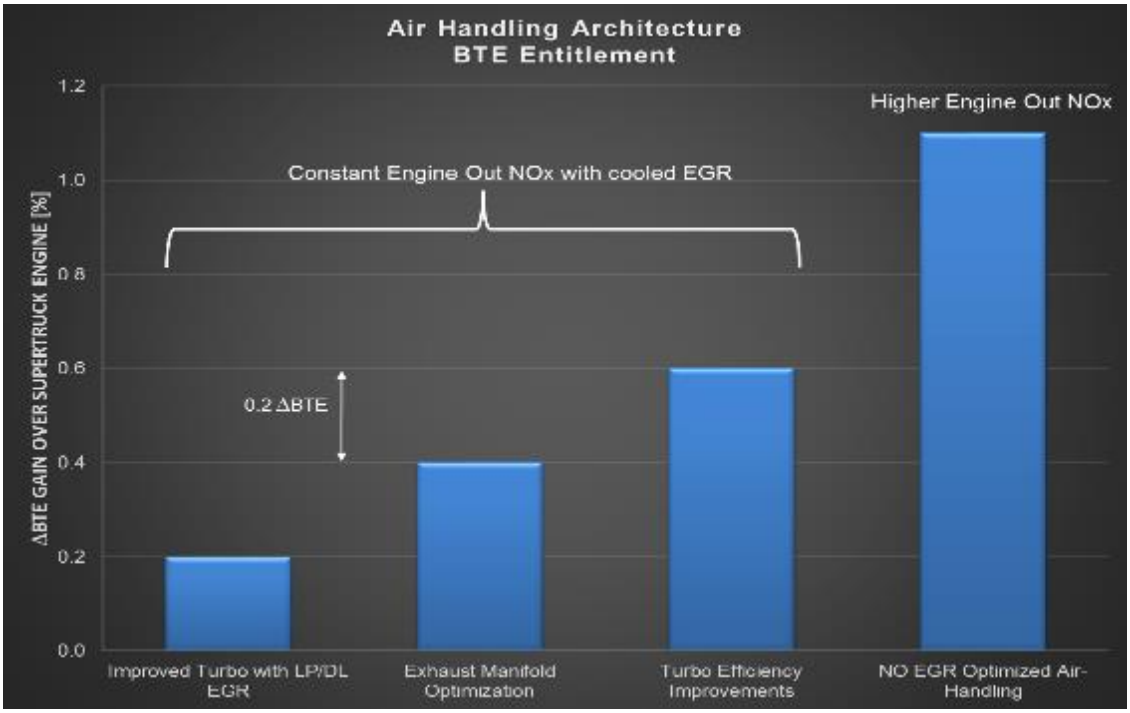

Figure 143: ΔBTE Entitlement Projection for Air Handling Technologies

With the given target BTE of 51% for engine only demonstration, still significant improvements need to come from the air-handling technology to compliment closed-cycle efficiency improvements and mechanical friction reduction efforts. With some preliminary analysis, it was possible to quantify ΔBTE gains that would be needed from different areas of air-handling architecture as shown in Figure 143.

Future work will involve analysis as well as experimental efforts to explore and pursue some of the highlighted technologies. Interest in NO EGR architecture still exists due to the potential BTE gains it offers with the ability to run higher EO BSNOx emissions. However, more consideration needs to be given to Aftertreatment technology improvements in order to make this happen.

On the turbocharger topic, future work will look into improving compressor efficiencies through means of abradable coatings on housing, fluid honed core for improved surface finish, minimum clearance parts to achieve maximum efficiency gains as well as LP EGR coating on the impeller to provide corrosion and erosion resistance. The turbine side will also consider diffuser, abradable coatings on the housing, optimizing variable geometry nozzle-shroud clearance, mixed flow turbine wheel, divided entry turbine housing and roller element bearing technologies. Figure 144 shows a turbine map for the fixed geometry divided entry mixed flow turbine. Potential opportunities exist to scale the map to the desired operating area to maximize turbine efficiency as well as BTE through housing design changes or a wheel change as well as a combination of both. On the other hand, if coating and bearing technologies can be leveraged to provide the same efficiency gains, it would be value added as well.

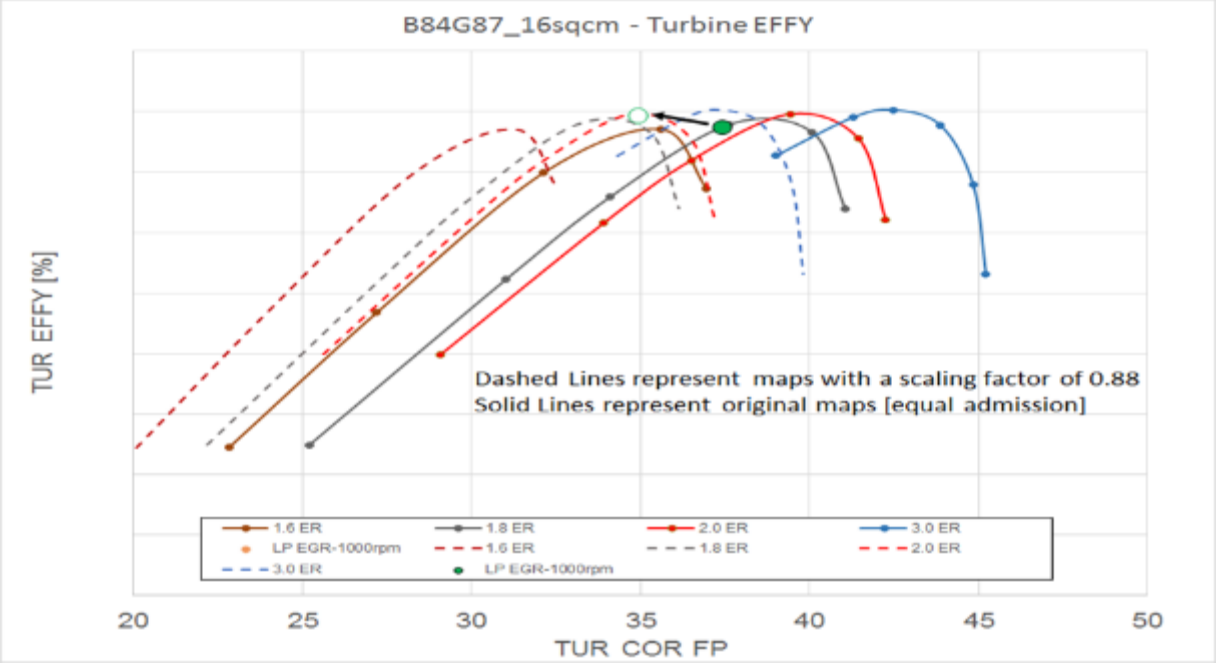

Figure 144: Potential Opportunities to Improve Turbine Efficiency

In addition to focusing on the best BTE point at 1000 RPM engine speed, careful attention was paid to other conditions like CP2 point at 1125 RPM and points along the torque curve to ensure that the air-handling system architecture will be capable to deliver a 425 - 450 hp rating. During operating under higher engine speeds near rated power, DL EGR architecture provides the flexibility to use HP EGR loop as a wastegate to ensure the operating points are still within the compressor map without choking the turbomachinery. Preliminary analysis suggests that it is possible to match a VGT for achieving best BTE at 1000 rpm as well as able to meet the torque curve requirements. Figure 145 shows the compressor map of K98K68 with the operating points. The color contours represent compressor efficiency islands.

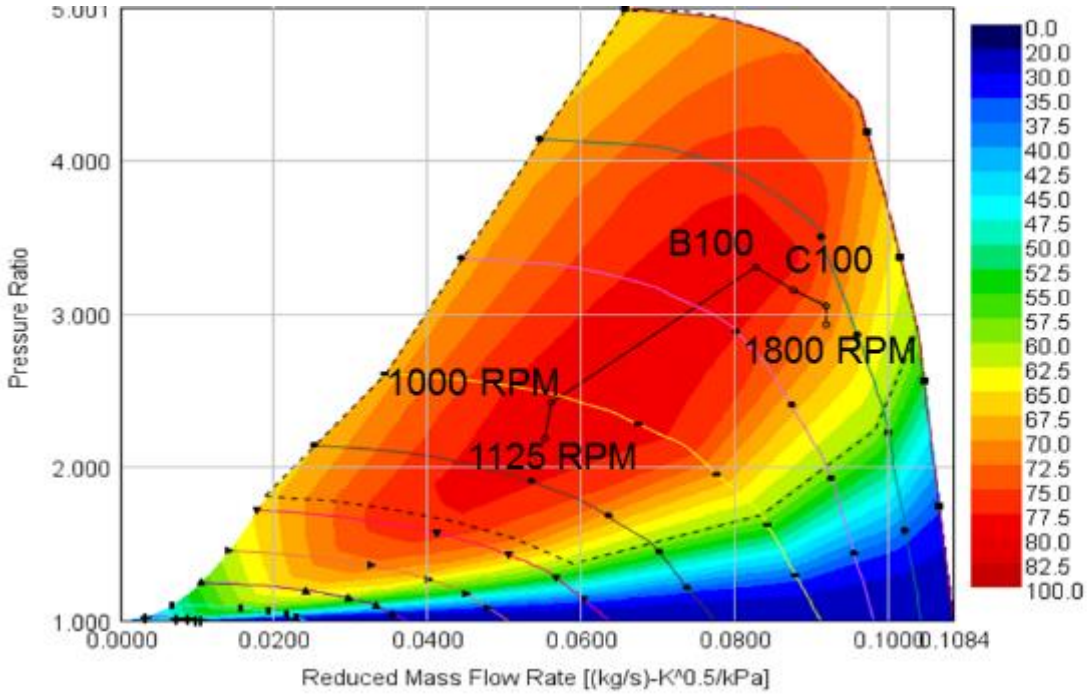

Figure 145: K98K68 Compressor Map with Operating Points

At this point, the efforts were to continue in the direction of the following:

- Evaluate improved VGT technology on engine
- Experimental evaluation of higher cup flow injectors on engine and perform model validation
- Continue to work with CTT in delivering improved turbo technologies.
- Exhaust manifold CFD optimization for improving OCE.

At this point, the cycle simulation work was focused around improving model predictions and fidelity based on engine test data with the baseline hardware configuration. The baseline engine data was run with 600pph cup flow injectors and HE400 VGT moving shroud turbocharger. The DI-Pulse predictive combustion model in GT-Power was calibrated to engine data set at 1130 RPM & 1000 RPM steady-state operating conditions.

GT-POWER Model Calibration (A baseline model)

Previously generated injection rate shapes from the SuperTruck program were used for this model calibration exercise. In future, further refinement may be necessary with an updated version of injection rate shape profiles that accurately represents the hardware configuration. The model calibration was carried out at two points, namely CP2 – 1130 RPM & BP1 – 1000 RPM.

Table 6 : Engine Data vs Model Comparison [CP2]

		TC203 Data - GINA 1712	Model Calibration [Dipulse]	% Error
ENG_SPD	rpm	1130	1130	0.0
Air_Flow	kg/min	13.35	13.4	-0.2
Fuel_Rate	kg/min	0.510	0.510	0.0
A:F Ratio	none	26.2	26.4	-0.8
EGR_FR	%	24.40	24.44	-0.2
VOL_EFF	%	92.92	94.70	-1.9
BSFC	g/kw.hr	179.82	179.68	0.1
BRK_TRQ	Nm	1437	1438	-0.1
BRK_PWR	kW	170	170	0.0
BTE	%	46.8	47.3	-1.1
CCE	%	51.3	51.8	-1.0
OCE	%	97.0	96.8	0.2
FMEP	kPa	58.75	56.93	3.1
PMEP	bar	-0.4	-0.42	
TOT_FUELING	mg/st	150.4	150.3	0.1
PCP	bar	194.7	200	-2.7
CMP_IN_P	kPa	-0.74	-1.00	
CMP_OT_P	kPa	107.7	102.1	5.2
CMP_PR	none	2.11	2.04	3.3
CMP_IN_T	K	297	301	-1.3
CMP_OT_T	K	392	392	0.0
CMP_MRA	(kg/s)-K^0.5/MPa	39.36	39.2	0.4
CMP_EFF	%	74.3	74.3	0.0
TUR_IN_P	kPa	111.4	114.0	-2.3
TUR_OT_P	kPa	5.92	6.10	-3.0
TUR_PR	none	2.01	2.04	-1.5
TUR_IN_T	K	686	675	1.6
TUR_OT_T	K	579	594	-2.6
TUR_EFF	%	75.2	74.7	0.7
TRB_SPD	krpm	83.25	84.30	-1.3
TUR_MRA	(kg/s)-K^0.5/MPa	28.9	28.5	1.4
INT_MNF_P	kPa	101.6	97.5	4.0
INT_MNF_T	K	312	309	1.0
VGT Position	%Closed	42.5	40	
BSNOx	g/kw.hr	8.27	8.51	-2.9

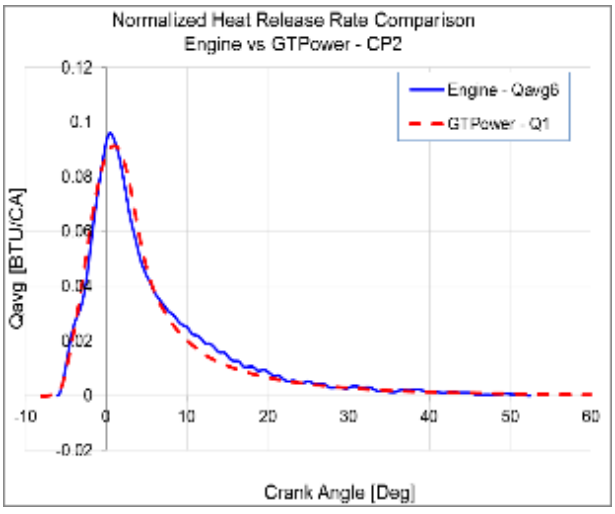

Figure 146: Heat Release Rate & Log P- Log V Comparisons between Engine & Model [CP2]

Table 6 shows the key performance metrics between the model and engine data after the calibration exercise. The DI-Pulse model's coefficients were tuned to capture the normalized apparent heat release rate as closely as possible to match test data. Figure 146 shows the comparison of heat release rate and the LogP - LogV plot between engine and model. The compressor and turbine map efficiency multipliers were calibrated to reflect the actual hardware's performance on engine along with the NOx multiplier to match test data.

A similar exercise was performed at the BP1 engine operating point and Figure 147 shows the heat release rate and LogP – LogV plot comparisons.

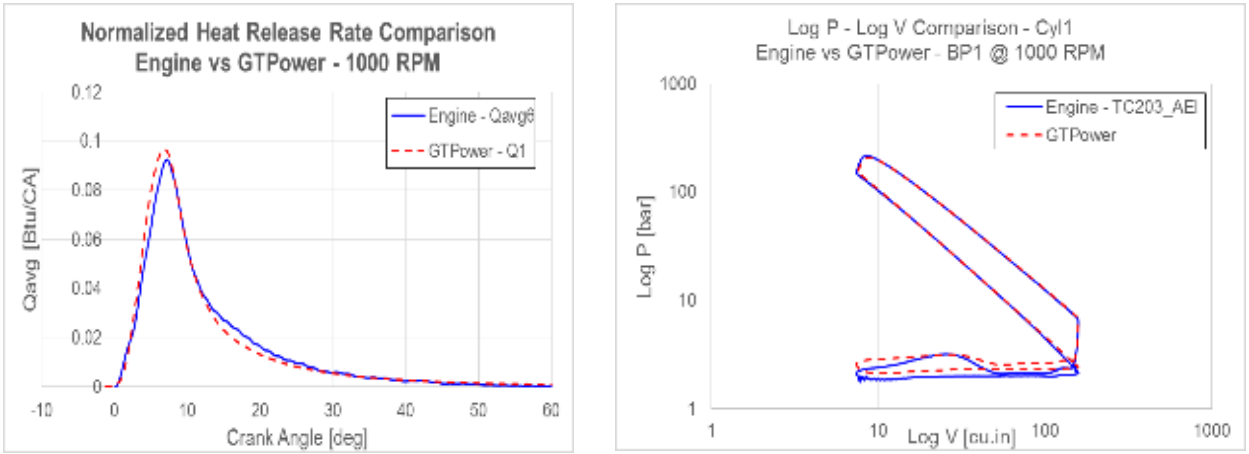

Figure 147: Heat Release Rate & Log P – Log V Comparisons between Engine & Model [BP1]

The calibration process helped to readjust the model against baseline engine data and was used in further exploring different air-handling architectures towards BTE improvement.

Air Handling Technologies Path to 55% BTE

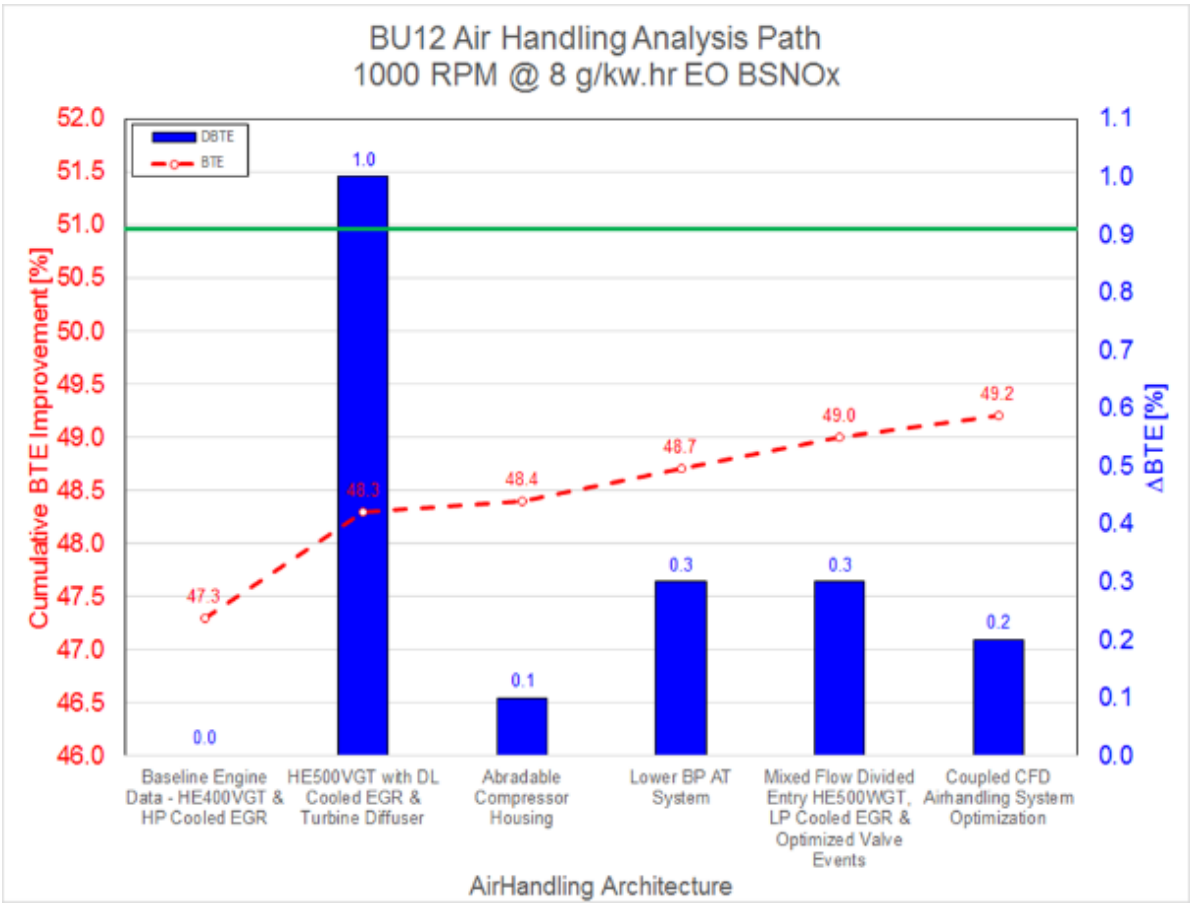

Figure 148: Path to BTE Improvements

The calibrated GT-Power model was exercised to explore further BTE improvements towards achieving 55% BTE. With the milestone of achieving 51% BTE on engine without WHR by the end of this year, Figure 148 shows the cumulative BTE improvements with different technologies as well as the dBTE contribution from these respective technologies. With lower backpressure aftertreatment systems, it was further possible to gain 0.3% dBTE as represented in Figure 148. Exhaust manifold optimization with turbocharger using coupled CFD analysis could additionally yield up to 0.2% dBTE. Based on analysis, the projected benefit from air-handling technologies is approximately 1.9% dBTE towards achieving a goal of 51% engine only BTE.

Asymmetric Turbine Analysis

The divided manifold and fixed geometry symmetric turbine setup favors all the EGR to be driven from the low pressure loop to reach the best brake thermal efficiency while meeting target NOx levels of 6 g/hp.hr. The purpose of this exercise was to evaluate asymmetric turbine with DL EGR for improving the overall BTE by achieving better OCE. The GT Power model used in this study was calibrated for predictive combustion with 450pph injectors. The model was also calibrated to predict NOx emissions. All the analysis was performed at 1000 RPM. The speed and fueling conditions have been picked from SuperTruck program's best BTE point. The GT Power model was run in open loop fueling for the analysis performed as shown in Table 7.

Table 7: Fixed Speed and Fueling Conditions for Asymmetric Analysis Work

Eng_Spd	1000	RPM
Rail_P	1374	bar
Inj_Qty	203.3	mg
SOI	5.94	bTDC

The model was set to run asymmetric turbine coupled to a divided manifold up to the turbine housing entry. The asymmetric turbines were modeled using 2 simple turbine objects, each turbine representing one scroll of the asymmetric turbine. The orifice diameter can be changed in each of the turbine objects and by having different combinations of orifice diameters in each turbine objects, asymmetry in turbines can be varied. The two turbine objects are coupled to 'K98' compressor map. Each bank of the exhaust manifold was coupled to one turbine object as shown in Figure 149.

High pressure EGR take off pipe was from one bank of the exhaust manifold connected to smaller turbine and the low pressure EGR pipe was downstream after the exhaust gases expand through the turbine. The model was configured for dual loop EGR setup. All the analysis work was performed with EGR pulled from both the high pressure and low pressure loops. ISX99 valve events shown in Figure 150 were used for this analysis, as these valve events predict the best brake thermal efficiency in conjunction with the current divided manifold setup.

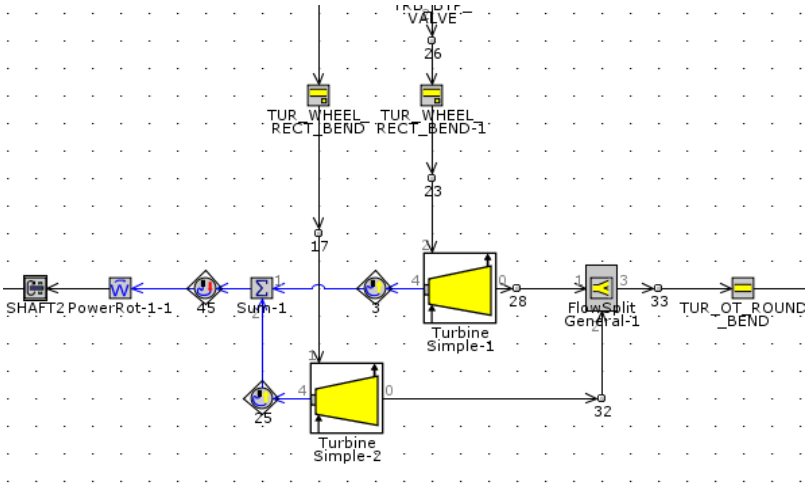

Figure 149: Black Box Asymmetric Turbine Model Layout

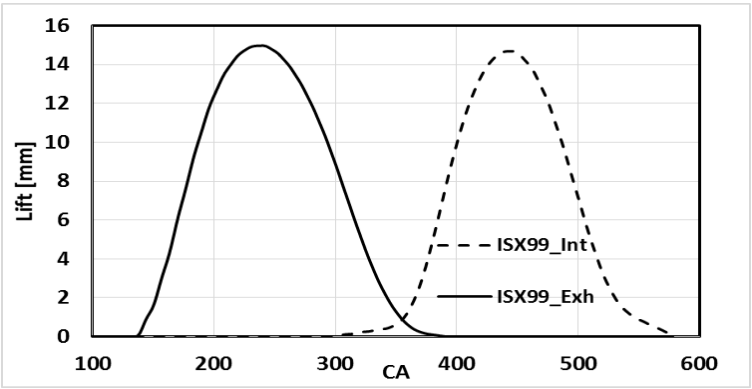

Figure 150: Model Year 99 ISX Valve Events

For modeling the asymmetric turbine using black box turbine object in GT Power, suitable size and efficiencies should be selected for proper evaluation. A single turbine object with around 35-37 kg/sec-K^0.5/MPa of corporate flow parameter was shown earlier in Qtr1 report to have the best brake thermal efficiency. A single black box turbine with orifice diameter of 35 mm coupled to the divided manifold would result in this corporate flow. The two turbine sizes should be such that the sum of their areas equals the area of a single 35mm black box turbine. Four different turbine sizes are evaluated in this study as shown in Table 8. The areas of the turbine objects are split in 4 ways as shown in Table 8 to give different levels of asymmetry. Turbine 1 with 50/50 area split would represent a symmetric turbine and turbine 2, 3 and 4 would represent increasing asymmetric turbine setups. As the asymmetry in turbine increases it will be easier to flow EGR through the high pressure loop and will reduce the use of exhaust throttle to drive the EGR through low pressure loop.

Table 8: Area Splits for Asymmetric Turbine

	1	2	3	4
area split	50/50	52/48	54/46	56/44
	Area (mm)			
turb1	481.1	500.3	519.5	538.8
turb2	481.1	461.8	442.6	423.3
Total Area	962.1	962.1	962.1	962.1
turb area ratio	1.00	1.08	1.17	1.27
	diameter (mm)			
turb1	24.7	25.2	25.7	26.2
turb2	24.7	24.2	23.7	23.2

In this analysis, the efficiency of the larger turbine was kept constant at 75% and evaluated conditions with varying efficiencies on the smaller turbines. In the asymmetric turbines, as the asymmetry increases the turbine efficiency on the smaller scroll is expected to drop. Figure 151 shows different efficiencies evaluated on turbines. The overall turbine efficiency is the weighted efficiency based on corporate flow in each of the turbine objects.

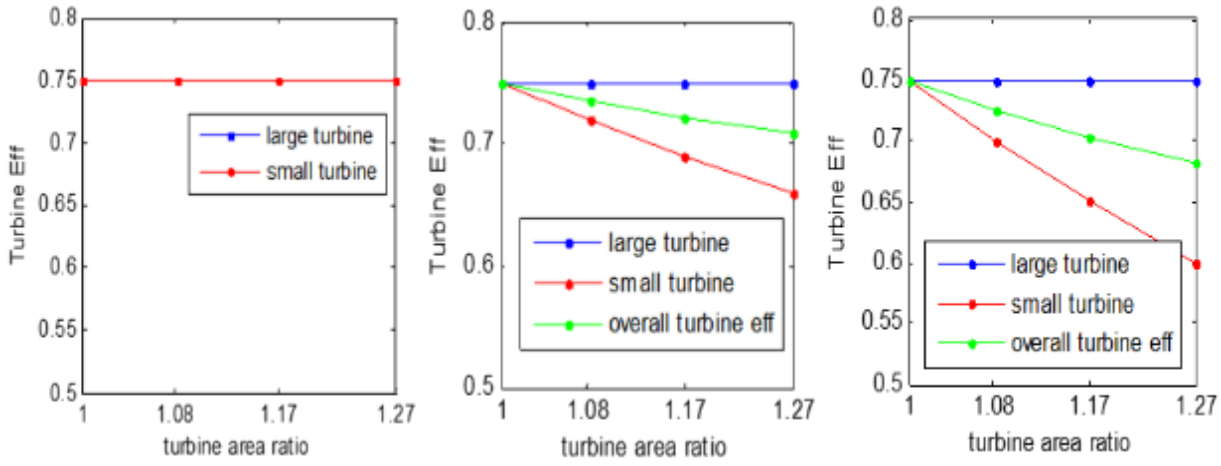

Figure 151: Constant Turbine Efficiency & Reducing Turbine Efficiency in Smaller Turbine

The analysis was performed for BSNOx levels of 6, 7 and 8 g/(hp-hr) engine out NOx. When the turbine efficiencies are kept constant in each of the turbine objects, BTE increases as shown in Figure 152. This is primarily due to the reduced dependence on exhaust throttle to drive a certain amount of EGR through the low pressure loop. For a completely symmetric setup even though the HP EGR valve is wide open there is no EGR flow through the HP loop, but as the asymmetry of the turbine increases, additional flow is observed from HP loop and the use of exhaust throttle is reduced as seen in Figure 153. This helps in increasing the open cycle efficiency. The charge fuel ratio and closed cycle efficiency slightly decreases in this scenario for increasing asymmetry. But the higher gains in open cycle efficiency leads to increased brake thermal efficiencies.

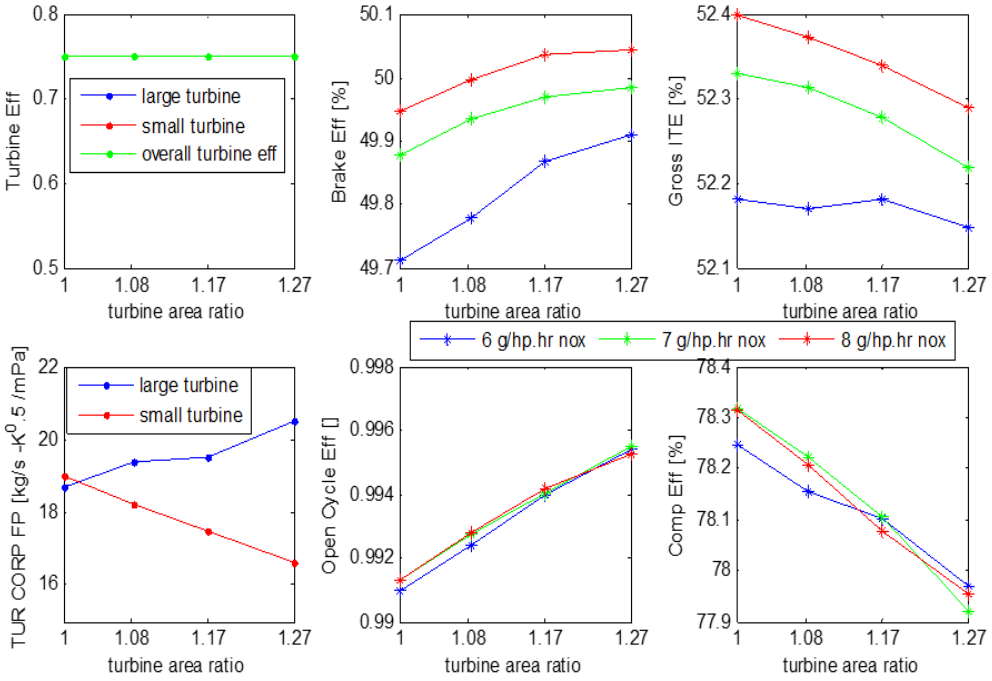

Figure 152: Engine Performance with Constant Turbine Efficiency in Both Volutes

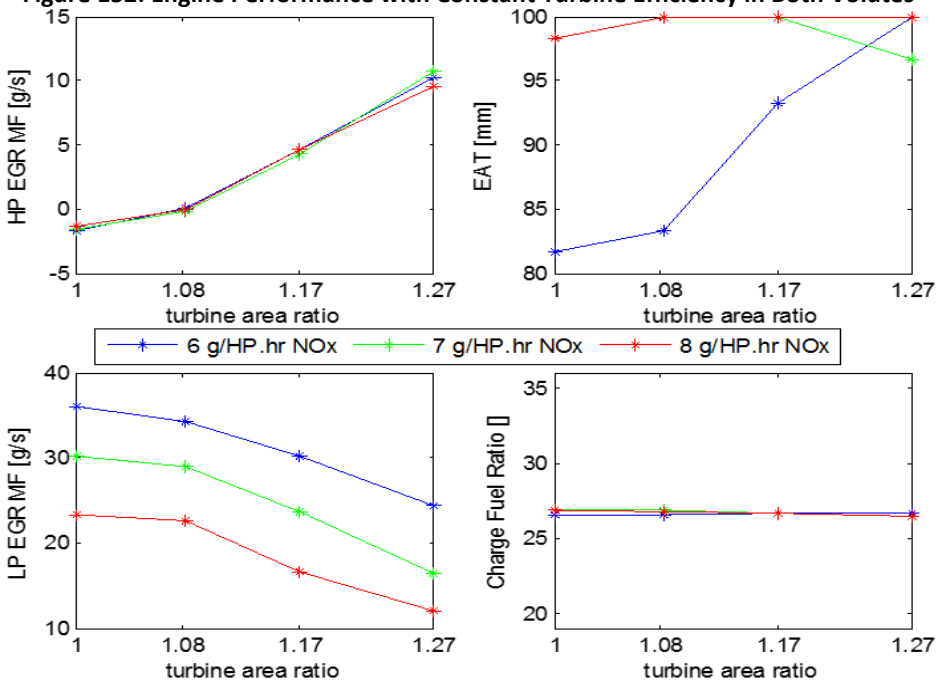

Figure 153: EGR Flow Rate, C:F Ratio & Exhaust Throttle Position with Constant Turbine Efficiency in Both Volutes

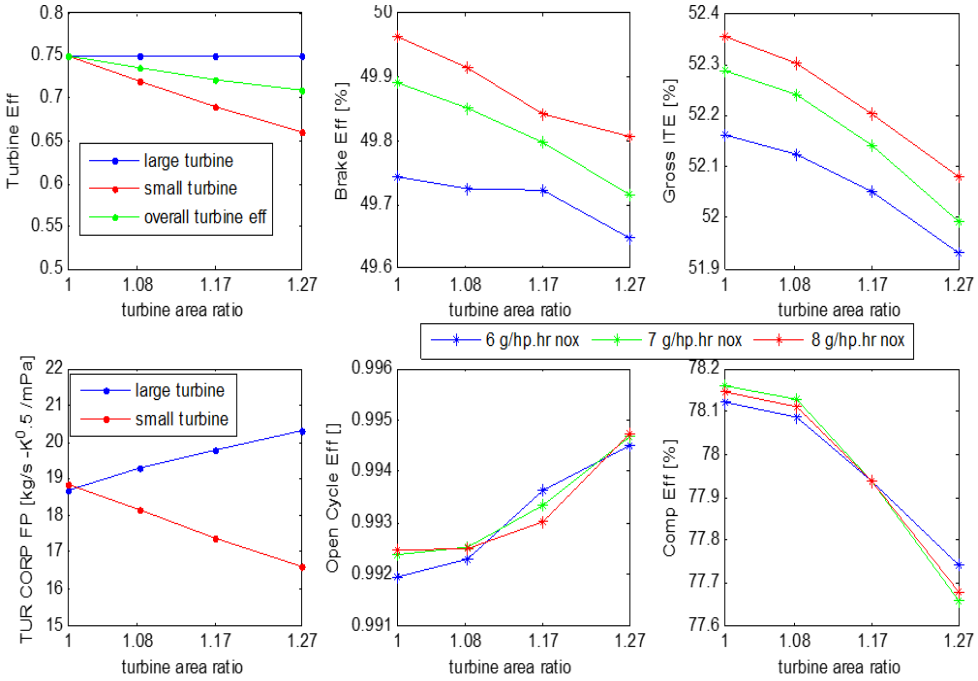

Figure 154: Engine Performance with Decreasing Turbine Efficiency in Small Volute

Constant efficiency on both the turbine objects even with increasing asymmetry is an ideal scenario and provides the baseline for evaluation. The asymmetric turbine analysis was also performed with reducing efficiency on the smaller turbine as shown in Figure 154. In this case, it can be seen again that HP EGR flow rate increases with increasing asymmetry as seen in Figure 155, and thus an improvement in open cycle efficiency with reduced dependence on exhaust throttle. But the decrease in charge fuel ratio and closed cycle efficiency is higher in this case compared to the previous case and the gains in overall brake thermal efficiency can no longer be seen with increased asymmetry.

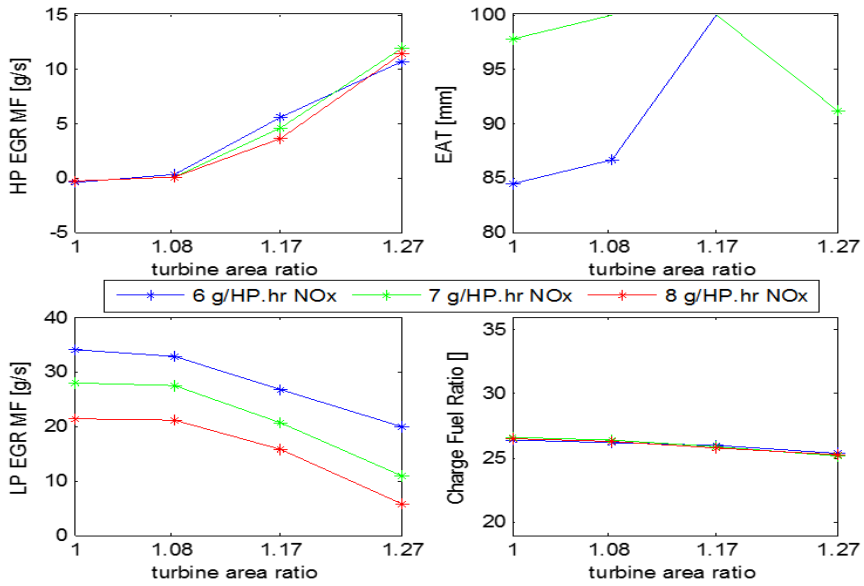

Figure 155: EGR Flow Rate, C:F Ratio & Exhaust Throttle Position with Decreasing Turbine Efficiency in Smaller Volute

The efficiency on the small turbine is bound to drop with increasing asymmetry and from the simulation results it can be seen that overall brake thermal efficiency is largely dependent on the efficiency of the smaller turbine. Increasing asymmetry helps in improving the open cycle efficiency but the charge fuel ratio decreases leading to a reduced closed cycle efficiency. BTE improvements can be observed with asymmetric turbine only if the efficiency on the smaller volute can be maintained at relatively constant levels with improved manufacturing technologies and ensuring tight clearances between the wheel and the housing. It is also important to note that the asymmetric turbine could still be tailored to deliver optimal performance in a key operating area of the torque curve, but would lack the benefits of VGT to cover a wide operating map to meet both emissions and performance.

Valve Optimization Simulations

Simulations were also performed in GT-POWER for optimizing the valve lift profiles to check if any additional BTE benefits can be obtained by modifying the cams. The cams evaluated for optimization were MY2017-PPT, MY2017-Production, and ISX99 cams as shown in Figure 156.

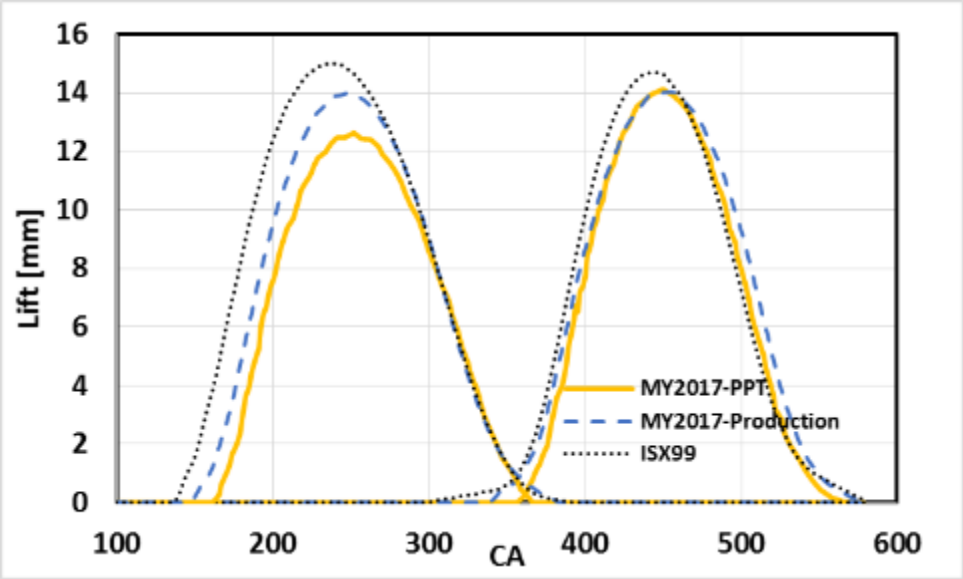

Figure 156: Comparison of MY2017-PPT, MY2017-Production, and ISX99 Valve Lift Events

These valve lift profiles were evaluated with aggressive opening and closing ramps, cam phasing, early exhaust valve opening with the same intake and exhaust overlap, late intake valve closing with the same intake and exhaust valve overlap as shown in Figure 157. The cams were evaluated for best BTE while meeting a target engine out NOx of 8 g/(kw-hr). Modified MY2017-PPT and MY2017-Production cams were evaluated with the model calibrated for variable geometry turbo and DL-EGR set up, whereas the modified ISX99 and MY2017-PPT cams were evaluated on a model calibrated for the fixed geometry turbo and LP-EGR set-up. All the model evaluations were done at 1000 RPM and 2034 Nm operating condition.

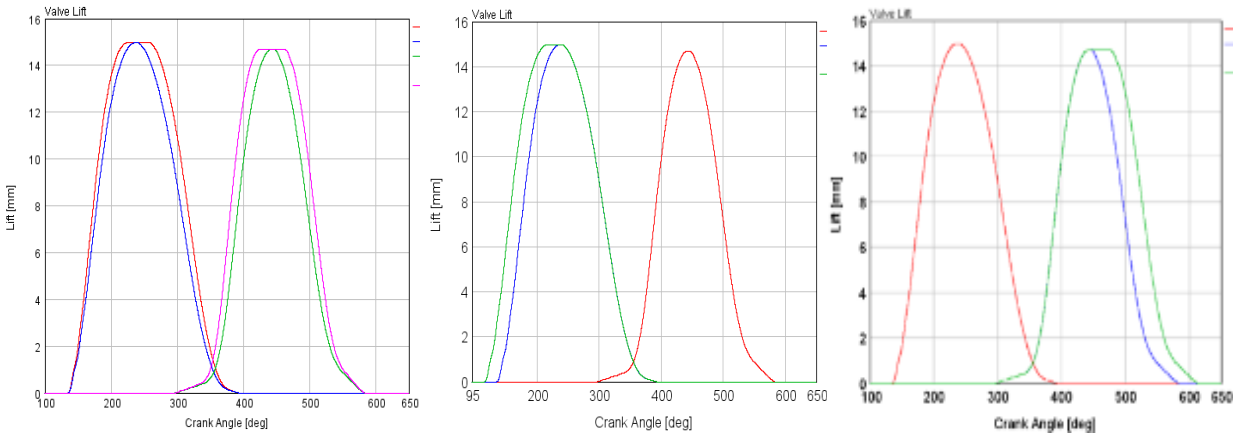

Figure 157: Aggressive Opening / Closing Ramps [left]; Extended Exhaust Duration [middle]; Extended Intake [right]

The simulation results showed that having an aggressive opening and closing ramps can have a maximum BTE improvement of 0.15 – 0.18 BTE in the VGT model for a target NOx of 8 g/(kw-hr) as shown in Figure 158. Cam phasing and extended durations for intake and exhaust valves do not show any improvements in BTE if the engine out NOx level is optimized at 8 g/(kw-hr). For the fixed geometry model, the simulation predicts a maximum gain of 0.1 BTE with aggressive opening and closing ramps in the intake and exhaust valve lifts at a target NOx of 8 g/(kw-hr). Even for the fixed geometry model, the simulations did not show any significant improvement for cam phasing or extended durations.

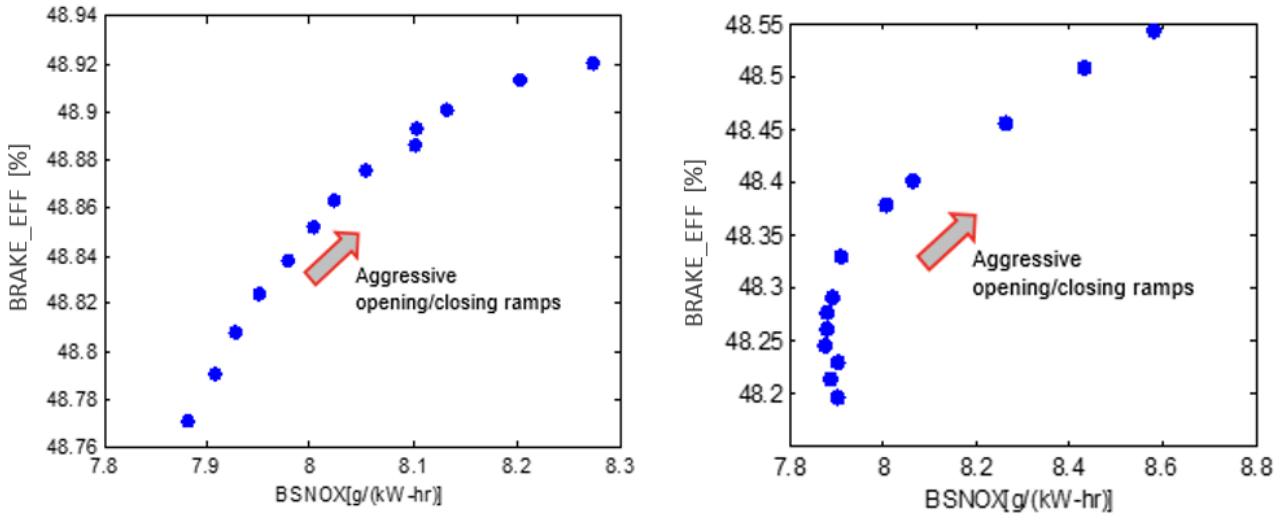

Figure 158: Aggressive Opening / Closing Ramps for VG Model [left]; WGT Model [right]

Fixed Geometry Turbine Simulations

At this point, cycle simulation activities deviated from VGTs to FGTs. Main reasons being looking for high turbine efficiency (for overall system efficiency) and aided by the fact that no EGR was being realized as the prime path (utilizing high NOx path for efficiency). Accordingly, efforts were focused around understanding sensitivities to turbine housing critical area with respect to model calibration parameters. As discussed earlier in the report, the mixed flow divided entry turbocharger B84G87 with 16 cm^2 turbine casing was flowing 6% more on engine in comparison to the provided maps and GT-POWER predictions. Hence, the turbine mass

flow multiplier parameter had to be calibrated in the model based on acquired engine data at 1000 RPM, 2033 Nm.

High speed exhaust manifold pressure sensors were then installed at turbine front and rear inlet locations on engine to obtain crank angle resolved pressure data on both A84K83, 16 cm^2 & A84K83, 13 cm^2 turbine casings. The data was then supplied to the turbo supplier to help them come up with new proposals on the turbo hardware to achieve improved charge fuel ratio at a higher open cycle efficiency.

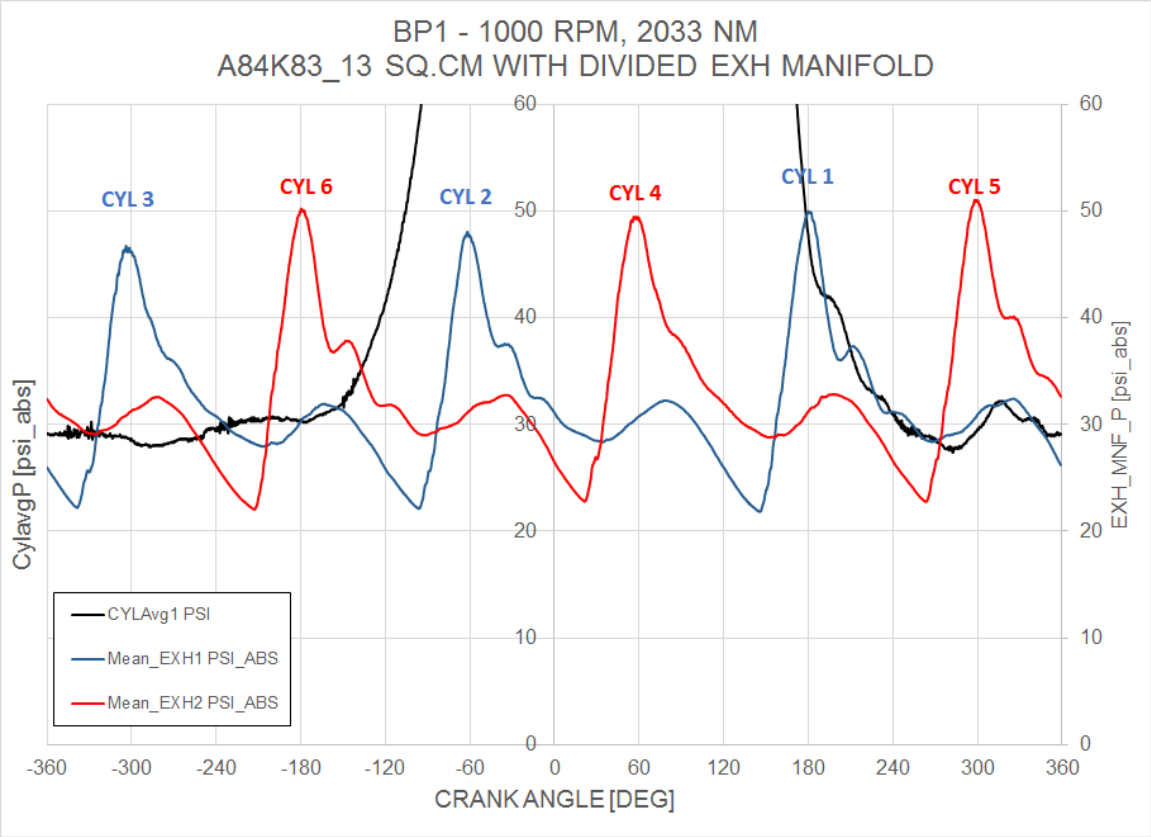

Figure 159: High Speed Exhaust Manifold Pressure Measurements

Figure 159 shows the high speed crank angle resolved exhaust manifold pressure measurements averaged from 200 cycles at turbine front inlet and rear inlet for the A84K83, 13 cm^2 turbine casing. Clearly, the divided entry exhaust manifold and turbine architecture provides significant benefits in keeping the pressure pulsations separate between cylinders 1,2,3 [front volute] & cylinders 4,5,6 [rear volute]. There is some interference between the two volutes based on pressure pulsations and could possibly be improved by eliminating the adapter between the exhaust manifold and turbine inlet which is currently in use. New exhaust manifold design will eliminate the need for this adapter and hardware will become available in 2nd quarter of 2017.

Data collected from engine on all turbine casings were provided to the turbo supplier and based on further analysis, made the following recommendations to improve charge fuel ratio that could potentially improve BTE on engine.

- B84 mixed flow turbine wheel with 79 trim and 11.3 sq.cm turbine casing – Designed for the desired turbine swallowing capacity at the expense of turbine efficiency

- B84 mixed flow turbine wheel with 80 trim and 12.8 sq.cm turbine casing – Designed for the desired efficiency at correct turbine pressure ratio at the expense of swallowing capacity.

Currently design work is in progress on the above proposal and the tentative delivery of hardware is expected to be around late March 2017.

At half-way of the program, it was realized that FGTs were going to be prime path and with supplier recommendation the focus was going to be on mixed flow turbines. Hence, much of system solution efforts focused on getting a good baseline model calibrated with predictive combustion model and secondly predicting the performance of mixed flow turbines {especially with 12.8 cm^2 critical area, using their predicted performance maps (based on CFD analysis by the turbo group)}.

Earlier attempts at a baseline model development were made with TPA mode of combustion model (non-predictive, cylinder pressure imposed). However, this model is not a good representative to perform any further air-handling analysis. With that in mind, a new FHRR (fixed heat release rate) model was developed, for the same test data point. While FHRR model was reasonable to perform air-handling analysis, desire was to get a predictive combustion (DI-PULSE) model developed, for the same test data. The next segment of the report focuses mainly on the DI-PULSE model and mixed flow turbine analysis results using that model. The maps available for the MF (mixed-flow), at this point, were still predicted from CFD. Thought was to assess the performance benefit and directionality of the solutions optimal solutions just around the expected best efficiency point (i.e., BP1). Results were also compared to the turbo with the best radial turbine.

Mixed flow turbocharger performance analysis

Once the new baseline model was developed, several mixed flow turbines were evaluated using their predictive operating maps. The compressor was kept the same in all turbos including the baseline radial, which is what reflects in actual hardware as well. The analysis procedure is as follows:

- As a first step, the respective turbine map is first dialed in.
  - Next a DoE is run with Speed/Torque/SOI as independent parameters.
    - Speed: ±100 rpm
    - Torque: ±100 N.M
    - SOI: -12.5 t0 -2.5 ATDC
- Optimal solution for best BTE was found then from the DoE, by filtering out for PCP (235 bar limit), convergence criteria, best A/F (if more than one solution exists).

The speed and torque are only varied in a very small region around the baseline BP1 (1000 rpm, 2011 N.M) for the following reasons:

Best efficiency operating point is not expected to deviate much around the BP1, even if we wanted to move that around (for various practical reasons, we may want the operating point to stay at BP1; however, for analysis purposes, it's fine to try to find an operating point that may work out to be the best).

Following high level observations are made from the results.

- Optimal solution at similar BTE, however, with a lower speed (900 rpm)
- ***BTE – up to 0.3 pts benefit***

- Benefit all came from mostly from OCE (eng_dp is appreciably lower)
- CCE is slightly down (rounded off)
- MCE slightly up (rounded off)
- A/F is slightly lower

In a similar fashion, rest of the mixed flow turbines were analyzed and combined plots for their performance predictions are shown next. All the turbines shown here have critical surface area of 12.8 cm^2. Compressor (K98K68) is kept the same as it was in the baseline radial turbo (also the same compressor in the exercise shown above as well).

Figure 160 shows the optimal operating points that the analysis gave for the three mixed flow trims (with 12.8 cm^2 critical area) along with the best point for the baseline radial. Analysis shows that the turbos with these new turbines seem to want to go to the left of the design point (BP1) – i.e., lower speed and also lower load as the trim reduces (i.e., as the housing becomes more restrictive).

Figure 161 shows the system efficiencies compiled in a chart of the optimal solutions for all the mixed flow turbines along with the baseline radial turbine. The following are the main observations from this plot:

- With MF 12.8 cm^2 turbines (comp staying the same)- GT says that G83 trim has the best potential of the turbines analyzed
- A/F however, is lower than the baseline in all cases; this could be important from the closed cycle efficiency perspective

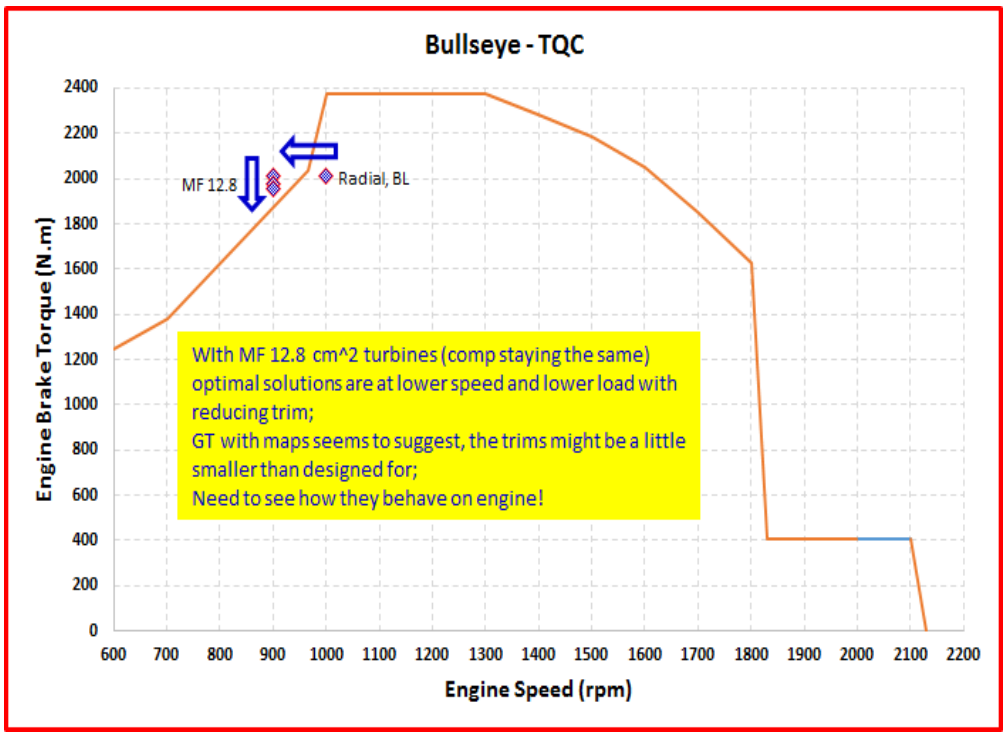

Figure 160 : Optimal points with MF turbos (w/ 12.8 cm^2) shown on torque curve compared to optimal radial baseline

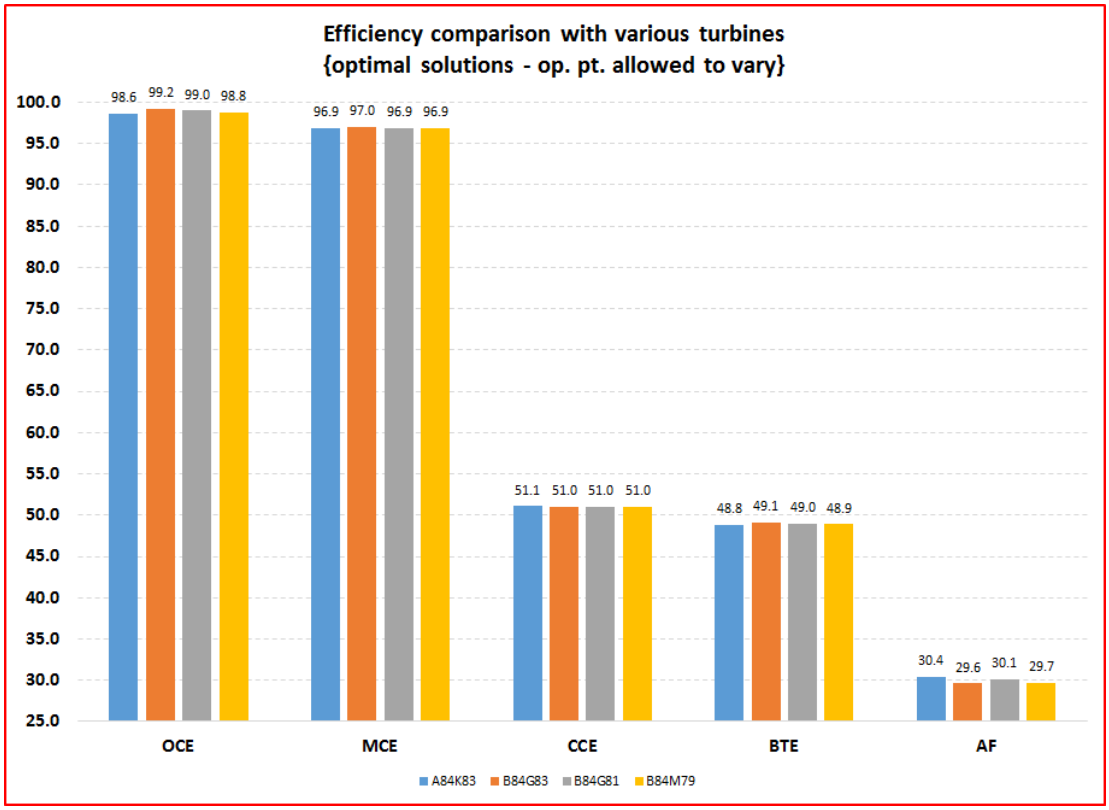

Figure 161 : System efficiencies comparison of optimal solutions w/ all MF turbos vs. optimal radial baseline

Waste-Gate Performance Requirements

Analysis looking at the wastegate requirement assessment was performed in order to supply that information to the turbocharger supplier. Also, at this point of the program, after thorough evaluation of several mixed-flow turbochargers that were built and supplied by the supplier, the decision was made to keep the A84 radial turbo as the prime path.

With the prime path turbocharger being the A84 radial turbine with K98 compressor. Although it was not needed at the design point, it's known that waste-gating is necessary for higher speeds and higher loads. Conditions beyond B100 need waste-gating (Figure 162). Question was how much waste-gating was necessary? This information was requested by the turbo supplier group in order to ensure that the wastegate design would be sufficient.

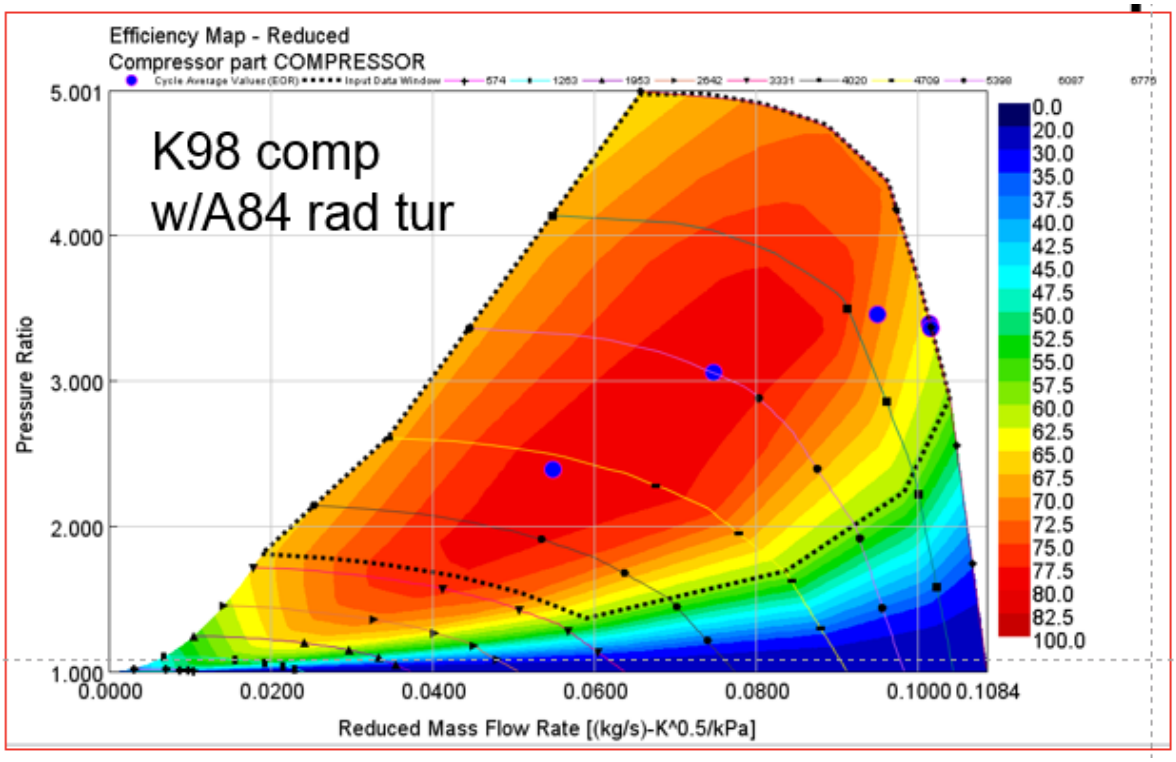

Figure 162 : Torque curve points on prime path compressor map

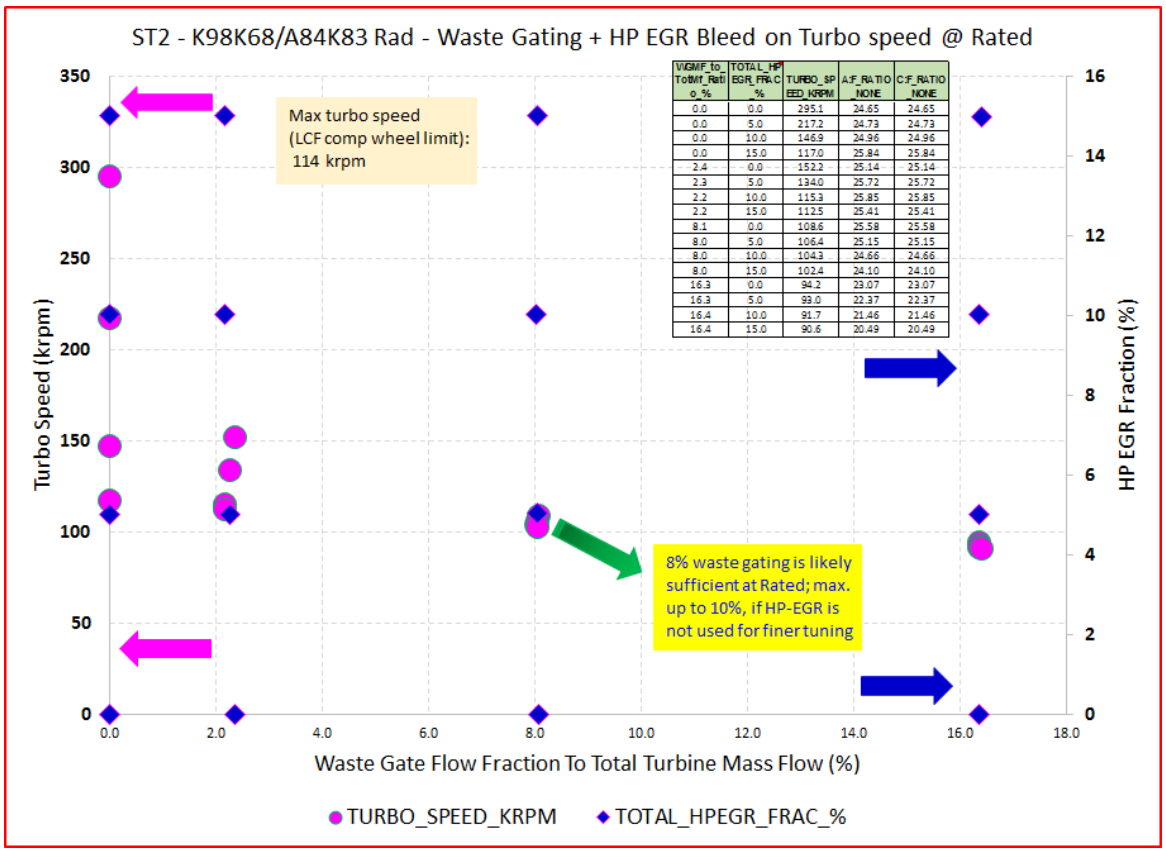

VIGMF_to_TotMf_Ratio_%	TOTAL_HPEGR_FRAC_%	TURBO_SPEED_KRPM	A/F_RATIO_NONE	C/F_RATIO_NONE
0.0	0.0	295.1	24.65	24.65
0.0	5.0	217.2	24.73	24.73
0.0	10.0	146.9	24.96	24.96
0.0	15.0	117.0	25.84	25.84
2.4	0.0	152.2	25.14	25.14
2.3	5.0	134.0	25.72	25.72
2.2	10.0	115.3	25.85	25.85
2.2	15.0	112.5	25.41	25.41
8.1	0.0	108.6	25.58	25.58
8.0	5.0	106.4	25.15	25.15
8.0	10.0	104.3	24.66	24.66
8.0	15.0	102.4	24.10	24.10
16.3	0.0	94.2	23.07	23.07
16.3	5.0	99.0	22.37	22.37
16.4	10.0	91.7	21.46	21.46
16.4	15.0	90.6	20.49	20.49

Figure 163 : Waste-gating % requirement estimation on the current prime path turbocharger

Analysis (Figure 163) showed that about 8% (max to 10%) waste-gating should be sufficient in order to keep the turbocharger speed under the maximum allowable speed. Analysis also shows that the

turbocharger/engine should be able to provide sufficient air at rated (at which the analysis was performed). Although, HP-EGR can help fine tune this scenario, it's not as sensitive as waste-gating to affect the turbocharger speed. However, HP-EGR might be a very strong lever from an overall system optimization standpoint (e.g., to keep the NO_x emissions under control aiding the LP-EGR at some of these conditions or even taking a larger portion).

New best BTE operating condition/recipe & model results

At this point in program, highlight of system solution was to work on updating the steady state models at the latest best BTE operating recipe (engine only best BTE – 49.6%). The calibration process was kept essentially the same.

Since the last recipe that was used for modeling, engine had gone through significant technology trials and builds. From a modeling perspective, much of the critical hardware stayed the same e.g., turbocharger. Whatever inputs that need changed, e.g., friction map was all changed. Slight corrections had to be made the way LHV is overridden in the model. Also, a slight correction was made to the SOI in order to match the SOC – this is simply part of calibration tuning.

Typically, the recommendation from the turbo group is to keep the mass/efficiency multipliers at 1 (unchanged) when using SAE adjusted maps. However, after much deliberation, it was decided to try out changing the turbine efficiency multiplier in order to get a decent match of predicted cylinder pressure against the test data. As for heat transfer model, it was decided to keep the same model that was finalized in the previous best BTE model. This should be a very reasonable assumption, since it's essentially at the same part of the map (speed/bmep) & the combustion hardware hardly changed.

The turbine efficiency multiplier was changed for a couple of reasons. A.) The on-engine turbine efficiency is significantly higher than what the map predicts B.) Without the intended turbine efficiency correction, the P@IVC, A/F were also significantly lower despite ensuring every other input correct in the model

Figure 164 shows some engine data plotted on the SAE adjusted map of the turbo tested for this condition. The data is a cluster of points where SOI was swept at the BP1 condition. The take-away point here is that flow parameter matches reasonably (only a point higher) while the efficiency is clearly way off the map (5% - 7% higher than what the map indicates).

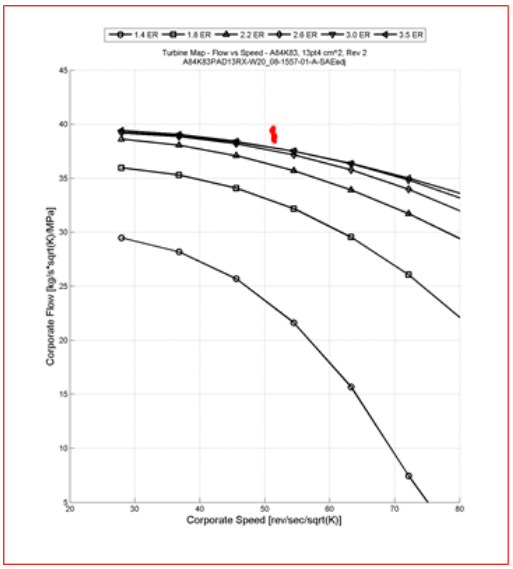

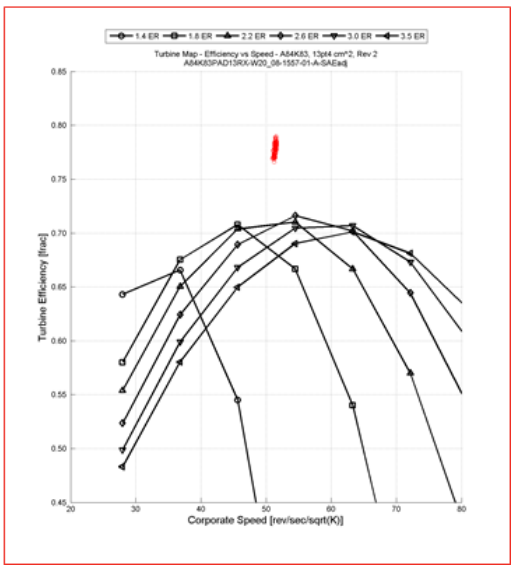

Figure 164 : On-engine (efficiency and flow parameter) data plotted on turbine map of A84 (13 cm^2)

This was the prime motivation for trying to change the efficiency multiplier for calibration of the model. Efficiency multiplier was changed just enough so the predicted turbine efficiency matches the on-engine efficiency.

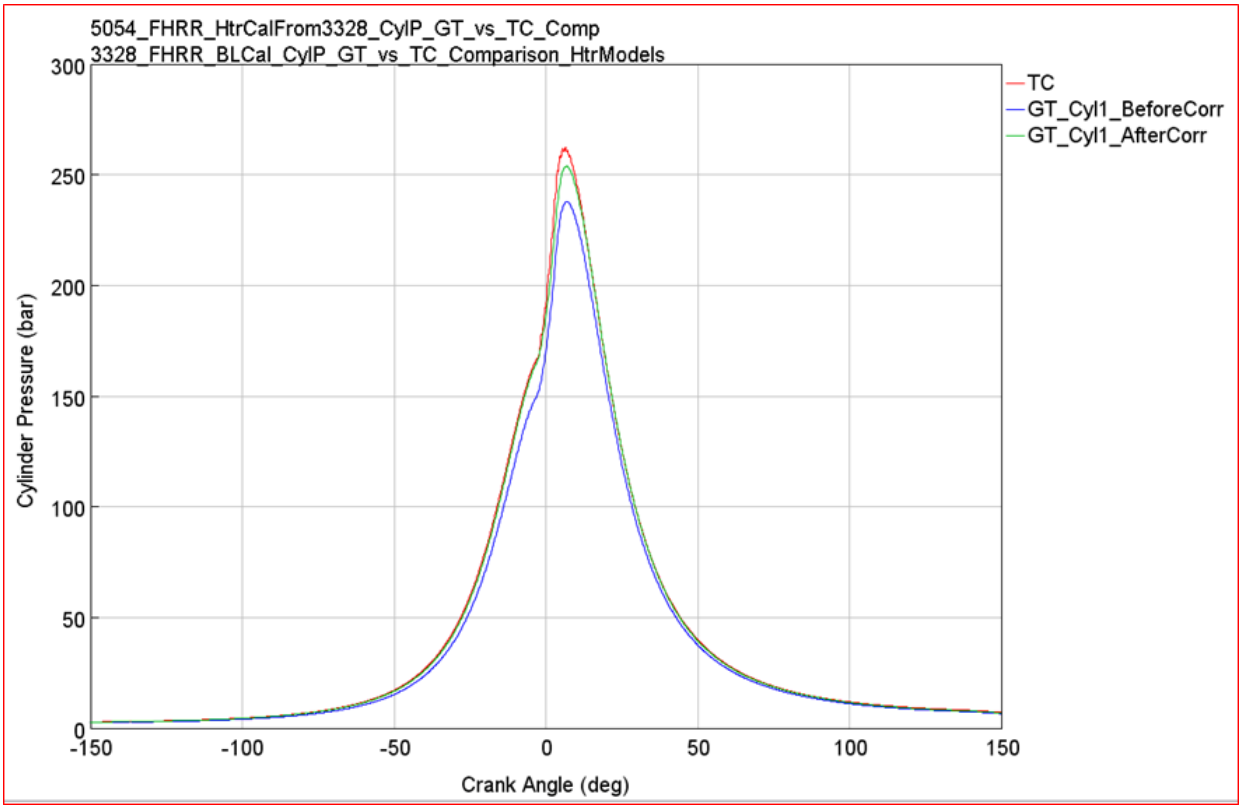

Figure 165 : Cylinder pressure trace comparison of predicted vs test data with efficiency correction

Figure 165 clearly shows what the simple turbine efficiency correction did to the cylinder pressure prediction. It essentially transferred more power to the compressor by increasing the turbo speed and in turn compressor increasing the air flow. With that the compression line matches lot better and the overall matching of cylinder pressure trace is acceptable. This also helped give more credence to the on-engine turbine efficiency is actually true.

The energy balance, heat transfer distribution, and further calibration details are shown in the following Figure 165, Figure 166, Figure 167, Figure 168, and Figure 162. They essentially show that it's a decent calibration for the model and hence can be used for any further modeling exercises as a baseline model.

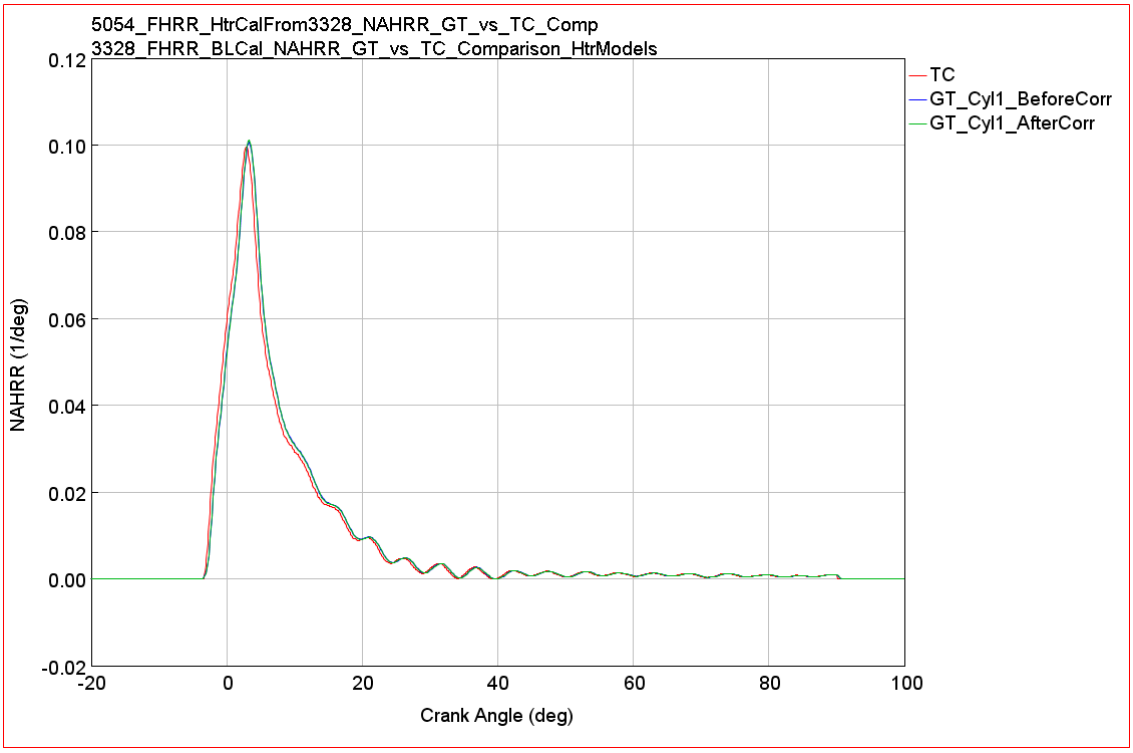

Figure 166 : NAHRR comparison of predicted vs. test data (it's FHRR model so good match expected)

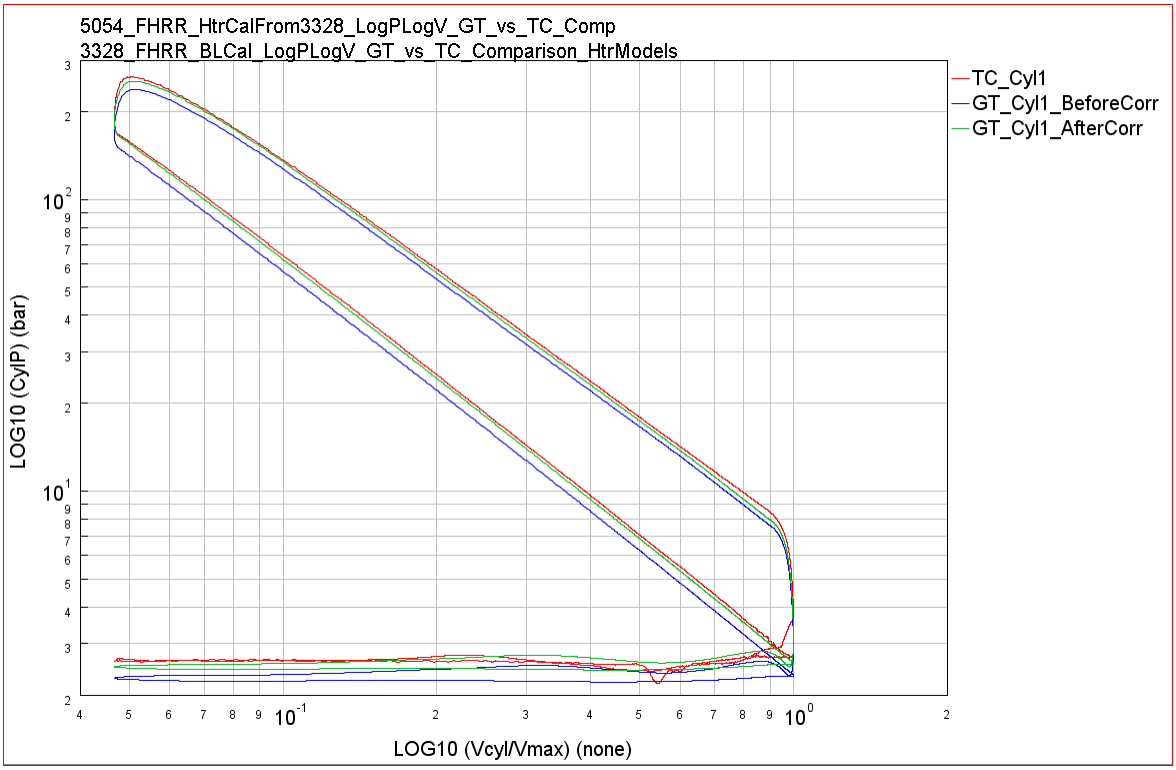

Figure 167 : Log P/Log V comparison (clearly shows the effect of boost pressure on compression stroke)

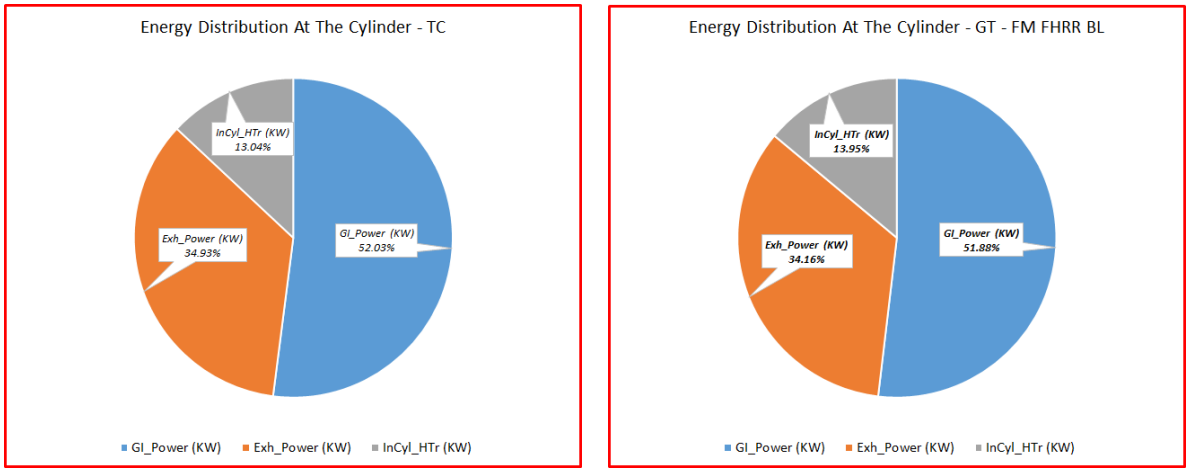

Figure 168 : Energy balance at the cylinder comparison – test data vs. model

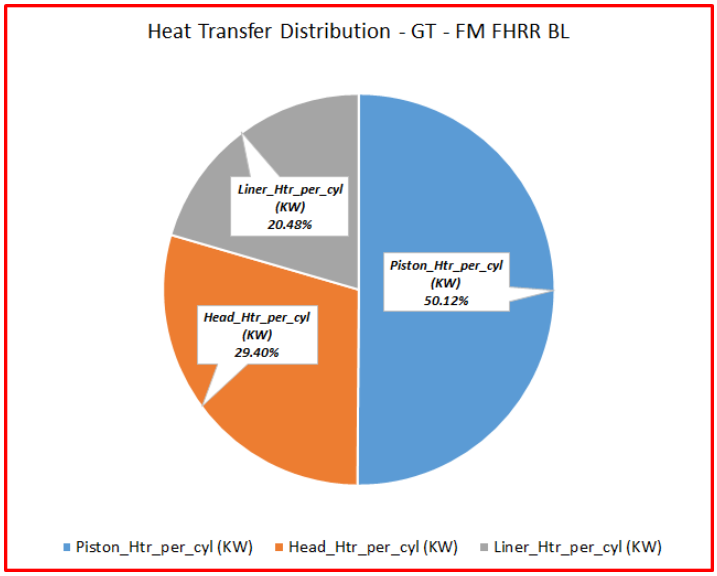

Figure 169 : Heat transfer distribution at the cylinder (reasonable from prior expectations – CFD studies)

Comparison of exhaust pressure signatures

At this point, attention was focused on to look at the exhaust pressure pulses – to check whether there is a good agreement between the test data and prediction.

Figure 163 shows the exhaust pulse comparison of test data against the model prediction. While the phasing looks good, the peak/shape/magnitude of exhaust pressure signal deviates considerably from the test data. For example, on the front (from cylinders 1-2-3), after the initial blowdown (the high peak), the model predicts two smaller peaks. Typically, only a single smaller peak is expected as shown in the test data (as the piston is still moving up to TDC, with the exhaust valve still open, a slight push on pressure is expected).

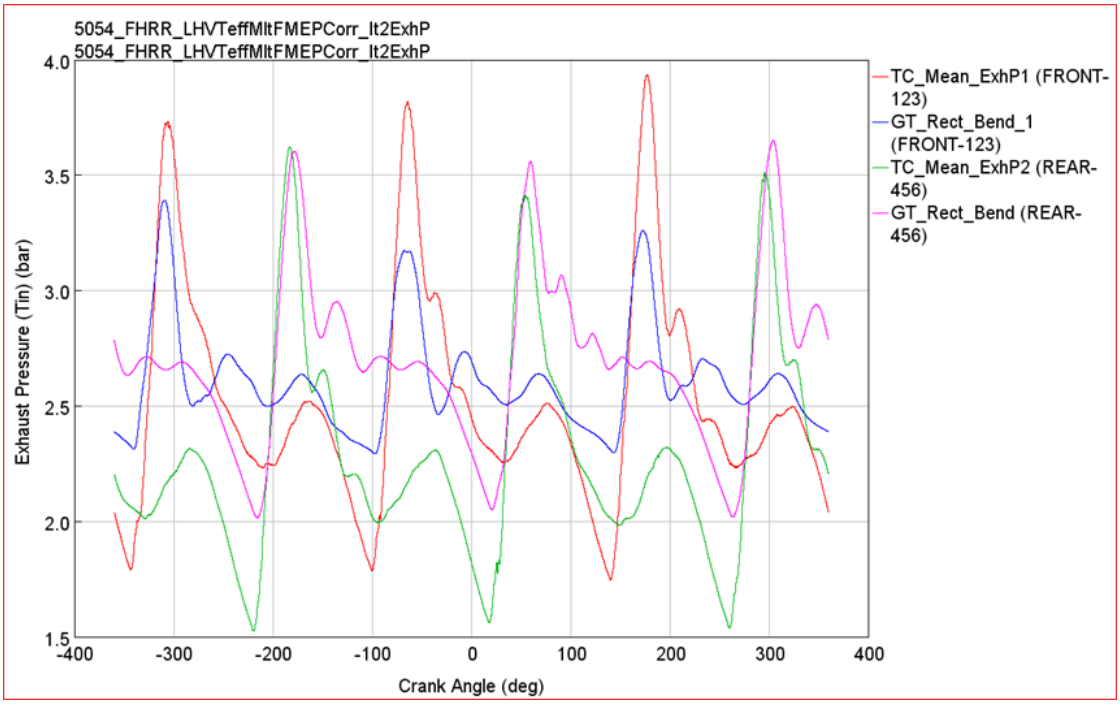

Figure 170 : Exhaust pressure (tur_in_p) pulse comparison

This was the focus for troubleshooting in the rest of the program, as is considered important, especially for other programs. It's the pulsation energy that determines the deviation of turbine efficiency on-engine compared to even the maps generated on experimental flow bench (mainly because the flow is kept steady). Hence, it's considered worth the effort to continue to resolve this issue. The path taken for this resolution is to model the turbine through 3-map method. However, it didn't seem to have fixed the pulsation matching (the realization was that the 3-map method will only give incremental improvement for models, but not a radical fix). These details, however, are not discussed in this report.

3.4 Advanced Controls Development

The controls system development for the project is to demonstrate robust flow measurements and Air-Handling (A/H) controls system integration. Various prototype sensors and virtual sensing technique were evaluated. One of robust flow measurement methods was integrated with the closed-loop controls system. Various controls system techniques were also evaluated.

Controls System Integration

Figure 171 illustrates overall controls system diagram. It includes newly-added actuators and sensors, Waste Heat Recovery (WHR) controls system components, and After-Treatment (A/T) components connected to the central controls system module integrated using the dSPACE system. Smart components with J1939 CAN-based communication protocol are connected to total of seven network channels for robust network communication. Each of network channels are managed to avoid heavy communication busloads.

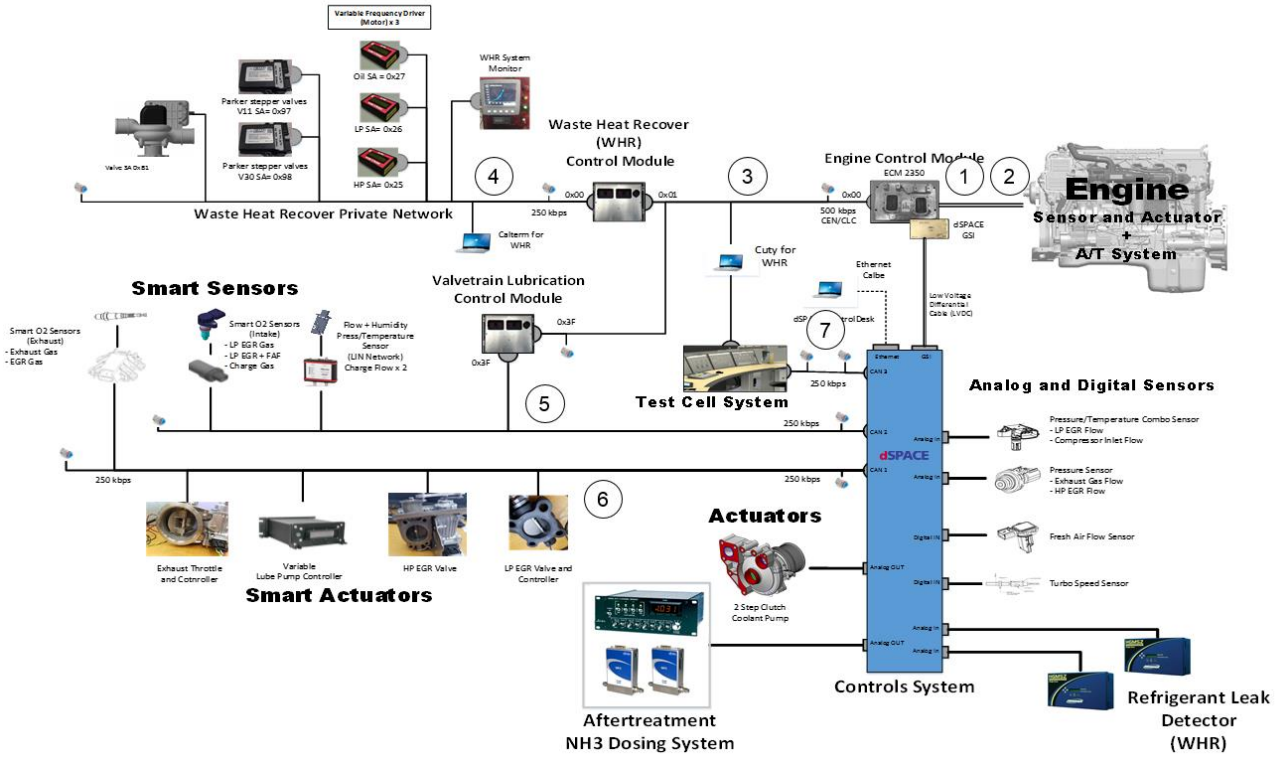

Figure 171: Controls System Integration with J1939 CAN Networks – 1 & 2: Engine Public/Private Network, 3: Engine Private Network #2, 4: WHR Private Network, 5: dSPACE Sensor Network, 6: dSPACE Actuator Network, and 7: dSPACE Private Network

Air Handling Controls System Integration

Simulation study is performed using the data collected from the engine. Low Pressure (LP) EGR flow and charge flow measurements are collected while Exhaust Throttle (ET) and LP-EGR valve are actuated. Mathematically estimated models are used for simulation study with various closed-loop control architecture using a Proportional and Integral (PI) control algorithm;

Single-Input and Single-Output (SISO): The LP EGR valve actuator is controlled only by the feedback error between the LP EGR flow reference and its measurement. The exhaust throttle is similarly controlled only by the error between the charge flow reference and its measurement. It is the simplest form; however, the controller has slower response to the coupling dynamics.

Single-Input and Single-Output (SISO) with system decoupling: System decoupling technique is applied to the SISO control architecture. Singular Value Decomposition (SVD) technique decouples the system architecture so that the SISO controls architecture can achieve the improved response with respect to the coupled dynamic response, which is not considered in SISO controls architecture.

Multiple-Input and Multiple-Output (MIMO): PI closed-loop controls are applied to every input and output combinations. For LP-EGR flow and charge flow control using an LP-EGR valve and an exhaust throttle, Two-Input and Two-Output (TITO) PI-control system are implemented. In this case, four pairs of P- and I-gain are to be calibrated, while two pairs of gains are to be calibrated for SISO controls architecture.

Figure 172 shows the simulation results with respect to step reference changes. When coupling dynamics are not considered (SISO PI-Control case in figure), the larger coupling response and the slower control response are observed --- Charge flow coupling response by the LP EGR flow control with respect to the LP EGR flow reference change is observed at around 50 second mark (See the bottom plot in Figure 172), and LP EGR flow coupling response by the exhaust throttle is observed at around 100 second mark (See the upper plot in Figure 172). Such coupling dynamics are reduced with system decoupling technique, and further reduced with MIMO PI-control technique.

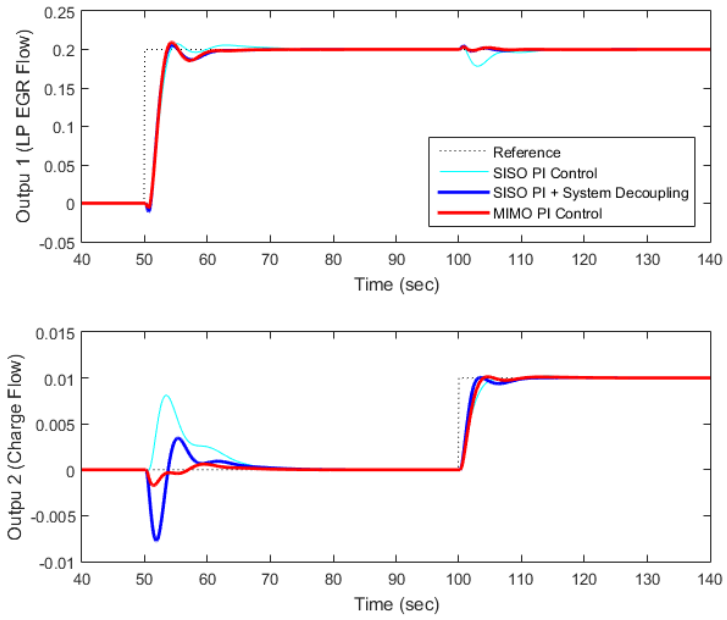

Figure 172: Simulation Results with Different Closed-Loop Control Architectures

Virtual Sensor Development

A virtual sensor is developed for the Low-Pressure (LP) EGR flow. Several different prototype EGR flow sensors and computation methods are evaluated. And it is selected to compute the flow using oxygen sensors. The virtual sensor for LP-EGR flow is calibrated using test cell measurements at steady state and it is validated in transient. Figure 173 shows the calibrated LP-EGR flow with respect to the random LP-EGR valve position. The virtual sensor has good response with respect to the valve position.

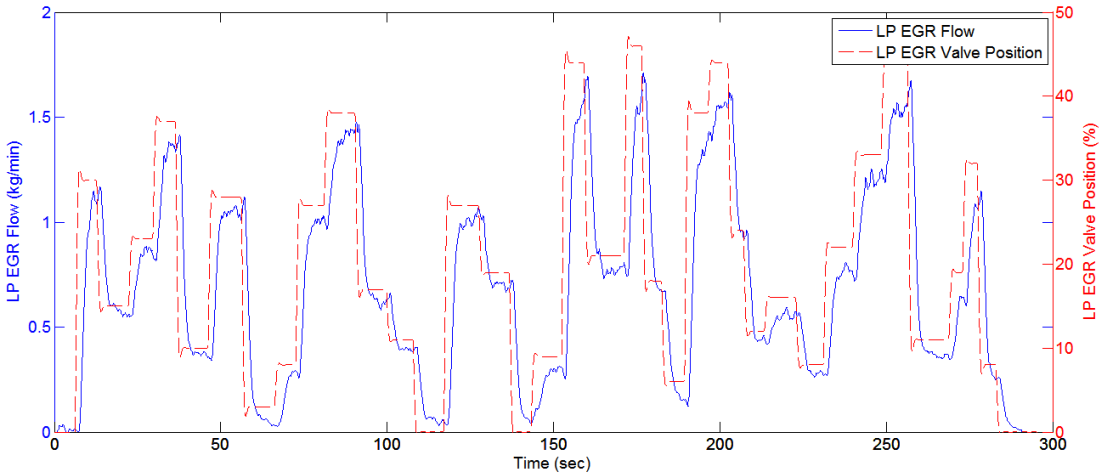

Figure 173: LP EGR Flow Virtual Sensor Response with respect to Random LP EGR Valve Position

Figure 174 shows the calibrated LP EGR flow response with respect the step valve position change from 10% to 50% openings. The LP EGR flow measurement is compared to the Test Cell measurement which is used for engine performance analysis. As seen in the figure, the Oxygen-based measurement responds fast enough to be used for controls.

Closed-loop PI-control technique was applied for LP EGR flow control. Figure 175 shows controls responses of reference, flow measurement, valve position, and feedback error. In the flow response plot, the flow measurements are also compared to the Test Cell flow measurements.

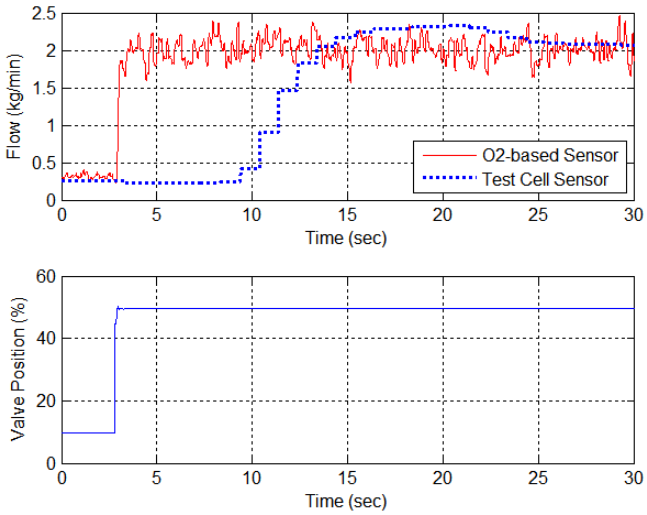

Figure 174: Oxygen-based flow measurement response (Top) to the step LP EGR valve position changes (Bottom)

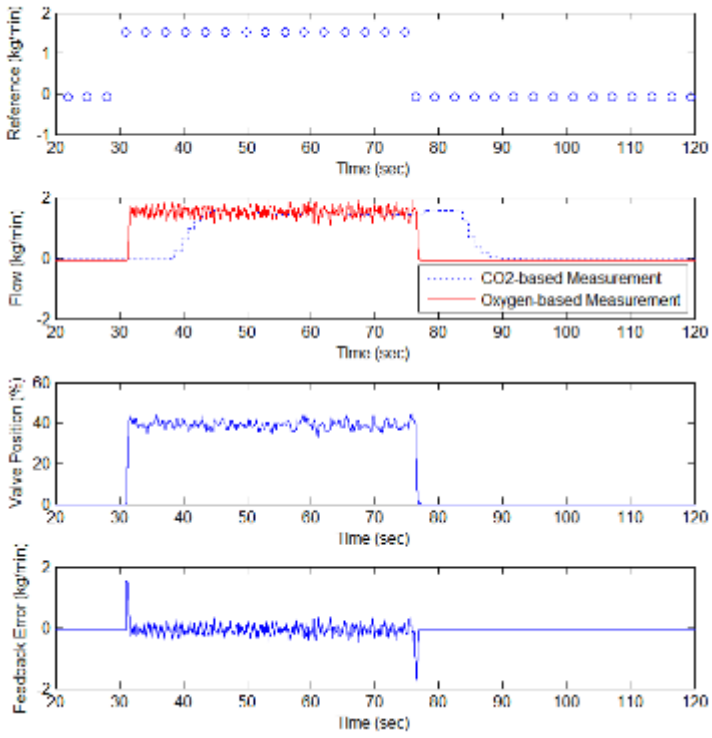

Figure 175: Closed-Loop Control Step Response: Reference Flow (Top), Flow Measurements, Valve Position, and Feedback Error Response (Bottom)

Multiple Single-Input and Single-Output (SISO) Proportional and Integral (PI) control algorithm is implemented for LP-EGR flow and charge flow control using LP-EGR valve and Exhaust Throttle (ET), respectively. The developed virtual LP-EGR flow sensor is sued for LP-EGR flow measurements and the charge flow information is updated from Engine Control Module.

First demonstration is to control LP EGR flow while the charge flow reference is controlled to be fixed. Figure 176(a) shows the charge flow response and the exhaust throttle valve position and Figure 176(b) shows the LP-EGR flow response and the LP-EGR valve position. As seen in Figures, exhaust throttle is to be controlled to move from ~80% to ~90% while the LP-EGR flow reference changes.

Second demonstration is to control charge flow while the LP-EGR flow is controlled to be fixed. Small reference changes in charge flow in the demonstration is to avoid the exhaust throttle position saturation. Figure 177 (a) and (b) show the charge flow response with the exhaust throttle response and the LP-EGR flow response with the LP-EGR valve response, respectively.

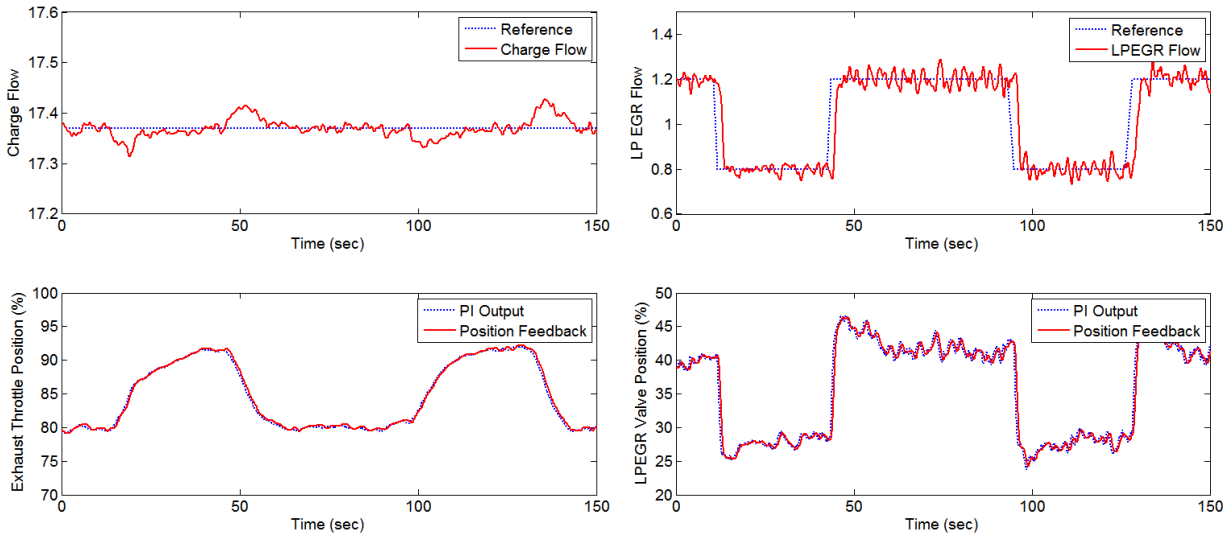

(a) Charge Flow Control (b) LP-EGR Flow Control

Figure 176: Closed-Loop Response with LP-EGR Flow Reference Changes: (a) Charge Flow Response with Exhaust Throttle Valve Position, (b) LP-EGR Flow Response with LP-EGR Valve Position

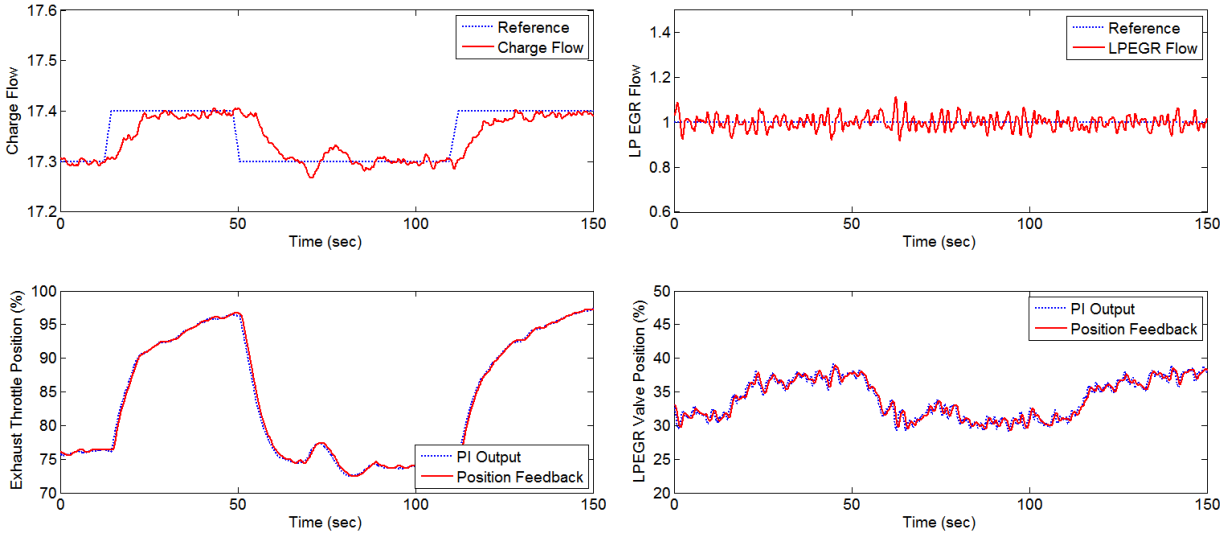

(a) Charge Flow Control (b) LP-EGR Flow Control

Figure 177: Closed-Loop Response with Charge Flow Reference Changes: (a) Charge Flow Response with Exhaust Throttle Valve Position, (b) LP-EGR Flow Response with LP-EGR Valve Position

3.5 Engine Friction Reduction Testing

Engine Friction Reduction Path

Figure 178 shows the breakup of engine systems into sub systems that were the prime focus for friction reduction efforts.

Starting with the coolant and lube system, which form the accessory loads on the engine, these can be considerably reduced especially at part engine loads. Fixed flow pumps for both lube and coolant are utilized on current engines which consume the same amount of power at part load conditions. The approach here is

to integrate variable flow pumps in the current engine architecture to achieve lower flows part load engine conditions without greatly affecting pump efficiencies and engine durability.

Figure 178: Areas to explore to reduce engine friction

The valve train parasitic was an area not explored during SuperTruck. Changes to the valve train for lower friction contribution were explored included weight reduction, reduced spring preload, and reduced spring rates. Also explored were rollerized camshafts and roller bearings at other interfaces.

Power cylinder friction is known to be the highest contributor to engine friction and focus here was to reduce the ring friction by use of coatings, smaller cross sections, and lower ring tensions. Various liner coatings were also investigated for frictional benefits. Liner and block designs were also considered for reduction of bore distortion which thereby enabled the lower tension rings.

Variable Flow Lube Pump

Figure 179 and Figure 180 show the Concentric variable flow lube pump developed for this program. The gear pump is designed to have the flow capability of the 2017 ISX 450 HP and is solenoid controlled that allows for control of flows and pressures feeding the gallery. The pump is controlled by use of a solenoid valve where the solenoid controls the center distance of the gears to control the gallery pressure.

Figure 179: Concentric Variable flow lube pump

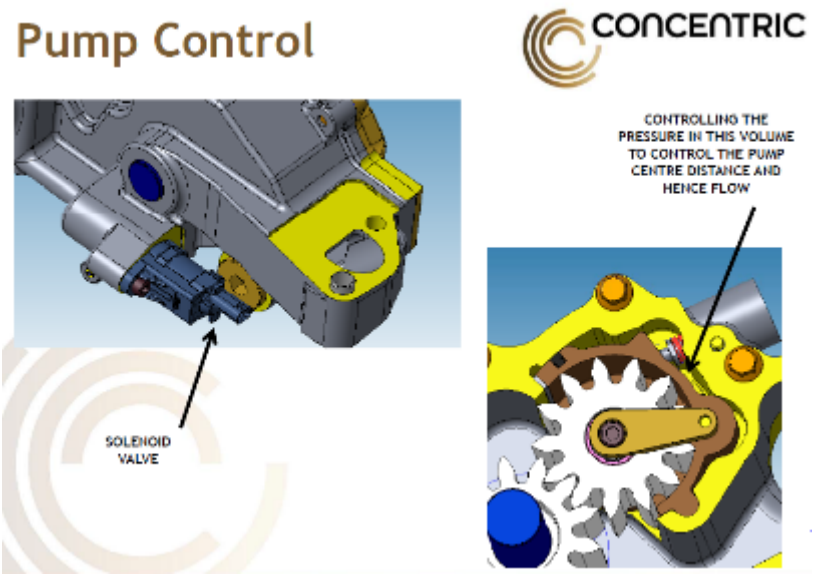

Figure 180: Concentric variable flow lube pump controls

The lube pump and lube system development were an important task when working on engine parasitic reduction. Key factors that aid in reducing power consumption from lube system are:

- Reduced flow requirements for lube system
- Reducing pressure drop across the system
- High pump efficiencies over entire range of operation

The flow requirement from lube pump was significantly reduced from 40 gpm at 1200 RPM needed for the current product to 28 gpm at 1200 RPM. The on-engine performance results are shared in the Engine Testing section.

Two Speed Water Pump

The two-speed water pump uses a clutch for flow control between full flow and low flow (caused due to slip condition). The savings achieved from the variable flow pumps can be useful in reducing power consumption at a design point as well as over a duty cycle. A magnetic clutch is integrated to control the flow mode. When the clutch is fully engaged the pump flows like the current fixed flow water pump would, but when the clutch is disengaged the pump provides considerably less flow than typical flow requirements and therefore consumes less power to run. At the design point for 55% BTE, with the water pump at 50% flow conditions, it was estimated to save 0.7 hp. On-engine performance is shared in the Engine Testing section.

Cylinder Head and Valve Train FMEP

The torque required to drive the baseline camshaft in an ISX 15L cylinder head was quantified on the motored engine rig and the friction mean effective pressure (FMEP) was calculated. Figure 181 shows the baseline cylinder head on the 75hp rig.

In addition to the baseline ISX 15L cylinder head and valve train, a camshaft and valve train with roller bearings and reduced stiffness springs was also tested. The details of this valve train design are documented in the Design section. One of the key benefits of the roller bearing valve train is that it enables less oil flow to the overhead, thus the parasitic losses from the lube pump are reduced. To understand the potential efficiency gains from reduced oil flow to the overhead, the amount of oil flow to the baseline cylinder head must be known. The lube system schematic with the flow meter for the rig test is displayed in Figure 182. Finally, a Polytec laser Doppler vibrometer (LDV) was setup to measure the valve train dynamics (see Figure 183) since the valve spring stiffness has been drastically reduced compared to the baseline springs. The valve head's displacement and velocity were output from the LDV and acquired in the cam angle domain.

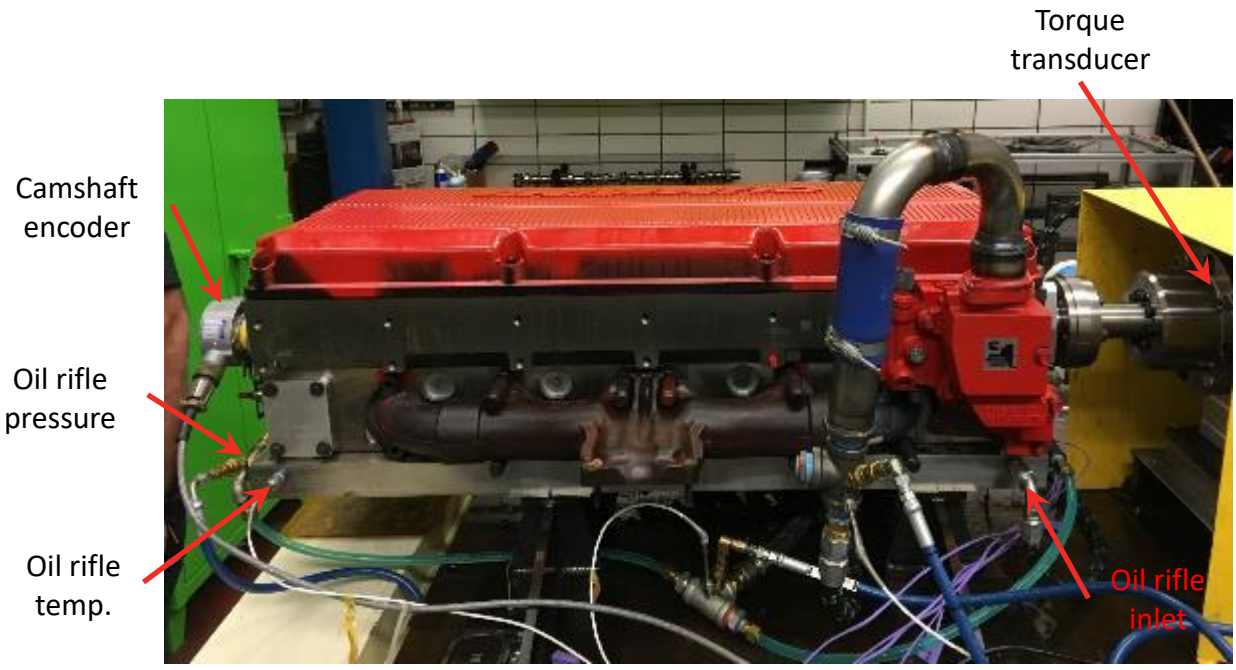

Figure 181: The baseline 2017 ISX 15L cylinder head on the 75hp rig at the Mechanical Efficiency Lab.

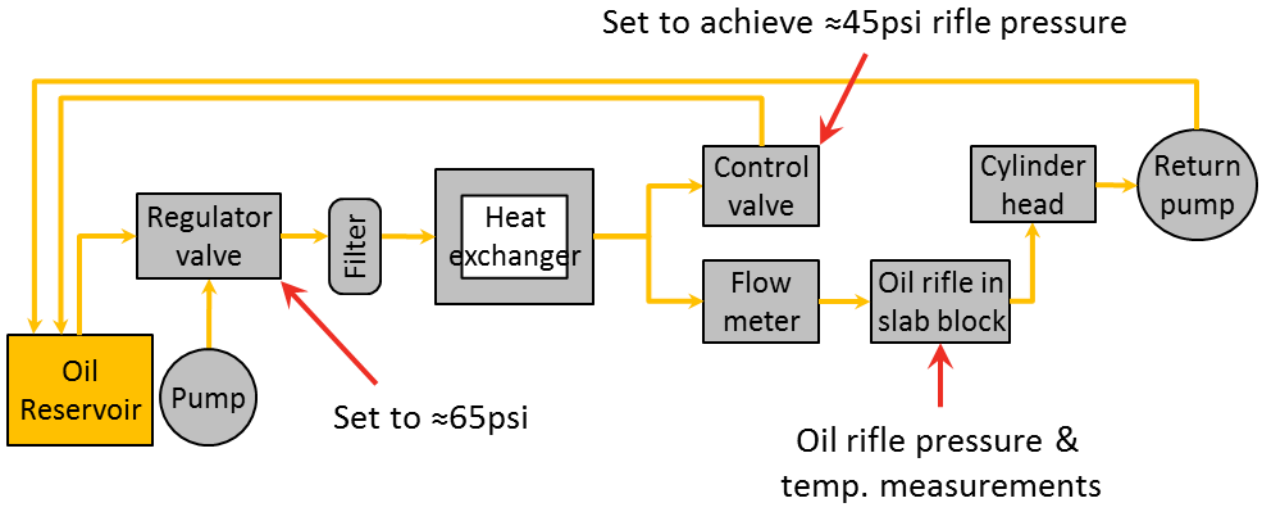

Figure 182: A schematic of the lubrication system with the Coriolis flow meter on the 75hp rig at the Mechanical Efficiency Lab.

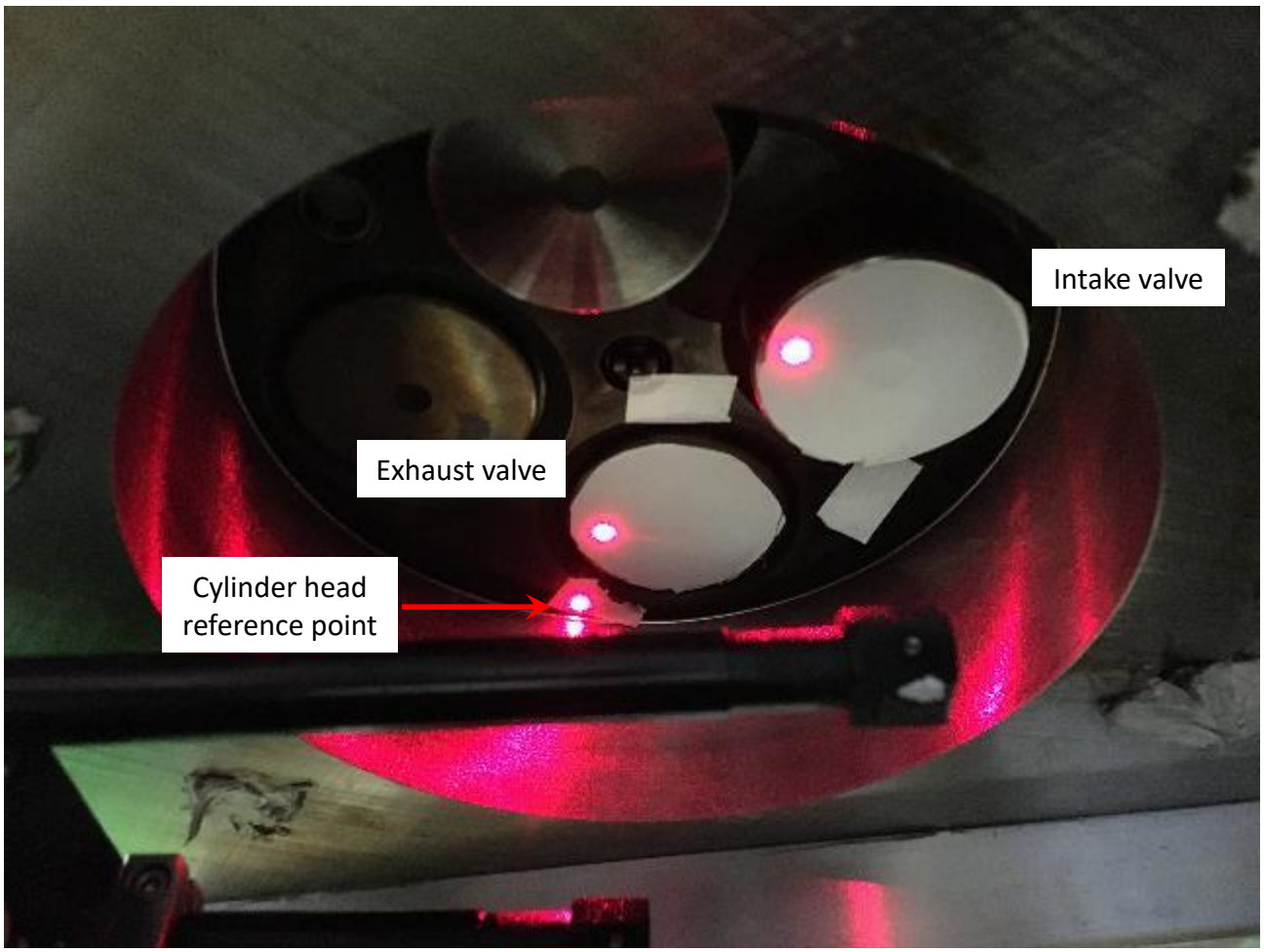

Figure 183: A view of the combustion face of the cylinder head. The red dots are the measurement points using the Polytec laser Doppler vibrometer (LDV) for the valve train dynamics studies.

The friction differences between the roller bearing valve train and the baseline cylinder head are displayed in Figure 184 and Figure 185. The largest difference of 0.43 kW or 13.5 Nm was observed at low

speeds and high oil temperature. This is likely because the journal bearing valve train (i.e. baseline) is operating in the boundary lubrication regime for these conditions while the roller bearing valve train would be in the elastohydrodynamic regime. This friction reduction at low speeds and high oil temperature would prove very beneficial if there were frequent start-stop events in the application's duty cycle. At 500 cam rpm and 108°C oil temperature, the roller bearing valve train requires approximately 4 Nm less torque than the baseline overhead, which equates to 0.2 kW (0.27 hp) less power.

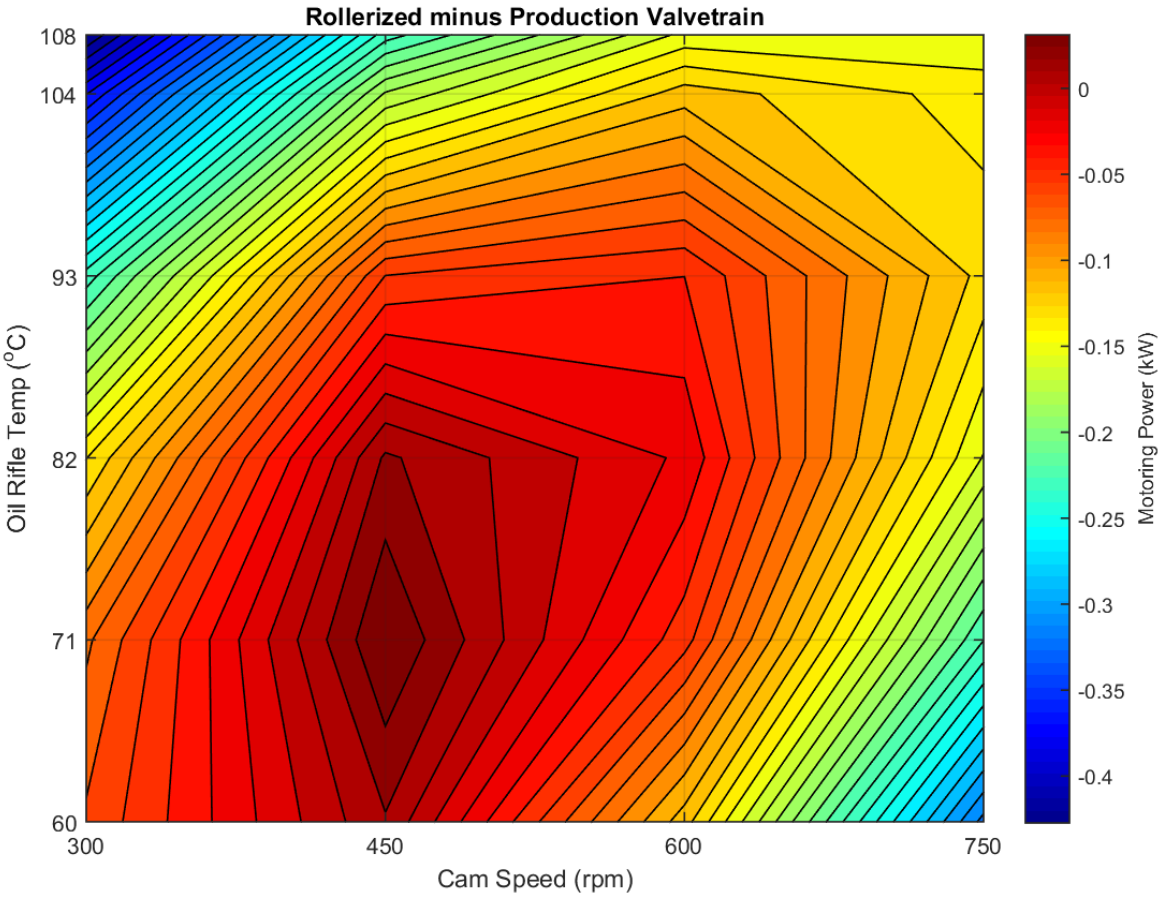

Figure 184: The friction power of the roller bearing valve train minus that of the baseline valve train.

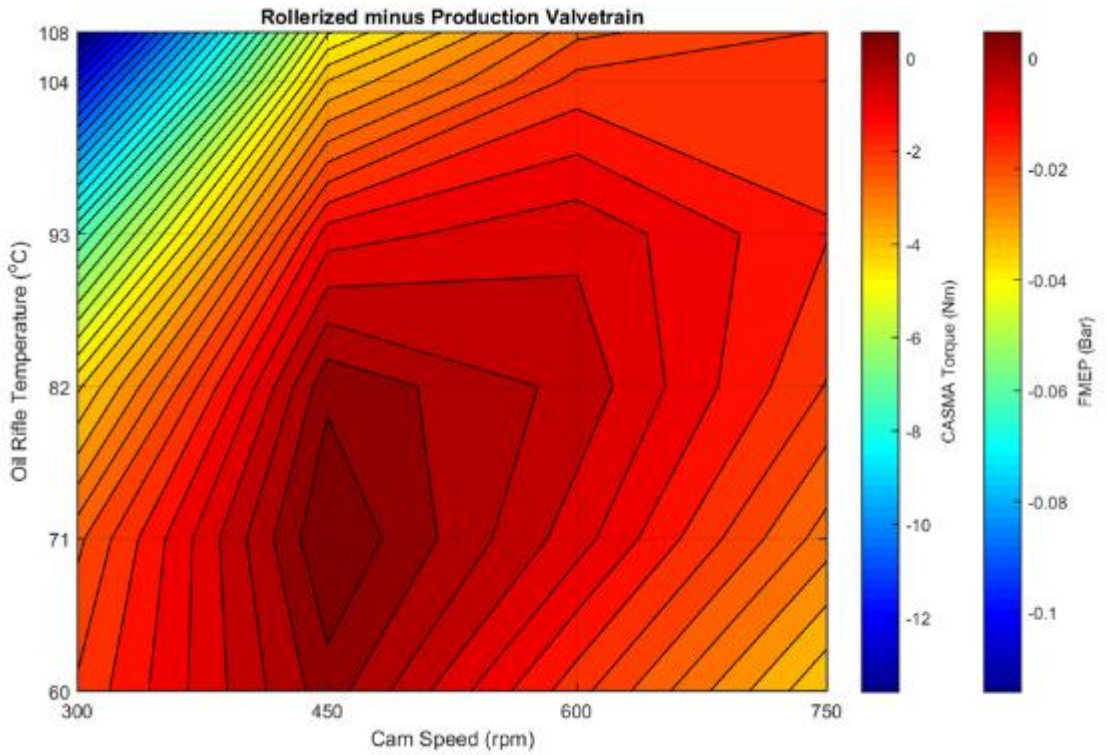

Figure 185: The friction torque/FMEP of the roller bearing valve train minus that of the baseline valve train.

Figure 186 shows the oil flow rate to the baseline cylinder head for a variety of oil temperatures. At 1000 engine RPM and an oil temperature of 108°C, the flow rate to the baseline cylinder head was 6.8 gpm (25.7 L/min). However, the flow rate to the roller bearing valve train via dripping oil from the valve cover was 0.65 gpm (2.46 L/min), resulting in a flow reduction of 6.15 gpm (23.3 L/min). Therefore, the roller bearing valve train is expected to improve the friction and reduce the lube pump parasitic loss compared to the baseline head.

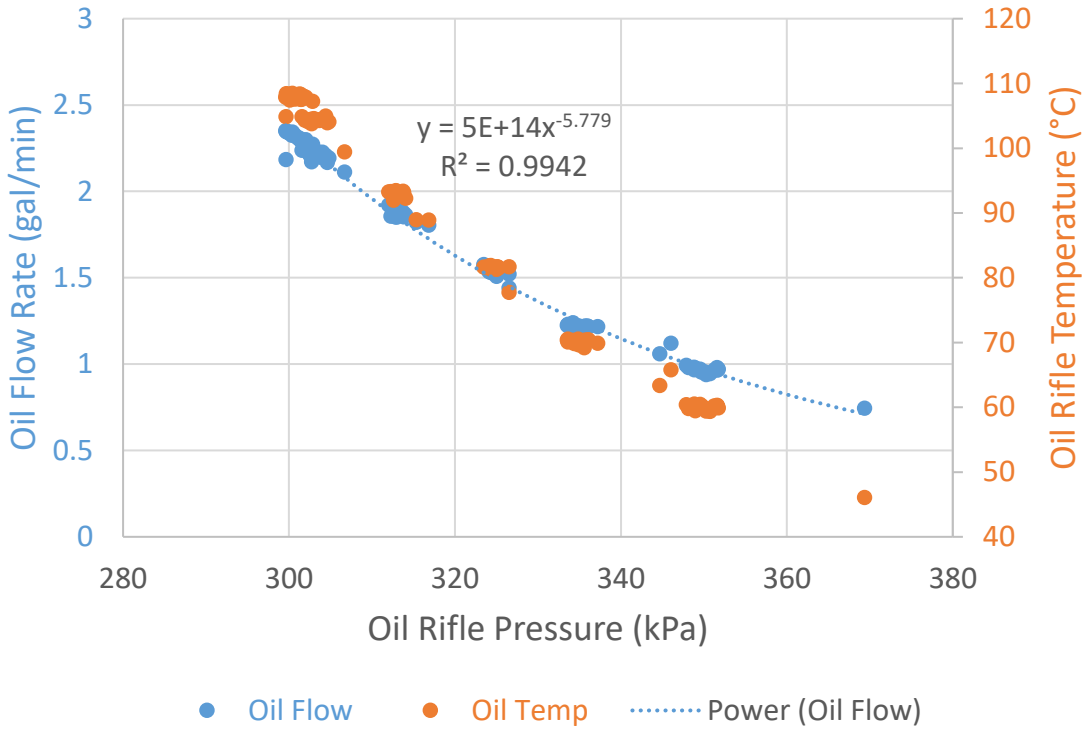

Figure 186: The measured oil flow rate to the baseline cylinder head.

The dynamics of the roller bearing valve train are displayed in Figure 187. The valve displacement data at 300 cam rpm (idle) is provided as a reference for how the lift profile should appear. The red box at peak lift highlights the valve floating (i.e. no follow) event for the 850 cam rpm data. Additionally, the valve velocity is highly erratic and shows signs of bouncing at the peak lift event. The dynamic analysis was estimating the no follow condition should not occur until at least 1300 cam rpm. However, the analysis was conducted to simulate firing conditions on a running engine where the valves must open against in-cylinder gas pressure. When the analysis was performed again to simulate the rig test conditions (i.e. the valves open to ambient air pressure), the no follow condition was estimated to occur between 850 and 900 cam rpm which agrees well with the measured data.

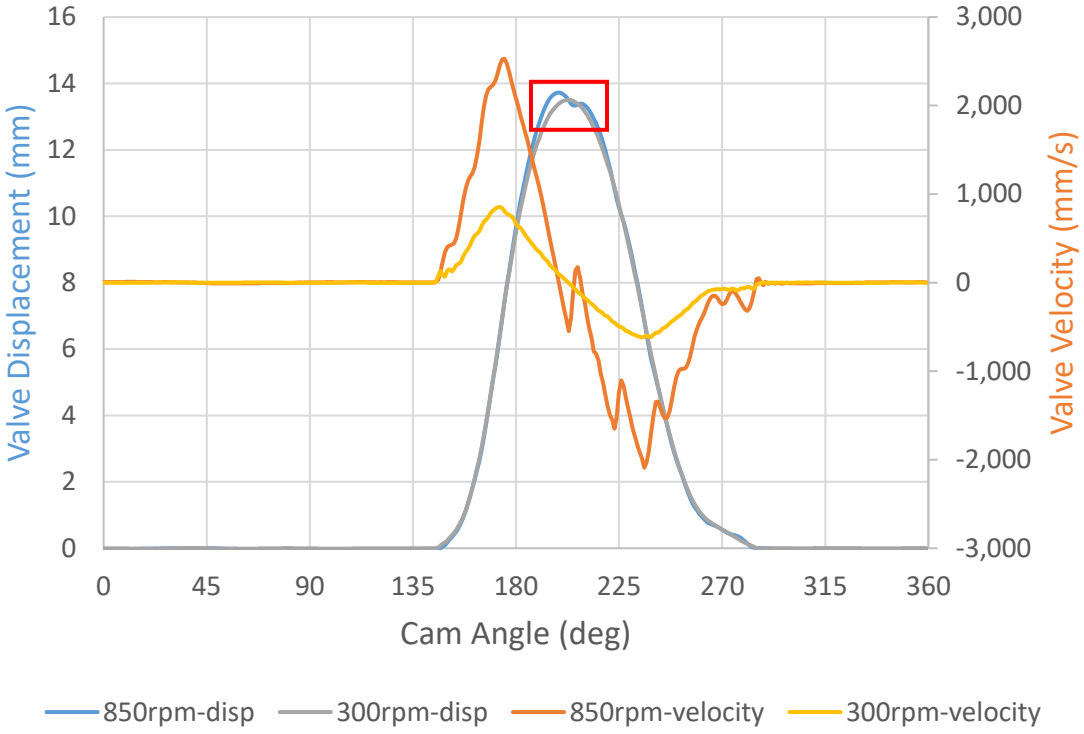

Figure 187: The exhaust valve displacement (left ordinate axis) and velocity (right ordinate axis) for one cycle measured by the Polytec laser Doppler vibrometer at 300 cam rpm and 850 cam rpm. The red box highlights the valve floating (i.e. no follow) event.

Demo Engine FMEP

The key friction reduction technologies that were built into the 50% demo engine are detailed below.

1. Pistons. LHT pistons from supplier A were installed. The main unique features of the pistons compared to the current product pistons were: (1) a thermal barrier coating (TBC) on the crown, (2) compression ratio of 21:1, (3) no oil cooling gallery, and (4) air gaps beneath the bowl rim and crown/pip regions.
2. Piston rings. The sum of tangential tension for all 3 rings is 49 N which is a 40% reduction from the current product ISX15, and the axial height of all rings are on average 33% thinner than current product rings. The top and oil rings have a DuroGlide® (i.e. DLC) coating to improve friction and wear performance.
3. Variable flow lube oil pump. pump can reduce its flow by approximately 45% to decrease parasitic losses. The pump is controlled electronically via the engine control module (ECM) by supplying the target oil rifle pressure.
4. Piston cooling nozzles (PCNs). A PCN that has a check valve integrated into the banjo bolt so that the flow can be turned on or off by controlling oil pressure. The PCNs completely shut off at an oil rifle pressure below roughly 28psi, and are at full flow for rifle pressures above 30psi as demonstrated in the flow test data of **Error! Reference source not found.**. At low engine l oad operating conditions, the pistons require less cooling so the PCNs can be turned off. This

results in drastically less lube pump work since standard PCNs consume about 50% of the engine's total oil flow. The full benefit of these checked PCNs is only realized when used in conjunction with the variable flow lube pump.

5. Oil type. A low viscosity 5W-30 oil, which is a FA-4 formulation, was used to decrease the work required to pump oil thru the engine's circuit.

6. Water pump. A two-speed, single outlet water pump was utilized so that the coolant flow (i.e. parasitic loss) could be reduced at certain engine operating conditions. The pump is actuated by an electromagnetic clutch. When the clutch is engaged, the pump is in full flow mode because the impeller shaft speed is equivalent to the pulley speed. When the clutch is disengaged, the pump is in low flow mode because the impeller shaft can slip relative to the pulley.

7. Crankshaft seals. The front and rear crankshaft seals were replaced with MicroTorq® seals from Federal-Mogul. Testing at 1000-1200 rpm with 105°C oil temperature has shown an FMEP and power reduction of 2.5kPa and 0.34kW, respectively, compared to the current product seals.

Once the buildup of the demo engine was complete, it was motored at the Mechanical Efficiency Lab (MEL) and the friction mean effective pressure (FMEP) was calculated. The engine was operated at steady state conditions over a speed range of 600-2000 rpm and a range of 50-116°C oil rifle temperature. In-cylinder pressure was sampled in the crank angle domain such that the pumping mean effective pressure, PMEP (open cycle work), and gross indicated mean effective pressure, GIMEP (closed cycle work), could be subtracted from the motoring torque to yield the friction torque and hence FMEP. A crank angle sampled moving average (CASMA) filter was applied to the torque data.

To assess the impact of turning PCNs on or off, the test was conducted when oil rifle pressure (ORP) was set to 25 psi (172 kPa) and 30 psi (207 kPa). At 1200 rpm and 110°C oil temperature, changing ORP from 30 psi to 25 psi decreased power by 0.32 kW and FMEP by 2.2 kPa – a reduction of roughly 5%. However, it is important to note that even though the ORP was set to 25 psi there were significant portions of the speed vs. oil temperature map where it was not achieved due to limitations of the variable flow pump. This was particularly problematic in the low speed, high oil temperature region (i.e. pump could not build enough pressure) and the high speed, low oil temperature region (i.e. pump could not drop pressure enough). However, the 25-30psi ORP range was able to be realized at points that are representative of cruise conditions (e.g. 1000-1200rpm and 100-115°C oil temperature).

The friction and parasitic improvements of the key technologies described above were most significant – 20% torque reduction – under the high speeds, low oil temperature conditions. This can be attributed mainly to differences in the lube pump work. The ORP at high speeds, low oil temperature conditions for the current product engine was roughly 45psi compared to 32psi for the demo engine. At 1000-1200 rpm and 110°C oil temperature, the friction power reduction of the demo engine compared to the current product ISX15 was 1-1.6 kW or FMEP reduction of 7.7-10.6 kPa.

Low Heat Transfer Power Cylinder Development

Piston Cooling Nozzles with Check Valves

Bontaz helped to develop checked (check valves incorporated into the nozzle) PCNs. The concept of moving to checked PCNs is to reduce the total oil flow requirements at low engine load points. The PCNs consume approximately half of the pump flow provided to the total engine. With the variable flow lube oil pump technology available, the pump flow can be turned down and in combination with the checked PCNs the oil flow requirements can be reduced up to 40%.

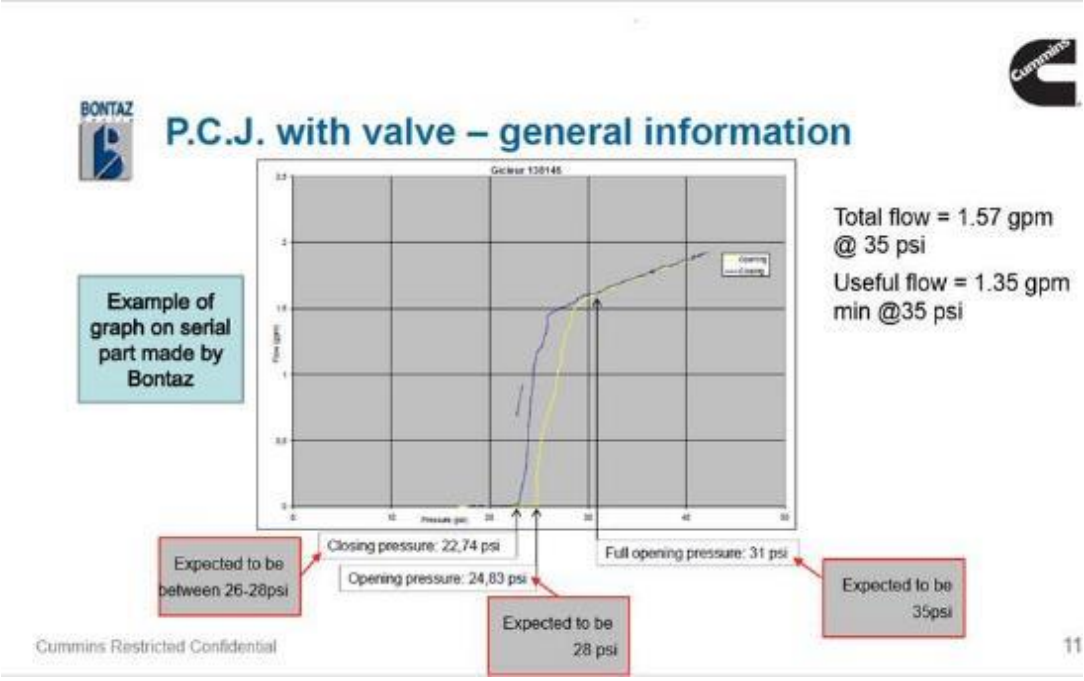

Figure 188: Desired PCN Specifications Provided to Supplier

The PCNs are designed to shut off below a gallery pressure of 28 psi. Above 26 psi, the valves begin to open and let oil flow to the pistons. This functionality of checked PCNs when combined with the variable flow lube oil pump helps to achieve further savings in lube pump work as flow requirements are drastically reduced at low engine load points.

Low Heat Transfer Pistons

The low heat transfer (LHT) piston development was conducted with two separate suppliers. Both suppliers utilized a current product ISX engine to evaluate their concepts.

Piston supplier A completed a templug/thermal paint test, 92-hour cyclic durability test, and a 100-hour steady state durability test. For the templug test, the engine was operated for 4 hours at CP2 (1130 rpm, 1437 Nm). The peak temperatures were 590°C for the piston design 1 and 540°C for piston design 2, which were observed at the bowl edge/rim location. Since the design 2 piston had a thermal barrier coating (TBC) applied to the top surface, the metal temperatures around the bowl rim were on average 59°C cooler than the design 1. This suggests that the TBC was indeed performing as expected – reducing the amount of heat that is transferred through the piston thus raising the exhaust gas temperatures.

In addition to the templug temperatures which are merely sub-surface point measurements, a thermal paint was applied to the top of the piston to provide a full-field temperature distribution of the piston's surface. After the test, the change in luminescence of the thermal paint is non-destructively recorded which is calibrated to the peak operating temperature. The mean, maximum, and minimum temperatures of the design 2 piston's surface were 519°C, 764°C and 383°C, respectively. The maximum temperature on the surface was 224°C hotter than the maximum temperature observed in the templugs. This demonstrates that there is a large temperature gradient from the surface of the TBC to the templug location, which was only

1.9mm below the surface. Work is currently underway by the combustion CFD team to model the design 2 piston and calibrate the analytical predictions to the templug and thermal paint results.

The duration of the initial cyclic durability test was planned to be 100 hours though it ended prematurely – at 92 hours. The test cycle was defined as: (1) low idle (600 rpm), (2) CP2 (1130 rpm, 1437 Nm), (3) BP1 (1000 rpm, 2034 Nm), and (4) peak torque (1400 rpm, 2034 Nm). Each point was held for 10 minutes followed by a 15 second ramp to the next point. After 92 hours, this equates to approximately 135 complete cycles. The test shut down at 92 hours due to high blowby which was discovered to be caused by a hole in the design 1 piston in cylinder #5. The design 1 pistons in cylinders #2 and #5 were oxidized around bowl rim. The design 1 was intended to be able to withstand higher temperatures than steel without requiring a TBC, however, the 400hp peak torque point (1400 rpm, 2034 Nm) was clearly beyond its oxidation limit which is estimated to be 680-700°C. The temperature measurements from the templug test (i.e. 599°C at the sub-surface bowl rim location) suggest that the oxidation limit may be exceeded even at CP2 conditions. The durability test was repeated again, except under steady state conditions at CP2. Indeed, after 100 hours the design 1 piston still showed signs of oxidation around the bowl rim though not as severe as in the cyclic durability test.

After the 92-hour cyclic durability test, the TBC had delaminated on design 2 pistons in cylinders #3 and #6. However, the TBC on these design 2 pistons was applied in a different manner than the pistons which Cummins received. The supplier sent our design 1 pistons to Cummins because they believed the TBC thickness to be more uniform on our samples than theirs. The TBC on the design 2 pistons in cylinders #1 and #4 did not show evidence of delamination after the 92-hour cyclic durability test. Finally, the TBC did not flake off on any of the design 2 pistons after the second 100-hour durability test at CP2.

To explore the degree of non-uniformity in the TBC thickness, the top surface of one HiTherm (revision 4) piston was quantified with a coordinate measuring machine (CMM). The bowl profile measurements were compared to the nominal geometry in the 3D CAD model which did not include the TBC. It is evident that the TBC thickness along the bowl profile is highly non-uniform. The thickest portion of TBC (roughly 0.5-0.6mm) was at the crown/pip and ramp to the bowl. The bowl rim, which is generally the hottest region of the piston, had essentially no TBC (0mm). Federal-Mogul has quoted the TBC as 0.4mm thick, which is true on average, although there is a great deal of variation locally.

Additionally, the TBC surface roughness of one HiTherm piston was measured with a profilometer. The average roughness (Ra) and the average peak to valley roughness (RzDIN) of the design 2 TBC was 8.5 µm and 47 µm, respectively. This Ra value is approximately 30 time higher than a current product piston (no TBC) and 13 times higher than a ceramic TBC studied for the SuperTruck program. The high surface roughness of the design 2 pistons is speculated to be the cause of several adverse engine performance characteristics (e.g. lower peak heat release rate and higher smoke) that were observed at the test cell.

Simultaneous to the work performed at Supplier A, Supplier B has completed a templug test of a design 1 piston without a TBC. Likewise, the templug test was conducted for 4 hours at CP2 (1130 rpm, 1437 Nm). The average bowl rim temperature at the templug locations (1.5mm sub-surface) was 490°C, which is 97°C cooler than Supplier A's design 1 piston and 38°C cooler than the Supplier A's design 2 piston at similar locations. The peak temperature was 547°C for the piston – observed at the center crown location. There is good agreement between the simulation and experimental temperatures, especially since no adjustments were made to the model to enhance the correlation. The bow rim temperatures were predicted to be 19°C higher than the templug data. However, the predicted crown temperature was 23°C cooler than the templug result.

Cylinder Liner Friction

A 2014 ISX 15L long block was used to evaluate and compare the friction of six-cylinder liner variants. The key elements of this long block assembly pertaining to FMEP consisted of the block, head, power cylinder, gear train, valve train, lube pump, and the intake and exhaust manifolds. It was run under motoring conditions and the friction mean effective pressure (FMEP) was calculated. The long block was operated at steady state conditions over a speed range of 600-2000 rpm and a range of 50-116°C oil rifle temperature. In-cylinder pressure was sampled in the crank angle domain such that the pumping mean effective pressure, PMEP (open cycle work), and gross indicated mean effective pressure, GIMEP (closed cycle work), could be subtracted from the motoring torque to yield the friction torque and hence FMEP. A crank angle sampled moving average (CASMA) filter was applied to the torque data.

The six-cylinder liner variants tested were:

1. Baseline ISX15 non-APR liner
2. Liner with a mechanochemical surface treatment from Applied Nano Surface (ANS)
3. Compacted graphite iron (CGI) liner that was “green” (i.e. had not been run-in)
4. Compacted graphite iron (CGI) liner that was had been run-in for approximately 680 hours
5. Liner that was laser honed at the top of bore
6. Liner that has a smoother surface finish, referred to as “GKN smooth”

All the liners had been run-in prior to the testing at MEL except for the ANS liners and the “CGI green” liners. Furthermore, the exact same pistons and rings and a 5W-30 oil were used in all tests.

The lowest friction was measured with the CGI liners that had been run-in for approximately 680 hours on a fired engine. The friction power and friction torque/FMEP of the CGI run-in liners are displayed in Figure 189 and Figure 190, respectively. A comparison of all liners tested at 1000 rpm and 100°C oil is presented in Table 9 and in Figure 191 with the amount of variation quantified between runs. The FMEP decreased by 3.2 kPa (or 0.4 kW of friction power) from a green CGI liner to one that had been run-in. The largest FMEP difference was measured to be 9.8 kPa (or 1.2 kW of friction power) between the CGI run-in and the ANS liners.

The highest friction was measured with the ANS liners. This was a surprising result since these were the smoothest (Rpq = 0.05 μm) of all the liners tested. Thus, this finding highlights that the friction of the power cylinder, specifically the contribution of the liner, is much more multifaceted than simply surface roughness. In an effort to understand the key surface finish parameters, the Pearson correlation coefficient was computed to evaluate if there is a linear relationship (i.e. correlation) between each of the 50 surface finish parameters measured and the FMEP at 1000 rpm, and 100°C oil rifle temperature. The Rvc (valley count), Rk (core roughness), Rvk/k (ratio of Rvk to Rk), and Wq (root mean square waviness) were the most strongly correlated – statistically significant at 95% confidence level. The surface finish parameters that are specified on the current product drawing are given in Table 10 for all the liners.

It is speculated that the CGI liners exhibited the lowest friction for two main reasons. Chiefly, the elastic modulus of CGI is 40-50% higher (i.e. stiffer) than that of cast gray iron which was the material of all the other liners. A stiffer liner will result in less bore distortion once the liner is assembled in the long block. Less bore distortion causes the piston rings to slide more freely up and down the bore rather than yielding local, high wear regions due to the poor cylindricity. The second reason that the CGI liners performed the best is suspected to be because the thermal conductivity of CGI is roughly 30% less than that of cast gray iron. This will reduce the amount of heat transfer to the coolant jacket; thus, raising the temperature of the liner. The higher temperature liner leads to a reduced oil viscosity which lowers the hydrodynamic power losses from shearing the oil. To better understand and verify the fundamental mechanism(s) that is causing the friction improvement with the CGI liners, bore distortion measurements are planned for several different liner materials.

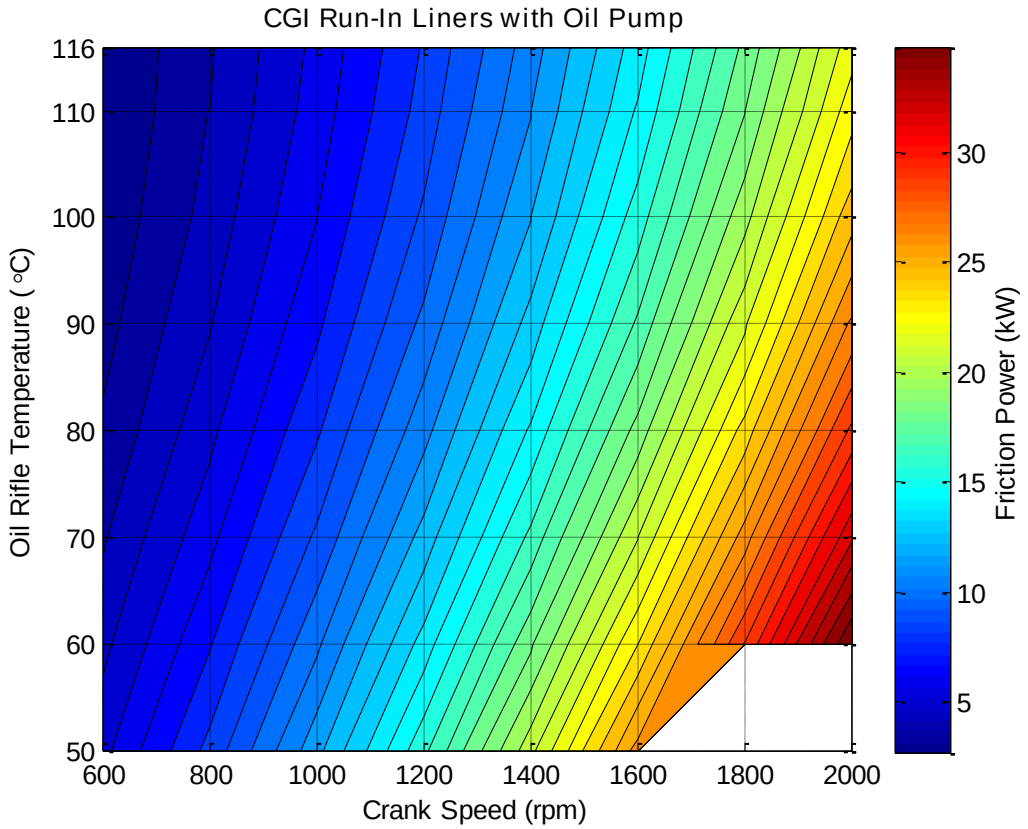

Figure 189: The friction power as a function of engine speed and oil temperature of the CGI liners that had been run-in.

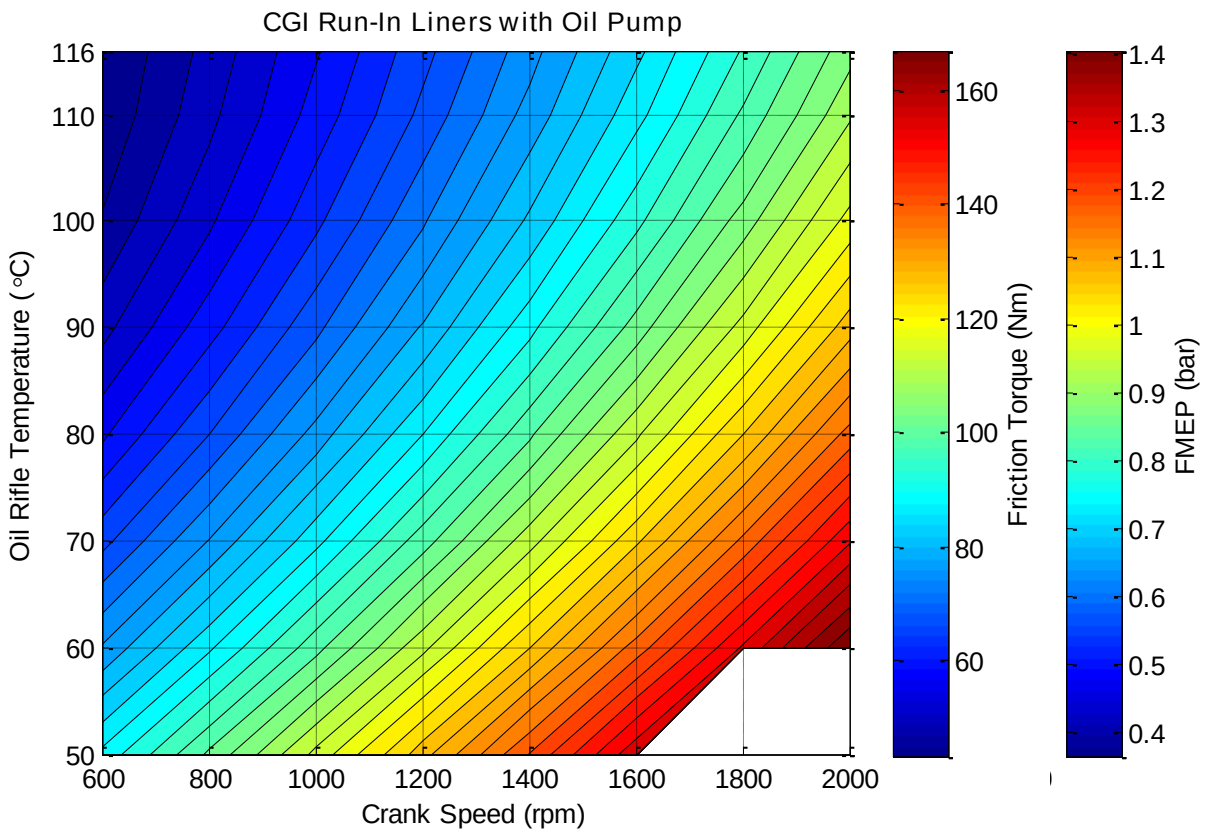

Figure 190: The friction torque/FMEP as a function of engine speed and oil temperature of the CGI liners that had been run-in.

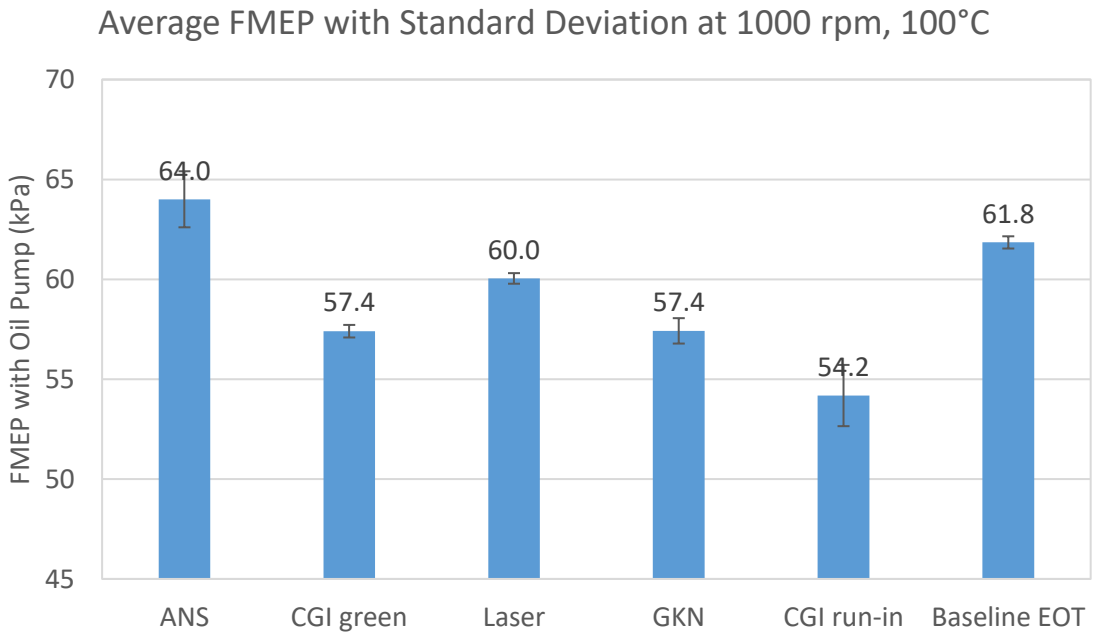

Figure 191: The average FMEP with standard deviation shown as error bars for the several repeat points conducted on each set of liners.

Table 9: The average friction torque, FMEP, and friction power at 1000 rpm and an oil rifle temperature of 100°C for all the liners tested.

Liner	Friction Torque (Nm)	FMEP with Oil Pump (kPa)	Friction Power (kW)
ANS	76.13	64.00	7.97
CGI green	68.28	57.40	7.15
Laser honed	71.42	60.04	7.48
GKN smooth	68.30	57.42	7.15
CGI run-in	64.45	54.18	6.75
Baseline EOT	73.57	61.85	7.70

Table 10: The surface finish parameters specified on the drawings. These measurements were acquired before the liners were run-in.

	From drawing - not measured	Measured values - average of top and bottom of bore			
Parameter	**Baseline**	**ANS**	**CGI green**	**Laser honed**	**GKN smooth**
Rpq (µm)	0.1 - 0.35	0.05	0.19	0.20	0.17
Rvq (µm)	1.3 - 5	2.68	2.70	15.27	2.26
Rmq (%)	75% - 97%	84.5%	94.2%	97.9%	85.2%
Rmr2 (%)	-	70.1%	82.0%	84.2%	78.2%
Rvc (at 3µm depth)	5 - 35	49.83	10.91	19.49	11.26
RzDIN (µm)	3 - 10	4.25	3.00	4.03	4.05
R3z (µm)	-	2.76	1.93	2.33	2.59
Ra (µm)	-	0.29	0.25	0.29	0.31

Since the elastic modulus of CGI is 40-50% higher than that of cast gray iron, it was hypothesized that there should be less bore distortion which may have facilitated lower friction. To better understand and verify the fundamental mechanism(s) that was causing the frictional improvement with the CGI liners, bore distortion measurements were conducted for four different liner materials. The four liner variants were:

1. Current product, baseline liners. Induction hardened standard pearlitic cast gray iron alloy.
2. Compacted graphite iron (CGI) liners.
3. Carbon steel liners.
4. Mk82A liners. Non-induction hardened high strength pearlitic cast gray iron alloy with the same elastic modulus as a bainitic alloy.

The bore distortion of all 6 cylinders was measured using an Incometer. Data was acquired for 18 axial levels, 10mm apart, starting at 15mm below the head deck with 1-degree circumferential resolution around each level. The same block and head were used for all liner tests. After the block and head was assembled, the head bolt preloads were measured ultrasonically and tuned to reduce variation. Additionally, liner protrusion was measured pre- and post-test.

Fourier analysis of bore profile allows one to analyze specific orders of distortion. For an ISX15 engine, the 6^{th} order distortion has been proven to be crucial for many issues, such as oil consumption and blowby, because the high order distortions challenge the conformability of the piston rings. The percent decrease in the 6^{th} order distortions compared to the baseline liners is given in Figure 192. The largest differences were seen at the top of the bore (i.e. 15mm depth) and at liner-to-block seat region (i.e. 125mm depth). The 6^{th} order distortion at the top of the bore was reduced by 23% for the CGI liner compared to the baseline liner. It is speculated that reducing bore distortion at the top of the bore is the most critical area because the piston

rings are likely in the boundary lubrication regime so there will be asperity contact which leads to higher friction. The greatest improvement in bore distortion with the CGI liners was seen for the 6th order. The other orders and the radial distortion traces did not show any substantial reductions which was confounding.

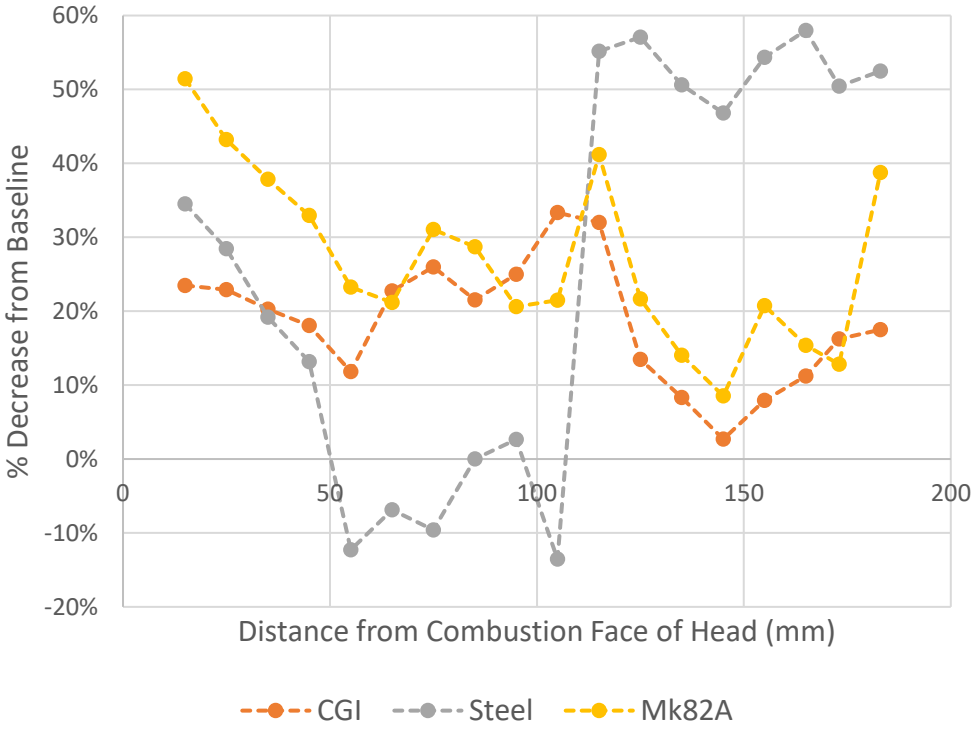

Figure 192: Percent decrease in 6th order distortion compared to the baseline liner.

Low Viscosity Oil

Motored friction and parasitic evaluation of six lubricating oil variants was conducted at the Mechanical Efficiency Lab. The distinguishing factor in these oils was the High Temperature High Shear (HTHS) value which is the dynamic viscosity measured at 150°C. The six oil variants tested were:

1. 15W-40, CK-4 style. HTHS = 4.3 cP
2. 5W-30, CJ-4 style. HTHS = 3.22 cP
3. Lubrizol HTHS = 2.84 cP – SAE viscosity grade 30
4. Lubrizol HTHS = 2.58 cP – SAE viscosity grade 20
5. Lubrizol HTHS = 2.3 cP – SAE viscosity grade 16
6. Lubrizol HTHS = 1.92 cP – SAE viscosity grade 8

One of the tradeoffs of moving to lower viscosity oils, is the risk of increased wear due to metal-to-metal (i.e. asperity) contact because of thinner oil films. This was observed on the overhead components after the tests with the 2.3 cP and 1.92 cP oils. To understand if other (non-visible) tribocouple interfaces were experiencing heavy wear, a full tear down inspection was completed for the engine that was used for the motored friction tests.

The wear patterns in the main and rod bearings shown in Figure 193-Figure 196 were typical of those seen in ISX15 engines. Cavitation erosion on the main and rod bearings was only superficial and therefore not a concern in their current state. There was a deep scratch in main #2 bearing (see Figure 193) but this

was caused by debris likely introduced during the engine assembly and not due to the low HTHS oil. Figure 195 shows the cavitation and pitting around the 6 o'clock position and at the parting line for the lower rod bearings. The wear was not penetrating through the nickel layer of the bearings so it was not classified as a failure.

Figure 193: The lower main bearings after the tests with the low HTHS oils. There is a deep score in the main #2 bearing from debris.

Figure 194: The upper main bearings after the tests with the low HTHS oils.

Figure 195: The lower rod bearings after the tests with the low HTHS oils. Cavitation and pitting can be seen at the 6 o'clock position and at the parting line.

Figure 196: The upper rod bearings after the tests with the low HTHS oils. Cavitation can be seen in a crescent shape around the oil hole. There's also a deep mark on rod #3 breaking from debris.

Even though the main and rod bearings looked acceptable, the wear on the overhead (i.e. valve train) components was more severe. Figure 197 and Figure 198 show the wear at the rocker pivot bearing and the underside of the rocker shaft, respectively.

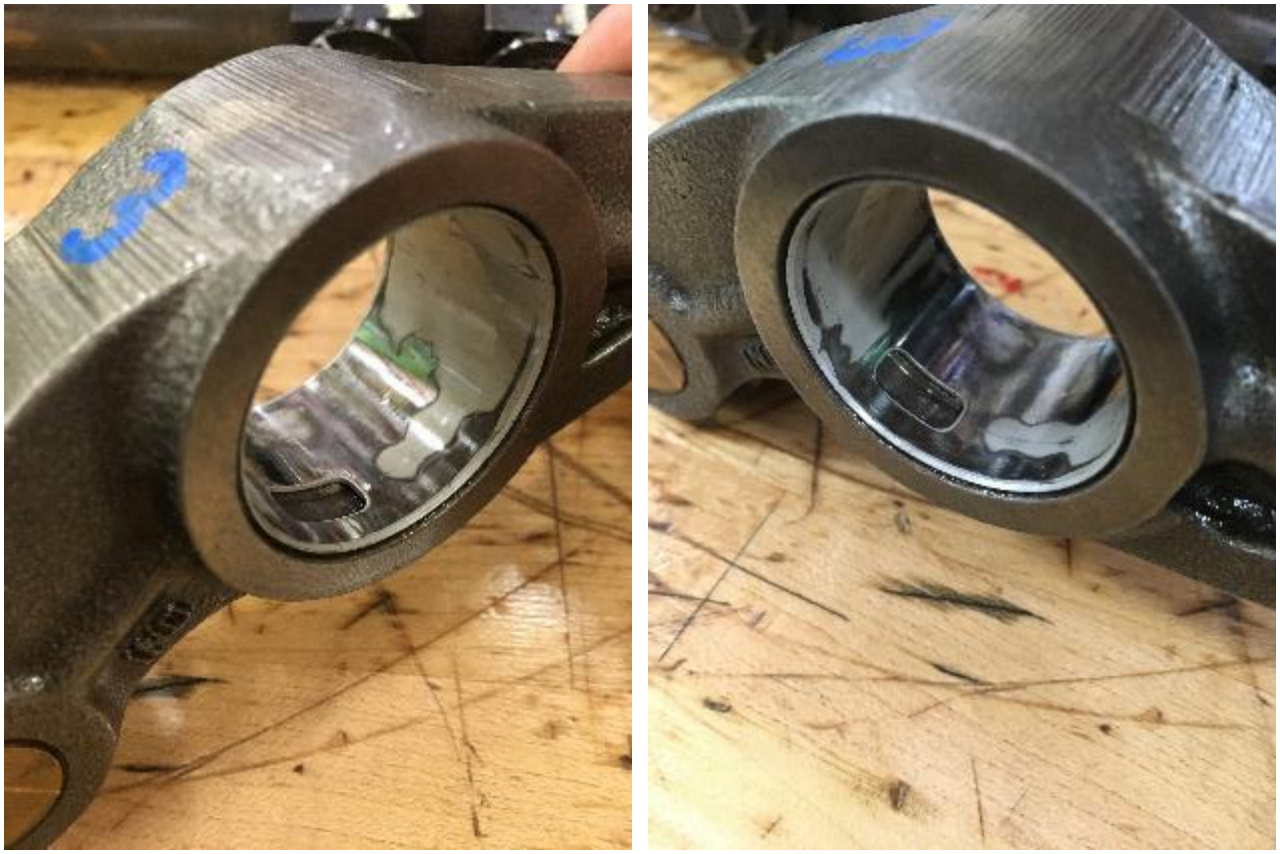

(a) (b)

Figure 197: The exhaust rocker lever of cylinder #1 after the tests with the low HTHS oils seen from an (a) exhaust side view and (b) intake side view.

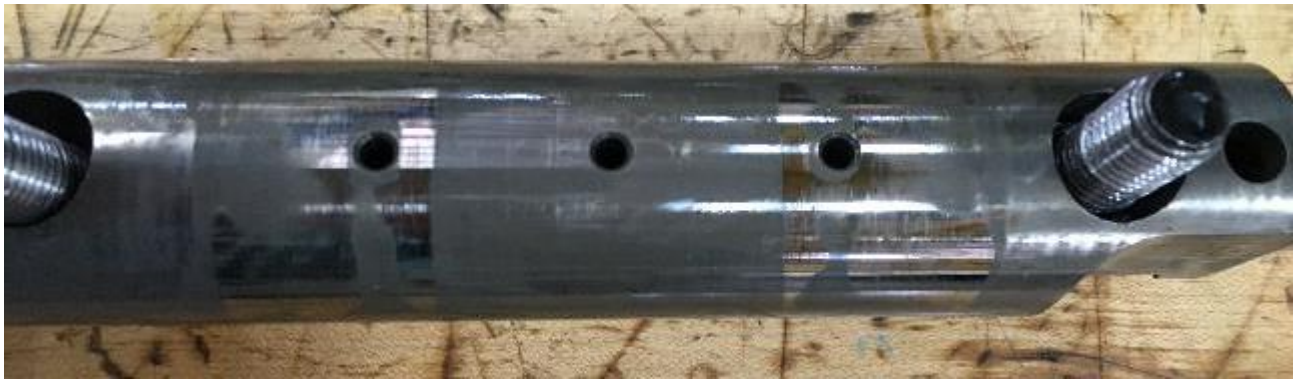

Figure 198: The bottom side of the rocker shaft for cylinder #1.

The motored friction and parasitic evaluation on an ISX15 long block revealed a friction reduction when moving to a lubricating oil with reduced High Temperature High Shear (HTHS) viscosity. However, heavy overhead wear (i.e. cam follower roller) was observed after the tests with 2.3 cP and 1.9 cP oils. Therefore, even though the FMEP for the entire long block decreased with the 1.9 cP oil, the friction of some systems (e.g. valve train) may have increased but their contribution to the overall FMEP is small. A follow-up test was conducted at the Mechanical Efficiency Lab to quantify the motoring friction of the valve train only for two different oils. The two oil variants tested were:

1. 5W-30, FA-4 style. HTHS = 3.1 cP
2. Low HTHS = 1.92 cP – SAE viscosity grade 8

The test article was initially run for approximately 5 hours at 116°C oil rifle temperature and a variety speeds. A “crank only” test was conducted first where the camshaft gear was removed so that the camshaft was not spinning. This allowed the friction contribution of the main bearings, gear train, and lube pump to be subtracted from the long block (without rods and pistons) to isolate the friction of the valve train only. Thus, the valve train friction was obtained by subtracting the crank only torque from the long block (without the rods and pistons) torque. The test was conducted at steady state conditions over a speed range of 600-2000 rpm and a range of 60-116°C oil rifle temperature.

The valve train friction power and friction torque/FMEP difference between the 5W-30 and 1.9 cP oils are displayed in Figure 199 and Figure 200, respectively. As suspected, the valve train friction with the 1.9 cP oil was higher than that with the 5W-30 oil for all speeds and oil temperatures. The largest valve train friction power difference was measured to be 0.3 kW at high speeds and hot oil. At low speed and hot oil temperatures, which is the condition most representative of the boundary lubrication regime, there were no valve train friction differences between the two oils. This is because oil viscosity is not a significant factor to friction in the boundary lubrication regime since it is mostly dominated by metal-to-metal (i.e. asperity) contact.

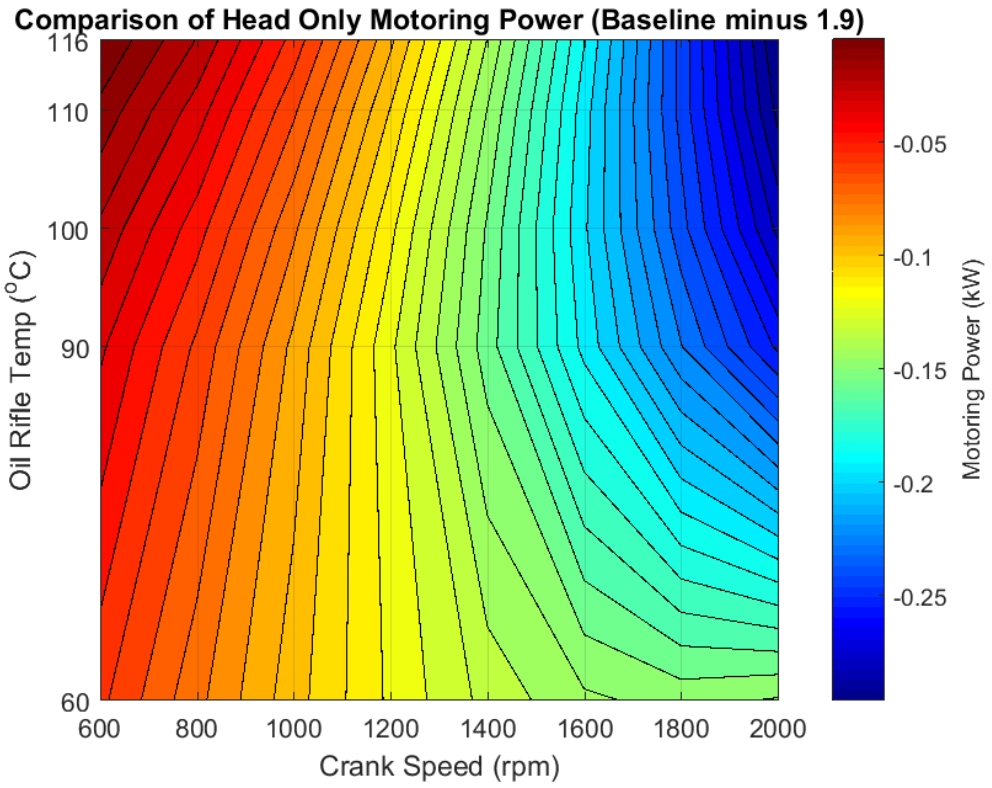

Figure 199: Friction power differences of the valve train only between the 5W-30 and the 1.92 cP HTHS oils as a function of engine speed and oil temperature.

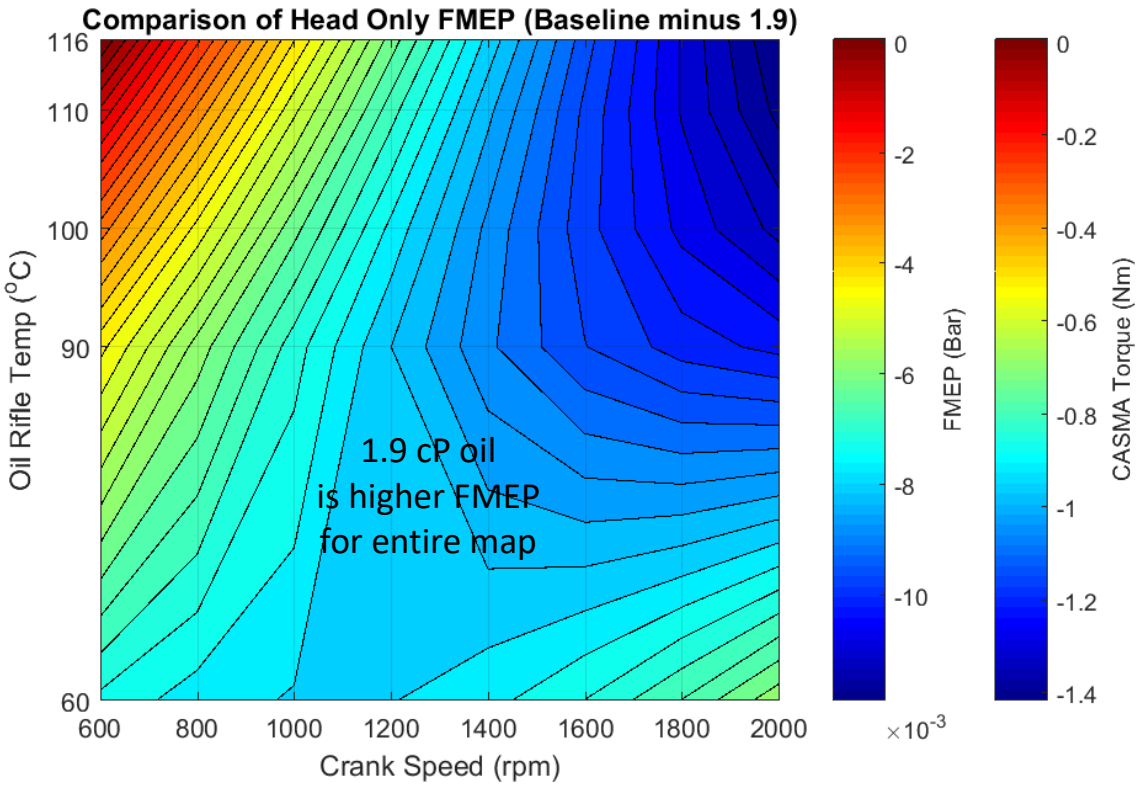

Figure 200: The friction torque/FMEP differences of the valve train only between the 5W-30 and the 1.92 cP HTHS oils as a function of engine speed and oil temperature.

The wear patterns on the overhead components were very similar to that seen after previous tests. The cam follower rollers had a frosted and dull appearance evident to naked eye with streaks covering nearly the full width of the roller although they were not able to be felt by a fingernail. Additionally, the wear on the rocker lever bushing penetrated the flash tin layer at certain regions. Figure 201 shows the wear marks on the cam follower roller after the test with the 1.9 cP oil.

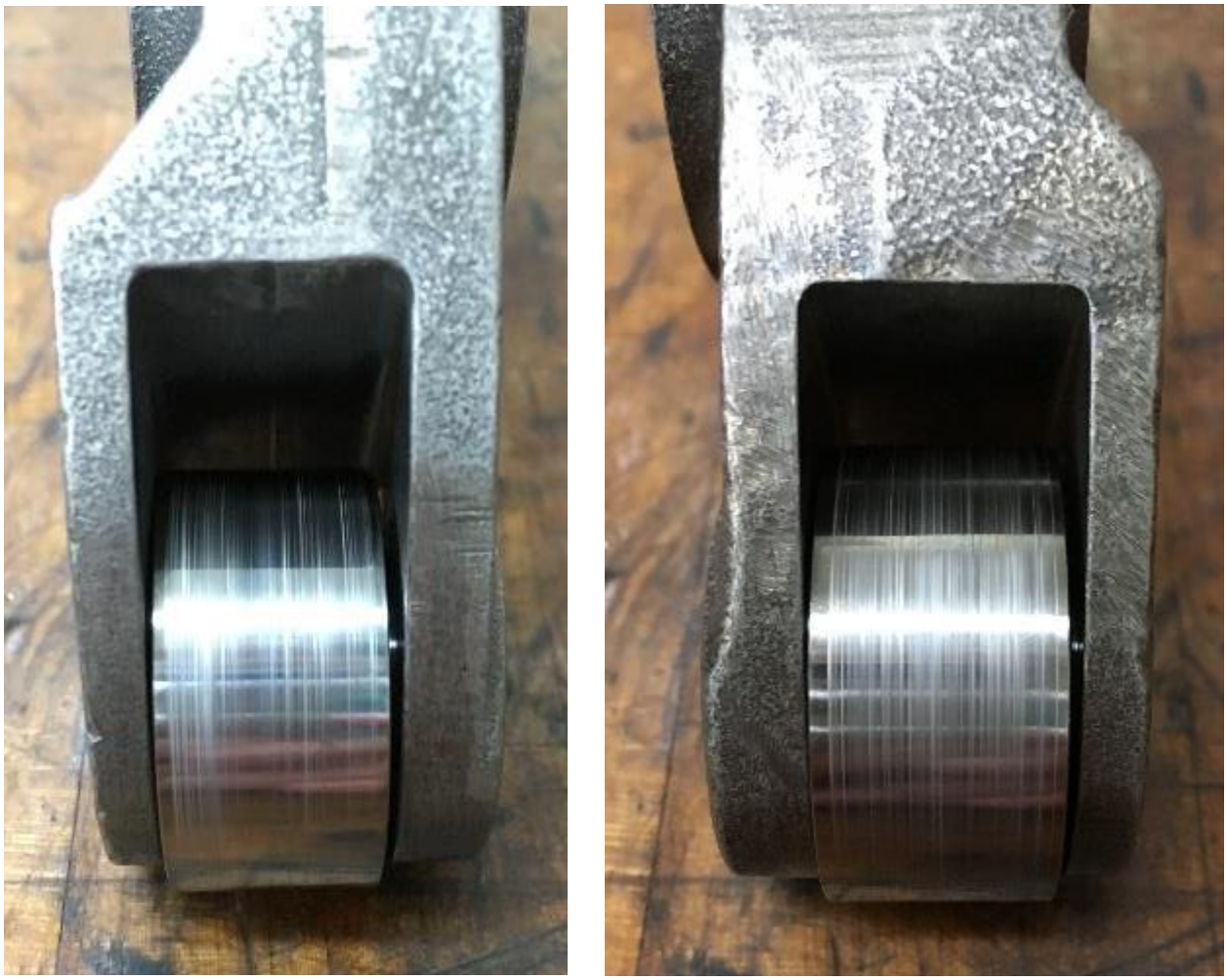

(a) (b)

Figure 201: Wear marks on the cam follower rollers after the test with the 1.9 cP oil for the (a) intake roller of cylinder #5 and (b) exhaust roller of cylinder #4.

3.6 Engine System Integration Testing

Executive Summary

Peak System BTE Demonstration

Engine system testing yielded a peak system BTE of 53.6%. Variables included in the system optimization are included below in Table 11.

Table 11: System Independent Variables

Engine Speed	RPM
System Power	kW
Main Injection Timing	dBTDC
Rail Pressure	bar
Intake Manifold Temperature	deg C
Condenser Pressure	kPa

Refrigerant Flow	kg/min

The system efficiency breakdown is shared below in Table 12. Given that the WHR system was delivering power back to the crankshaft versus an independent dyno, the breakdown of the engine versus WHR power was unknown. The two lines in Table 12 reflect two different strategies to identify the engine and WHR system efficiencies. The first strategy assumes a 96% mechanical efficiency to identify the engine BTE. The WHR delta BTE (dBTE) is the difference between the measured system BTE and the inferred engine BTE. The 96% mechanical efficiency was identified by running the engine at the peak BTE condition with the WHR belt removed. The second strategy utilizes WHR models run off-line to calculate the WHR system power, with the engine power contribution being the difference between the measured system power and the modeled WHR power.

Table 12: Demonstrated Peak BTE System Efficiency Breakdown

	Closed Cycle Efficiency [%]	Open Cycle Efficiency [%]	Mechanical Efficiency [%]	WHR dBTE [%]	Engine BTE [%]	System BTE [%]
Assumed 96% Mechanical Efficiency	51.7	98.9	96	4.5	49.1	53.6
WHR Estimated Power	51.7	98.9	96.4	4.3	49.3	53.6

RMCSET and FTP Cycle Results

The program's final cycle values are shared below in Table 13. The system out BSCO2 values over the RMCSET meet the Phase 1 Greenhouse Gas 2017 standard of 460 g/(hp-hr) (2010 limit of 490 g/(hp-hr) and the BSNOx limit of 0.2 g/(hp-hr) for a heavy-duty engine. Similarly, the hot-FTP met the 0.2 g/(hp-hr) BSNOx limit.

Table 13: RMCSET and FTP Cycle Summaries

Cycle	BSNOx		BSCO2		BSFC	BTE
None	g/(kW-hr)	g/(hp-hr)	g/(kW-hr)	g/(hp-hr)	g/(kW-hr)	%
RMCSET	0.20	0.15	607.65	453.12	184.29	45.64
Hot FTP	0.22	0.16	648.98	483.94	206.80	40.68

Revised Path to 55% BTE

Given the program did not fully achieve the target of 55% BTE, additional modeling efforts were conducted to identify a revised path to 55% BTE. This revised path is shared below in Figure 202 where each incremental improvement is bounded by a low side and high side estimated delta BTE improvement.

Working through the identified improvements, the WHR tailpipe boiler system resulted in additional engine back pressure than had originally been planned. Steps to reduce this were identified but were not implemented prior to completion of testing. On the turbocharge side, the demonstrated turbine and compressor efficiencies were slightly lower than the original program targets. In addition, due to the late changes in planned turbomachinery the original plans for a roller-element bearing turbine housing were unable to be realized. Early evaluations of low heat transfer (LHT) pistons did not fully realize original closed

cycle efficiency expectations; however, with piston design improvements there is still additional efficiency gains that are expected.

On the waste heat recovery side, as the engine efficiency is increased the waste heat available to the WHR system is reduced. Despite that, improvements were identified that could have been realized on the original test cell installation but again were unable to be implemented. These improvements included resizing the WHR system pulley to correct the WHR turbine speed to target the peak turbine efficiency and applying additional insulation to the exhaust system and refrigerant lines. While these items could have been implemented on the original installation, additional improvements also could have been realized with a system redesign. These include a redesign of the WHR turbine nozzle and blade geometry and changes to the plumbing to reduce pressure losses.

The final line item in the revised path to 55% BTE includes significant improvements to the turbocharger that would be in-line with current industry state-of-the-art. The cumulative effect of these improvements is estimated to yield a BTE between 55% and 56% BTE.

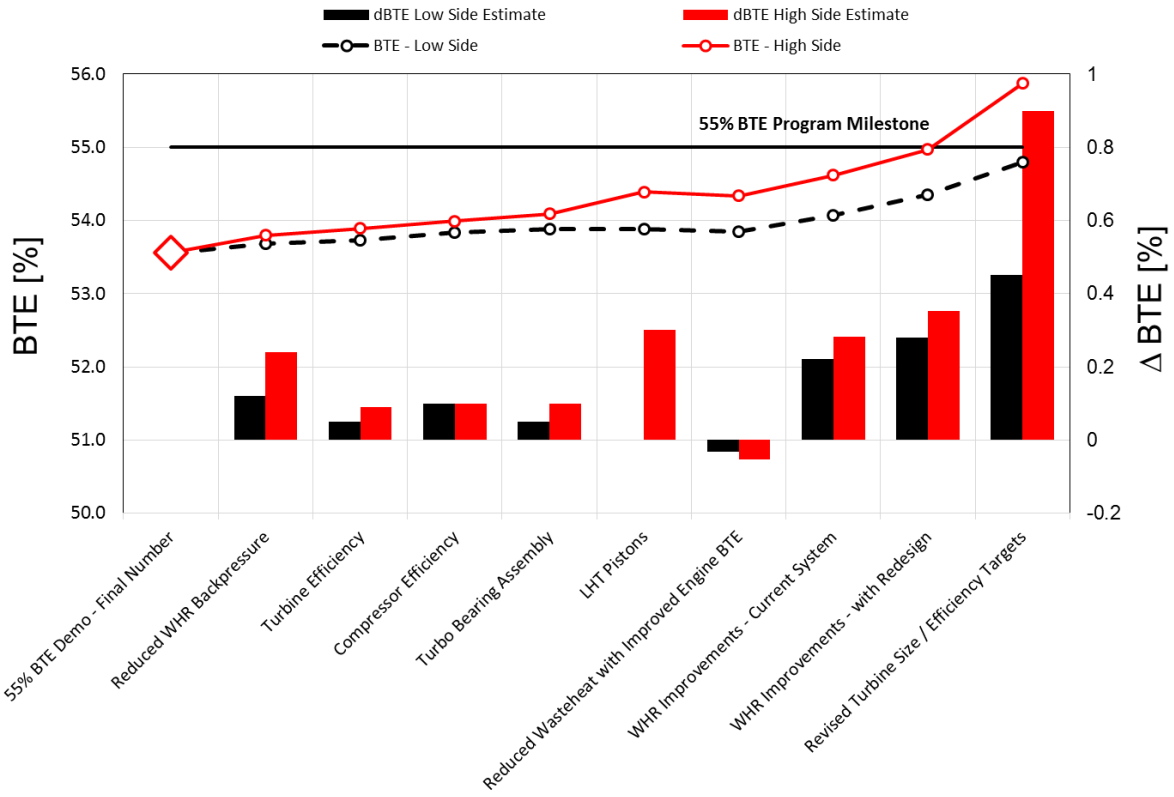

Figure 202: Bridge Path to 55% BTE from Program Demonstration Peak BTE

Air Handling

Turbocharger Comparisons

As the program has moved from the original High-Pressure (HP) EGR system to the Low-Pressure (LP) and Dual-Loop (DL) EGR configurations this has necessitated new turbomachinery matches. The aero specs and

size details are shared below in Table 14. With the exception of the components called out in Table 14 the remaining engine components remained the same.

Table 14: Turbo Hardware Test Specifications

Description	Compressor	Turbine	Turbine Size	Camshaft	Exhaust Manifold
HE400 VGT	L85J73	F72E83		2013 Production	Log
HE500 VGT	K98K68	A84M81	31 cm^2	2013 Production	Log
Mixed Flow FGT	K98K68	B84G87	16 cm^2	1999 Production	Split, no HP-EGR
Radial Flow FGT	K98K68	A84K83	16 cm^2	1999 Production	Split, no HP-EGR

Figure 203 shows the cycle efficiency breakdown across the four hardware units tested. A few things are particularly noteworthy, the first being the poor performance of the HE500 VGT hardware as demonstrated in the BTE vs BSNOx plot. This issue is largely due to the fact that the turbo had a larger swallowing capacity than what had been simulated and planned for. Another item to note is the improving trend in open cycle efficiency as we have moved from the HE400 VGT hardware to the HE500 units. The Mixed Flow and Radial Flow FGT units are demonstrating open cycle efficiencies exceeding 100% whereas the HE400 unit was showing a peak of roughly 98.5%. Looking at the mechanical efficiency, it is observed that the mechanical efficiency of the engine seems to have degraded from the HE400 VGT hardware to the three HE500 units. Despite the degradation of the mechanical efficiency, the brake efficiency of the two fixed geometry units does show a slight improvement relative to the original HE400 VGT data.

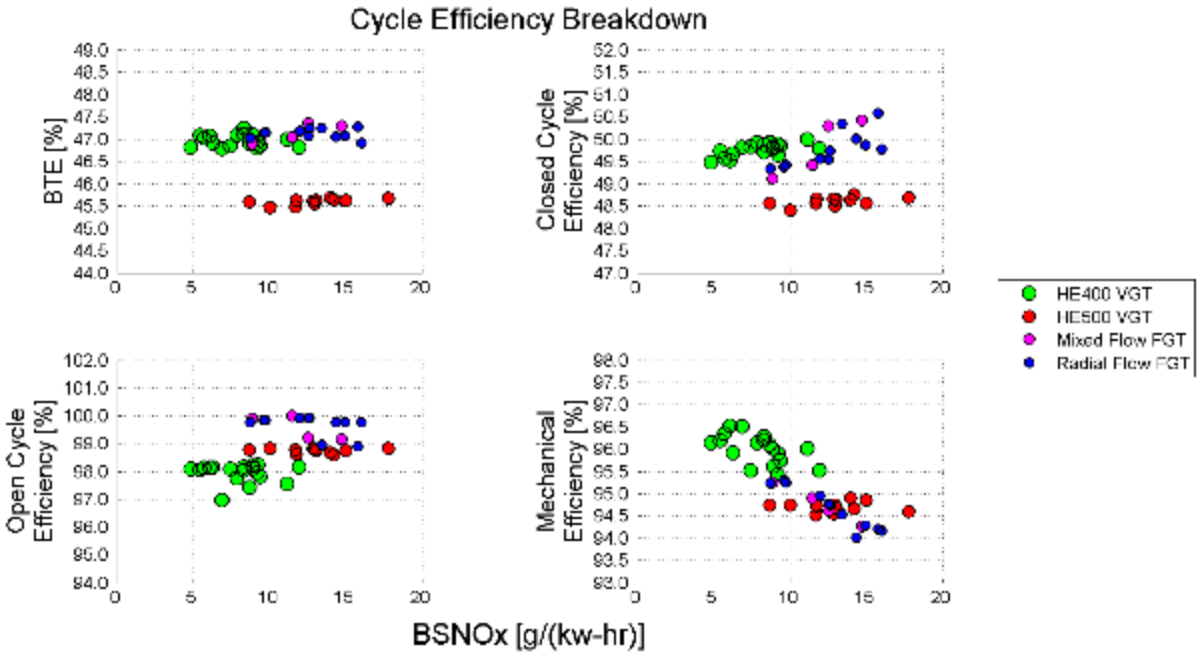

Figure 203: Turbo Comparison - Cycle Efficiency Breakdown

Considering the previously addressed mechanical efficiency issues, rather than looking at the system performance on a brake specific basis which would include the engine friction losses, Figure 204 shows the engine Net Indicated Efficiency (NIE) vs. BSNOx. The NIE only accounts for the open and closed cycle performance. In this view it is clear that the HE500 fixed geometry units are yielding a 1%-point improvement relative to the HE400 VGT unit. With the engine friction is sorted out, this improvement would be expected to translate to the brake-specific efficiency as well.

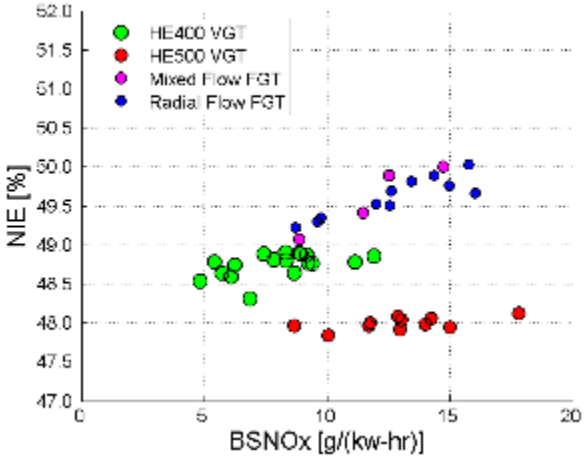

Figure 204: Turbo Comparison - Net Indicated Efficiency (NIE) vs. BSNOx

Figure 205 shows a comparison of the turbocharger performance of each of the four units. The turbine efficiency plots show that the fixed geometry units are realizing a 5-8% point improvement relative to the two variable geometry units. Similarly, the compressor efficiency is also higher for the fixed geometry units. The turbine corporate flow plot shows that the fixed geometry units are also larger than desired at 40-42 corporate flow parameter versus a targeted size of 35-38 corporate flow parameter.

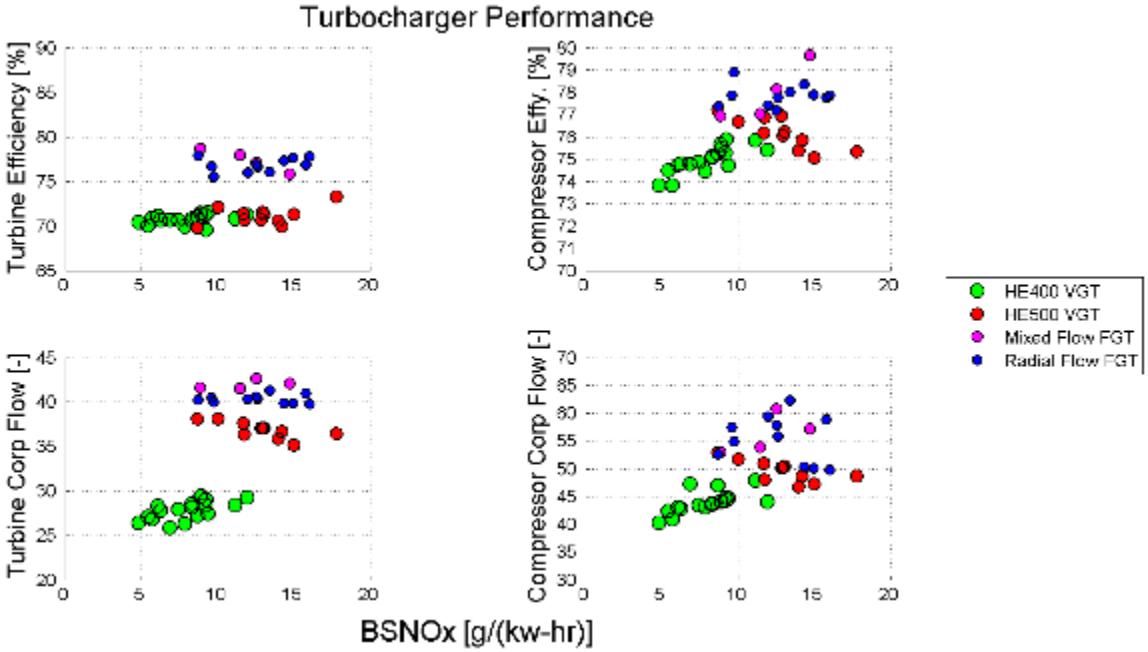

Figure 205: Turbo Comparison - Turbocharger Performance

In order to better understand sizing implications on engine performance, a 16, 13, and 10 cm^2 A84 FGT were all tested. Figure 206 compares the cycle efficiency breakdown for all three turbine options where the data has been filtered to show the peak BTE points, regardless of speed / load operating condition. In this view, it is apparent that the 10 cm^2 turbine housing is too small as it takes a significant hit in open cycle efficiency relative to the other two turbine housing options. From a BTE perspective, the 13 and 16 cm^2 turbine housings both resulted in similar BTE performance. The 16 cm^2 turbine housing tended to perform best at higher power levels with improved open cycle efficiency. The 13 cm^2 turbine housing performed

better at more optimal power levels with improved closed-cycle efficiency relative to the 16 cm^2 unit due to higher charge-fuel ratios, as illustrated below in Figure 207.

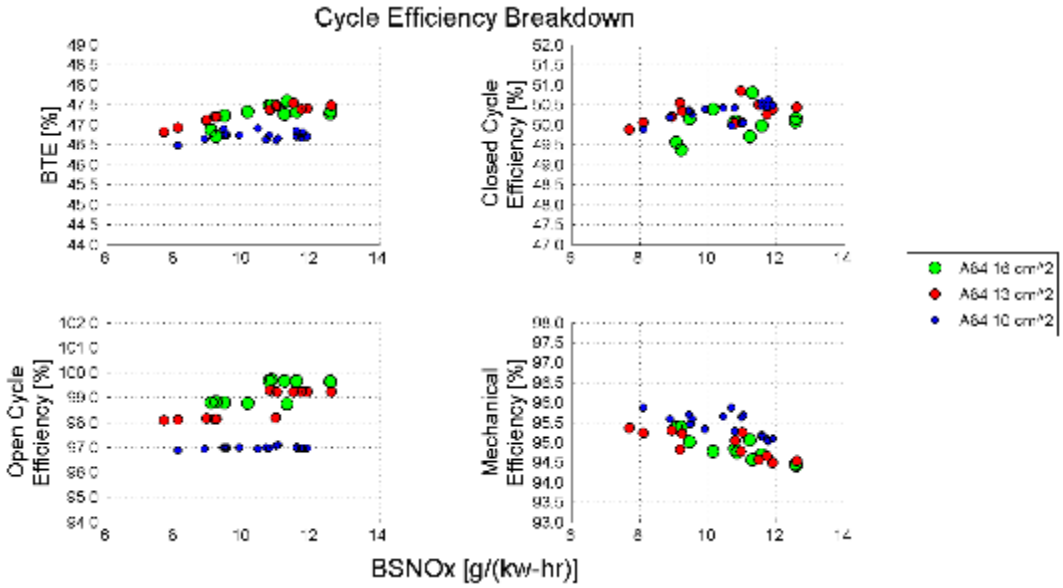

Figure 206: Cycle Efficiency Breakdown Comparing A84 16, 13, and 10 cm^2 Turbine Housings

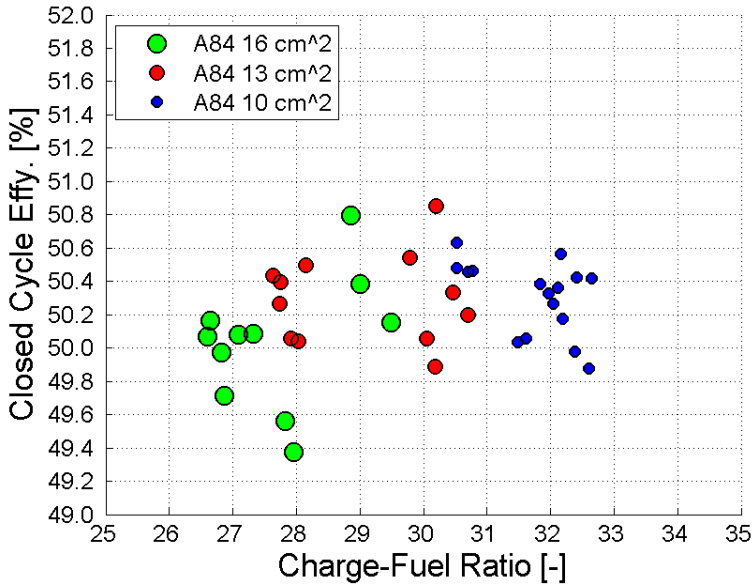

Figure 207: Closed Cycle Efficiency vs. Charge-Fuel Ratio Comparing A84 16, 13, and 10 cm^2 Turbine Housings

Mixed flow turbine housings designed as specified by the program targeted a smaller critical area to generate additional turbine power (12.8 cm^2). The increased turbine power would in-turn result in increased air flow.

Performance metrics for the turbocharger system are shown below in Figure 208. The compressor specifications for the three units were the same. The mixed flow units designed for the program that were tested included the Turbo 1 and Turbo 2, respectively.

From Figure 208 it is apparent that the turbine efficiency of the original radial flow turbine (Turbo 3) is the highest. Figure 209 below illustrates that this 2% and 5% turbine efficiency penalty results in an open cycle efficiency penalty of approximately 1-2% and a corresponding reduction in BTE of 0.4-0.8%. Although the efficiency of the mixed flow units is down, the reduction in critical area did yield the intended increase in air flow, shown below in Figure 210 where the mixed flow units are showing an increase in airflow of approximately 0.8 kg/min. Comparing the measured turbine efficiency of these units to the maps, the mixed flow units (Turbo 1 and Turbo 2) match the map performance; whereas, the radial flow turbine is exceeding the map by 5-7% points of turbine efficiency.

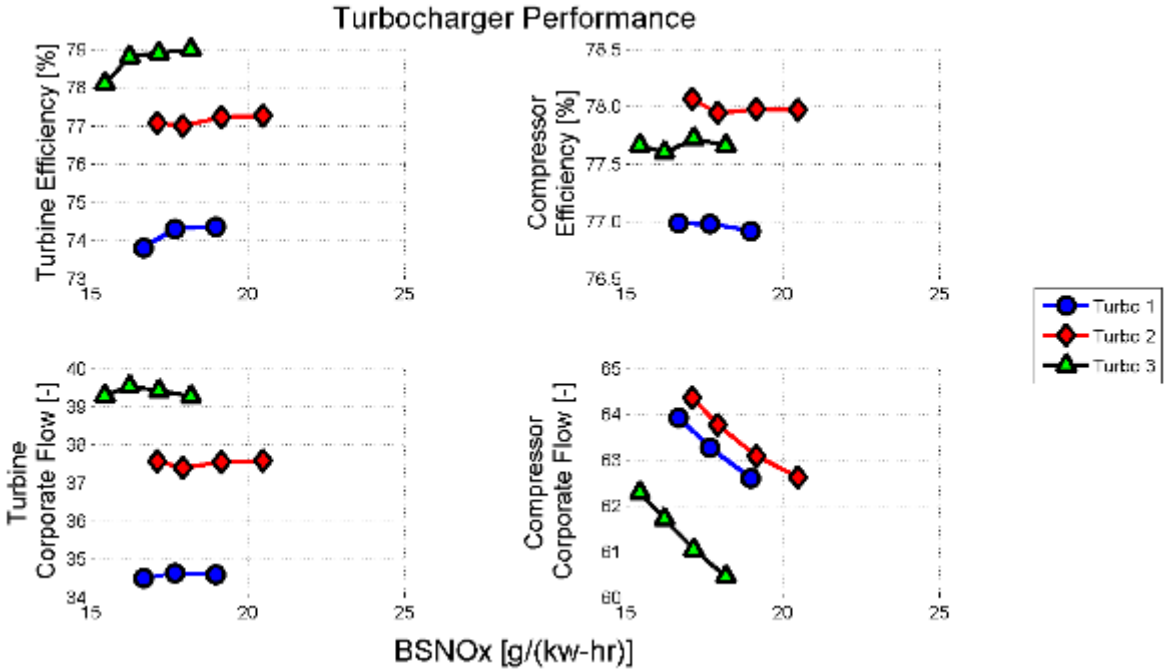

Figure 208: Mixed Flow Turbine Comparisons – Turbo Performance

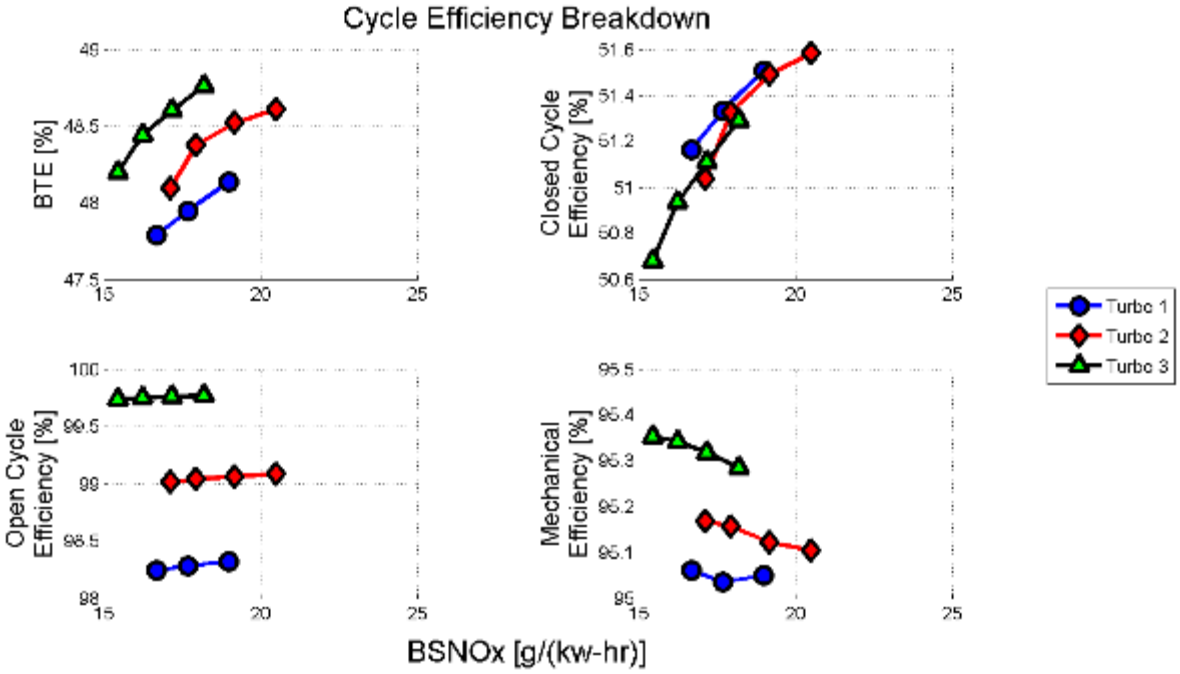

Figure 209: Mixed Flow Turbine Comparisons – Cycle Efficiency Breakdown

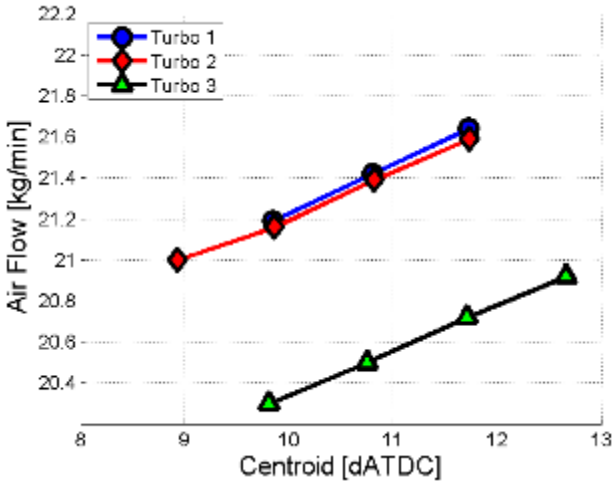

Figure 210: Mixed Flow Turbine Comparisons – Air Flow vs Centroid

Component level improvements to the compressor consisted of a fluid honing process being applied to the compressor housing volute to improve the surface finish. Prior testing at had indicated that this process could yield up to 1% compressor efficiency improvement relative to the worst surface finish observed in production parts (production Ra = 11 vs fluid hone Ra = 1). However, the prior work also revealed that a production cast part on the lower end of surface roughness scale (Ra = 6) nearly completely eliminated the performance improvement of the fluid honing process.

The surface roughness of the parts tested with this work was not quantified. The parts considered were a production as-cast compressor housing and a production housing that had gone through the fluid honing process. Both compressor housings were installed on the same compressor wheel, turbo bearing housing, and turbine system. In Figure 211 below, engine data shows that the fluid honed compressor housing

demonstrated slightly more than 1% compressor efficiency improvement relative to the production non-honed part.

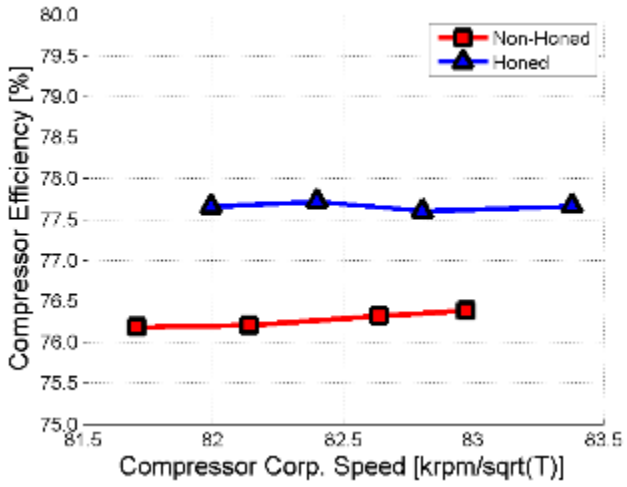

Figure 211: Fluid Honed Compressor Efficiency Comparison

Exhaust Manifolds

The fixed geometry, divided-entry turbine housings favor the use of a divided exhaust manifold to the single-exit log manifold. The HE500 divided-entry wastegate turbo (K98/A84 radial flow) was connected to both the manifolds.

		Log Manifold	ISX99 Manifold
Engine Speed	[rpm]:	999	999
Brake Torque	[Nm]:	2034	2033
BTE	[%]:	45.17	45.64
BSNOx	[g/kw-hr]:	16.15	17.35
Closed Cycle Effy.	[%]:	47.75	48.39
Open Cycle Effy.	[%]:	99.15	99.02
Firing FMEP (direct)	[kPa]:	87.99	91.07
Air Flow	[kg/min]:	16.12	17.54
Fuel Flow	[kg/min]:	0.661	0.654
Air-Fuel Ratio	[-]:	24.38	26.81
EGR Fraction (CO2)	[%]:	0.11	0.04
Volumetric Effy. (egr)	[%]:	93.87	94.09
BSFC	[g/kw-hr]:	186.24	184.32
PCP	[bar]:	159.5	170
Intake Manifold Temp.	[K]:	332	332
Turbine power	[kw]	29.84	35.18

Table 15: Comparison of Log Manifold and Divided Manifold (ISX99)

Table 15 shows the comparison of the production log manifold and the divided manifold for the same operating condition and hardware. The divided manifold shows an improvement of around 0.5 BTE at the 1000RPM/2034 Nm operating condition. The divided manifold is able to generate higher exhaust pressure

pulses and convert this energy resulting in higher turbine power and higher air-fuel ratios which leads to an improvement in closed cycle efficiency. The open cycle efficiency for both manifolds is similar.

Hardware was evaluated to better understand the effect of exhaust manifold designs intended to capture pulse energy. Figure 212 shows the flow domain views of the original manifold (BU Log) and the new design (BU Pulsed). Notable changes include moving the high pressure EGR take-off from the front of the engine to a central location prior to the turbine inlet. A new design technique was also employed that incorporated a linear area schedule from the cylinder head to the turbine inlet with improved flow direction at junctions in the exhaust manifold.

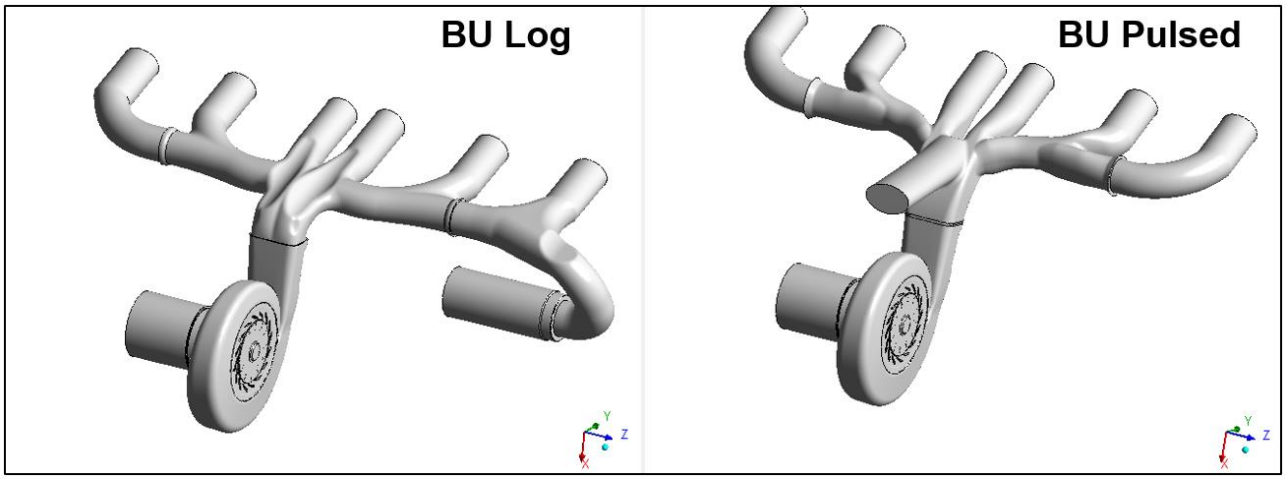

Figure 212: Variable Geometry Turbo Pulse Manifold Design Comparison

Engine data run for comparison between the two manifolds included sweeps of VGT positions under fixed start of injection, rail pressure, and high pressure EGR positions. Figure 213 shows an example set of data to demonstrate the improvement observed with the Pulse manifold. In this case the start of injection was fixed at 0 deg, rail pressure at 1490 bar, and the high pressure EGR valve position was closed. Earlier analysis had predicted the approximate 0.2 delta BTE number that was observed on-engine; however, the expectation was that the improvement would come from open cycle efficiency. This was not necessarily observed. As seen in Figure 213, the improvement is observed in the closed cycle efficiency performance with open cycle efficiency actually being a very slight detriment relative to the baseline Log manifold. Figure 214 shows that the slight penalty in open cycle efficiency does come with a 0.2 kg/min increase in air flow at the same VGT position. This increase in air flow is thus leading to the increase in closed cycle efficiency.

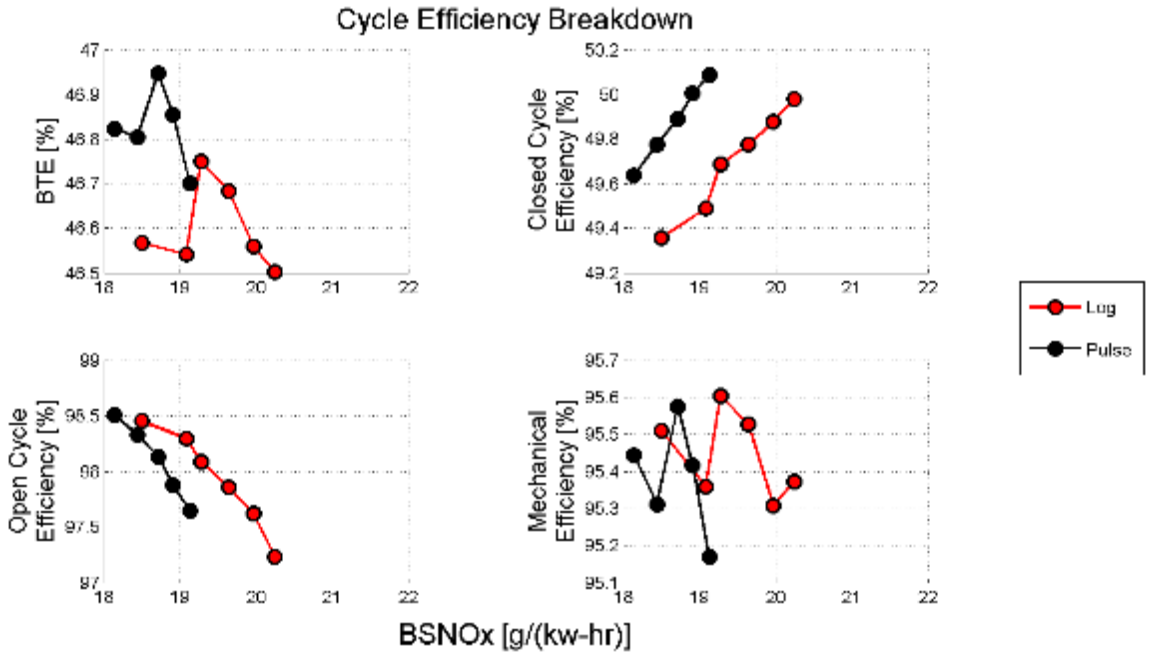

Figure 213: Cycle Efficiency Breakdown at 1000 RPM, 2034 Nm for Manifold Comparison

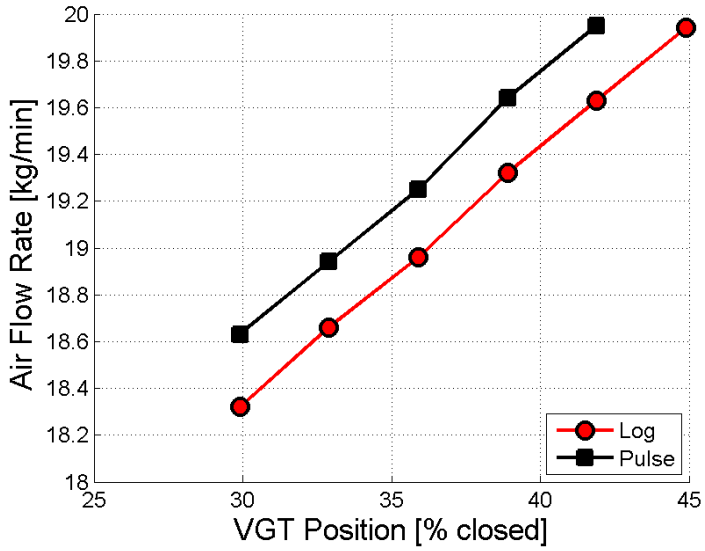

Figure 214: Air Flow Rate vs VGT Position at 1000 RPM, 2034 Nm for Manifold Comparison

Cam Optimization

Figure 215 shows the valve events for the baseline cam and the Early Exhaust Valve Open (EEVO) cam. Simulation had predicted an improvement of almost 0.5 BTE with the EEVO cam compared to the baseline cam when combined with the divided manifold and a divided fixed geometry turbine. The EEVO cams have a similar intake event as compared to the baseline cam but the exhaust event is earlier and has a higher lift resulting in a small overlap area.

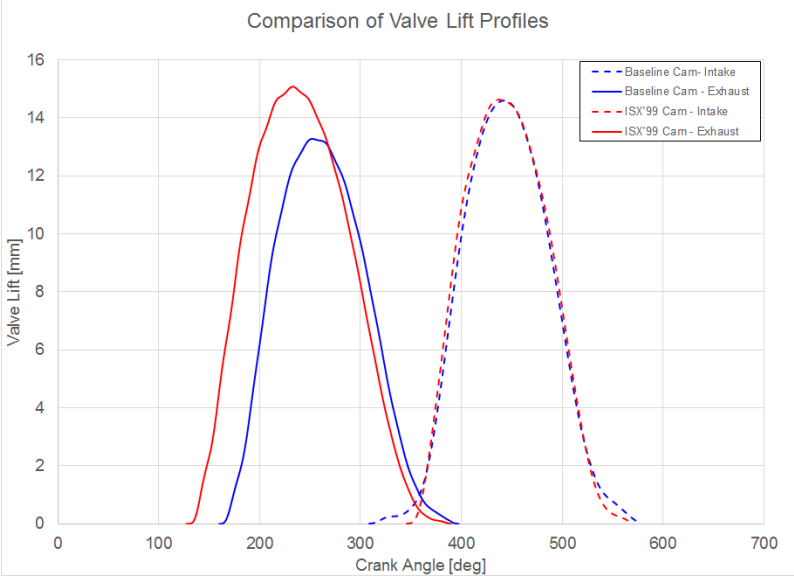

Figure 215: Baseline vs Early EVO Valve Lift Profiles

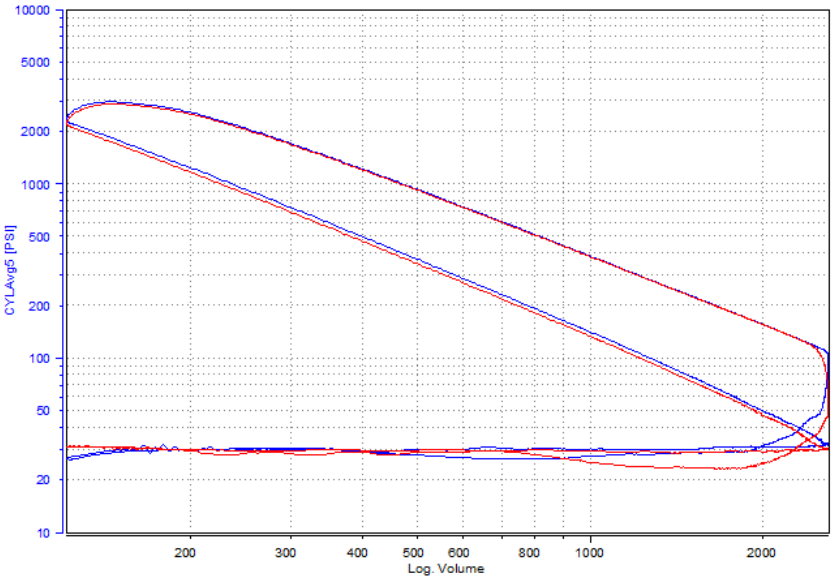

Figure 216: LogP-LogV Plot of Baseline vs ISX99 Cam

For the same SOI, rail pressure and LP EGR valve position, the EEVO cam showed around 0.2 BTE improvement compared to the baseline cam. Figure 216 shows the LogP - LogV diagram of the points run with the baseline (blue) and EEVO (red) cams. The improvement in BTE can be seen from the difference in the end of the expansion stroke and start of the exhaust stroke.

Mechanical

50% Demo Engine Friction Assessment

A new engine was installed that was built-up with additional friction improvements and actuators to enable reduced parasitic power. These included Low Heat Transfer (LHT) pistons with ring grooves to accommodate a low friction ring pack, an electrically variable flow lube pump, a 2-step water pump, and checked piston cooling nozzles (PCNs). The expectation with the 50% BTE demo engine was that the motoring

friction performance would be on-par or improved from any evaluations completed to date. Figure 217 shows the motoring Friction Mean Effective Pressure (FMEP) performance of the original configuration of the 50% BTE demo engine relative to the final Mule engine configuration, as well as the best motoring FMEP performance observed on the SuperTruck program. From this it was apparent that the engine friction was higher than anticipated.

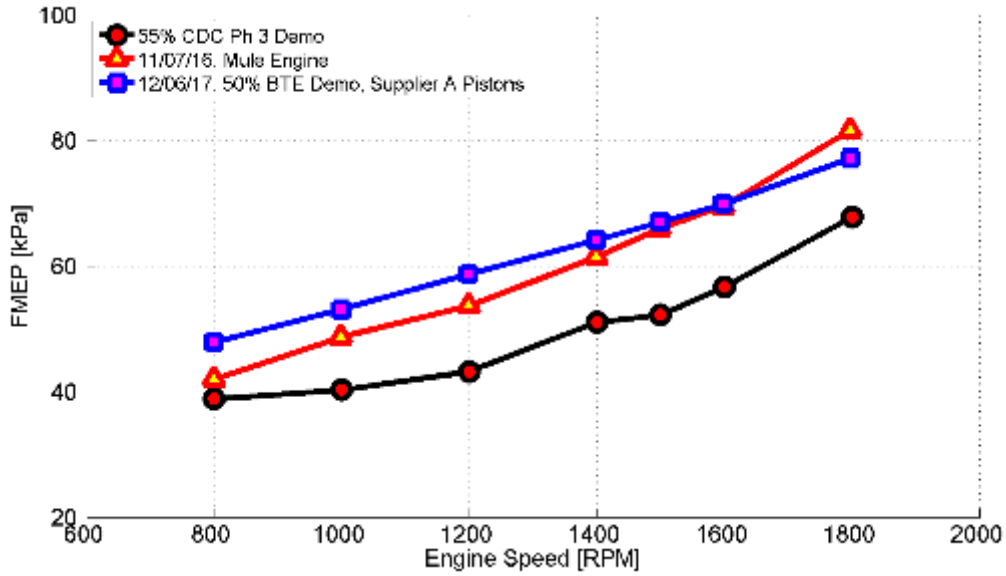

Figure 217: Motoring Friction Performance of Original 50% BTE Demo Engine Build

The component with the most uncertainty from a friction / parasitic standpoint with the 50% BTE Demo engine were the LHT pistons. These pistons were run in the Mechanical Efficiency Lab (MEL) to characterize their friction performance where they also showed increased friction; however, they were not broken in prior to running in MEL. Thus, there was a level of uncertainty to the MEL data.

Given the uncertainty and the friction level observed on-engine, a set of pistons from another supplier (Supplier B) that had been run previously were installed to isolate the friction performance of the pistons. The Supplier B pistons necessitated either running stock PCNs or no PCNs due to the slight difference in piston skirt geometry. This set of pistons had an Inconel insert and had previously been run on the SuperTruck program with telemetry data and no PCNs. The telemetry data indicated the pistons were safe up to approximately 280 kW without PCN flow; therefore, the pistons were run with the PCN's blocked closed. In addition to the blocked PCN setup, the pistons were not cut to accommodate the low friction ring pack; therefore, they were also installed with a standard ring pack. Figure 218 demonstrates the motoring FMEP performance improvement that was observed following the break-in of the Supplier B pistons.

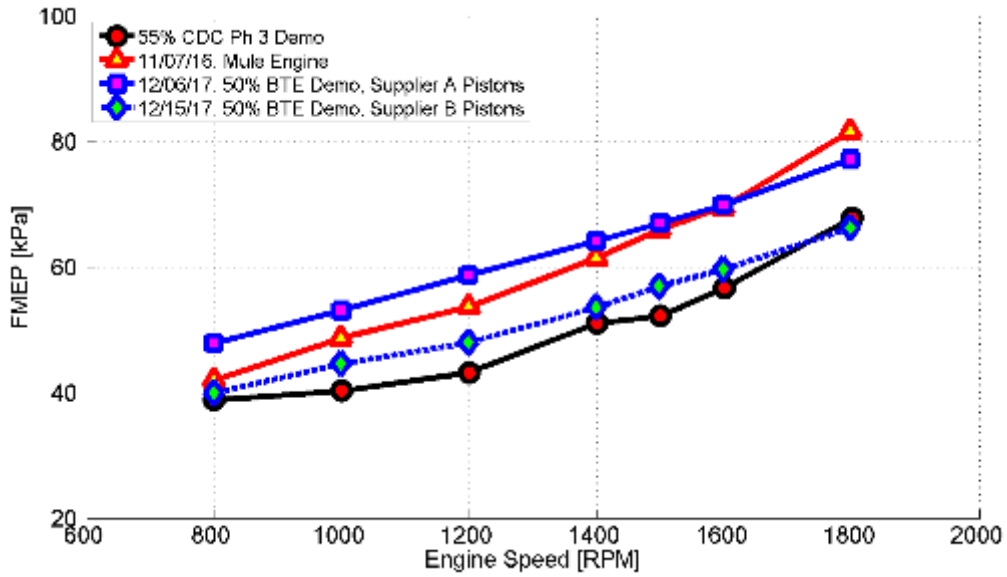

Figure 218: Motoring Friction Performance Comparison between Supplier A and Supplier B Pistons

As observed in Figure 218, the motoring FMEP was significantly improved with the Supplier B pistons relative to the performance with the Supplier A pistons. To continue pushing motoring FMEP lower, a set of Compacted Graphite Iron (CGI) liners with a smoother hone were installed next. The CGI liners were expected to have less bore distortion due to improved material properties. With the lower bore distortion, a smoother hone could be utilized.

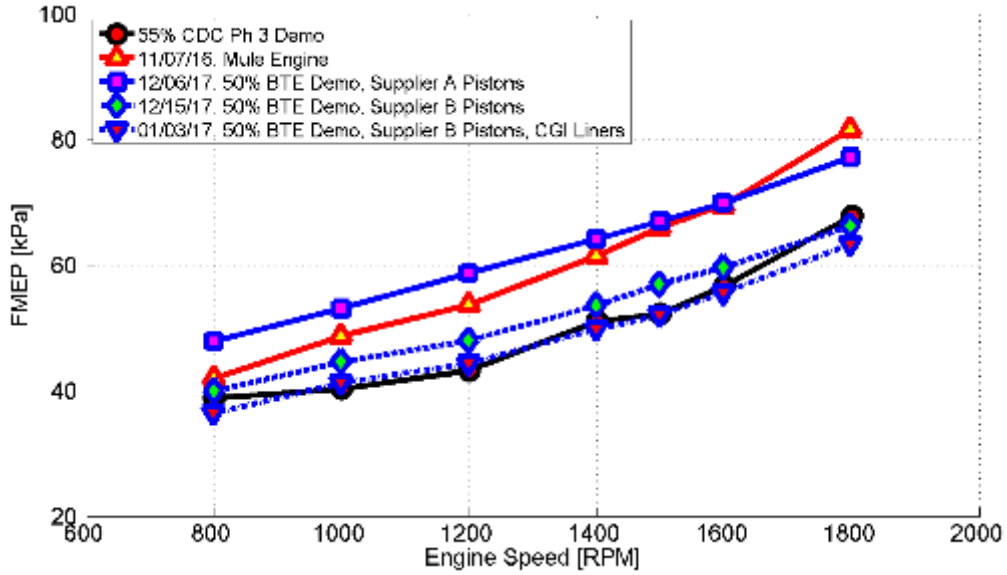

Figure 219: Motoring Friction Performance Comparison between Standard and CGI Smooth Hone Liners

Figure 219 illustrates the final improvement in motoring FMEP observed with the 50% demo engine. This final curve illustrates the cumulative impact of:

- Electrically variable flow lube pump
- 2-step water pump (high flow setting)
- Blocked piston cooling nozzles
- Supplier B pistons

- CGI, smooth hone liners

Impact of Rifle Pressure / PCN Flow on Motoring FMEP

As previously mentioned, the 50% BTE demonstration engine was built with a new electrically variable flow lube pump. The control the lube pump provided was necessary to incorporate on / off PCN flow functionality through the checked piston cooling nozzles. Figure 220 compares the motoring FMEP curves between high (30 psi) and low (25 psi) oil rifle pressure targets with both high and low flow water pump settings. The curves show approximately 5 kPa motoring FMEP improvement in the change from high rifle pressure to low. Given the bench testing performance of the checked piston cooling nozzles, piston cooling flow should be off at the low rifle pressure setting and on at the high rifle pressure setting. The bench testing results from the manufacturer indicate the piston cooling nozzles are near full flow at 30 psi rifle pressure and are off at 25 psi rifle pressure.

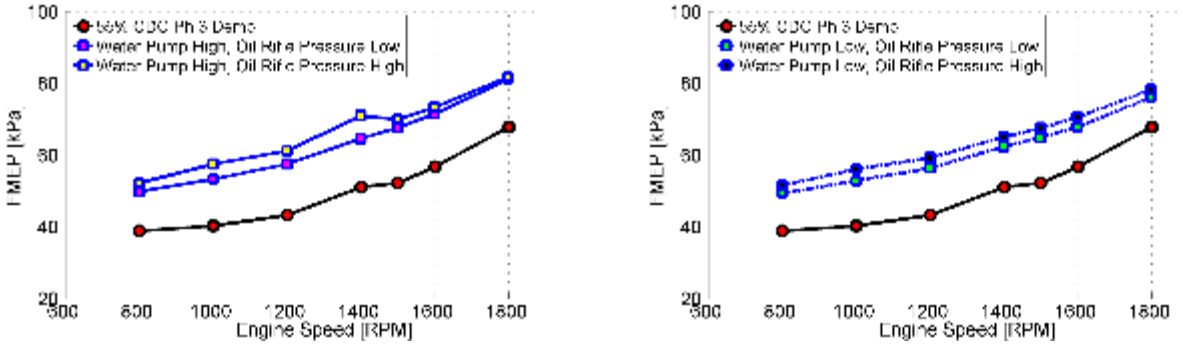

Figure 220: Motoring Friction Performance Comparison between High and Low Oil Rifle Pressure

Impact of Coolant Flow on Motoring FMEP

The 50% BTE demonstration engine was also equipped with a 2-step water pump. The water pump either operated in a clutched or un-clutched position, where clutched operation corresponded to the high flow setting. Given the water pump is typically sized for heat rejection at the engine rated operating condition, it is significantly oversized for operation at part-load. The design intention with the 2-step water pump was that at the peak engine efficiency operating condition it could be run in the un-clutched position resulting in up to a 1 kW parasitic power reduction relative to a current product water pump. Results from running the water pump in the clutched and un-clutched positions at the high and low oil rifle pressure settings are compared below in Figure 221. The motoring FMEP curves indicate an approximately 1 kPa FMEP improvement at 1200 RPM with high oil rifle pressure and less than 1 kPa FMEP delta with low oil rifle pressure.

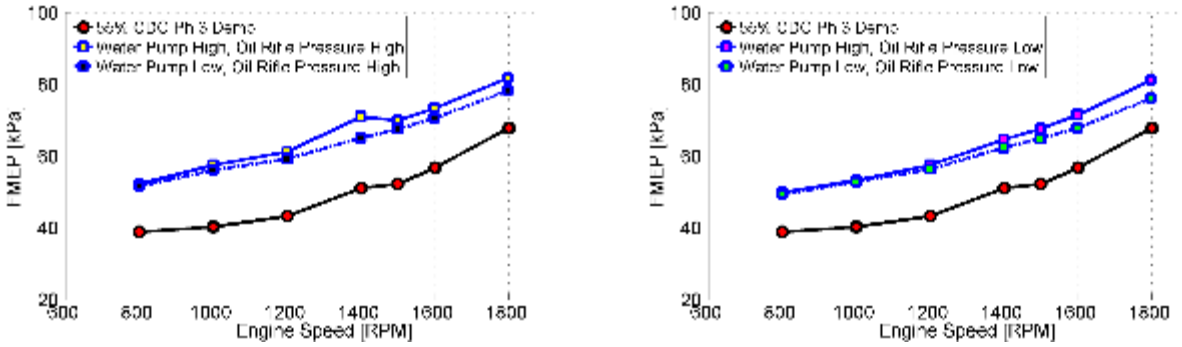

Figure 221: Motoring Friction Performance Comparison between High and Low Water Pump Flow

Roller Overhead

Prior analysis and bench testing had indicated that friction savings would be very minimal; however, the reduced lube pump flow requirements could yield up to a 0.16% dBTE improvement.

Initial motoring FMEP results, shown below in Figure 222, demonstrated an approximately 5 kPa penalty in motoring FMEP performance at the targeted demonstration speed of 1000 rpm. However, in Figure 223 below, the fired Mechanical Efficiency is similar to the journal head setup. The system benefit shows approximately +0.1% delta BTE improvement with the roller head setup, attributable to an improvement in closed cycle efficiency. Figure 224 shows that with the same centroid of combustion, the roller head is yielding a +0.1% delta Closed Cycle Efficiency improvement.

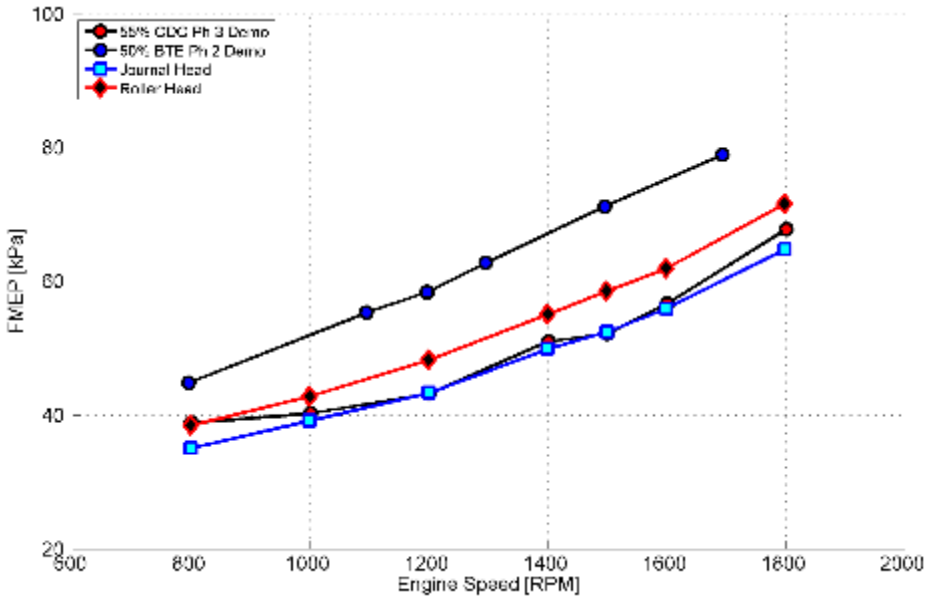

Figure 222: Roller vs Journal Head Motoring FMEP Comparison

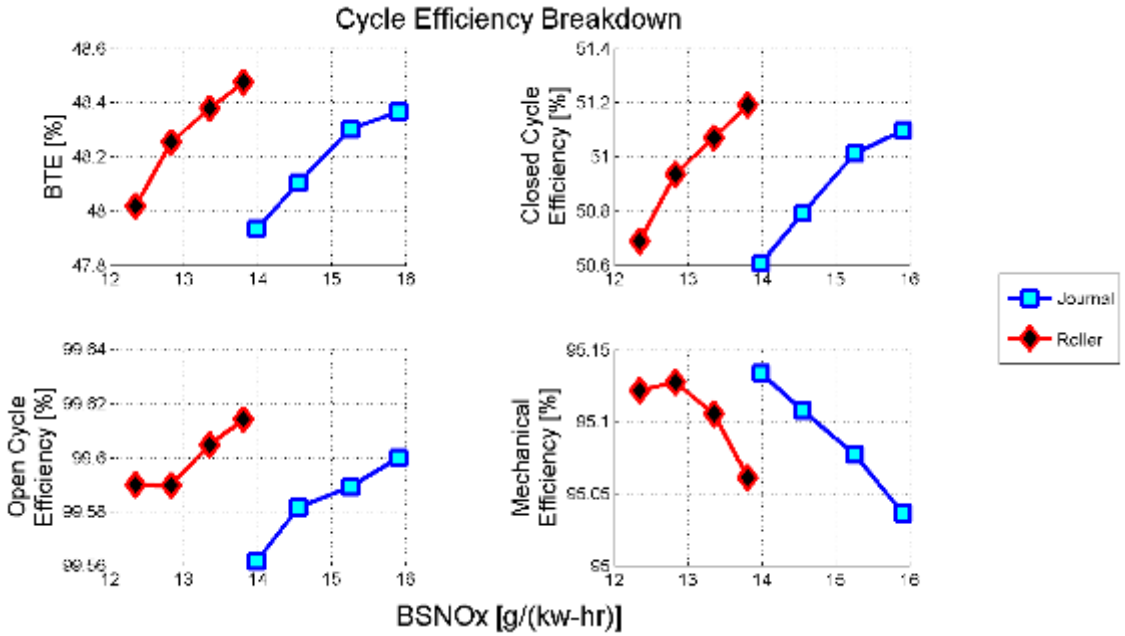

Figure 223: Roller vs Journal Cycle Efficiency Breakdown

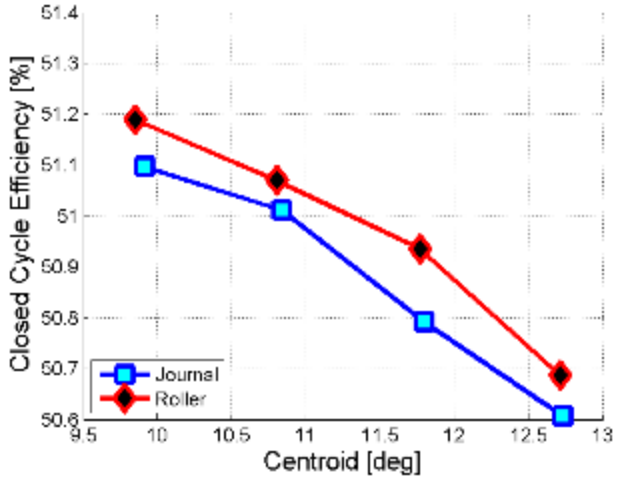

Figure 224: Roller vs Journal Closed Cycle Efficiency vs Centroid

Closed Cycle

Injectors

Initial injector evaluations as part of the program were a series of higher cup flow injector evaluations. Higher cup flow injectors had been evaluated as part of earlier SuperTruck activities; however, that testing was generally confounded with other hardware changes. The intention of the testing conducted here was to retain the base engine system in a constant configuration and only change through the various injectors available. The injector specifications are included below in Table 16 with 235 pph being the nominal cup flow. Of note, with the exception of the 235 pph injectors, all were built with similar nozzle configurations (8-hole, 17-degree spray angle). Though nominally the 235 pph injectors have a 16-deg. spray angle, the expectation is that the 1 deg. difference in spray angle is within the manufacturing tolerances.

Table 16: Injector Specifications for Hardware Tested

Description	No. of Holes [-]	Spray Angle [deg]	Cup Flow [lb/hr]
235 pph	8	16	235
450 pph	8	17	450
600 pph	8	17	600
750 pph	8	17	750

The theoretical intention of higher cup flow injectors is to increase the rate of heat release to drive improvements in closed-cycle efficiency. This is accomplished by increasing the peak injection rate of the injector, as reflected in Figure 225. In addition to increasing the peak injection rate, additional injector internals can be modified to also change the opening and closing ramp rates. These considerations will be considered in later program evaluations.

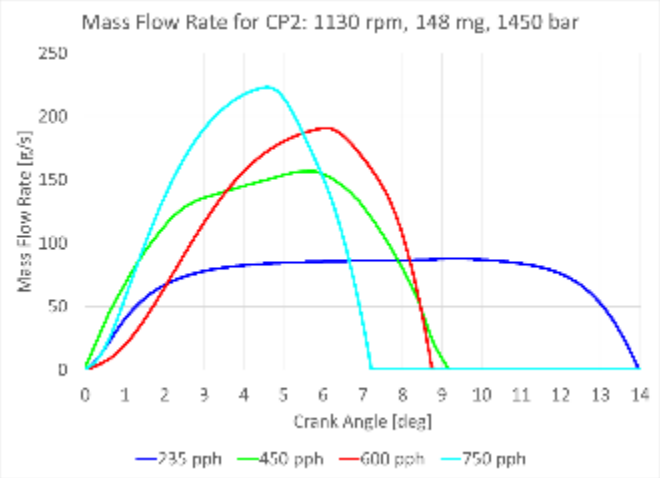

Figure 225: Modelled Injector Flow Rates at 1130 rpm, 1450 bar Rail Pressure, and 148 mg/str

Experimental evaluations with the higher cup flow injectors were conducted at two engine operating conditions, shown in Figure 226 with the engine torque curve, where BP1 (Best Point 1) is 1000 RPM / 2034 Nm and CP2 (Cruise Point 2) is 1130 RPM / 1437 Nm.

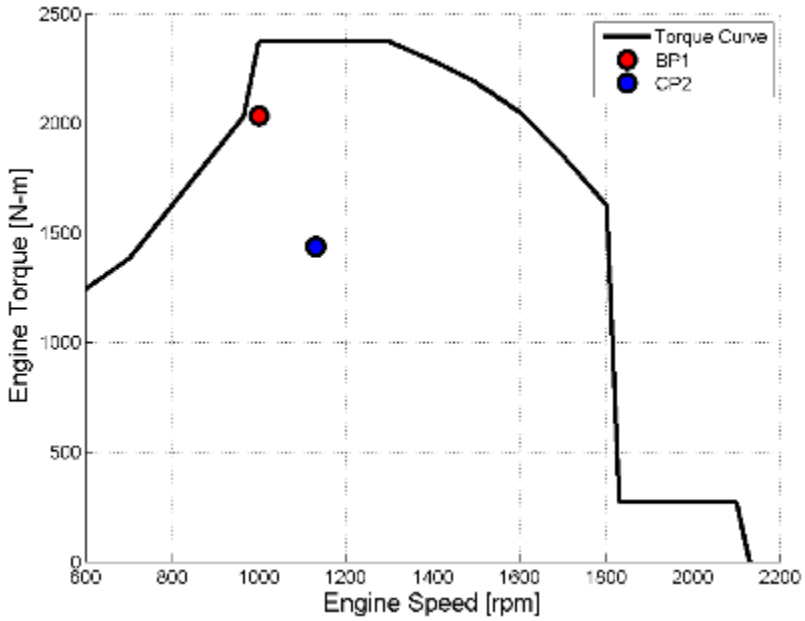

Figure 226: High Cup Flow Injector Evaluation Operating Conditions

At each operating condition, the testing consisted of a random space-fill design of experiments (DOE) with independent variables of start-of-injection (SOI), rail pressure, EGR valve position, and VGT position. The DOE data generated was the utilized to create a Multi-Linear Regression (MLR) model. This MLR model was then utilized to optimize the system under the constraints of maximized brake efficiency at a target BSNOx level while targeting cylinder pressure less than 238 bar.

Results from the high cup flow evaluations at BP1 are reflected in the cycle efficiency breakdowns in Figure 227. From this comparison, the 600 pph injectors yielded the highest closed-cycle efficiency with nominally similar brake efficiency to the 235 pph injectors. The 750 pph injectors also yielded an improvement in closed-cycle efficiency relative to the 235 pph; however, they also ran with significantly higher smoke, shown in Figure 228. Given the smoke performance of the 750 pph injectors additional investigations are planned to try to mitigate the smoke production.

Figure 229 shows a comparison of the apparent heat release rates for the CP2 repeat point across all of the higher cup flow injectors tested. From this view, it is apparent that the higher cup flow injectors did result in higher peak heat release rates. Additional studies are on-going to understand additional details of the efficiency break-down across the series of injectors tested.

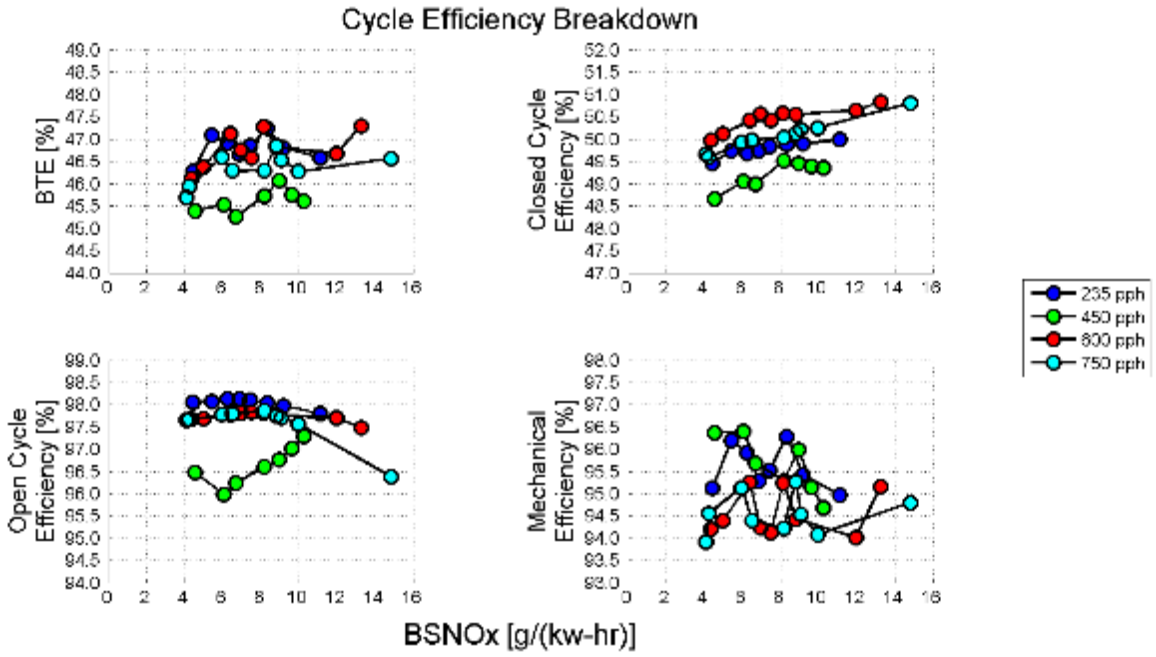

Figure 227: BP1 (1000 RPM / 2034 Nm) Cycle Efficiency Breakdown

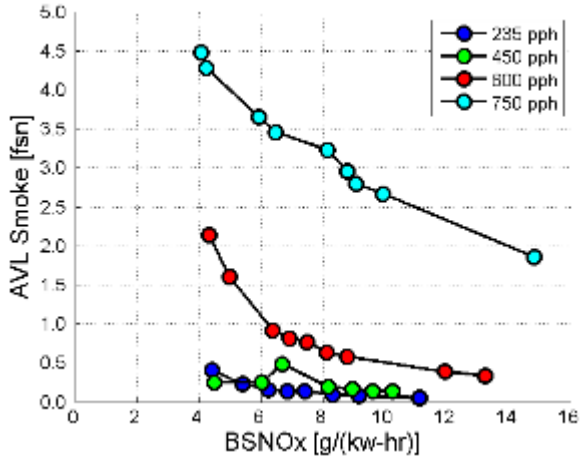

Figure 228: BP1 (1000 RPM / 2034 Nm) Smoke vs. BSNOx Plot

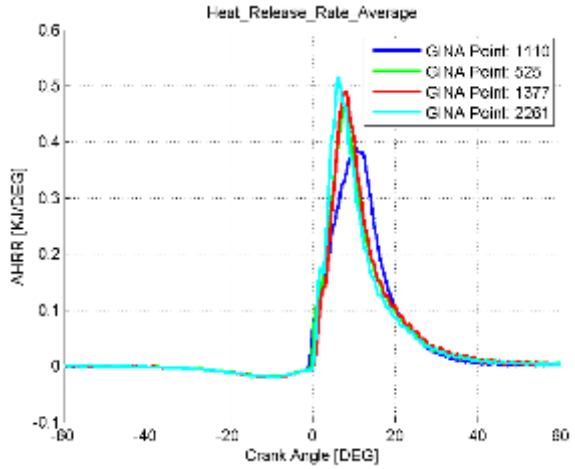

Figure 229: CP2 Repeat Point Apparent Heat Release Rate Comparison

A second round of injector testing was conducted with a new set of 750 pound per hour (pph) cup flow injectors with a few modifications relative to the first set. The first set of 750 pph injectors tested demonstrated a significant smoke penalty relative to the 600 pph injectors. This second set of 750 pph injectors were reconfigured to attempt to address the high smoke performance of the first set. The new set utilized different geometry at the needle seat location to reduce throttling losses across the needle, increased the number of nozzle holes, and reduced the nozzle hole diameter. These changes were in an effort to increase the injection velocity of the fuel. Figure 230 shows the significant improvement in smoke from the original 750 pph injectors to the new ones as well as how they perform relative to the 600 pph injectors.

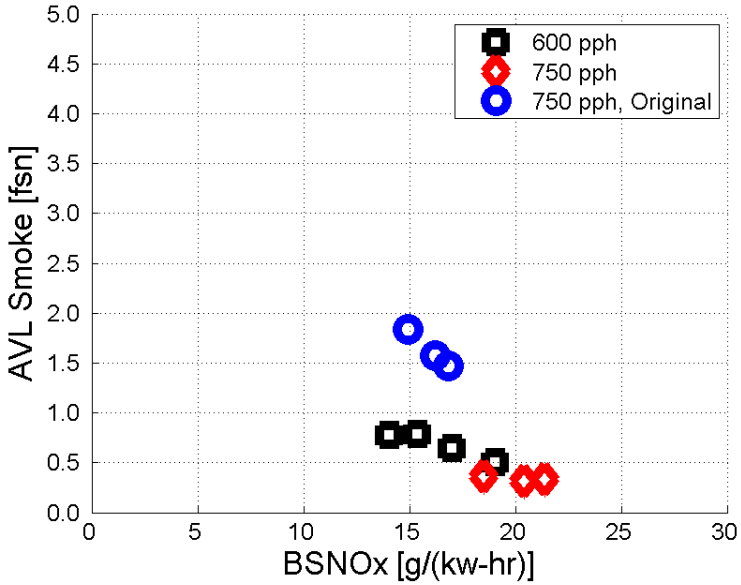

Figure 230: Smoke vs BSNOx for High Cup Flow Injector Comparison

Figure 231 shows the cycle efficiency breakdown comparing the 600 pph injectors and the new 750 pph injectors. From this view, it shows an improvement in closed cycle efficiency. Also seen is an improvement in mechanical efficiency at higher BSNOx levels. The mechanical efficiency improvement is likely not attributable to the difference in injectors, but more likely the pistons / rings continuing to break-in.

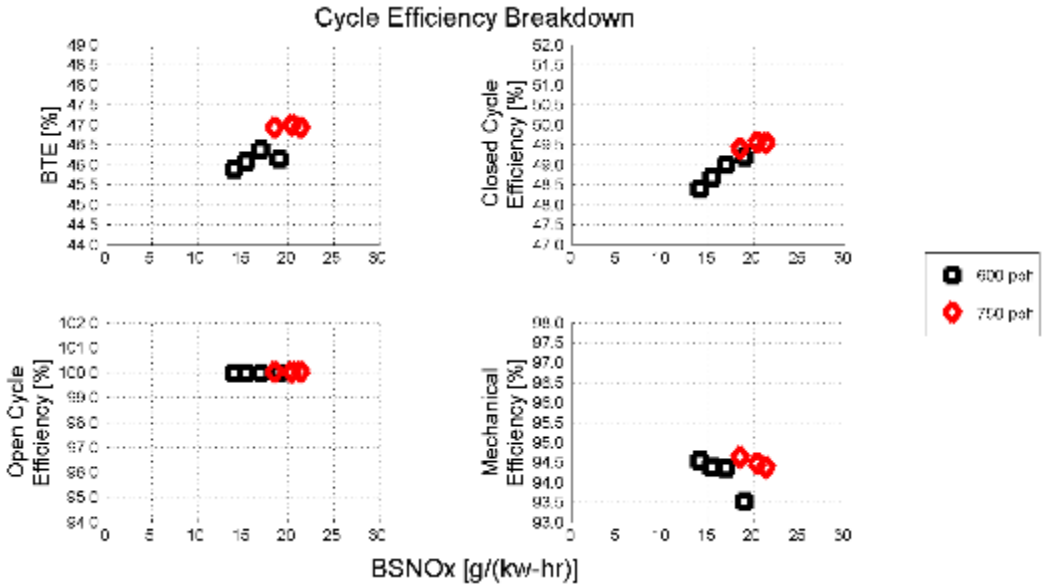

Figure 231: Cycle Efficiency Breakdown Comparison of 600 pph vs 750 pph Injectors

Additional efforts were also spent with the 750 pph injectors pursuing opportunities to further increase the rate and shorten the duration of the heat release. This was accomplished by increasing the rate of fuel injection through injector nozzle and needle changes.

As previously mentioned, additional methods were tested in the 750 pph injector evaluation to continue to increase the opening injection rate of the fuel injector. A comparison of these injectors at 1000 RPM, 210 mg/stroke, and 1500 bar is shared below in Figure 232 where the peak rate of the opening injection rate is observed to be approximately 40% faster than the original.

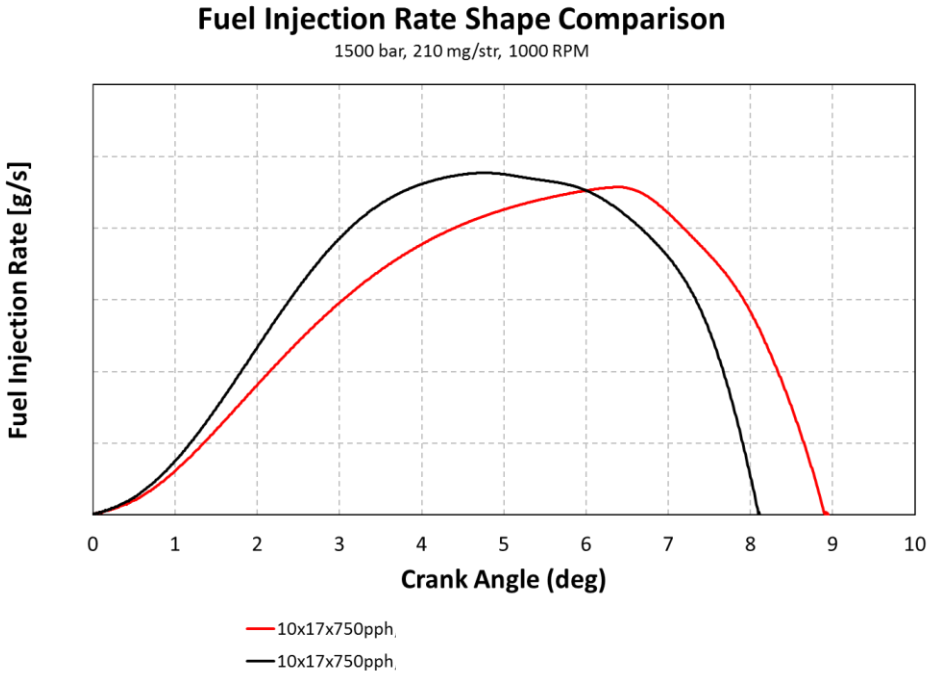

Figure 232: Comparison of Fuel Injection Rate for 1860 and 3000 pph Needles

The increased rate of injection observed in Figure 232 resulted in the closed cycle efficiency shared below in Figure 233. The data shared in Figure 233 is generated by sweeping the start of injection at a fixed rail pressure, in this case 1200 bar.

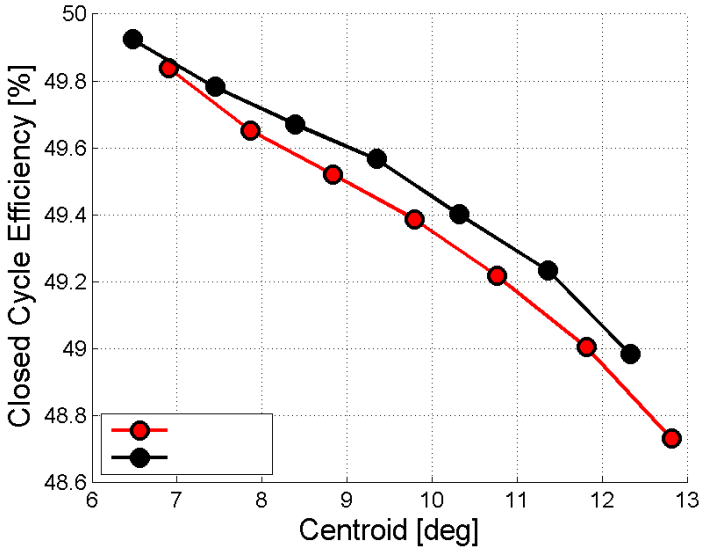

Figure 233: Closed Cycle Efficiency Comparison at 1000 RPM, 2034 Nm (~210 mg/stroke) for 1860 and 3000 pph Needles

A comparison of the heat release rate corresponding to a start of injection of 3 dBTDC from the data shared in Figure 233 is shared below in Figure 234. The heat release shows how the faster rate of fuel injection increases the rate of heat release of the initial burn and increases the peak heat release rate.

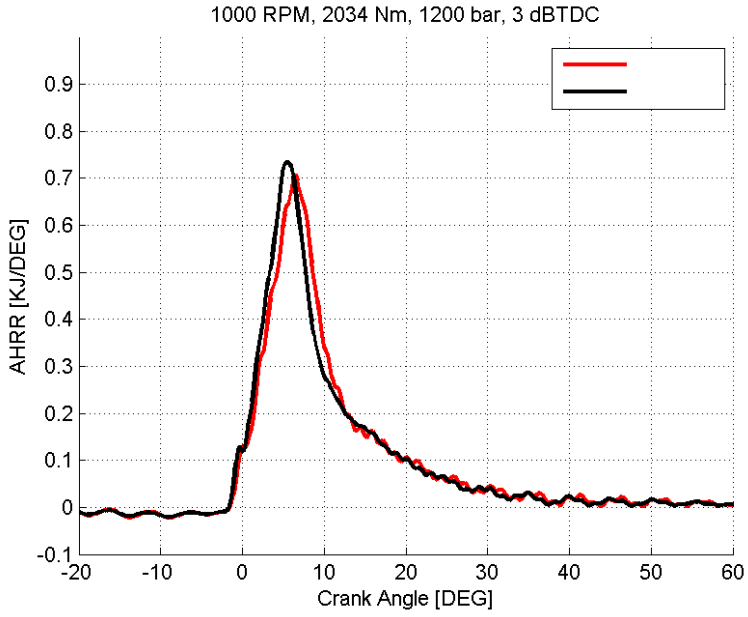

Figure 234: Heat Release Rate Comparison at 1000 RPM, 2034 Nm, 1200 bar, 3 dBTDC

Similar to method #1, method #2 can be implemented to increase the rate of fuel injection during the initial opening ramp of the needle. Figure 235 below demonstrates the increased rate of method #2 relative to the previously observed method #1. Note that the method #1 curve (black) is the same curve as shared in

Figure 232. In this case, the peak rate of the needle opening is increased by approximately 50% over the method #1 curve and 100% increase relative to the previously shared baseline curve (red in Figure 232).

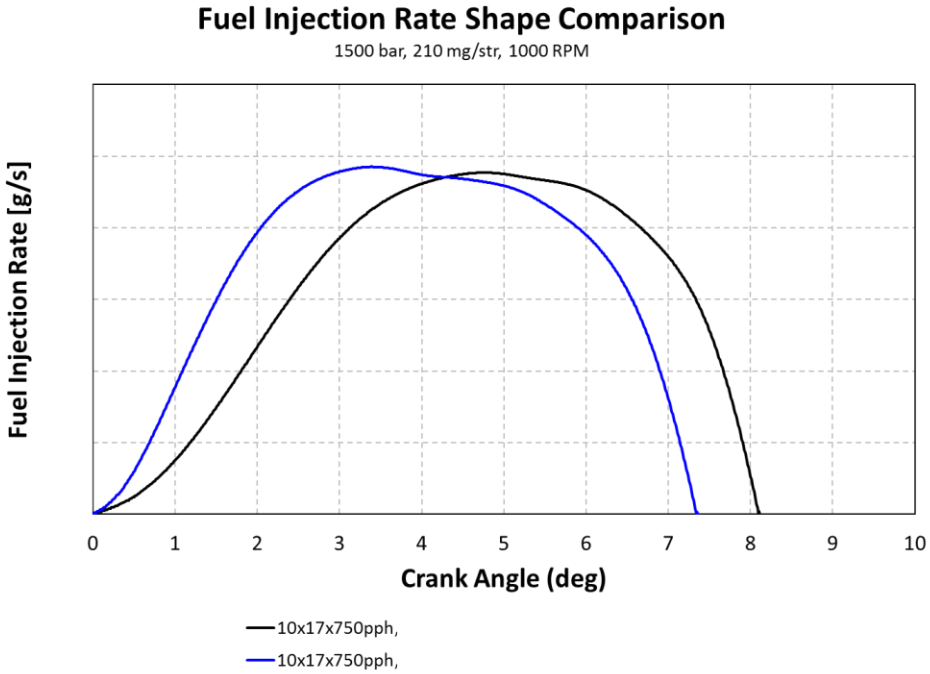

Figure 235: Comparison of Fuel Injection Rate for Method #1 and Method #2

The increased rate of injection observed in Figure 235resulted in the closed cycle efficiency shared below. The data shared in Figure 236 is again generated by sweeping the start of injection at a fixed rail pressure, in this case 1200 bar.

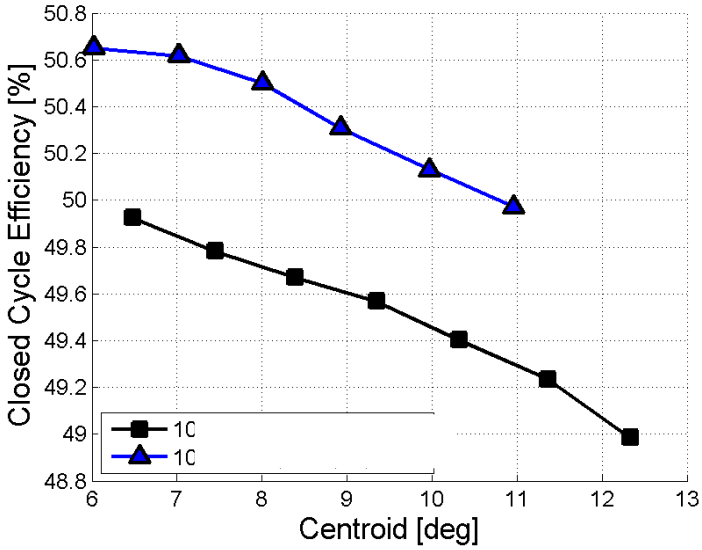

Figure 236: Closed Cycle Efficiency Comparison at 1000 RPM, 2034 Nm (~210 mg/stroke) for Method #1 and Method #2

A comparison of the heat release rate corresponding to a start of injection of 3 dBTDC from the data shared in Figure 236 is shared below in Figure 237. The heat release shows how the faster rate of fuel injection increases the rate of heat release of the initial burn and increases the peak heat release rate.

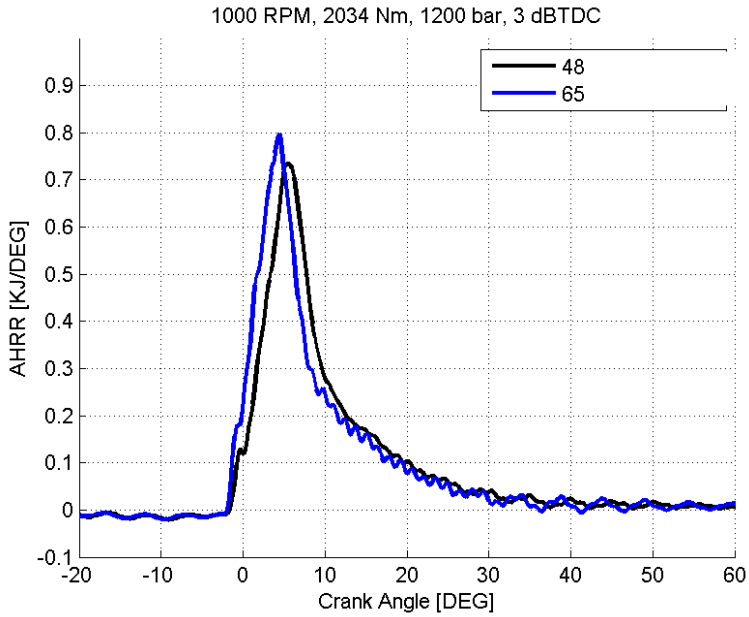

Figure 237: Heat Release Rate Comparison at 1000 RPM, 2034 Nm, 1200 bar, 3 dBTDC for Method #1 and Method #2

The next modification in the injector evaluations was a modification to the location of the needle guide, changing from an upper guided needle to a lower. In this case there were no changes to the injector rate shape, yielding an as expected similar heat release rate, seen in Figure 238. However, an unexpected significant change in closed cycle efficiency was also observed, shown below in Figure 239.

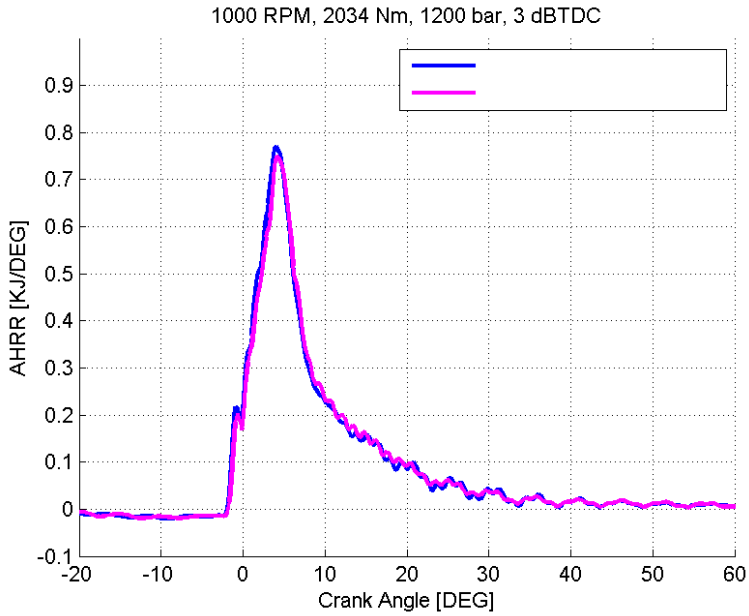

Figure 238: Heat Release Rate Comparison at 1000 RPM, 2034 Nm, 1200 bar, 3 dBTDC for Upper and Lower Guided Needles

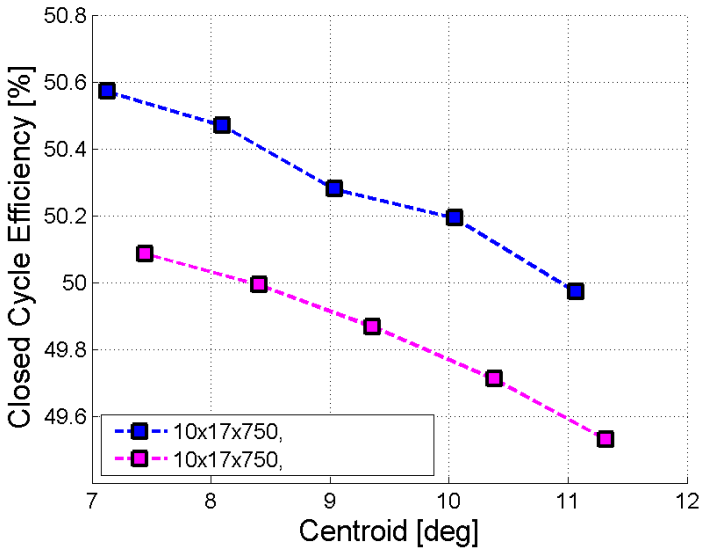

Figure 239: Closed Cycle Efficiency Comparison at 1000 RPM, 2034 Nm (~210 mg/stroke) for Upper and Lower Guided Needles

The final injector revision was limited to an increased opening injection rate. Figure 240 below illustrates the increased rate yields a 100% increase in the rate of the initial injection ramp.

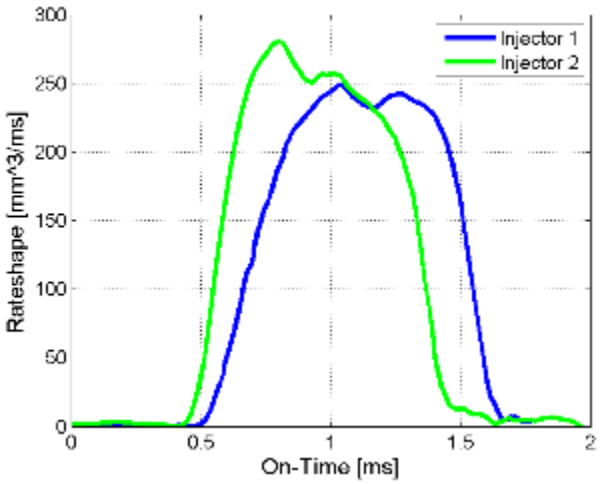

Figure 240: Increased Injector Opening Rate Shape Comparison

The corresponding heat release comparison for the increased outlet orifice injectors is found in Figure 241. The heat release corresponding to the increased outlet orifice (Injector 2) exhibits additional premixed heat release at the onset of combustion, a result of additional fuel being injected prior to the initiation of combustion.

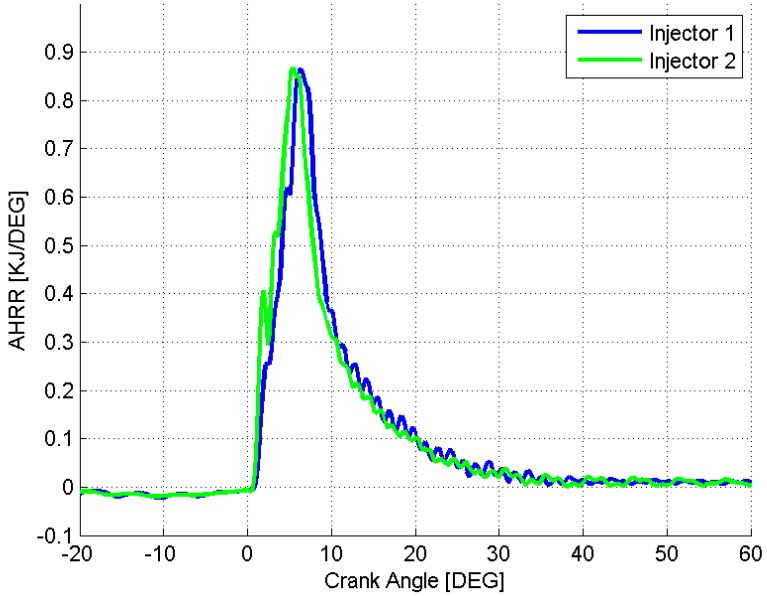

Figure 241: Increased Injector Opening Heat Release Comparison

Piston Bowl Designs

During the prior SuperTruck project a Genetic Algorithm (GA) process was followed in combustion CFD to explore the space of piston bowl profiles with a higher cup flow injector (600 pph). The process was guided by a merit function that was optimized at two operating conditions (A100 and C100). The inflection points utilized in the GA process are shown in Figure 242 and the combustion CFD predicted performance improvement at A100 is shown in Figure 243. The resulting GA optimized piston bowl profile is shown in Figure 244 as "Gen 116, Indiv 3 profile".

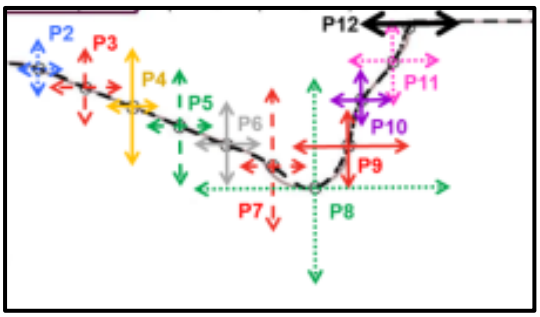

Figure 242: Genetic Algorithm Inflection Points

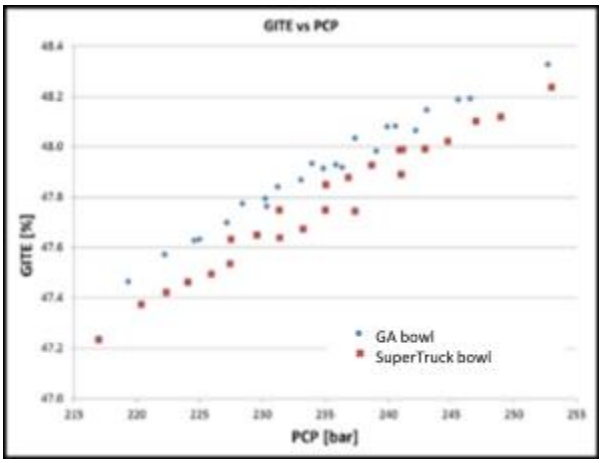

Figure 243: Combustion CFD Genetic Algorithm Performance Comparison at A100

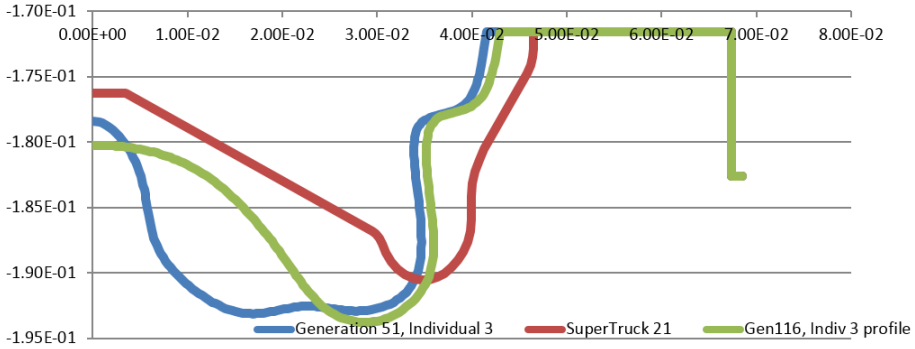

Figure 244: Genetic Algorithm Optimized Piston Bowl Profile

Like the testing process completed with the higher cup flow injectors, the GA pistons were run through a random space-fill DOE design with independent variables of main SOI, rail pressure, EGR valve position, and VGT position. The resulting engine data was then used to create an MLR model which was optimized to maximize brake efficiency at a given BSNOx level while staying within mechanical limits.

Results from the BP1 engine data optimization are shown in Figure 245. CFD analysis had previously indicated an approximately 0.2% closed-cycle efficiency improvement at A100 (1000 RPM, 2373 N-m), shown in Figure 245, however, engine testing at BP1 (1000 RPM, 2034 N-m) showed an approximately 0.3% closed-cycle penalty. Where the GA pistons did demonstrate an improvement was with smoke, a comparison plot is shared in Figure 246. Given the smoke challenges that have been found with the higher cup flow injectors, this smoke improvement could be an enabling technology.

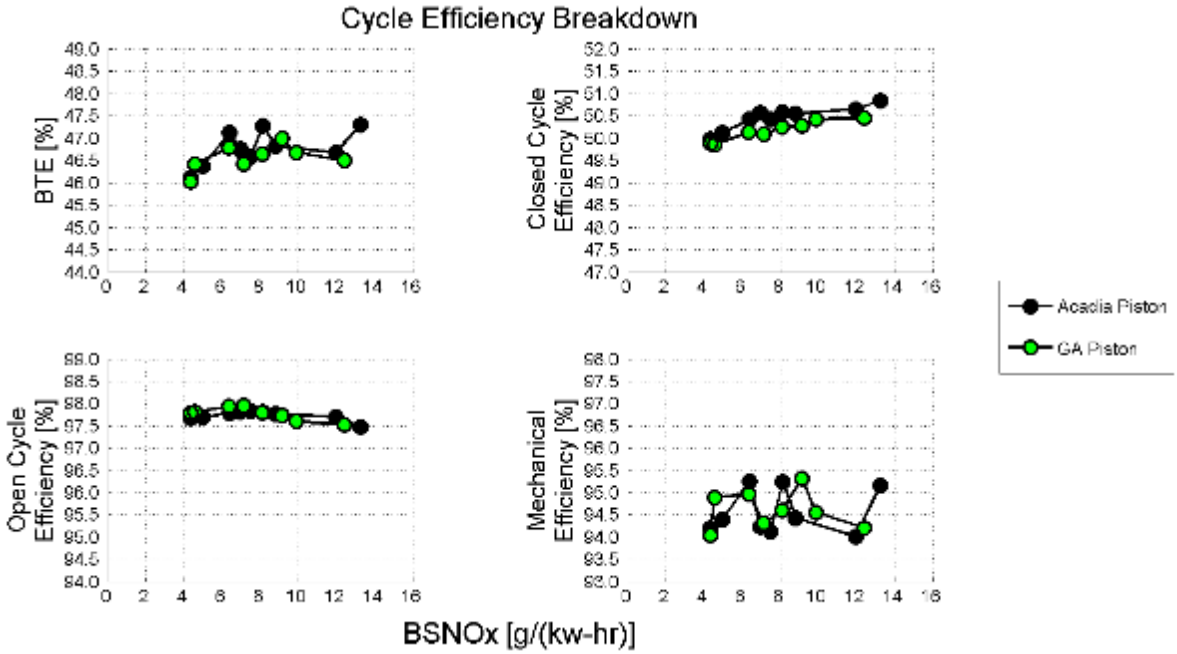

Figure 245: GA Piston Performance at BP1, Cycle Efficiencies vs. BSNOx

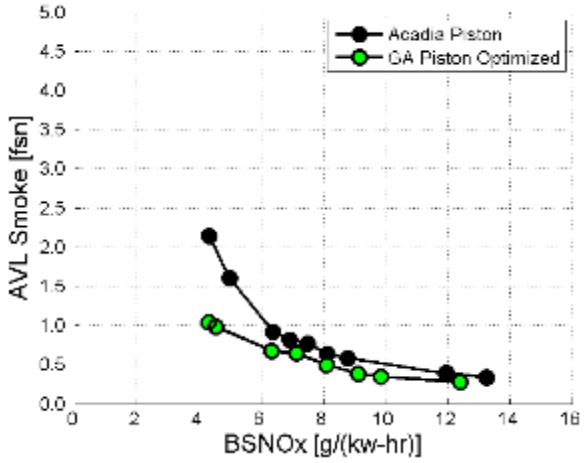

Figure 246: GA Piston Performance at BP1, Smoke vs. BSNOx

Engine testing was also completed at CP2 (1130 RPM, 1437 N-m) where the GA pistons yielded a larger performance penalty as reflected in the brake-thermal efficiency and closed cycle efficiency performance shown in Figure 247.

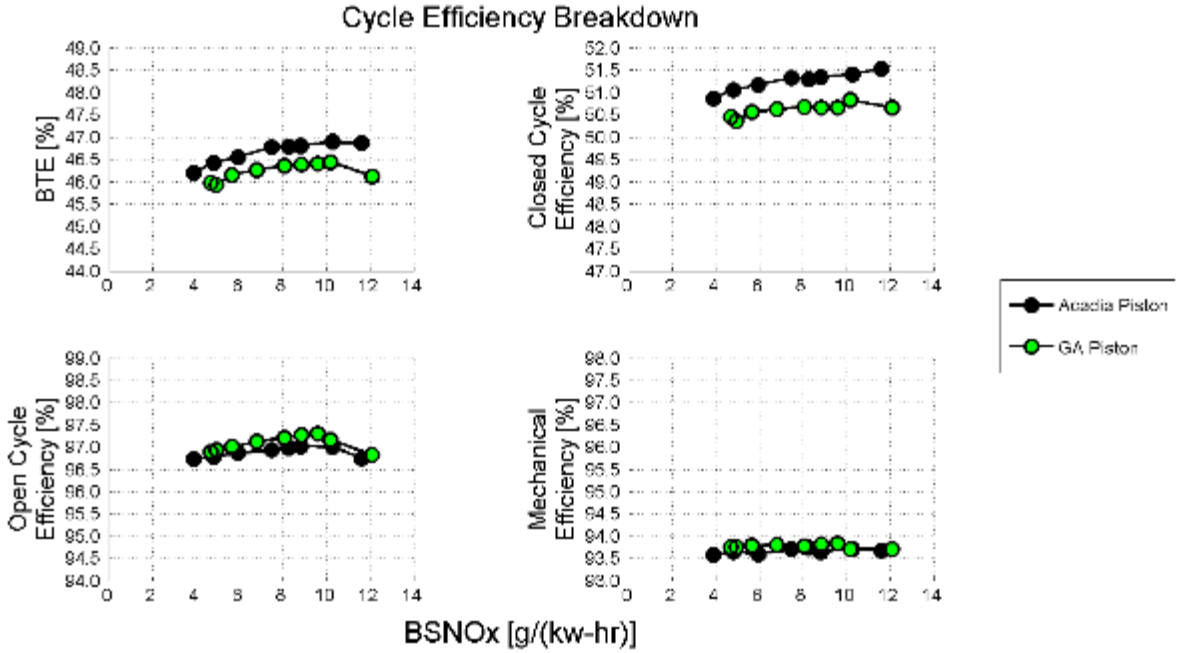

Figure 247: GA Piston Performance at CP2, Cycle Efficiencies vs. BSNOx

3.7 Aftertreatment Integration Testing

The program has the main objective of demonstrating 55% 'peak BTE'. Hence, the program focused on achieving this at a fixed operating point, or extended in speed/torque space to a very small region around the selected nominal operating point. Program also has a secondary objective of demonstrating 2010 tail pipe emission levels on certification cycles (FTP & RMCSET). A program level decision was also made to focus on demonstrating emissions reduction performance for a 'hot' FTP only. With all these objectives, from

Aftertreatment sub-system architecture selection standpoint, the focus was on lowering the system delta-P as much as possible, while ensuring sufficient NOx conversion efficiency for a hot FTP cycle, with relatively simple Ammonia injection strategies.

Improving BTE on engine leads to reduced turbine out temperatures with higher close cycle efficiency. Engine out NOx increases with higher BTE engines due to hotter in-cylinder combustion flame temperatures and the lower back pressure provided by the aftertreatment materializes into BTE improvements due to improved open cycle efficiency. Therefore, primary focus initially was:

- Redesign and optimization of the aftertreatment system to meet program goals of emission compliance and BTE improvement

System Backpressure Study

A study to lower system back pressure was conducted evaluating:

- Substrates for wall flow filters.
- Decomposition reactor design.

Two primary systems utilized for LP EGR evaluation are the current product ISX switch back [SW] system and the next generation single module [SM] system. The two systems are shown in Figure 248 below.

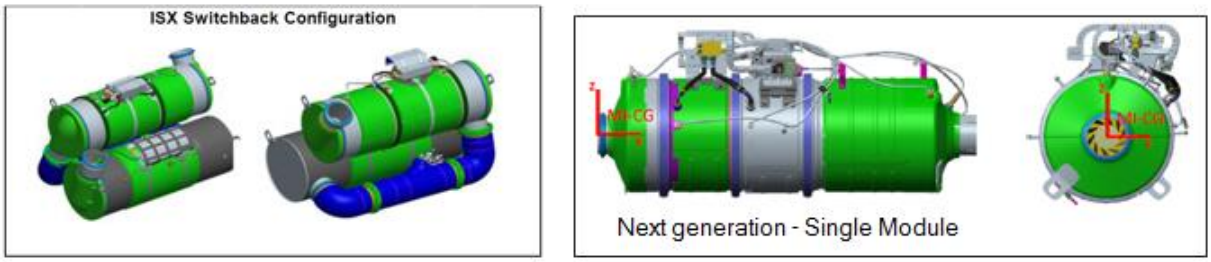

Figure 248: 55BTE Mule Aftertreatment System

On the mule aftertreatment system, ~30% of system back pressure is contributed by the diesel particulate filter. Supplier information, model estimation of back pressure and historical testing data on prototype type substrates has led to more than 50% reduction in backpressure at the chosen BTE demonstration point as shown in Figure 249. Estimations are based on supplier provided information for a clean (0g/L) soot load filter.

Wall flow filters with SCR wash coat [SCR+F] have also been investigated for the provision of close coupling of the SCR catalyst without significant tear up of the mule aftertreatment system. With higher engine out NOx, maximizing SCR warm up rates to peak operating temperatures are critical for compliance in emissions. Tradeoffs with SCR+Fs are back pressure increase, lower passive oxidation (NO_2 based) of particulate matter [PM] in the filter and increase active regeneration. These effects can be mitigated by significantly lowering engine out PM. Figure 249, shows the total back pressure with an SCR+F.

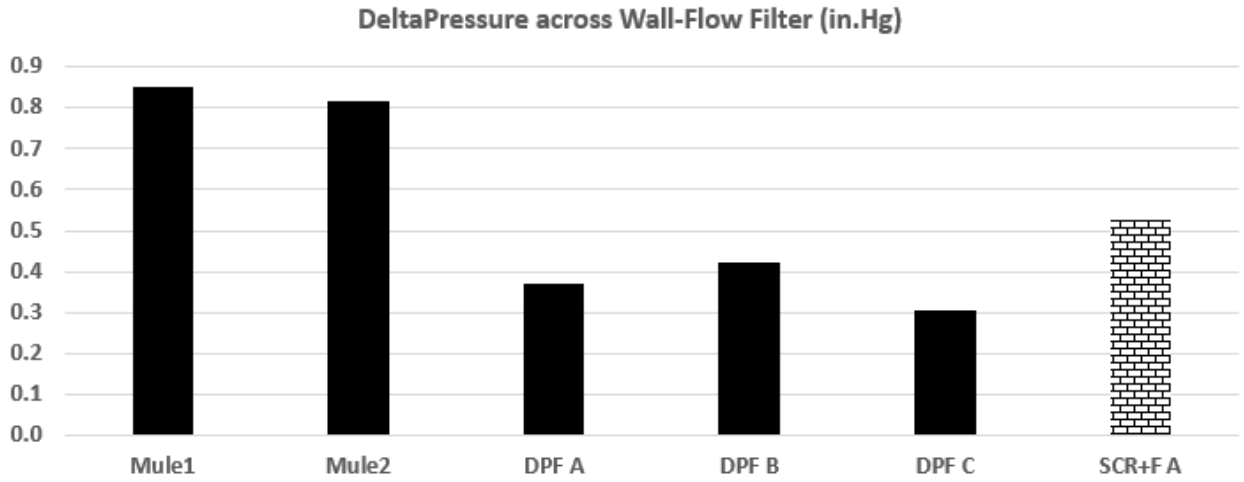

Figure 249: Delta Pressure across Wall Flow Filters (in. Hg) @ 0.375 ACMS

Based on back pressure reduction for various prototype substrates investigated, hardware investigation of 3 DPF substrates and at least 1 SCR+F substrate will be conducted to optimize back pressure, NOx reduction and mechanical robustness.

Utilization of Ammonia as the reductant instead of Diesel Exhaust Fluid [DEF] will enable earlier injection during warm up, better uniformity and mixing of the exhaust gas and ammonia. Another key benefit is the reduction of the complex decomposition reduction tube to a short mixer as ammonia readily participates in the reduction reaction and is a gas to gas mixing which is easier. Design and CFD work has been initiated to start development based-off and in-house ammonia gas mixer developed for a light-duty application. Design freeze and prototype order of the mixer will be accomplished in Q1 of 2017. Figure 250 shows expected reduction in system back pressure as a function of volumetric flow of exhaust.

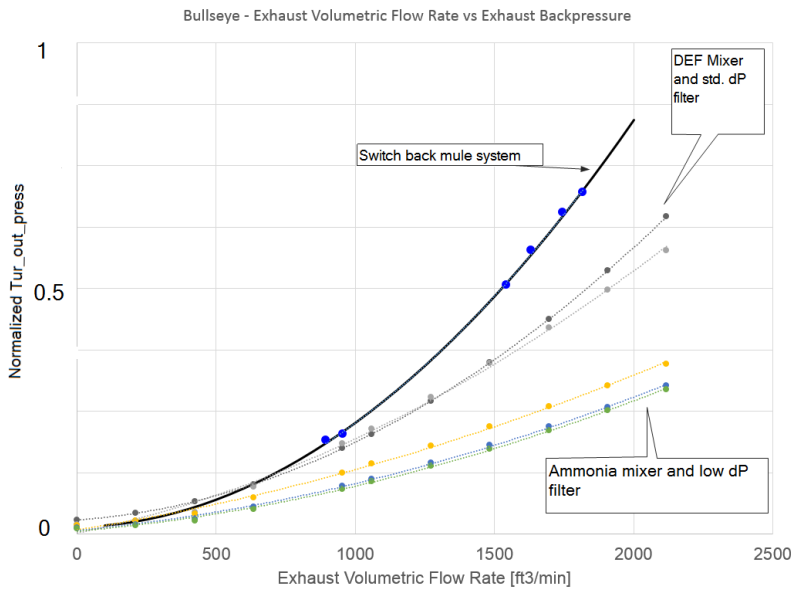

Figure 250: Normalized System Backpressure vs. Volumetric Flow Rate

NOx Reduction Study

With expected increase to engine out NOx for high BTE engines, aftertreatment requirements for reduction of NOx over the FTP cycle is shown in Figure 251 below. For engines with engine out NOx greater than 6 g/hp.hr requires improvement of NOx reduction on both cold and warm FTP compared to expected mule aftertreatment performance. Performance outside the green highlighted region in Figure 251 requires changes to the baseline aftertreatment architecture.

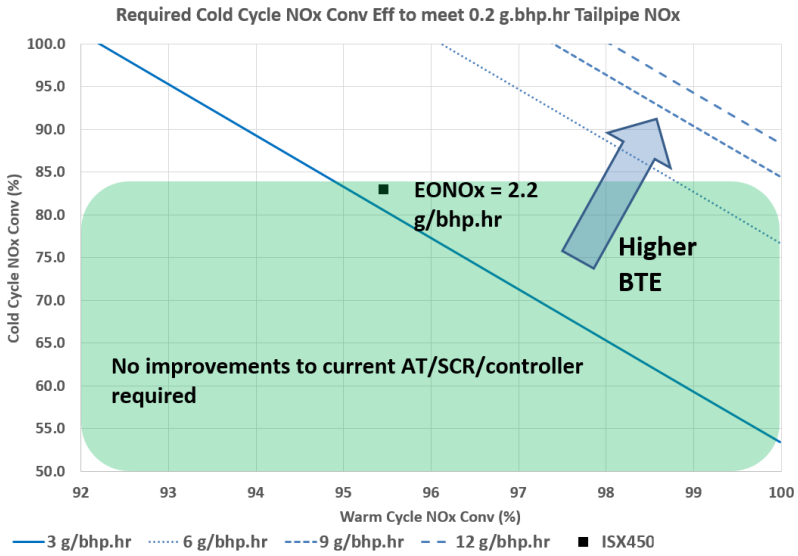

Figure 251: Cold vs Warm FTP NOx Reduction Requirement (%)

Based on the FTP data on current production systems, NOx released at the tail pipe during the warm up portion of the cold FTP is more than 50% of the composite. Methods to improve NOx reduction during warm up are:

- Reduction in upstream thermal mass of the SCR,
- Higher turbine out temperatures,
- Passive NOx adsorbers
- Lower engine out NOx during warm up
- SCR catalyst technology (wash coat and substrate)

Utilizing AVL BOOST simulation, the impact of order of catalysts and SCR location in the aftertreatment was evaluated. Figure 252 shows the time taken for the SCR bed temperature to reach 190°C, which is the minimum temperature to observe >90% NOx reduction in favorable reactant composition. Four architectures were simulated utilizing three inlet conditions, which can impact the aftertreatment inlet gas temperature. Underfloor system utilizes an 8 feet down pipe, whereas the adiabatic insulation is the entitlement of external insulation on the down pipe. The close coupled architecture simulates the removal of the down pipe itself to further reduce thermal mass upstream of the aftertreatment. Up to 35% reduction in warm up time is observed by relocating the DPF downstream of the SCR or by utilizing an SCR+F system. Utilizing these results, chemistry simulations with SCR and SCR+F will be conducted to analyze NOx reduction capabilities over the cold and warm FTP cycles. This analysis approach will help choose potential architectures for leveraging higher engine out NOx and remain emission compliant.

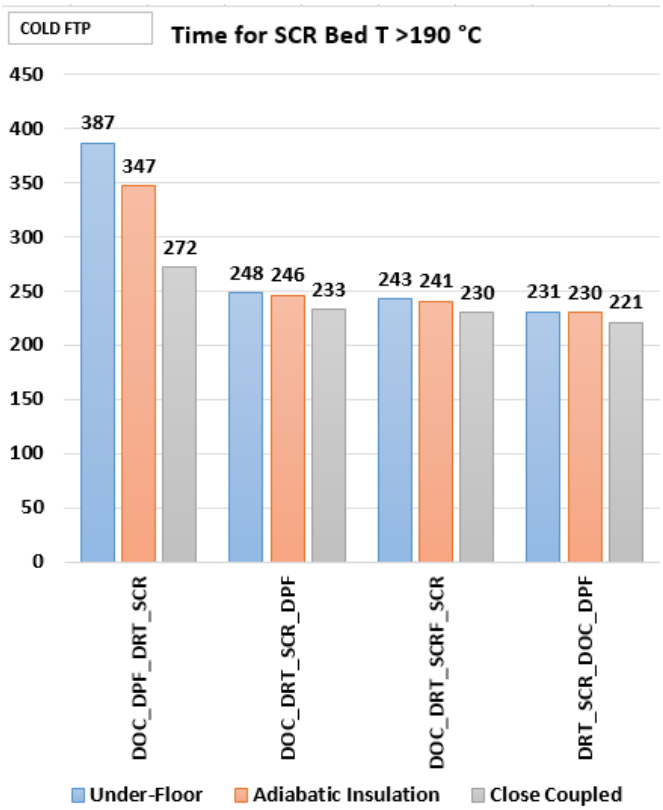

Figure 252: Time for SCR Bed Temperature exceed 190°C

With the studies conducted thus far, the next steps considered to continue the AT studies for the rest of the program are as follows:

- A simulation study evaluating the impact to tail pipe NOx for the architectures showing faster warm up are being conducted. Strategies to optimize ammonia delivery will also be investigated as part of the study.
- Wash coat selection for SCR catalysts based on reactor data and simulations
- Optimization of flow through substrates and aftertreatment packaging will be conducted to evaluate further reduction in system back pressure of the aftertreatment system.
- Design and analysis of the ammonia mixer
- Procurement and evaluation of low backpressure filter technologies

Optimization of the aftertreatment system to enable low pressure EGR, meet engine out back pressure limits and meet target tail pipe emission at higher engine out NOx levels are the key parameters taken into consideration. Following section is a summary of the simulation exercise conducted to:

- Study SCR NOX reduction performance utilizing AVL BOOST for higher levels of engine out NOx.

SCR Performance Study

Based on baseline aftertreatment cycle performance over the HD-FTP and RMCSET, performance over the cold FTP was the limiting factor to meet tail pipe targets considering the significant delay in warmup of the SCR. In the previous quarter, expected SCR warm up rate for various aftertreatment architectures were simulated utilizing AVL BOOST. Reducing thermal mass upstream of the SCR by close coupling and moving

the DPF downstream or utilizing an SCR on DPF was identified as the best approach to minimize warm up time for the SCR catalyst.

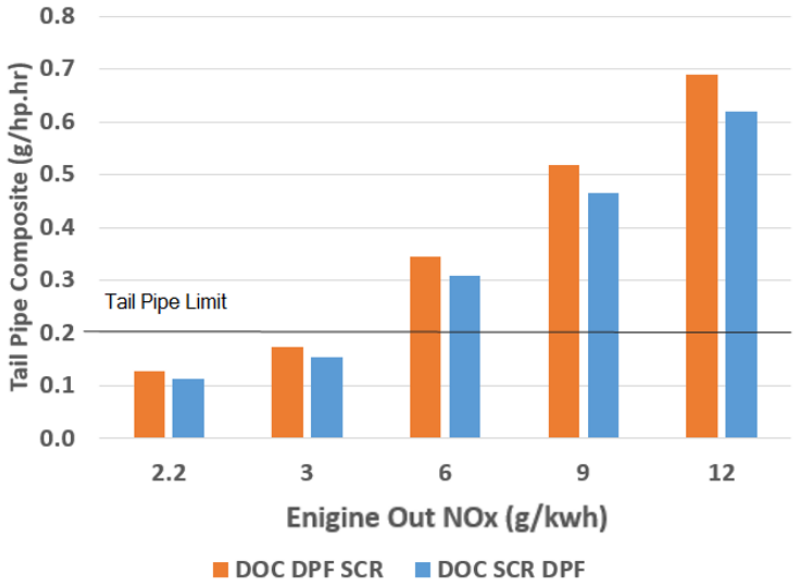

Figure 253: Expected Composite Tail Pipe NOx as a function of Engine-Out NOx (ANR: 1)

Figure 253 shows the expected tail pipe composite NOx over the HD-FTP when the ammonia controller is fixed at 1 ANR. The aftertreatment architecture with SCR upstream of the DPF indicates slightly better NOx reduction due to improvements observed during the warm up of the cold FTP. Tail pipe NOx levels are below 0.2 g/bhp.hr for lower levels of engine out NOx, which represents typical current product performance. With increase in engine out NOx, beyond a certain threshold, the amount of ammonia stored in the SCR during the warm FTP is significantly lower as this simulation utilizes a constant 1 ANR reductant dosing strategy. It is therefore observed that the level of ammonia storage becomes a limiting factor with increase in engine out NOx. With a higher weightage for the warm FTP, the composite tail pipe NOx levels exceed the US HD on-highway emission thresholds for the baseline SCR at a constant 1 ANR. To further probe the response of the SCR catalyst with higher levels of ammonia, another simulation study was conducted with the same boundary conditions except increasing the ANR dosing strategy from 1 to 2. Figure 254 shows the reduction in tail pipe composite NOx for the baseline aftertreatment system by doubling the rate of ammonia dosed. A significant improvement in SCR performance is observed due to increase level of stored ammonia in the SCR. Dosing at very high ANRs such as 2 also have detrimental effects such as poor ammonia slip control which can lead to creation of NOx over the AMOX and very low fluid economy. From these simulation studies, it can be inferred that both temperature and ammonia storage management are necessary for optimizing the SCR performance for higher engine out NOx levels.

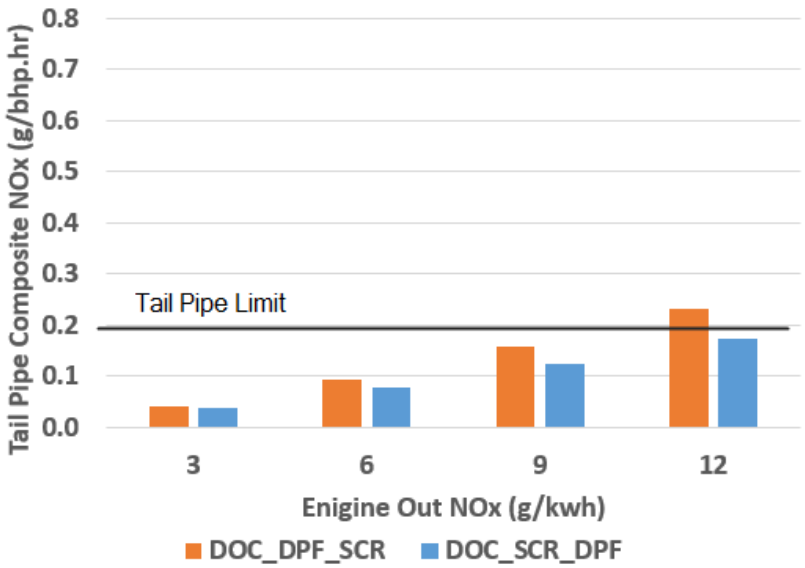

Figure 254: Expected Composite Tail Pipe NOx as a function of Engine-Out NOx (ANR: 2)

In order to enable optimal SCR function for operating with higher engine out NOx without negatively impacting engine backpressure, the following options are being considered:

- SCR on DPF catalyst enables a significant increase in total SCR wash coat volume maintaining total aftertreatment catalyst volume neutral
- Extruded SCR catalysts which significantly increases wash coat per unit volume of element
- SCR wash coated on high porosity flow through substrates, which also enables higher wash coat per unit volume of substrate
- Scaling of the ammonia mixer and delivery system to accommodate for higher reductant flow rates

With the backpressure studies and SCR performance simulation studies conducted thus far, the next steps considered to continue the AT studies for the rest of the program are as follows:

Sizing studies based on supplier data and simulation were conducted, as next steps, to integrate these technologies on the next generation single module system.

- Finalize SCR technology for single module system
- Design and analysis of the ammonia mixer
- Procurement and evaluation of low backpressure filter technologies

Aftertreatment Simulation and Analysis

Utilizing simulation results, supplier provided component level performance data, test cell spatial constraints and integration requirements with engine and waste heat recovery systems, in this quarter:

- Aftertreatment packaging for test cell evaluation was finalized by procuring the ammonia mixer and ordering low back pressure end cones
- Ammonia cart sizing requirements were completed and appropriate modifications have been ordered.
- Advanced SCR technology was procured to replace the production SCR upon completion of component evaluation.

Aftertreatment Packaging

The finalized aftertreatment packaging to be utilized for test cell evaluation that includes a Diesel Particulate Filter (DPF) is shown in Figure 255 and a similar system with a Selective Catalytic Reduction catalyst on DPF (SCR-F) is shown in Figure 256. This system takes into consideration the learning from the MY2017 production aftertreatment system to reduce back pressure and package in close proximity to reduce upstream thermal mass as compared to a MY2013 system. The modification to end cones and the reductant mixer will lead to an increase in overall length but significantly reduces back pressure while maintaining the required flow distribution as that of a production aftertreatment system.

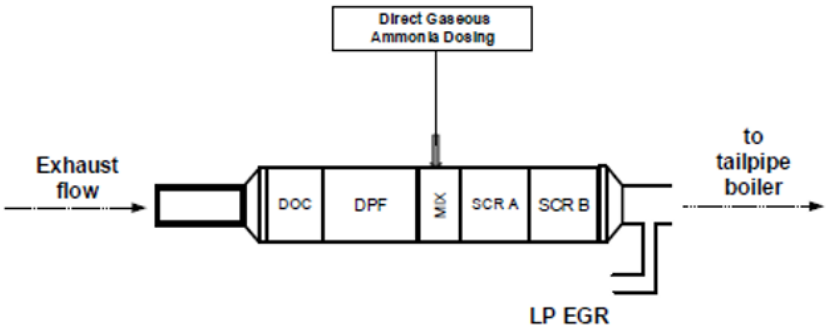

Figure 255: Aftertreatment Packaging Layout with DPF

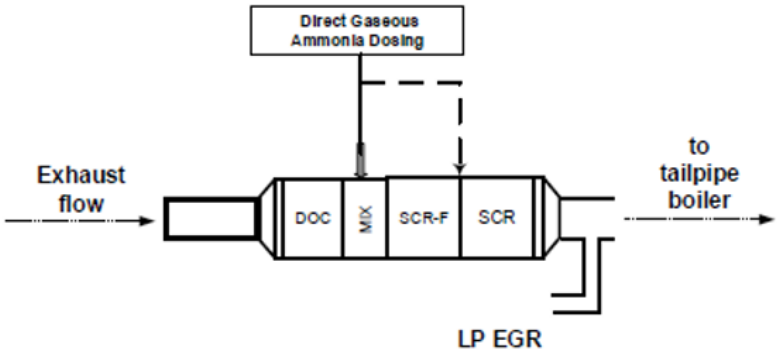

Figure 256: Aftertreatment Packaging Layout with SCR-F

Table 17 shows the various architectures that will be evaluated for back pressure. Based on availability of resources for reductant dosing and emission measurements, NOx reduction measurements during back pressure evaluation will be accomplished. Test cell results from back pressure testing and warm up rates of the aftertreatment system will help determine the optimal particulate filter and SCR technology that will be utilized for the final demonstration work.

Table 17: Aftertreatment Architecture for Testing

Architecture 1	DOC + DPF A + concentric mixer + SCR 1
Architecture 2	DOC + DPF B + concentric mixer + SCR 1
Architecture 3	DOC + DPF C + concentric mixer + SCR 1
Architecture 4	DOC + DPF C + concentric mixer + SCR 2
Architecture 5	DOC + concentric mixer + SCRF A + SCR 2

A concentric styled mixer was developed for introduction of gaseous ammonia as the reductant for reducing NOx over the SCR / SCR-F. CFD analysis was performed by the advanced design team to develop and finally procure the mixer. This mixer matches the space claim of the production urea decomposition reactor but reduces back pressure by ~99% and meets the required uniformity index to ensure optimal utilization of

the reductant to provide effective NOx reduction. The ammonia mixer development will be discussed in more detail in other parts of this report.

The end cones of the production aftertreatment system were designed taking into consideration space constraints on various applications, thereby increasing restriction. Efforts to optimize the end cones to better integrate in the test cell and mate efficiently with the waste heat recovery system led to the development of new end cones. A schematic of the proposed end cone is shown in Figure 257.

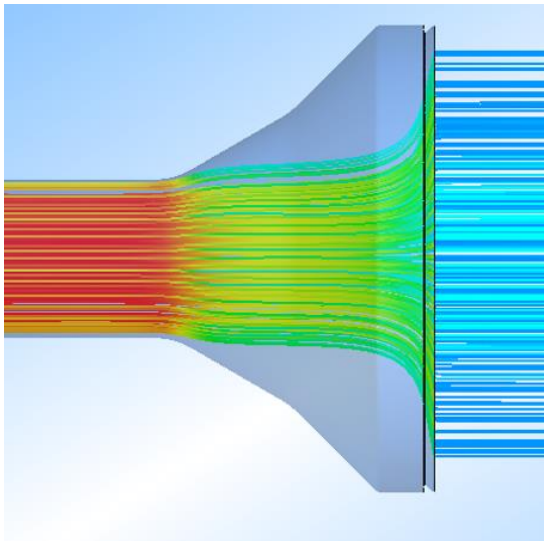

Figure 257: Schematic of Modified End Cone

Ammonia Cart Optimization

An existing ammonia cart utilized for the introduction of anhydrous ammonia will be utilized for test cell evaluation work. Modifications to the mass flow controllers are being made to ensure optimal delivery of ammonia. Taking into consideration expected engine out NOx flow rates and estimated ratio of ammonia to NOx for effective NOx reduction across the regulatory cycles, two mass flow controllers of 15 and 30 liters / minute have been ordered. The integration of the ammonia cart with the new mass flow controllers and required communication between engine and test cell will be completed in this quarter.

SCR Technology Selection

An extruded SCR technology has been considered as a potential replacement of the production SCR for this project. This technology shows the potential to reduce or maintain the overall size of the SCR required for higher engine out NOx systems by increasing the total available zeolite per unit volume of catalyst. This increase of total available catalyst, will provide a higher ammonia storage capacity, better NOx reduction during lower operation temperatures and similar or lower levels of back pressure. Test cell evaluation of this technology is required to better quantify its performance.

With all the analysis & supplier communication & procurement studies conducted thus far, the final and important step left in the program, from ATI (Aftertreatment Integration) standpoint:

- Test cell evaluation of the various aftertreatment architectures for back pressure and NOx reduction.

Aftertreatment System Development and Testing for Backpressure

The following section focuses on summary of testing results for meeting backpressure requirement:

Aftertreatment Systems Considered for BP and final testing

Figure 258 and Figure 259 illustrate various After Treatment Systems tested in the Test Cell. Figure 258 shows the DOC, DPF, NH3 Mixer, SCR and SCR/ASC installed in the test cell, with pressure sensors located at Turbo_out, DPF_in, DPF_Out and system out location. There was also a dP sensor across the DPF. Figure 259 shows the DOC, NH3 Mixer, SCRF and SCR/ASC installed in the test cell, with pressure sensors located at Turbo_out, SCRF_in, SCRF_out and system out location. There was also a dP sensor across the SCRF.

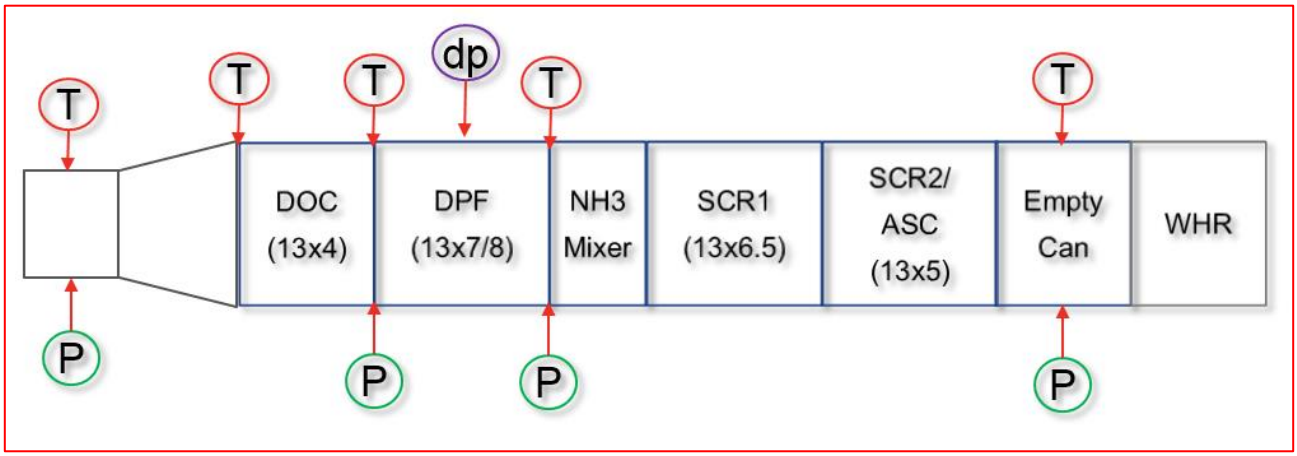

Figure 258: Aftertreatment System with DOC, DPF, NH3 Mixer, SCR1 and SCR/ASC with temperature, pressure and dP sensor locations

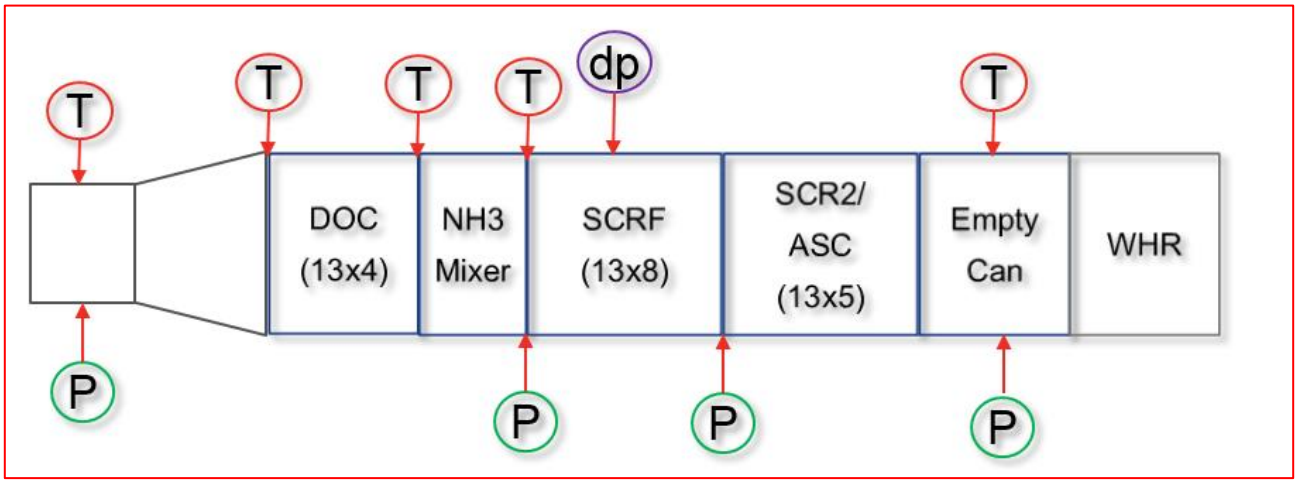

Figure 259: AT System with DOC, NH3 Mixer, SCRF and SCR/ASC with temperature, pressure and dP sensor locations

Substrate Types

The following three Diesel Particulate Filters and one SCRF units were tested as part of the Aftertreatment System to meet the Aftertreatment System backpressure requirement.

- DPF : Ibiden SiC - 13 x 7 (300/7)
- LDPF1 : Corning TWF – 13 x 8 (200/8)

- LDPF2 : Corning AC/ACT – 13 x 7 (300x9)
- SCRF : Corning ACT – 13 x 8 (300x9)

Results

The ATS were tested for backpressure at different flow rates around 1010 rpm. Figure 260 shows the comparison of DP of the various filter types vs flow rates. The results indicate the TWF of Corning has the lowest DP among the various filters. Figure 261 shows the comparison of various ATS DP vs flow rates. The results indicate the DOC, SCRF and SCR/ASC aftertreatment system has the lowest backpressure and meets the DP target of 1.5 inches of mercury at design point.

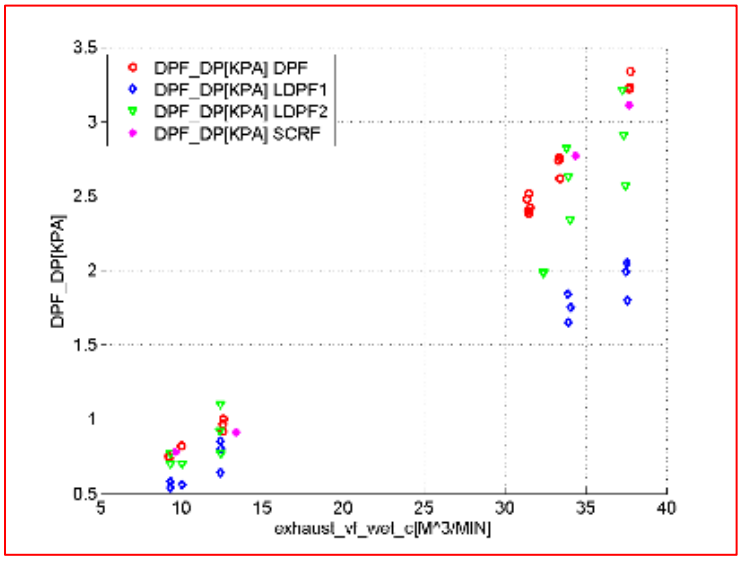

Figure 260 : Component dP vs Flow Results

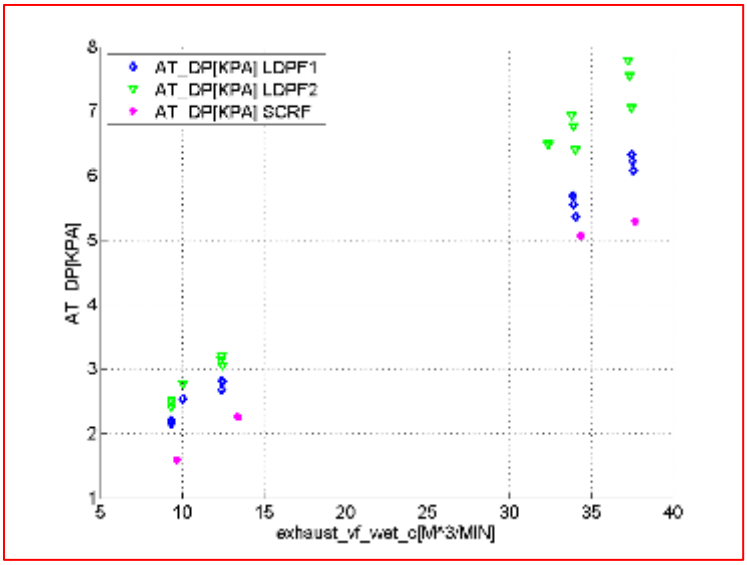

Figure 261 : ATS DP vs Flow Results

3.8 Waste Heat Recovery System Overview

The development of an advanced waste heat recovery (WHR) system to aid in achieving maximum engine thermal efficiency was a critical aspect of the 55% BTE program. To improve energy recovery, Cummins designed, produced, and demonstrated a unique dual-entry-turbine WHR system, based on organic Rankine cycle (ORC) technology. At the final engine demonstration point, the system provided 19.3 kW of net mechanical power back to the engine, improving engine BTE by 4.30 percentage points and exceeding the original performance estimates for the system. This was accomplished while using R1233zd(E) as the working-fluid; a non-toxic, non-flammable next-generation refrigerant with low GWP and near-zero ODP (reported values of 1.0 and 0, respectively).

Despite exceeding estimated performance predictions, analysis of the final performance data indicated a number of possible areas for improvement of the WHR system. These improvements were beyond the scope of the current 55% BTE project, but if fully realized, WHR net power produced at the final demonstration conditions could be increased an additional 2.8 kW, resulting in a total BTE benefit of 4.96 percentage points. Many of these potential improvements, as well as the successful WHR developments demonstrated during the 55% program, will be carried on to future Cummins WHR systems, including those deployed under on the Cummins SuperTruck 2 program.

Over the course of the 55% BTE program, WHR development was a continuous effort and was addressed in several stages including initial simulation and design, WHR shakedown testing, and final on-engine demonstration. A summary of the major tasks and results is given here.

Simulation, Architecture Selection, and Component Design

In Q1 of 2016, exploratory work began to identify a preferred WHR system architecture based on knowledge gained from previous Cummins ORC systems, and a desire to maximize the efficiency of the engine through an aggressive WHR effort. Estimates of the available waste heat, based on predicted engine performance, were provided by the system integration team and this information was used to simulate several possible WHR architectures.

Based on the scope of the program, and decisions not to investigate drivetrain integration or extensive use of electrification, it was determined that the ORC-WHR system would be mechanically coupled to the engine. An axial flow turbine was selected as the preferred expansion device based on prior experience, which demonstrated that such devices could achieve high efficiency in a compact and robust package, and with relatively low development costs. To accommodate the necessary turbine speed, a speed-reducing gearbox was deemed necessary. A fixed single-speed reduction was accomplished through a gear train lubricated with oil compatible with the ORC working fluid, and output was provided to a drive pulley integrated into the engine's front-end accessory drive (FEAD).

To achieve the maximum WHR benefit, the ORC system was designed to recover energy from recirculated exhaust gas (EGR), main engine exhaust, engine coolant, engine oil, and mixed charge gas (combined LP EGR and compressor-out charge air). To optimize the recovery of energy, an ORC architecture featuring a 'dual loop' working fluid flow path, composed of two separate streams of working fluid under different pressures, was selected. The higher-pressure stream recovers energy from higher-temperature sources and the lower-pressure stream recovers energy from lower temperature sources.

Both streams will pass through a common expander rotor but approach that rotor through different sets of expander stator nozzles.

The system model was refined and optimized for the high side pressure of each loop, peak cycle temperature, and arrangement of heat sources. This analysis was performed at the design point to determine turbine expander parameters, feedpump parameters and heat exchanger parameters to design around. The high pressure turbine was chosen to have an inlet pressure of 3100 kPa-abs, while the low pressure turbine was selected to have an inlet pressure of 1145 kPa-abs. Both are exhausted to a common low side pressure of 217 kPa-abs. The high side pressures chosen allow maximum heat extraction and utilization for conversion to shaft power for the WHR system. Figure 262 shows the Temperature-Enthalpy diagram for both loops with the waste heat sources overlaid on the graph.

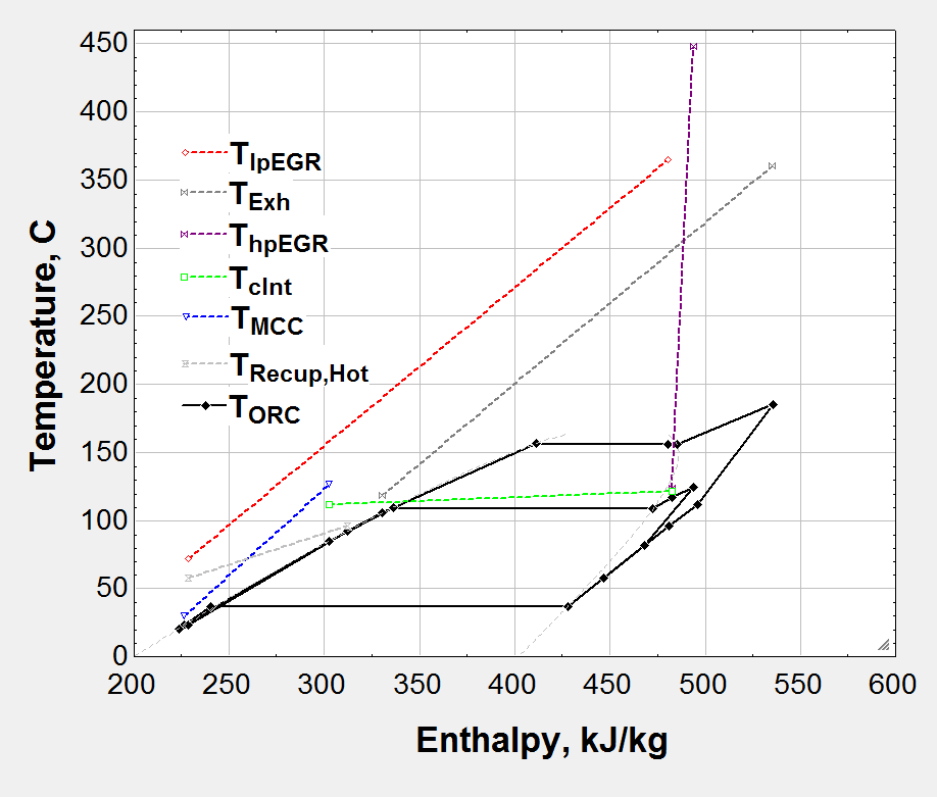

Figure 262: Temperature-Enthalpy Chart of Dual Loop ORC with Waste Heat Streams Overlaid

The Pressure-Enthalpy diagram is useful for examining the relative pressures of the dual ORC cycles and their pressure ratios across the dual entry turbine. Since the intent for the turbine expander is to have a combined wheel with separate inlet nozzles, the ratio of the pressure ratios is important to examine. The higher this ratio, the more difficult it is to design a wheel that accommodates both ORC loops with good efficiency. Figure 263 shows the P-h diagram of the cycle.

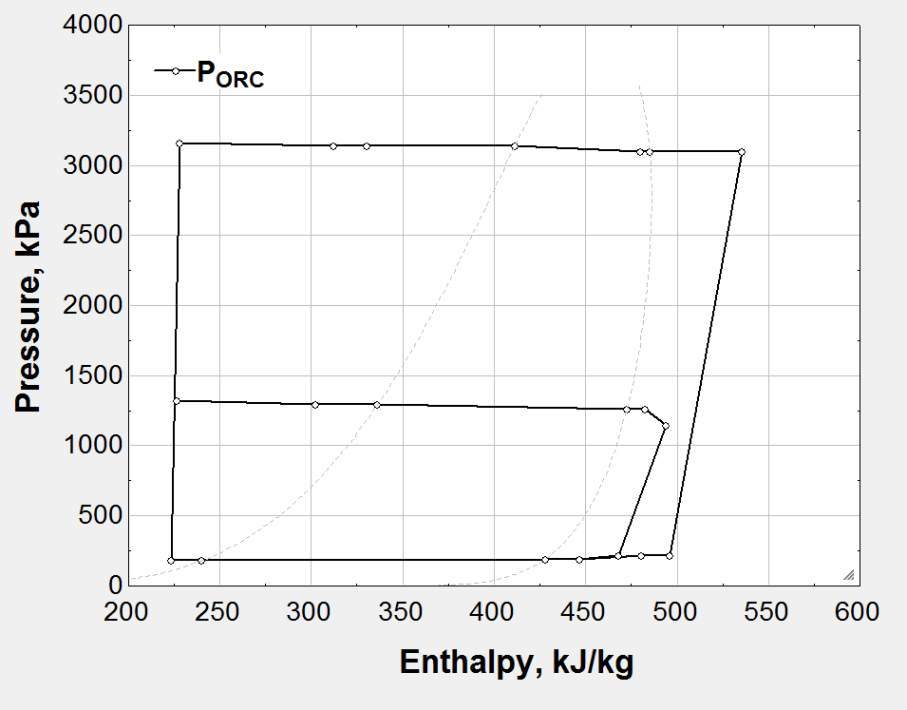

Figure 263: Pressure Enthalpy Diagram of the Dual Loop ORC

Figure 264 shows the initial WHR schematic used for the design and optimization of the turbine and key components of the system. Heat exchanger specifications were developed from the WHR cycle simulation using this architecture. It should be noted that the charge air is combined with the low-pressure loop EGR after being cooled by the EGR cooler and then this mixture is passed through the mixed charge cooler to reach the desired intake manifold temperature.

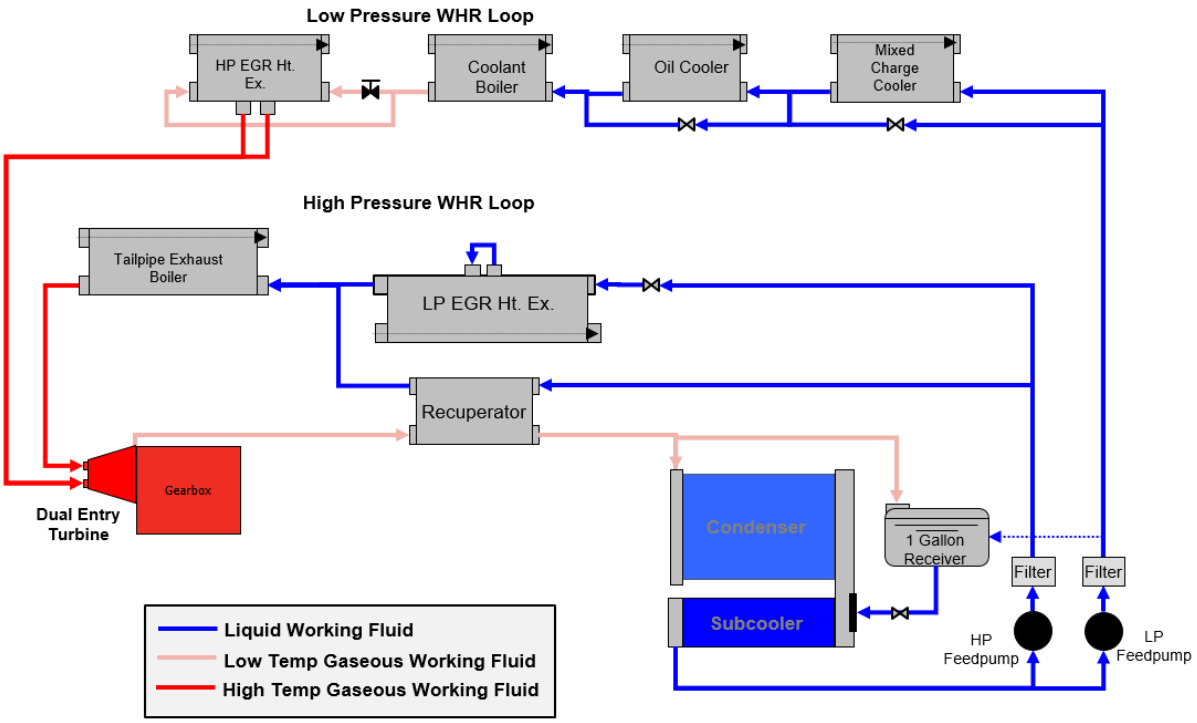

Figure 264: WHR Schematic Showing Heat Exchanger Configuration

After finalizing the system architecture and cycle-level models, work began on the design of the dual-entry turbine expander, with a planned delivered in early 2017. Barber Nichols was ultimately selected to produce the turbine based on their experience during the previous high efficiency engine demonstration and the benefits of reusing portions of the mechanical design from that effort. This helped in the cost and timeline of producing the turbine.

Analysis was conducted on the nozzle design for each loop as well as the turbine wheel. Barber Nichols was able to optimize the wheel to be capable of delivering relatively high efficiency for both loops and maximize net power output to the pinion gear. The predicted efficiency of the high pressure stage was 67% and the low pressure stage was 74%, both are total to static efficiencies. The combination of power output from the two stages was predicted to be 21.4 kW gross power at the wheel. Bearing losses and windage will reduce this power to a lower value at the pinion gear output from the turbine. The high pressure stage was predicted to produce 11.9 kW gross and the low pressure stage was predicted to produce 9.5 kW. The net power produced from the WHR system will be reduced from these values due to gearbox losses, the feedpumps and belt drive losses, which are discussed in more detail, below. Turbine analysis resulted in a design point speed of 28,000 RPM, which allowed for commonality with existing Cummins gearbox designs and facilitates re-use of the same gear design for the 10:1 gear reduction. Figure 265 shows a cross section of the design proposed by Barber Nichols for the expander.

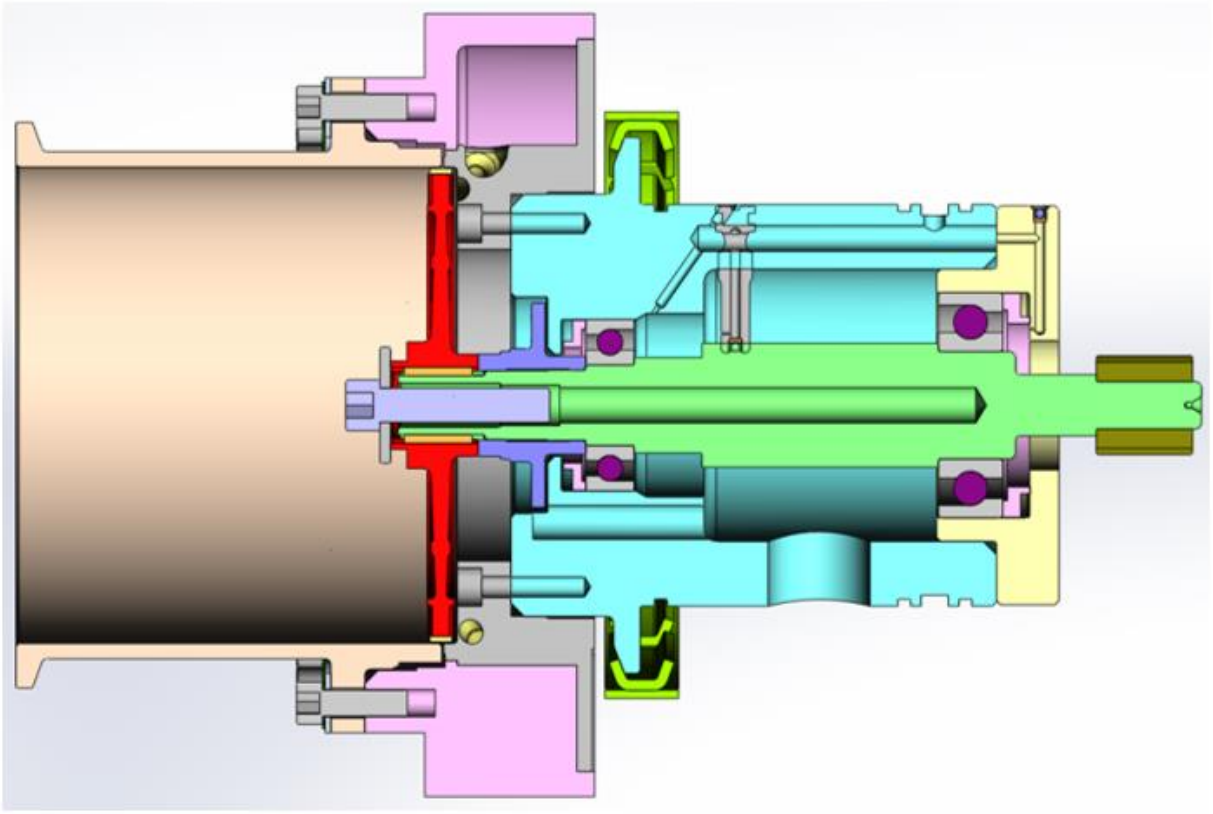

Figure 265: Cross Section of Dual Entry Turbine Expander

The analysis and design of the inlet volute was also conducted by Barber Nichols. Both a machined-from-solid version (MFS) and an additive manufacturing version (AM) were considered. AM technology would help to improve flow to the turbine nozzles and reduces issues with the internal volute seals. However, the decision was made by Cummins to proceed with the MFS version, due to lower risk of fatigue failures and porosity issues. However, the AM technology explored here is being considered for future WHR development efforts. The design of the MFS dual-inlet volute is shown in Figure 266.

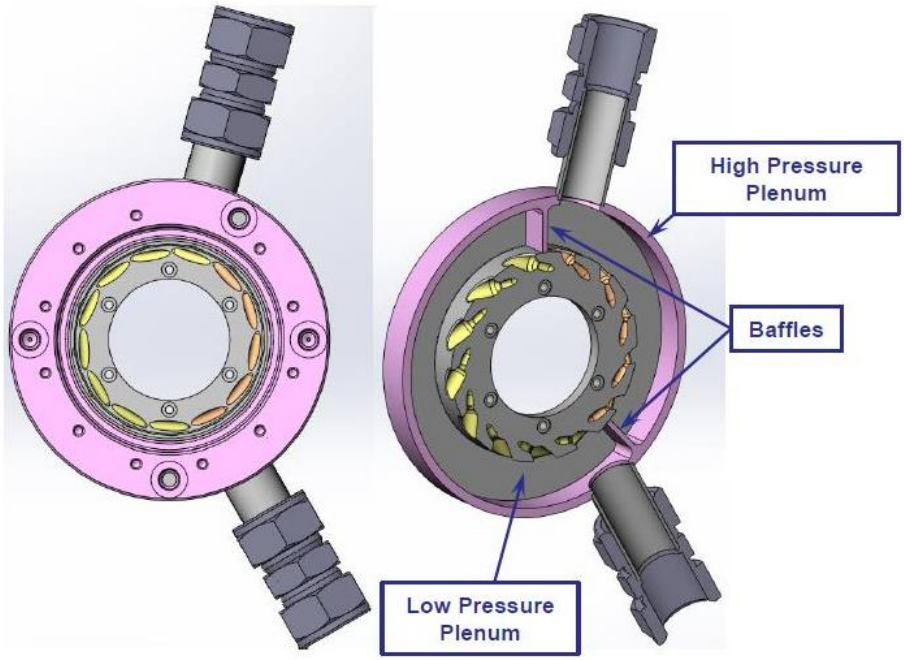

Figure 266: Machined-From-Solid Inlet Volute

The turbine design review was held with Barber Nichols in August of 2016 to review the analyses completed and overall design progress made toward meeting Cummins goals and requirements for the program. Instrumentation ports were added to the turbine housing at the inlet of each volute and the outlet of the turbine wheel to examine turbine performance at a range of operating conditions. Figure 267 displays the overall turbine assembly as designed, which was approved by Cummins for manufacturing.

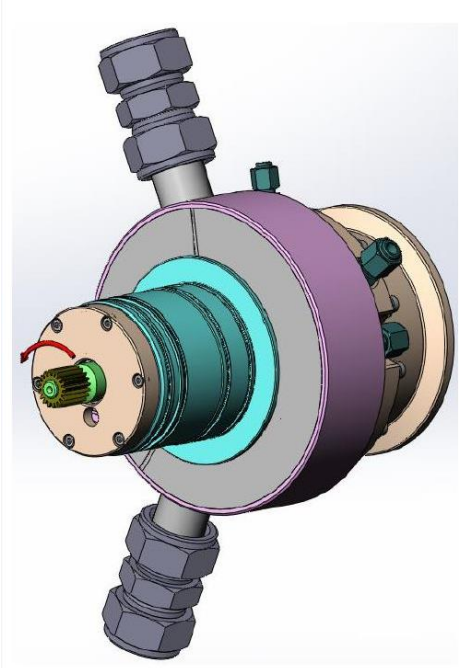

Figure 267: Barber Nichols Dual Entry Turbine

Following the turbine expander design review, the major WHR heat exchangers were ordered or procured from existing inventory. These heat exchangers enable heat extraction from charge air, high-

pressure loop EGR, exhaust, coolant, and oil. Heat exchanger specifications were developed from the WHR cycle simulation. It should be noted that the charge air is combined with the low-pressure loop EGR after being cooled by the tailpipe boiler and then this mixture is passed through the 'mixed charge cooler' to reach the desired intake manifold temperature. The schematic in Figure 268 shows the layout of heat exchangers relative to the engine processes. Note that no discrete low-pressure EGR cooler is used in this configuration, as all necessary heat removal is accomplished in the tailpipe boiler.

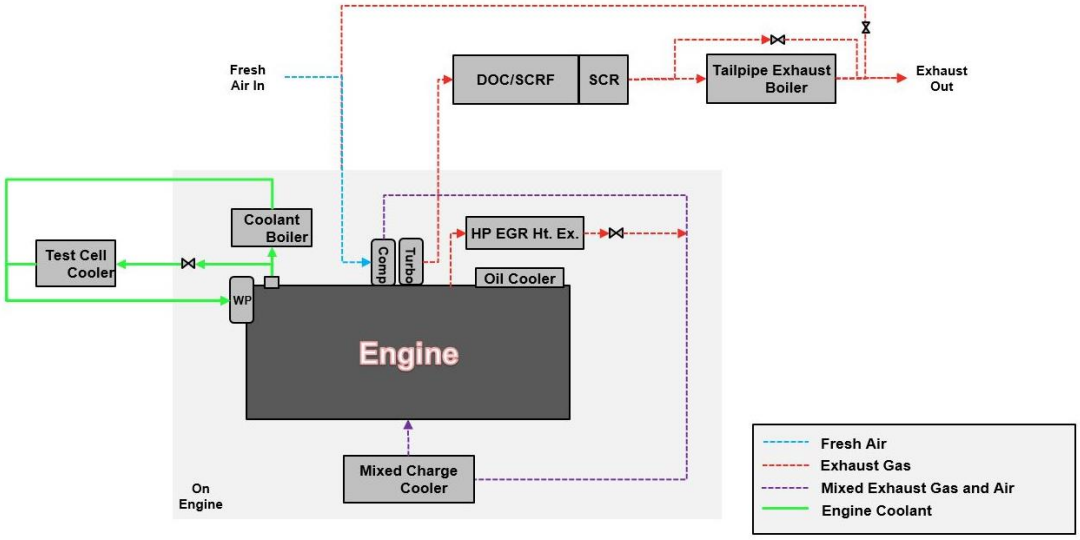

Figure 268: Schematic of Engine Layout with ORC

Component Development and Shakedown Testing

In late 2016 through early 2017, development and testing of several key WHR components was conducted. This was followed by assembly of a shakedown testing version of the WHR system, designed to allow for evaluation of key components, such as the turbine expander, lubrication system, and controls system, and to provide early experimental data on overall performance.

Component-level testing included evaluation of several possible feedpumps, an alternate mixed-charge cooler design, components of the gearbox lubrication system, gearbox windage reduction hardware, and several key system heat exchangers, such as the coolant boiler. Specifications for these components were based on cycle-level modeling and requirements for the turbine expander. The results of this early testing helped to identify the prime-path hardware for use in WHR system-level testing, and to identify areas where improvements could be made to the system as the program progressed.

By Q1 2017, all major components of the WHR system had been received, apart from the mixed charge cooler (MCC). The dual-entry turbine expander units were received along with the cast components for the gearbox and the fabricated WHR lubrication sump. These components are shown in Figure 269. All turbine and gearbox components were inspected, fit-checked, and prepared for initial leak-checks and testing.

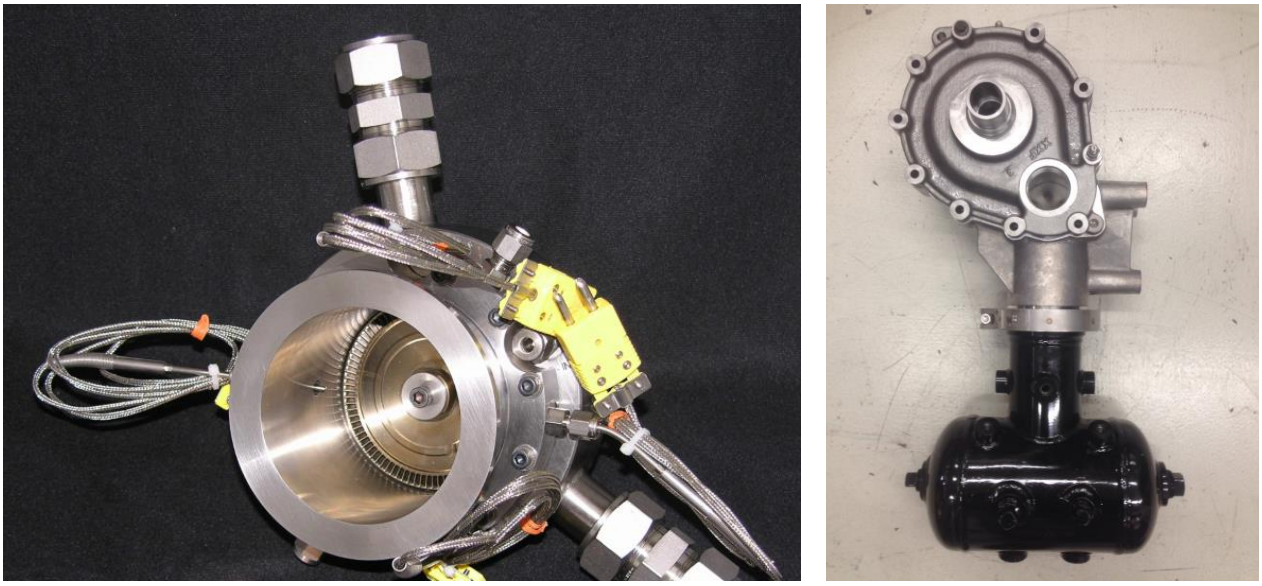

Figure 269: Complete Dual-Inlet Turbine Expander (Left) and Turbine Gearbox/Sump Assembly (Right)

With all necessary hardware for initial system testing received, assembly of the WHR shakedown system began. The purpose of the WHR shakedown system was to allow for evaluation of the key components and operating ranges of the system, without installation on a firing engine. This allowed for early experimental data to be collected and analyzed and served as a trial run for the majority of the WHR components. Before the system was assembled, a Process and Instrumentation Diagram (PNID) was completed for the shakedown system (Figure 270). From this PNID, each sensor, actuator and plumbing component was selected, procured, and assembled. This layout allows for detailed evaluation of the recuperator, condenser, turbine expander, and gearbox components, and will indicate whether the system is operating as designed prior to installation on the full 55% BTE demonstration engine.

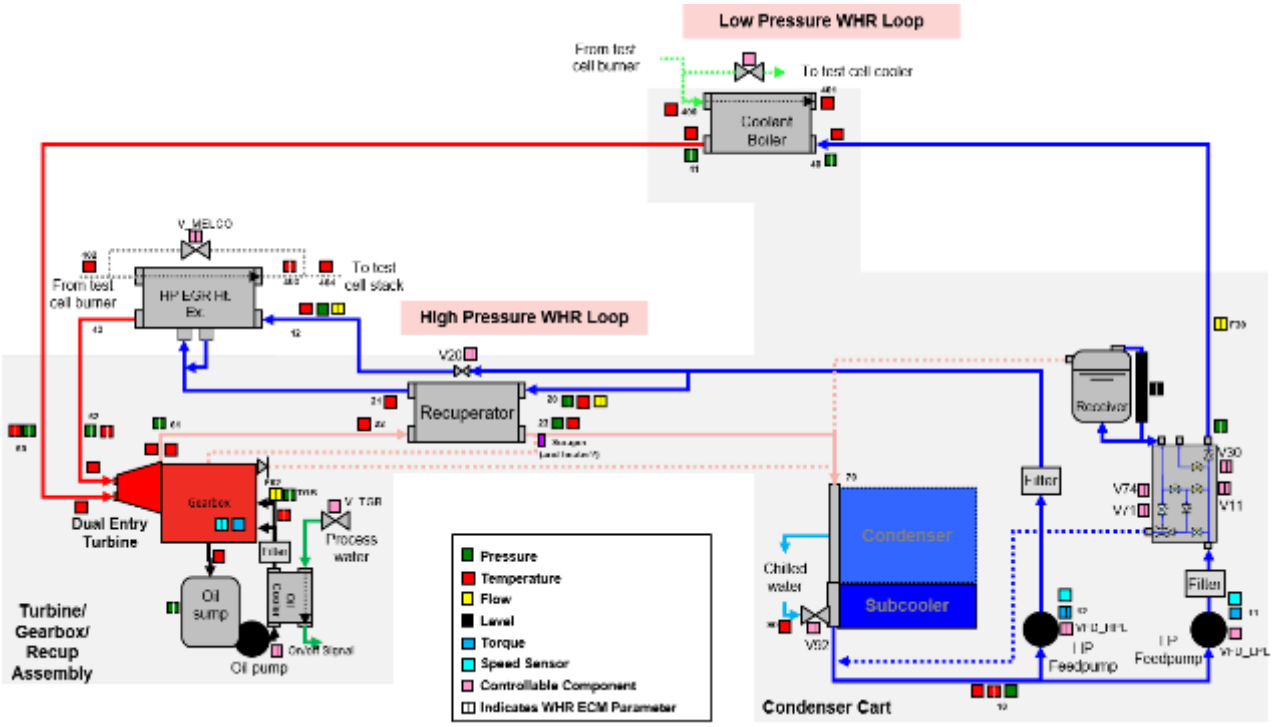

Figure 270: Process and Instrumentation Diagram for Shakedown Testing of the WHR System

Following the completion of the PNID for the shakedown system layout, construction began on the WHR cart. Figure 271 shows the cart, which supports the major components, instrumentation, plumbing, and actuators for the shakedown system, including the condenser, coolant boiler, recuperator, turbine/gearbox/sump assembly, high- and low-pressure pumps and motors, and receiver tank. The shakedown testing of the WHR system occurred in a dedicated WHR test cell, which allows for simulation of a wide range of operating conditions, including the design point for the 55% BTE demonstration.

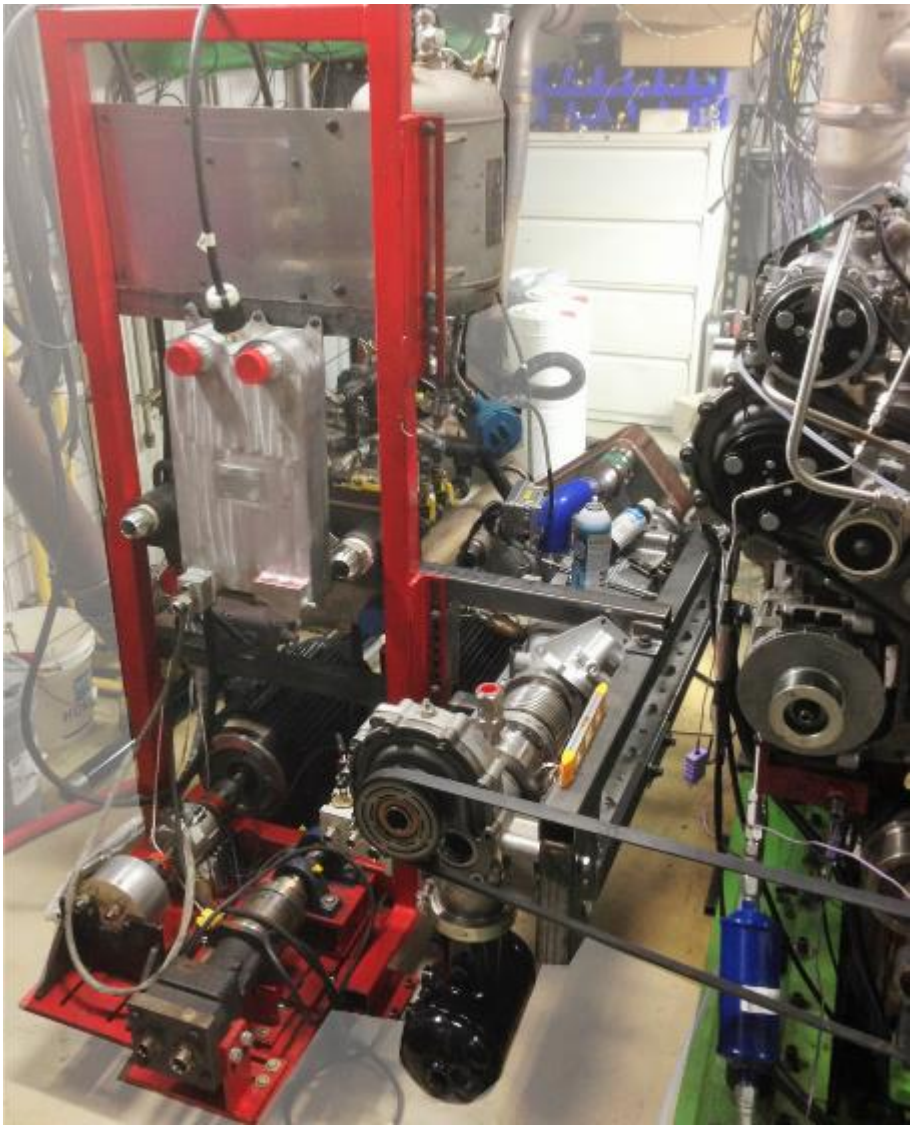

Figure 271: Waste Heat Recovery Cart for Shakedown Testing

After completing the final assembly of the WHR shakedown system, performance testing was conducted. During testing, the WHR system was coupled to a non-firing ISX15 engine and heat input was provided by natural gas burners. This allowed for more precise control and measurement of the heat inputs, and for testing to occur over a wider range of operating conditions than would be easily achievable with a firing engine. To simulate the waste heat conditions expected during the full 55% BTE demonstration, the heat input to the coolant boiler was increased (to include the heat input expected from the mixed-charge cooler and oil cooler), and a prototype exhaust gas cooler was used in place of the tailpipe boiler (for ease of installation in the experimental facility). These changes were not expected to have a large impact on WHR system performance, as compared to the final on-engine demonstration.

System performance was characterized at the expected conditions for the 55% BTE demonstration point. Additionally, off-design operation was studied to determine component sensitivity to various operating conditions, allowing for further optimization. This is particularly significant in the cases of the efficiency and power output of the dual-inlet turbine expander, which were expected to have relatively high sensitivity to rotational speed, inlet pressure, and flow rate. System heat inputs and power output for operation at the design point are shown in Figure 272. The high-pressure loop (HPL) and low-pressure loop

(LPL) heat inputs were determined to be 67.2 and 102.2 kW, respectively, totaling 169.4 kW. This compares well with the specified design-point conditions of 71 and 98 kW for the HPL and LPL, respectively, with the slight differences (lower HPL input and high LPL input) recorded during testing tending to give conservative results. Net gearbox power (power transmitted through the WHR belt drive - Figure 273) was calculated to be 20.7 kW, based on torque and speed measurements. With known gearbox parasitic loads, the actual turbine wheel power is calculated to be 22.2 kW. Based on the turbine design, performance was predicted to fall within the range of 21.4 to 23.4 kW, showing good agreement with the test results. By accounting for the power consumed by the system feedpumps and lube pump, the net power produced by the system is calculated at 18.2 kW at the design point. At the expected design point conditions, this results in a BTE improvement of approximately 4.2 percentage points.

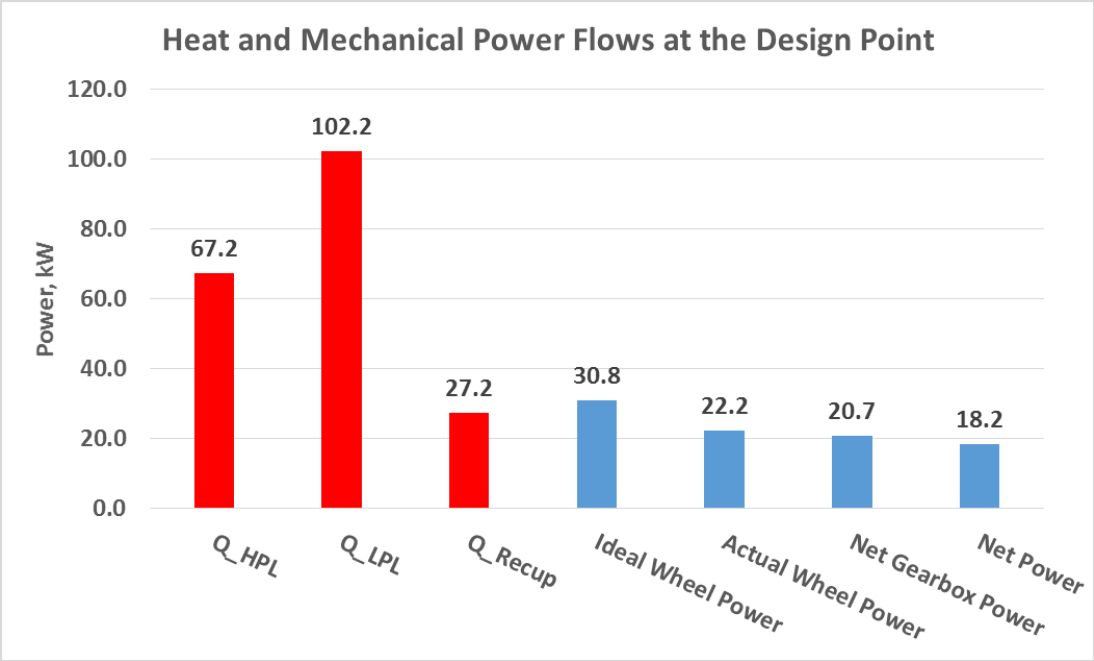

Figure 272: Shakedown Testing Design Point WHR Heat Input and Power Output

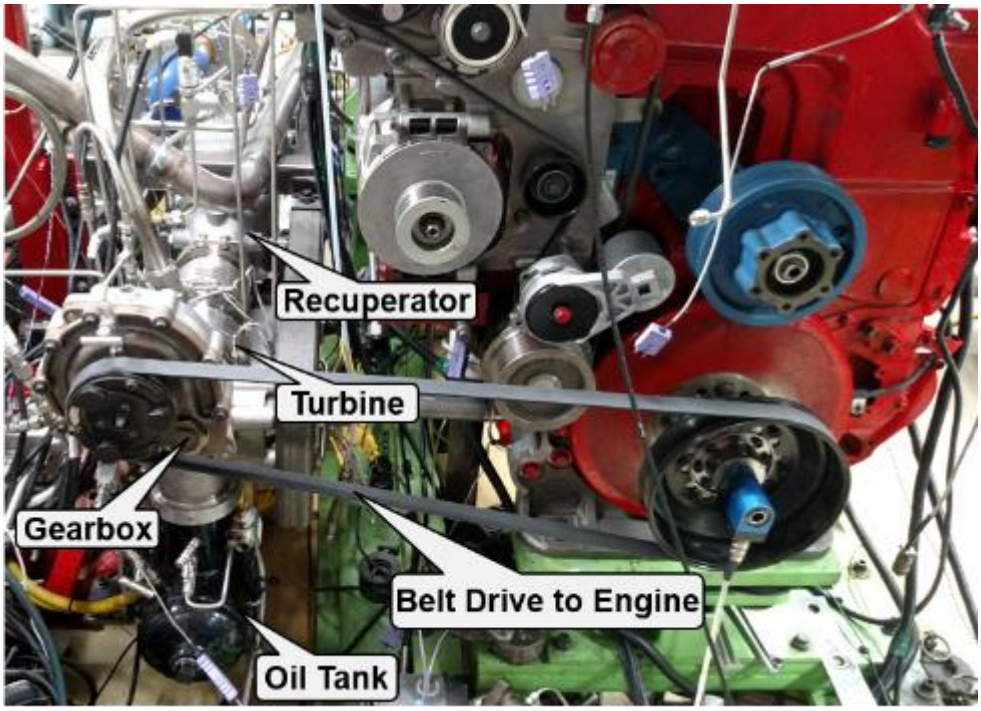

Figure 273: WHR Shakedown - Turbine and Belt Drive Systems

In addition to testing at the design point, parametric studies of turbine speed, turbine pressure ratio, and turbine oil flow were conducted. Figure 274 shows the influence of turbine speed on WHR power output. The mechanical-based data series show the power output based on measurements of torque and speed with subsequent corrections to account for pump power (to determine net WHR power) and belt-drive/gearbox parasitics (to determine gross turbine power). The thermodynamics-based calculation of gross turbine power was based on an unverified method for determining turbine outlet temperature for both the high- and low-pressure turbine sections and was found to result in low-accuracy predictions of turbine power. The data shown in Figure 274 indicates that peak net WHR power (at the design point) can be achieved with a turbine speed of approximately 30,500 RPM. This conclusion was used to guide subsequent re-design of the WHR belt drive for implementation in the final on-engine demonstration.

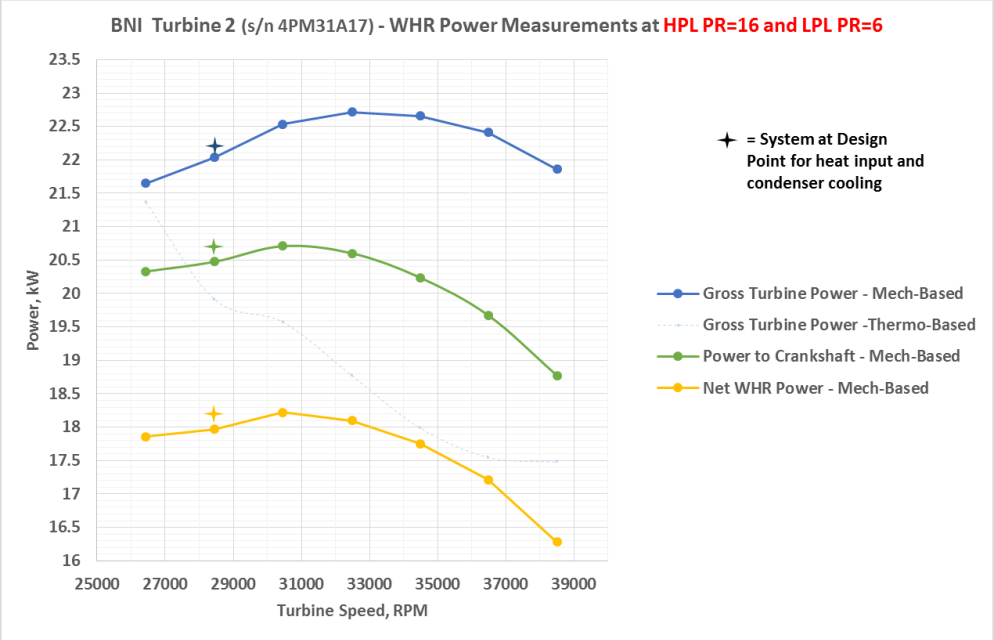

Figure 274: Influence of Turbine Speed on WHR Power Output

In addition to providing insight on the system-level and turbine performance, the data collected during shakedown testing was also used to determine the suitability of the WHR condenser, recuperator and pump components. At the design point, the recuperator provided 27.2 kW of heat transfer between the hot and cold refrigerant streams, an improvement of approximately 4 kW relative to the design conditions. This increase in performance is beneficial to system output, particularly considering that the component pressure drop was found to be at or below specification.

Condenser performance was likewise found to be acceptable. Throughout testing, the condenser capacity was sufficient to maintain the turbine outlet pressure at the specified design-point value while sustaining realistic temperatures for the simulated ambient temperature sink (conditions were set to be representative of ambient air temperatures of 12.8C).

The refrigerant feedpumps were also evaluated and found to produce the required flow rates during shakedown testing. Analysis of the data does indicate some opportunity for improvement of the pumps by investigating higher-efficiency units. Based on this, alternate piston-style pumps were identified for testing on the final on-engine demonstration.

On-Engine Demonstration Overview and Results

After completing the final shakedown testing and receiving the last of the required WHR system components, including the mixed-charge cooler core and headers, the WHR system was transported to the engine test cell for the 55% BTE demonstration. Work began on the installation of the WHR system in mid-2017. During installation, the full WHR system was assembled in the main engine demonstration test cell. The full WHR system included the engine-mounted mixed-charge cooler (MCC) and high-pressure EGR (HP EGR) cooler as well as a standalone tailpipe boiler (TPB) cart and WHR cart (Figure 275).

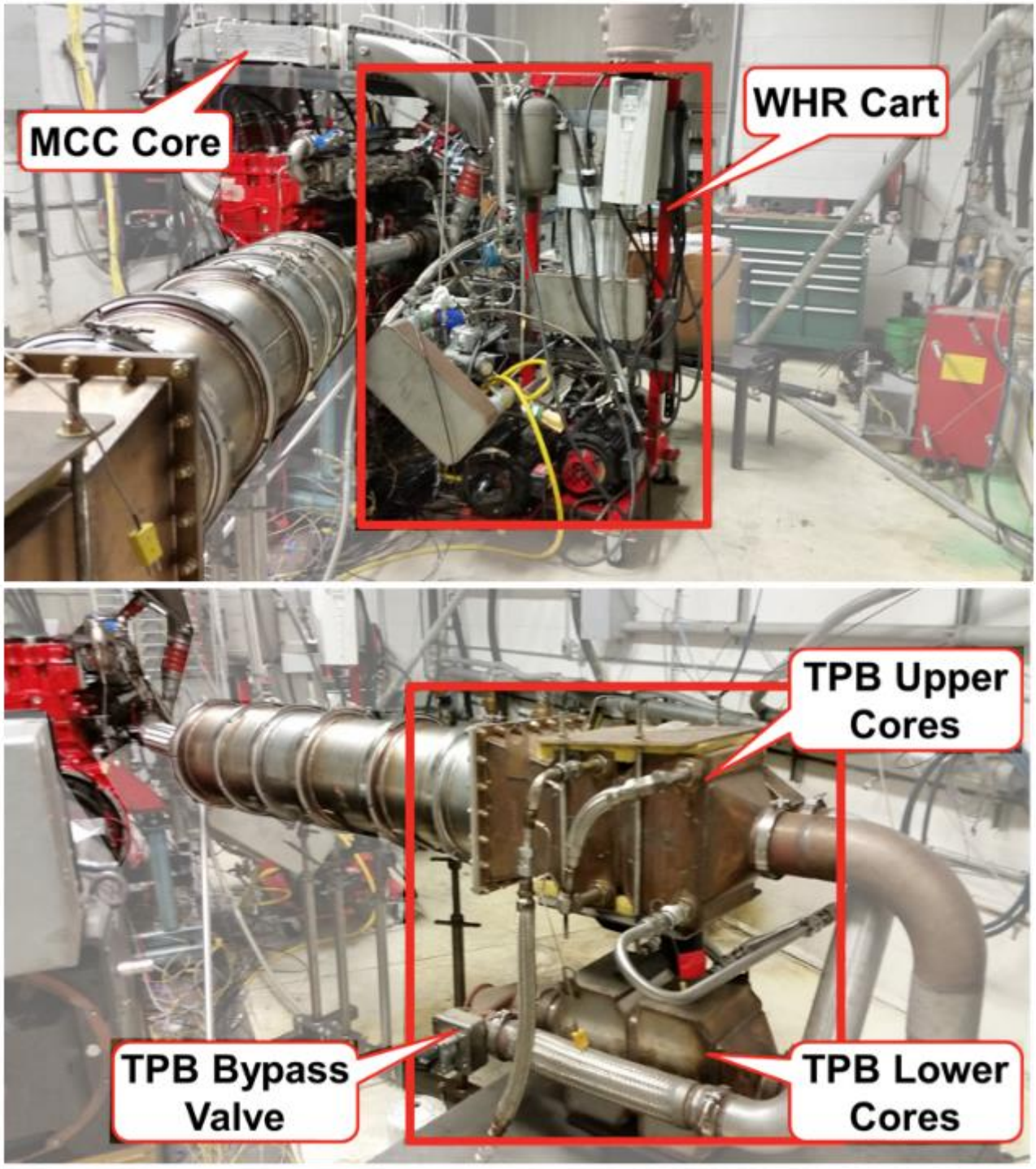

Figure 275: WHR Test Cell Installation

In this configuration, the heat input to the WHR system is supplied entirely from the waste heat streams of the demonstration engine. At the design point, waste heat is captured from the engine exhaust, mixed-charge, engine lube oil, and engine coolant. At off-design points, HP EGR heat may also be captured. Heat rejection from the WHR system to a simulated ambient is accomplished through use of facilities chilled water, with conditions set to replicate a practically feasible, vehicle-mounted air-cooled condenser. Power from the WHR turbine is transferred back to the engine crankshaft via a belt drive (Figure 276) and

WHR pump power is measured via speed and torque sensors and subtracted from the overall system power to provide a net power calculation.

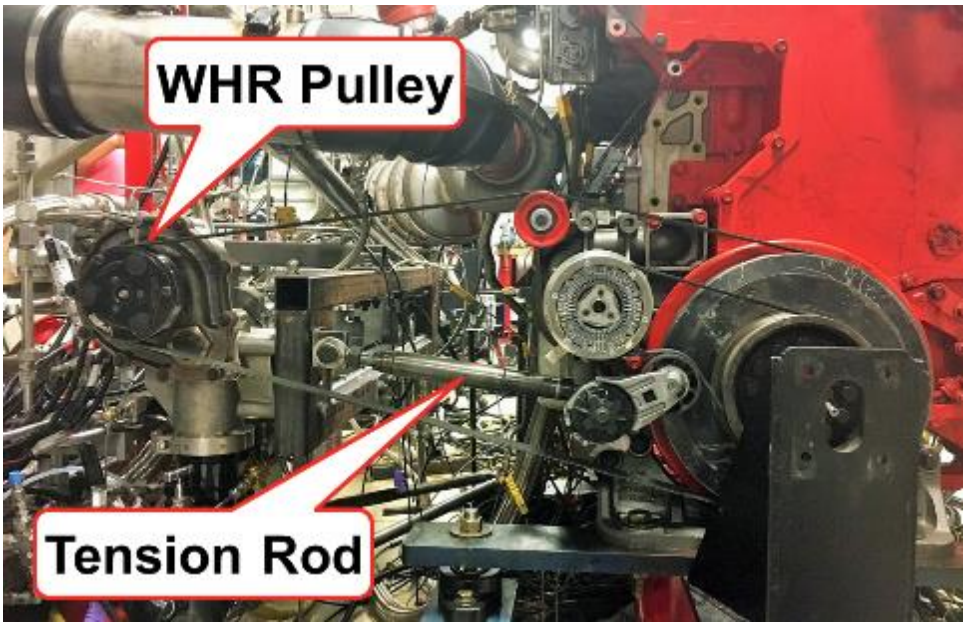

Figure 276: WHR Belt Drive

The WHR system is controlled via a dedicated Cummins WHR ECM. The controls algorithms actuate valves throughout the system and sets pump speeds to control refrigerant flow and liquid levels at the appropriate values, thus maintaining the desired system operation. Engine parameters, such as speed and fueling are passed to the WHR ECM. The WHR ECM returns calculated and measured system parameters and passes any system safety faults to the test cell interface and base engine ECM.

After completing installation, the system was charged with refrigerant and testing was started. During initial testing, the system maintained the target temperatures for engine oil, mixed-charge, and low-pressure EGR (LP EGR) at the design conditions. However, analysis indicated that additional cooling of the mixed-charge would be beneficial for engine performance. Additionally, excess heat was available from the engine exhaust and coolant heat was less than predicted. To resolve these issues, a revised system schematic was devised and implemented and a resized, dual-core oil cooler and larger condenser were installed. The revised WHR schematic is shown in Figure 277. This represents the final configuration testing during the program.

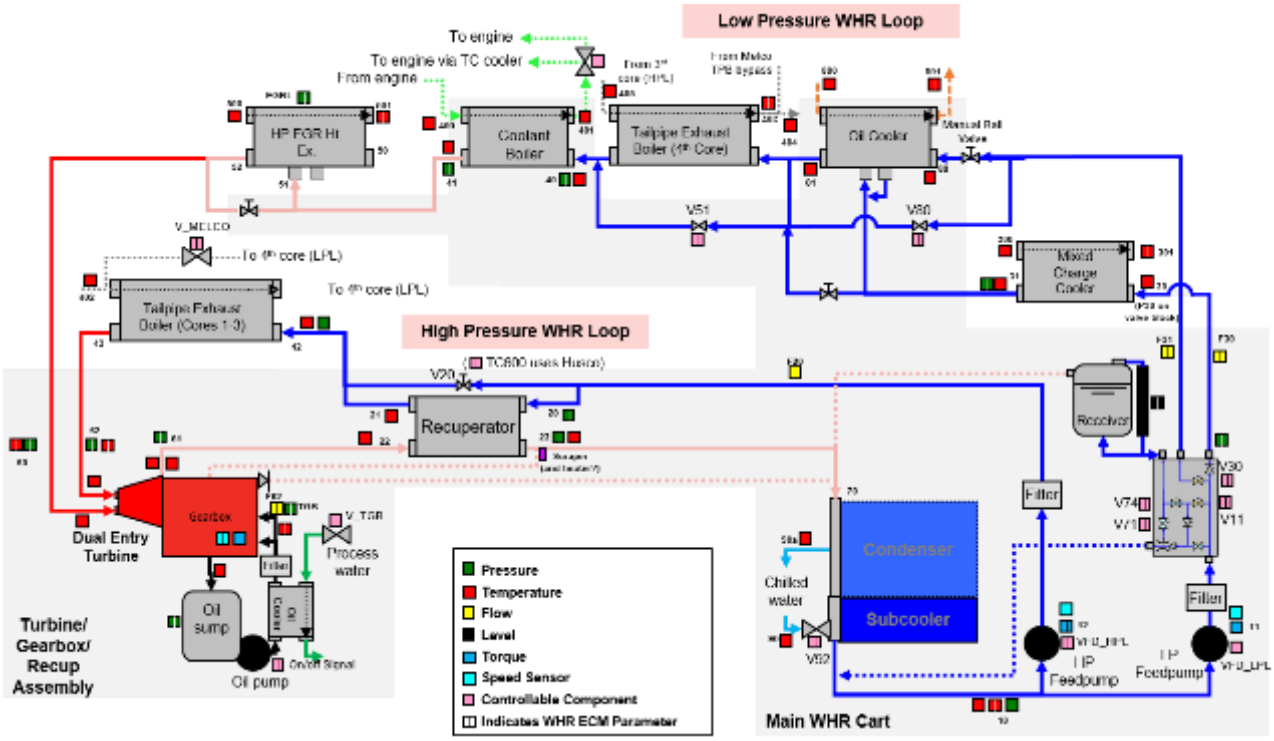

Figure 277: Final WHR Schematic

Following the revisions to the system layout, testing was continued to identify the most favorable conditions for peak engine BTE, and to identify additional areas for WHR improvement. By late 2017, the WHR system was able to demonstrate a BTE contribution of 4.07 points to the engine near the BP1 point (1000 RPM, 215 kW brake power), representing a net WHR output of 17.50 kW. While this surpassed the original modeling predictions for system output, additional revisions were implemented to increase WHR power. A pair of high-efficiency feedpumps were installed, raising efficiencies to 81.9% and 65.1% for the high-pressure and low-pressure pumps, respectively. This change is estimated to represent a 0.20-point increase in overall powertrain BTE. Improvements worth an estimated 0.06 BTE points were also made in exhaust heat recovery, by improving insulation and reducing pressure drop. A revised WHR best drive with reduced parasitics and an increased belt ratio was also fitted to the system. This raised turbine speed relative to earlier testing, placing the turbine operating conditions closer to the peak efficiency point. Finally, a significant effort was made to maintain condenser pressures at the specified value. By taking measures to mitigate leakage and purify the refrigerant charge, the condenser performance was ultimately improved and was able to perform as expected at the final demonstration point. At this point, a condenser pressure of 152 kPa was achieved at a condenser capacity of 166 kW. As shown in Figure 278, this is estimated to be equivalent to a vehicle with twice the cooling module capacity of the Cummins Gen4 WHR-equipped Navistar Prostar chassis tested previously by the WHR team. The data shown assumes the NOAA average ambient temperature (12.8°C) for North America.

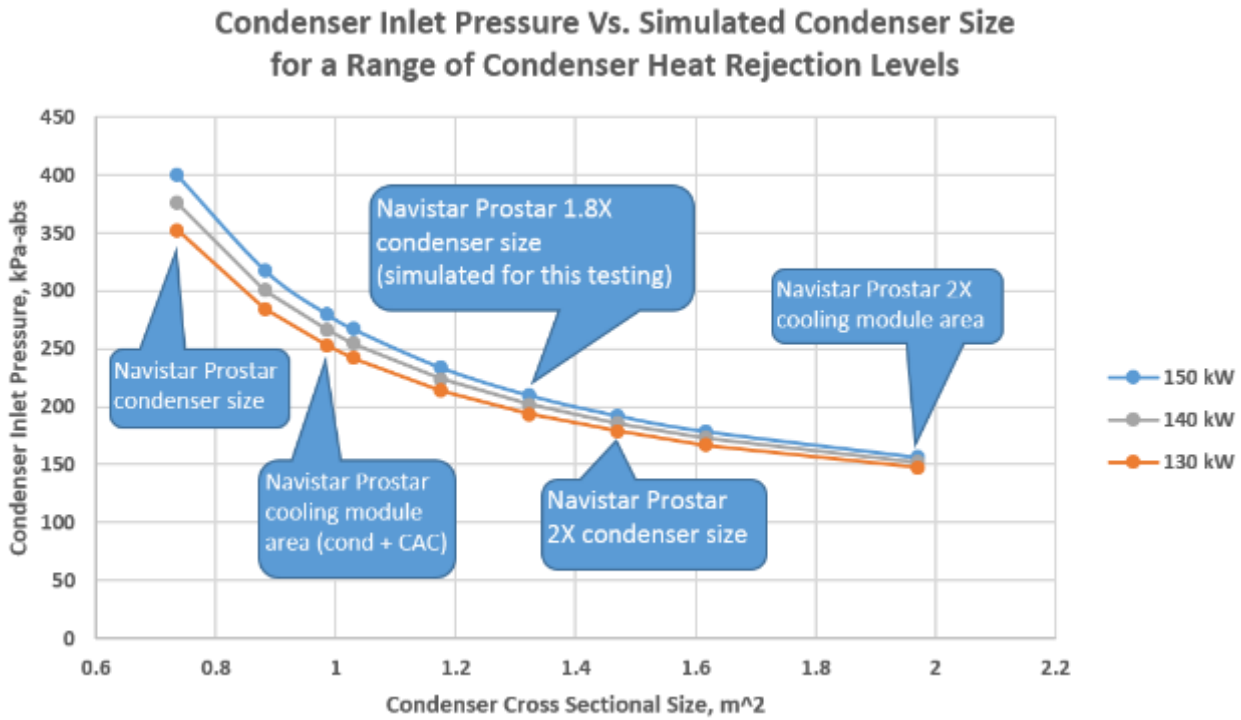

Figure 278: Condenser Inlet Pressures For Several Sectional Areas and Heat Duties

Following the optimization work detailed above, additional scouting was conducted and a final demonstration point was selected at slightly higher engine RPM and load, which gave the maximum observed overall BTE. The final "best BTE" point was identified at 1050 RPM engine speed and approximately 240 kW brake system power (combined WHR and engine power, measured at the dyno). At these conditions, the WHR system provided 19.3 kW net power to the engine; a WHR net BTE benefit of 4.30%.

The T-h cycle diagrams for the WHR system are shown in Figure 279 for the best BTE point and the original system model. Despite some minor changes implemented to the component layout, heat sources, and operating conditions, good agreement can be seen between the model and experimental results. Of particular note are the lower LPL superheat value at turbine entrance, and somewhat higher HPL temperatures (corresponding to higher HPL pressures) shown for the experimental data. The lower superheat value was found to produce optimal power from the LPL, at these conditions, and was modified based on results from the final testing. The higher HPL pressures were a result of the higher exhaust heat rejection rates, which were generally favorable for WHR, even though they cause a small decrease in turbine efficiency.

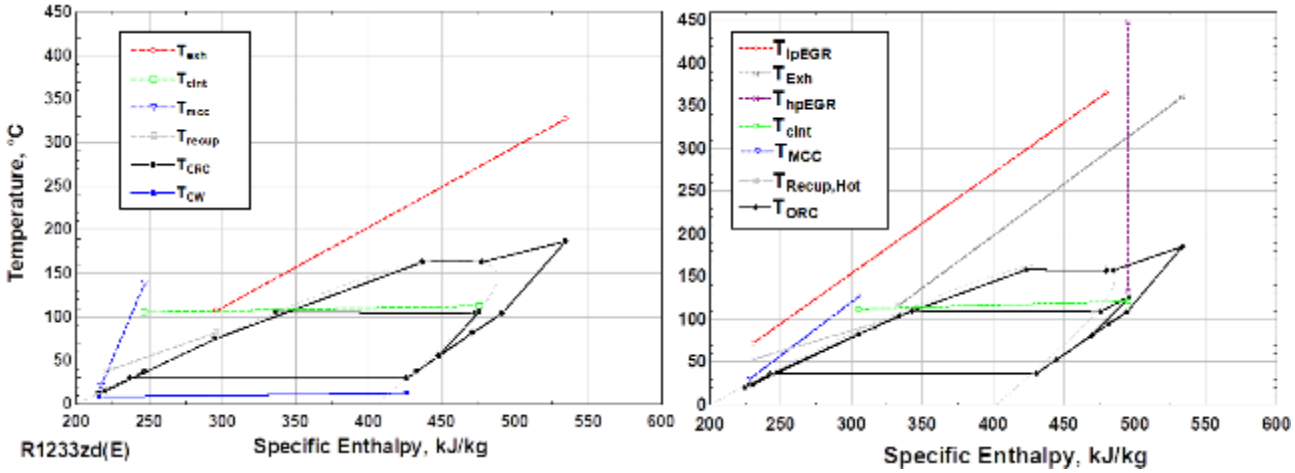

Figure 279: Cycle T-h Diagrams for Final Test Point (Left) and Original Model (Right)

The primary heat rates and mechanical power output of the WHR system are shown in Figure 280 for the final demonstration point ("best BTE"), the BP1 point, and the original WHR shakedown point. The original modeling predictions are also shown for reference. The experimental data indicates that, at the final, best BTE point, the WHR system received less overall heat input (due to lower coolant heat input) than expected during the shakedown test, which was conducted with simulated engine waste heat. However, the increase in exhaust heat input and reduction in required pump power resulted in an overall increase in net system power, which increased from 18.2 kW during shakedown to 19.3 kW (Table 18) at the "best BTE" point. Based on the total heat input and net system power, an overall WHR thermal efficiency of 11.6% is calculated for the best BTE point.

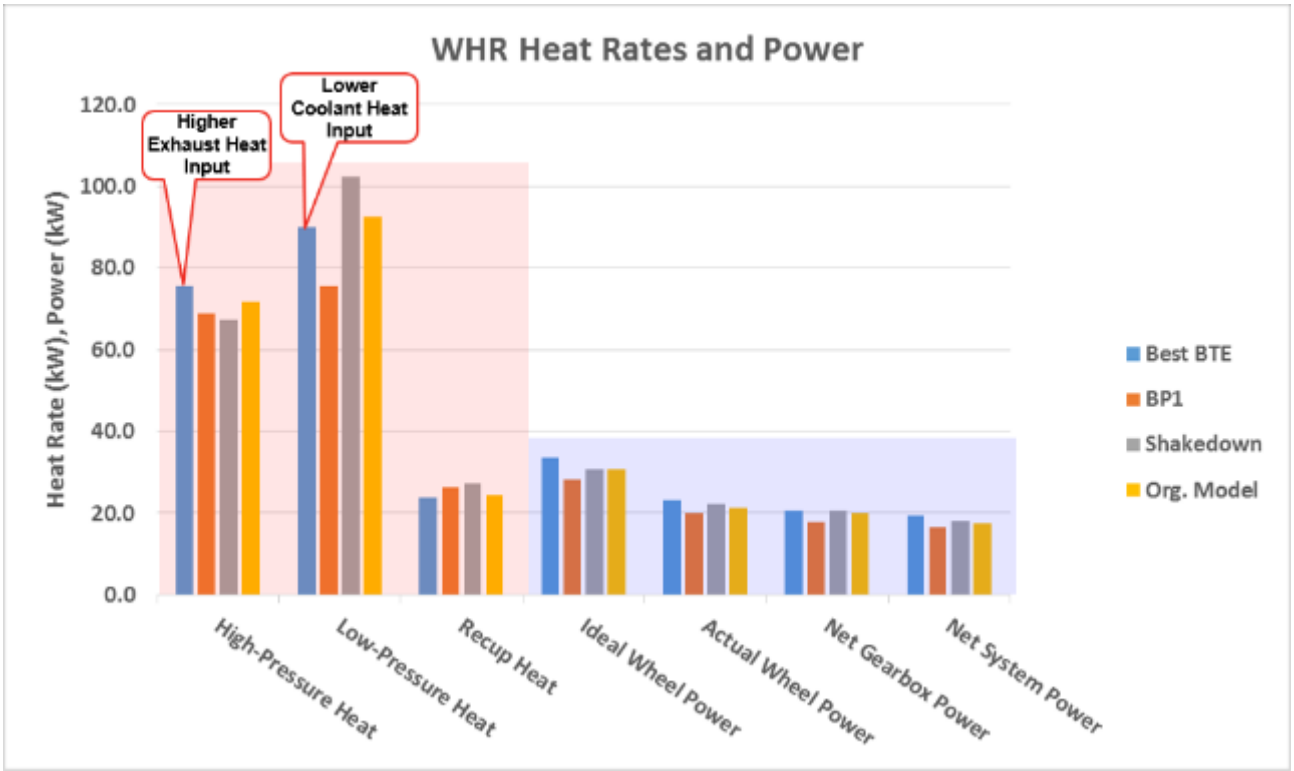

Figure 280: WHR Heat and Power Flow

Table 18: WHR Heat and Power Values for Best BTE, BP1, and Shakedown Test Points

Test Point	HPL Heat	LPL Heat	Recup Heat	Ideal Wheel Power	Actual Wheel Power	Dyno Power	Net Power	Pump Power	Gearbox Losses
-	(kW)	(kW)	(kW)	(kW)	(kW)	(kW)	(kW)	(kW)	(kW)
1157 (Best BTE)	75.5	90.1	23.9	33.7	23.0	20.8	19.3	1.5	2.3
1237 (BP1 Point)	68.8	75.5	26.4	28.1	20.0	17.9	16.6	1.3	2.1
Shake-down (Design Point)	67.2	102.2	27.2	30.8	22.2	20.7	18.2	2.5	1.6

Analysis of the mechanical power output and losses (Figure 281) indicates that the turbine efficiency is lower at the "best BTE" point, compared with the shakedown testing, as indicated by the larger drop in power between the ideal and actual wheel power. This is due to the higher pressure ratios observed in the final testing, and could be partially remedied with a turbine redesign that optimizes turbine nozzle and wheel/blade geometry for these conditions. Additionally, gearbox parasitics are 0.7 kW higher at the "best BTE" point, relative to shakedown. This is likely due to the higher turbine speed, which increases losses associated with the turbine and low-speed shaft bearings, windage, and belt drive. Feedpump power is reduced in the final demonstration, as discussed previously, due to the higher pump efficiency.

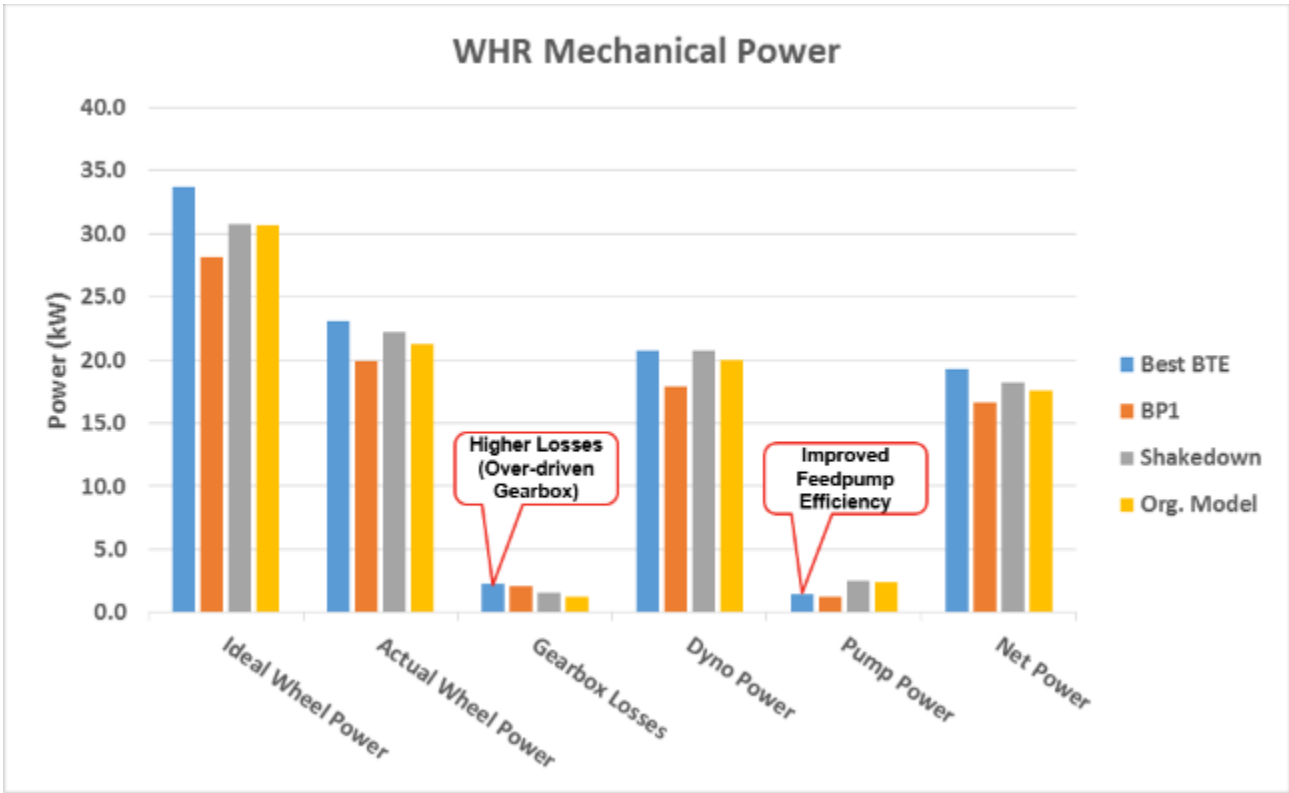

Figure 281: WHR Mechanical Power and Losses

These results provide experimental validation of the initial modeling work, which estimated that a WHR BTE benefit of greater than 3.7% could be achieved. The 4.3% (19.3 kW) benefit observed in the final demonstration, was made possible by the additional optimization and refinement of the system, which was conducted over the course of the program. Further analysis has been conducted to determine areas for

future improvement and to provide an estimate of the WHR performance that would be possible with additional development work and minor redesign of key components.

Summary of Potential System Improvements

The final on-engine testing of the Cummins WHR system demonstrated a net BTE benefit of 4.3%, exceeding original modeling predictions of 3.7%. However, analysis of the experimental results led to the identification of several additional system improvements, which could potentially increase the output of the WHR system beyond the levels demonstrated in the current program. These improvements are outside of the budget and timeline constraints of the current 55% BTE program, but identifying and quantifying these improvements helps to guide work for future WHR programs, and gives an indication of the entitlement for other advanced WHR systems deployed in future development efforts. In considering potential improvements, three categories are worth discussing here: items that have been optimized to the point where additional improvements are unlikely, areas of the system that could be improved with the currently available hardware from this program, and areas that could only be improved with redesigned hardware. The areas where improvements are possible, and the projected impact on WHR power, are given in Table 19.

Table 19: Potential Areas of Improvement and Impact on WHR Output

		Impact on WHR Power	Impact on System BTE
		W	%
Current Hardware	Speed Reduction	670	0.150
	Exhaust Insulation	225*	0.051
	Refrigerant Line Insulation	360*	0.081
	Subtotal	1255	0.282
Redesigned Hardware	Turbine Redesign	1500	0.337
	MCC and LPL Plumbing dP	40	0.009
	HPL Plumbing dP	30	0.007
	Subtotal	1570	0.352
	Total	2825	0.634

* Values given are the high-end of expected benefit

Examining areas of the WHR system where future improvements are unlikely to be significant, relative to the current hardware, the condenser and feedpump sub-systems are both likely operating near the limits of currently available technology for in-vehicle applications. As discussed above, and shown previously in Figure 278, the condenser used in the final testing achieved performance equivalent to a 2x increase in the cooling module effective area of a current production class 8 vehicle. This was identified as a feasible metric for a vehicle with a cooling module and aerodynamics that were optimized for WHR. However, it's unlikely that condenser performance beyond this point would be possible without a major departure from current vehicle design and air-side heat exchanger performance. Secondly, the working-fluid feedpumps utilized in the final demonstration had calculated efficiencies of 81.9% and 65.1% for the HPL piston pump and LPL gear pump, respectively. These values are among the highest observed across a wide range of feedpumps evaluated in Cummins WHR systems of these capacities and pressure ranges. Additionally, due to independent speed control for both pumps, no losses from fluid recirculation were incurred. As such, this is likely another area where minimal system-level improvements would be expected without a major development in pump technology.

Considering improvements that would be possible with the current hardware, three main items have been identified. Reducing the speed of the turbine to achieve peak power from the gearbox is the largest single improvement that could be made to the current system. While requiring a revised WHR belt pulley, a minor modification to the system, this would reduce the parasitic losses of the gearbox and turbine components with only a very modest reduction in the gross turbine power, resulting in a net increase in WHR system power of approximately 670 W (Table 19). The gross turbine and net WHR power are shown as a function of speed in Figure 282, illustrating the benefit of lowering turbine speed. The other two areas where improvements are possible with the current hardware are in improved thermal insulation of the exhaust system and high-temperature refrigerant lines. These factors were likely more pronounced in the current test cell demonstrations, as compared to expected vehicle testing, as test cell air temperatures are expected to be much lower than under-hood or under-vehicle temperatures. However, a combined 585 W of additional WHR power could be produced if these losses were eliminated (Table 19).

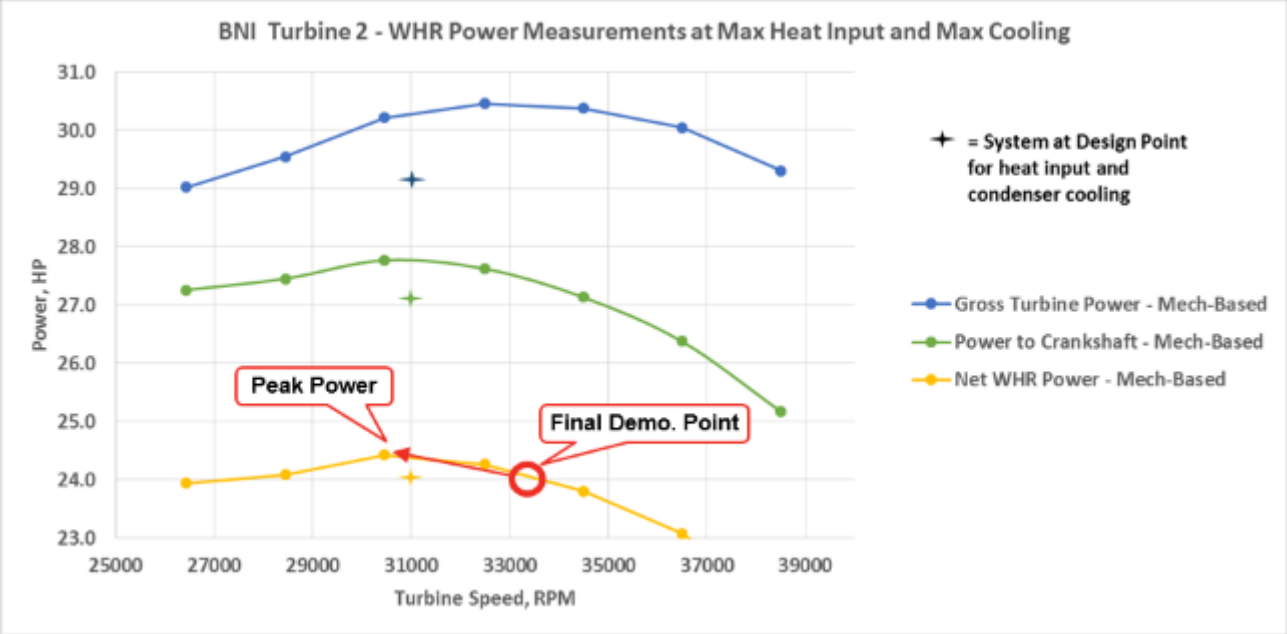

Figure 282: Influence of Revised Turbine Speed on WHR Power

The final areas of potential improvement identified would require redesigning significant portions of the system, but could be readily accomplished with additional resources. The major area for improvement in a redesigned system is the turbine expander. While the current unit performed at or above expectations, the final demonstration point, where best overall BTE was observer, deviated significantly from the original turbine design conditions. As such, if a new turbine were designed and produced to exactly match the final operating conditions, additional WHR output of 1500 W is expected (Table 19). This value is based on consultation with Barber Nichols, and is supported by the fact that 1240 W additional power could be produced if the turbine were simply to match the efficiencies observed in testing under the shakedown conditions, which were closely aligned with the design conditions. A final 70 W of additional WHR output could also be easily achieved by optimizing the design of ports, plumbing, and component headers to reduce pressure drop, thereby lower the required pumping power (Table 19).

Considering all areas where potential improvements have been identified, an additional 2825 W of WHR power could be achieved through a combination of optimizing the current hardware, and redesigning key components of the current WHR system (Table 19). Generally, these are feasible improvements with a clear path to achieving the stated increase in performance, but are beyond the scope of the current program. If all improvements were implemented, and engine and waste heat conditions were maintained, the resulting 2825 W of additional WHR power would result in a total WHR BTE benefit to the engine of 4.96 points.

Summarizing the major accomplishments of the WHR effort, the ORC-based system developed for the 55% BTE program demonstrated a benefit of 4.30 BTE percentage points in the final on-engine demonstration. At these conditions, the WHR turbine returned 19.3 kW of net power back to the engine crankshaft via a modified FEAD belt drive. This was done while providing all required cooling for the engine coolant, oil, LP EGR, and charge gases. Additional improvements identified in the final analysis would allow for a further 2.8 kW of net power output, raising the total BTE benefit of the WHR system to 4.96 points.

This success has helped to prove the feasibility of the novel dual-entry turbine used in this project, and much of the technology developed in this program will be utilized and refined in future programs.

4. Summary

The Cummins 55% BTE (55BTE) program has completed the planned technical work on the project. This work includes the planned engine system demonstration in pursuit of the goal of demonstrating a peak system brake thermal efficiency (BTE) of 55%. The engine system included a high efficiency diesel engine integrated with a state-of-the-art waste heat recovery (WHR) system and an advanced aftertreatment system capable of meeting the current emissions standards. While the ultimate program goal of 55% BTE was not fully achieved due to hardware issues during the final testing phase, the program demonstrated a significant increase in reported engine system BTE for a heavy duty sized engine. The previous demonstrations in the Department of Energy funded SuperTruck 1 programs ranged between 50% - 51% BTE. The Cummins 55% BTE program demonstrated 54% BTE. Additionally, the program established a revised path-to-target showing how the system could be improved to reach the ultimate program goal of 55% BTE with some minor modification to the engine system. The changes in the revised path-to-target were unable to be completed during the course of this program due to time and money constraints placed on the program.

The program's goals were challenging in both scope and timing. Although the program's goal can be simply stated in terms of demonstrating a system efficiency of 55%, the achievement of a heavy-duty diesel engine capable of full torque curve operation, adequate transient performance, low emissions and high brake thermal efficiency (>51% BTE) had not been previously demonstrated in a heavy-duty engine. The Department of Energy funded SuperTruck 1 program only demonstrated efficiencies of 50%-51% BTE. During these efforts, much of the more-easily implementable changes had been investigated and included. This makes follow on work aiming to further increase efficiency more difficult as the bigger improvements had already been incorporated. Additionally, there were virtually no subsystems that were not improved during the SuperTruck 1 programs. This meant that the team would need to go back and try to further improve virtually all subsystems again in this effort to achieve the stated program goals.

The program made several advancements in all system areas. The combustion system was re-designed for a shorter combustion duration and lower in-cylinder heat loss. This was achieved through optimization of the fuel injection rate shape, number of spray holes, piston bowl shape, compression ratio, piston oil cooling, heat flow through the piston and in-cylinder charge motion. The air handling system was re-designed to provide cooled EGR at virtually no pumping penalty. This was achieved through implementation of a dual loop EGR system, reduction of EGR system pressure drop, and implementation of advanced turbocharger efficiency technologies. The engine friction and parasitic signature was dramatically reduced by the program through adoption of variable flow pumps, advanced rings and coatings, rollerized valvetrain, adoption of low viscosity lubricants and reduction in cylinder line bore distortion. The aftertreatment system was optimized through use of low dP substrates and an ammonia gas injection system. The WHR system development included the use of a dual-entry turbine and a mixed charger cooler. Finding and implementing these solutions in a short two-year program at the budgeted funding provided the greatest challenge for the program.

The details of these advances are covered in Section III of the report.

Section II – Issues, Risks, and Mitigation

None to report.

Section III – Changes in Approach

None to report. No changes in approach occurred in this reporting period.

Section IV – Key Personnel

None to report. No changes in key personnel occurred in this reporting period.

Section V – Project Output

A. Publications

None to report. No publications occurred in this reporting period.

B. Technologies/Techniques

None to report. No technologies/techniques were developed in this reporting period.

C. Status Reports

None to report. No reports were delivered in this reporting period.

D. Media Reports

None to report. No media articles occurred in this reporting period.

E. Invention Disclosures

None to report. No invention disclosures were submitted in this reporting period.

F. Patent Applications

None to report. No patent applications were submitted in this reporting period.

G. Licensed Technologies

None to report. No technologies were licensed in this reporting period.

H. Networks/Collaborations Fostered

None to report. No networks/collaborations were fostered in this reporting period.

I. Websites Featuring Project Work or Results

None to report. No websites featured project work or results in this reporting period.

J. Other Products

None to report. No additional project output occurred in this reporting period.

K. Awards, Prizes, and Recognition

None to report. No additional awards or prizes occurred in this reporting period.

Section VI – Follow-On Funding

None to report. No follow-on funding was received to support the program in this reporting period.

Section VII – Recipient and Principal Investigator Disclosures

None to report. The Recipient and Principal Investigator do not meet any of the conditions listed in Section VII.

Section VIII – Conflicts of Interest Within Project Team

None to report. No conflicts of interest with the project team occurred in this reporting period.

Section IX – Performance of Work in the United States

None to report. No program work was performed outside the United States in this reporting period.

Section X – Project Schedule Status

The Cummins 55% BTE program consists of four phases carried out over a two-year period. An overview of the work contained within each phase is detailed below.

- **Phase 1, System Design & Analysis** to develop detailed component and system designs prior to the time and cost-intensive prototyping phase.
- **Phase 2, Design Procurement & Rig Validation** to refine component and system designs prior to the time and cost-intensive prototyping phase.
- **Phase 3, Multi-Cylinder Engine Development Testing** to validate the combined system level effects of proposed system architectures and components.
- **Phase 4, Final Multi-Cylinder Engine Demonstration** in a test cell of a diesel engine system with a peak efficiency of 55% BTE that meets 2010 emissions standards to address the ultimate technical objectives of the RFP.

The major program milestones contained in the Cummins – DoE contract are listed in Table 20. The program milestones are used to track the health of the program. The milestone attainment tracking of the program is shown in Figure 283.

Table 20: 55BTE Program Milestone Details

Milestone	Description	Anticipated Start Date	Anticipated Completion Date	% Complete	Comments
M1	Lube Pump Design Complete and Procured	1/1/2016	3/31/2016	100	**Complete**
M2	Air Handling Controls System Design Selection Complete	1/1/2016	6/30/2016	100	**Complete**
M3	Lube Pump Design Integration Complete	4/1/2016	09/30/2016	100	**Complete**
M4	WHR Turbine Expander Design Complete	1/1/2016	12/31/2016	100	**Complete**
GNG1	50% BTE (Engine Only) Demonstration Complete	1/1/2016	12/31/2016	100	**Complete**
M5	Aftertreatment System Design Complete	2/1/2016	3/31/2017	100	**Complete**
M6	SET Emissions Demonstration Complete	4/1/2017	6/30/2017	100	**Complete**
M7	Hot FTP Emissions Demonstration Complete	4/1/2017	09/30/2017	100	**Complete**
M8	55% BTE Final Demonstration Complete	4/1/2017	01/31/2018	100	**Complete**

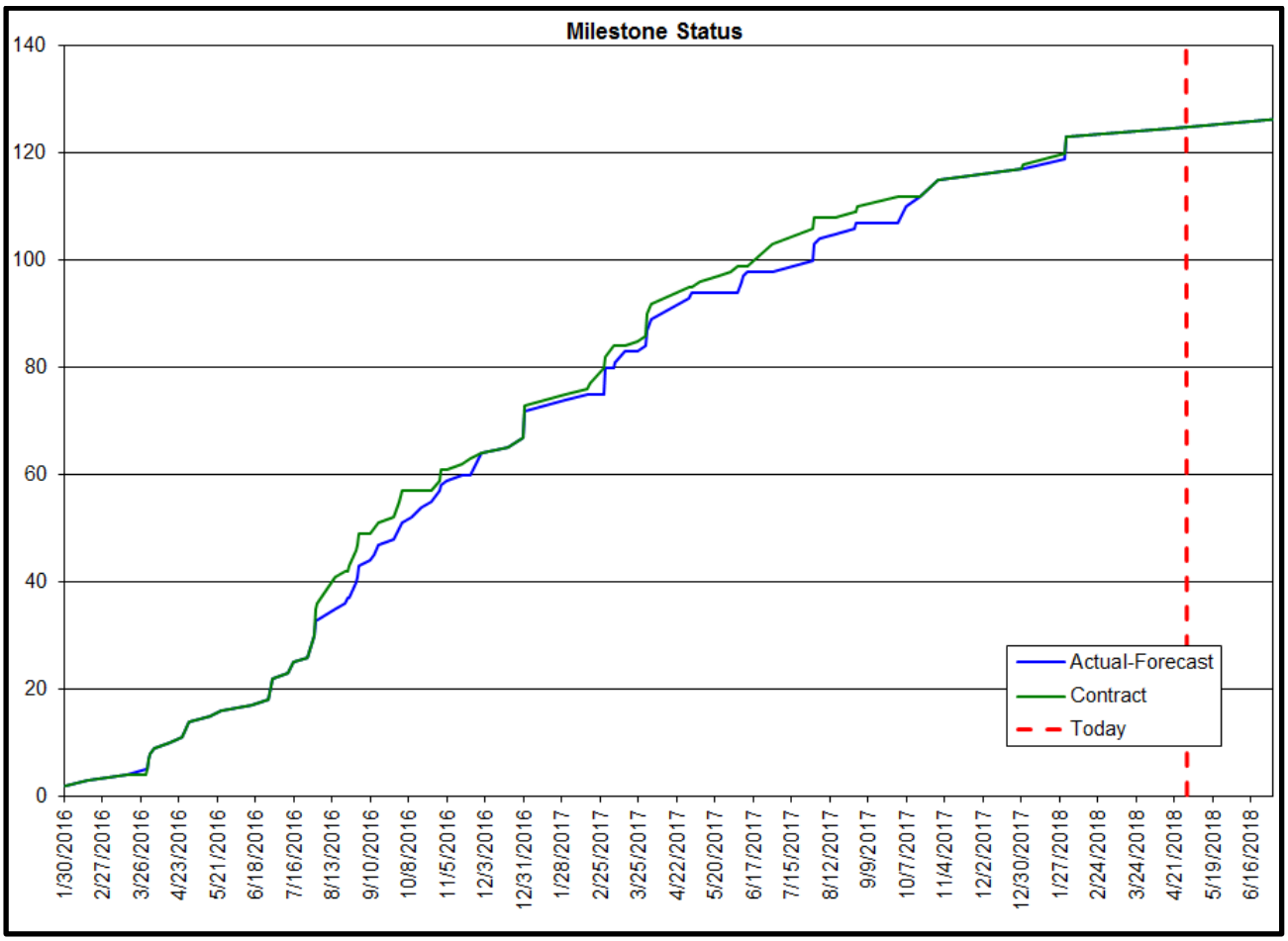

Figure 283: 55BTE Milestone Attainment Tracking Status of Q2 2018

Section XI – Budget Status – Prime Recipient

The total DoE spend to date is $4,481,115. The projected program spending is shown is shown in Table 21. The program received a no cost extension and will continue to operate with additional recipient funds as shown below.

Table 21: 55BTE Project Spend Plan

Project Spending Plan								
Budget Period	Quarter	From	To	Estimated Federal Share of Outlays	Actual Federal Share of Outlays	Estimated Recipient Share (Cost Share) of Outlays	Actual Recipient Share (Cost Share) of Outlays	Cumulative Actual Outlays (Federal + Recipient)
1	4Q15	12/1/2015	12/31/2015		$ -		$ -	$ -
1	1Q16	1/1/2016	3/31/2016		$ 263,700		$ 263,701	$ 527,401
1	2Q16	4/1/2016	6/30/2016		$ 494,364		$ 494,364	$ 1,516,129
1	3Q16	7/1/2016	9/30/2016		$ 946,625		$ 946,624	$ 3,409,378
1	4Q16	10/1/2016	12/31/2016		$ 849,673		$ 849,673	$ 5,108,724
2	1Q17	1/1/2017	3/31/2017		$ 788,917		$ 788,918	$ 6,686,559
2	2Q17	4/1/2017	6/30/2017		$ 681,639		$ 681,638	$ 8,049,836
2	3Q17	7/1/2017	9/30/2017		$ 381,197		$ 636,261	$ 9,067,294
2	4Q17	10/1/2017	1/1/2018		$ 75,000		$ 622,232	$ 9,764,526
3	1Q18	1/1/2018	3/31/2018		$ -		$ 309,233	$ 10,073,759
3	2Q18	4/1/2018	7/1/2018		$ 18,885		$ 2,527	$ 10,095,171
	Subtotals			$ -	$ 4,500,000	$ -	$ 5,595,171	
	Totals			**$**	**4,500,000**	**$**	**5,595,171**	**$ 10,095,171**

Special Status Report

None to report. No special events requiring special status report occurred in this reporting period.